Accurate Skull Modeling for EEG Source Imaging

Nauwkeurige schedelmodellering voor EEG-bronanalyse

Victoria Montes Restrepo

UNIVERSITEIT
GENT

Department of Electronics and Information Systems
Medical Image and Signal Processing Group
Faculty of Engineering and Architecture
Ghent University

MEDISIP
IBiTech - iMinds Medical IT Department
Campus Heymans, Blok B
De Pintelaan 185
9000 Ghent
Belgium

Promotors
Prof. dr. Stefaan Vandenberghe
Dr. ir. Pieter van Mierlo

Board of examiners
Prof. dr. ir. Patrick De Baets, chairman
Prof. dr. ir. Guillaume Crevecoeur, Ghent University, secretary
Prof. Dr.-Ing. habil. Jens Haueisen, Technische Universität Ilmenau
Dr. ir. Gwénaël Birot, University of Geneva
Prof. dr. Kristl Vonck, Ghent University
Prof. dr. ir. Hans Hallez, University of Leuven
Dr. ir. Pieter van Mierlo, Ghent University
Prof. dr. Stefaan Vandenberghe, Ghent University

Acknowledgments

We should consider every day lost on which we have not danced at least once

—FRIEDRICH NIETZSCHE

The moment you decide to pursue a PhD you have no idea what you are getting into. I came to Belgium with one objective: to become a Doctor in Biomedical Engineering. At the beginning, everything was very exciting and felt like a dream. Along the way, there were moments of doubt and frustration but also rewarding experiences that helped me in getting to the finish line. Then I realized what doing a PhD is: it is not only a learning period that makes you an expert in a very specific subject but, most importantly, it is a journey of self-discovery and self-assurance. At the end, whatever you do depends on yourself and, although there are many people around to support you during the process, only you can walk your own path.

In the path that I have walked, my supervisors **prof. dr. Stefaan Vandenberghe** and **dr. ir. Pieter van Mierlo** have led the way. I want to thank **Stefaan** for providing me with all the facilities to perform research at MEDISIP and for letting me finish my PhD even after some delay. **Pieter** was my colleague at the beginning and became supervisor in the final years of this PhD. I am really thankful for your continuous support from Geneva and your helpful comments while writing this manuscript.

I would also like to express my gratitude to **prof. dr. Steven Staelens** and **prof. dr. Hans Hallez**. To **Steven** for being my first supervisor and the person who gave me the opportunity to come to Belgium to do a PhD. **Hans** for being the first contact person in Belgium. I thank you for guiding me at the beginning of my PhD and even after joining the University of Leuven. Your advice was always helpful and insightful.

Furthermore, I want to acknowledge **prof. dr. Roel van Holen** and

Acknowledgments

My experience as a PhD student was enriched by the interaction with people from different departments. I want to thank the people from LCEN, particularly **prof. dr. Kristl Vonck** for her feedback regarding the clinical parts of my research; and **dr. Evelien Carrette** for providing me with the patient data and solving all patient-related questions. I would also like to thank **prof. dr. Guillaume Crevecoeur** for introducing me to MEG.

Moreover, I want to acknowledge my Colombian fellows who came to visit MEDISIP: **José David López**, **David Cárdenas**, **Ernesto Cuartas** and **Juan David Martínez**. I hope we can work together in the future.

Finally, I would like to express my most sincere gratitude to my family and friends. To my Colombian friends who always encouraged me to continue: **Paula Ramos**, **Diego Peluffo** and **Rubén Pinzón**. I admire you in the way you live your lives and achieve your goals. To the friends that I met in Ghent: **Jerika Lamas** and **Rosario Porras**, you are very strong women and I know I have a true friend in each one of you. A mi **familia**: Ustedes son el pilar fundamental de mi vida, lo que me ha mantenido luchando hasta alcanzar este logro. Muchas gracias por nunca haber dudado de mis capacidades. Aunque haya estado separada físicamente de Ustedes, siempre los he llevado conmigo en mi corazón. Lastly, I want to thank **Nikhil** for his endless support, patience and love. You are my angel and certainly the best person I could have ever met. Without you, this achievement would not have been possible. And for that, I will always be thankful!

<div align="right">

Victoria
November 2016
Brussels

</div>

Acknowledgments

Table of Contents

List of Figures

List of Tables

List of Acronyms

A

AED   Anti-Epileptic Drugs

B

BCI   Brain-Computer Interface
BEM   Boundary Element Method
BOLD   Blood-Oxygen-Level-Dependent

C

CNS   Central Nervous System
CSF   CerebroSpinal Fluid
CT   Computed Tomography

D

DBS   Deep Brain Stimulation

E

ECD	Equivalent Current Dipole
ECG	ElectroCardioGraphy
EEG	ElectroEncephaloGraphy
EIT	Electrical Impedance Tomography
EM	Expectation Maximization
EMG	ElectroMyoGraphy
EOG	ElectroOculoGraphy
EP	Evoked Potential
EPSP	Excitatory PostSynaptic Potential
ERP	Event-Related Potential
ESI	EEG Source Imaging
EZ	Epileptogenic Zone

F

FBP	Filtered Back Projection
FDM	Finite Difference Method
FEM	Finite Element Method
FID	Free Induction Decay
FINES	FIrst priNciple vEctorS
FSL	FMRIB Software Library
fMRI	functional MRI

G

GFS	Goal Function Scan
GM	Gray Matter
GOF	Goodness Of Fit

H

HU	Hounsfield Unit

I

IED   Interictal Epileptiform Discharge
IPSP   Inhibitory PostSynaptic Potential
IVEM   Invasive Video-EEG Monitoring
IZ   Irritative Zone

L

LORETA   LOw Resolution Electromagnetic TomogrAphy

M

MEG   MagnetoEncephaloGraphy
MN   Minimum Norm
MNI   Montreal Neurological Institute
MP-RAGE   Magnetization Prepared RApid Gradient Echo
MRF   Markov Random Field
MRI   Magnetic Resonance Imaging
MSI   MEG Source Imaging
MUSIC   MUltiple SIgnal Classification

N

NIRS   Near InfraRed Spectroscopy

P

PD   Proton Density
PET   Positron Emission Tomography
PSG   PolySomnoGraphy

R

REM	Rapid Eye Movement
RF	Radio-Frequency
RRE	Relative Residual Energy
RS	Resective Surgery

S

sLORETA	standardized LORETA
SNR	Signal-to-Noise Ratio
SOR	Successive Over-Relaxation
SOZ	Seizure Onset Zone
SPECT	Single Photon Emission Computed Tomography
SPM	Statistical Parametric Mapping
SVEM	Scalp Video-EEG Monitoring

T

TE	Echo Time
TR	Repetition Time

V

VNS	Vagus Nerve Stimulation

W

WM	White Matter
WMN	Weighted Minimum Norm

Summary

The electroencephalogram (EEG) is a tool that registers the electrical activity of the brain in a noninvasive way with electrodes fixed on the scalp. EEG source imaging (ESI) is a technique that estimates a 3D image of source activity in the brain from the EEG recorded at the scalp. To achieve this, ESI relies on three main elements: the source model, the volume conductor model and the EEG measurements. Furthermore, these three elements are connected from source to EEG measurements via the *forward model*, in which the propagation of electrical activity from the brain (sources) through an electromagnetic volume conductor model is defined. Conversely, the determination of brain activity (sources) from scalp EEG is denominated the *inverse problem*. This dissertation focuses on the accurate construction of the volume conductor model to improve the quality of ESI.

The volume conductor model, in the case of ESI the human head, can be represented with a single sphere or with highly sophisticated realistic compartments. Spherical head models have an analytical solution while realistic head models need numerical methods to be solved. The geometry of the realistic head models is derived from anatomical images of the subject's head usually acquired with Magnetic Resonance Imaging (MRI). A realistic head model is composed of soft tissues such as the scalp and the brain (gray matter and white matter) and a hard tissue such as the skull. In addition to an accurate geometry, realistic head models require the incorporation of precisely measured conductivity values for each of the described tissues.

In the generation of realistic head models, the modeling of the *skull* is important given its complex structure and low conductivity. The skull is a three-layered compartment, made up of a spongy bone layer surrounded by two compact bone layers. These layers have different thicknesses throughout the whole structure of the skull, making it inhomo-

geneous. The structure of the skull is not clearly visible in MR images. Although X-ray Computed Tomography (CT) is the preferred modality to image the skull, it is not routinely performed in patients who have EEG examination because it leads to ionizing radiation. Moreover, the conductivity of the skull is known to be *anisotropic*, i.e., not equal in all directions, with radial and tangential components. The low conductivity (or high resistivity) of the skull produces a smearing effect on the potentials measured on the scalp. As a result, the correct modeling of the skull and its conductive properties is crucial in the creation of realistic head models for ESI.

In this dissertation, multiple studies were performed in order to determine optimal guidelines for the construction of accurate skull models for ESI. In a first part, simulations were performed to investigate different aspects of skull modeling such as conductivity ratios, anisotropy and inhomogeneities. This is described in Chapter 4. In the next chapter, head models with skulls segmented from CT images were compared against MR-based models. Finally, in Chapter 6, the influence of skull modeling to localize the epileptic focus in patients was studied. In these studies, the forward problem was solved with the finite difference method (FDM). The studies presented in Chapters 4 and 5 followed the subsequent simulation setup: First, a reference head model with a realistic skull was established. Then, simulated potentials were computed by applying the FDM algorithm on the reference model. Afterwards, the inverse problem was solved on a test model with simplified skull, taking the potentials computed on the reference model as input. The error made by the inclusion of the test model was evaluated by measuring the distance between the original and the source found with the test model. In this way, the suitability of a particular skull model was investigated.

The simulation studies presented in Chapter 4 investigated the influence of different conductivity ratios, anisotropy models and inhomogeneities of the skull. In the first simulation study, the spongy to compact bone conductivity ratio was investigated with a three-layered realistic skull—based on CT—by analyzing the influence of conductivity perturbations of the compact and spongy bone compartments on ESI. As a result, we found that the conductivity of the compact bone is more relevant than that of the spongy bone for ESI. In the second simulation study, the anisotropy ratio (radial to tangential conductivity) was determined by using a spherical head model with a simplified three-layered skull as reference. Multiple test models with different anisotropy ratios were used in the simulation. The optimal anisotropy ratio was defined

as the test model with minimal error. Realistic head models with the optimal anisotropy ratio were also compared by investigating different methods to derive the radial and tangential conductivities of the skull. From this study, the preponderance of radial over tangential conductivity was determined. In the third study, the influence of not modeling some inhomogeneities of the skull such as the air cavities, was investigated by using realistic head models. The reference and test models incorporated CT-based skulls. We found that the air cavities of the skull have little influence on ESI. Overall, these three studies showed that if the skull is to be modeled as inhomogeneous (three-layered), the compact bone conductivity is the most relevant value in the skull model. Furthermore, if the skull is to be modeled as homogeneous with anisotropic conductivity, the radial conductivity is the most important in the anisotropy model of the skull. Finally, the air cavities of the skull might be neglected in the generation of realistic skull models for ESI.

In Chapter 5 we compared the influence of realistic head models with skulls segmented from CT against MRI on ESI. Taking the inhomogeneous CT-based skull as ground truth, several simplifications of the skull model were investigated. Geometry simplifications were analyzed by using skull models segmented from MRI versus CT. Simplifications in the conductivity modeling were also studied: homogeneous compartments with either isotropic or anisotropic conductivity, and isotropic inhomogeneous (or three-layered) compartment. We also investigated the influence of modeling the spongy bone compartment as an eroded version of the compact bone compartment. The analysis was performed for simulated EEG signals with 32 and 128 electrodes at different noise levels. The results of this study showed that the isotropic inhomogeneous conductivity modeling led to the smallest localization errors among all the tested approaches. Additionally, if the spongy bone compartment cannot be easily determined, it can be modeled by eroding the compact bone compartment. However, if the skull is better to be modeled as isotropic homogeneous, the conductivity value can be set equal to the radial component of the anisotropic model (~ 0.01 S/m), thereby avoiding the use of anisotropy. Moreover, this study helped to determine the level of detail required in the generation of realistic skull models for ESI, specifically the importance of accurately modeling the base of the skull. Ultimately, this study indicated the possibility of using realistic head models based solely on MR images in a clinical setup.

A common clinical application of ESI is in patients with refractory epilepsy, for which the zone in the brain responsible for the epileptic

events needs to be surgically removed. Thus, the precise localization of this brain area is of utmost importance for the success of the surgery. Our final study, Chapter 6, aimed at determining the role of skull modeling in ESI for patients with refractory epilepsy. For this purpose, data of six patients who later underwent epilepsy surgery was used. For each patient, four models with skulls based either on CT, MRI or a CT-template were compared. Epileptic events called *spikes* were used for the source localization procedure, at two time instants: half-rising phase and peak. The analysis was performed both with averaged and single spikes. The localization was validated against the resected zone in the brain as delineated from the postoperative MR image. In this study, we showed that we are able to estimate the irritative zone in all patients using models based on any of the three modalities: CT, MRI or CT-template. This demonstrates that MRI-based models are sufficient to be used in clinical practice for ESI with EEG recorded in a standard setup. No CT acquisition is required in these patients to model the skull. Although accurate skull modeling is important, it does not have a large effect on ESI when only a limited number of EEG electrodes is used and when the SNR of the spikes is low. As a result, all the test models can be used for patient diagnosis in the presurgical evaluation of epilepsy.

In conclusion, the role of skull modeling in ESI was investigated through several studies. The analysis was performed with simulated (one patient) and real (six patients) data. The obtained results allowed us to determine certain guidelines for skull modeling in ESI. Furthermore, they provided insight into how skull modeling errors affect the source estimation procedure. This is important in order to interpret ESI results in clinical practice, for instance in the presurgical evaluation of epilepsy patients. Hence, these guidelines will allow improving the generation of realistic head models in ESI for its inclusion in the presurgical evaluation of epilepsy.

Samenvatting

Electroencephalografie (EEG) is een techniek die met behulp van elektrodes op de hoofdhuid (scalp) op een niet-invasieve manier de elektrische activiteit van de hersenen opmeet. Met EEG-bronanalyse (of EEG source imaging (ESI) in het Engels) tracht men een driedimensionaal beeld van de bronactiviteit in de hersenen op basis van het geregistreerde EEG te schatten. Om dit mogelijk te maken, maakt ESI gebruik van drie onderdelen: het bronmodel, het hoofdmodel en de EEG-registratie. Deze drie componenten zijn van bron in de hersenen gelinkt naar EEG signalen via het voorwaartse model, waarin de propagatie van de elektrische activiteit in de hersenen door een elektromagnetisch hoofdmodel gedefinieerd wordt. Omgekeerd noemt men het bepalen van de hersenactiviteit (bronnen) op basis van het scalp EEG het inverse probleem. Het onderzoek binnen dit proefschrift richt zich op de nauwkeurige constructie van het hoofdmodel om ESI te verbeteren.

Het menselijke hoofd kan voorgesteld worden door een enkele sfeer of door een zeer geavanceerd en realistisch model met verschillende compartimenten. Het voorwaartse en inverse probleem kunnen in geval van een sferisch hoofdmodel analytisch opgelost worden. Bij realistische hoofdmodellen zijn echter numerieke technieken nodig om tot een oplossing te komen. De geometrische eigenschappen van realistische hoofdmodellen worden afgeleid uit anatomische beeldvorming van het hoofd van de proefpersoon of patiënt. Deze beelden worden gewoonlijk gemaakt met magnetische resonantie beeldvorming (of Magnetic Resonance Imaging (MRI) in het Engels). Een realistisch hoofdmodel bestaat uit verschillende zachte weefsels zoals de hoofdhuid en de hersenen (grijze en witte materie) en uit hard weefsel zoals de schedel. Realistische hoofdmodellen bevatten niet enkel een gedetailleerde geometrie, ze bevatten ook de precieze conductiviteitswaarden van elk van de gemodelleerde weefsels.

Bij het construeren van realistische hoofdmodellen speelt het modelle-

ren van de schedel een belangrijke rol, omdat deze niet alleen een complexe structuur heeft, maar ook een lage conductiviteit. De schedel bestaat uit drie lagen: een spongieuze beenlaag omgeven door twee lagen compact been. Deze lagen hebben een verschillende dikte over de gehele schedel, waardoor deze inhomogeen is. De structuur van de schedel is niet duidelijk zichtbaar op MR-beelden. Hoewel X-stralen computer tomografische beeldvorming (of Computed Tomography (CT) in het Engels) de voorkeur heeft om de schedel correct weer te geven, wordt deze methode niet standaard toegepast bij patiënten die een EEG onderzoek ondergaan, omwille van de ioniserende straling. Daarnaast is de conductiviteit van de schedel niet gelijk in alle richtingen, hij is anisotroop met radiale en tangentiële componenten. Bovendien zorgt de lage conductiviteit (m.a.w. de hoge resistiviteit) van de schedel ervoor dat de potentiaalverschillen gemeten op de hoofdhuid uitgesmeerd worden. Om deze redenen is het accuraat modelleren van de schedel en zijn conductieve eigenschappen cruciaal bij het construeren van realistische hoofdmodellen voor ESI.

In dit proefstuk werden verschillende studies gedaan om richtlijnen te vinden voor het optimaal modelleren van de schedel bij ESI. In het eerste deel werden simulaties uitgevoerd om verschillende aspecten van schedelmodellering zoals de conductiviteitsverhoudingen, anisotropie en inhomogeniteiten te onderzoeken. Dit wordt in Hoofdstuk 4 beschreven. In het volgende hoofdstuk worden hoofdmodellen met een schedel gesegmenteerd van CT beeldvorming vergeleken met MR-gebaseerde modellen. Tenslotte wordt in Hoofdstuk 6 de invloed van schedelmodellering op het lokaliseren van de epileptische focus in epilepsiepatiënten onderzocht. In deze studies werd het voorwaartse probleem opgelost met de eindige-differentiemethode (of Finite Difference Method (FDM) in het Engels). De studies in hoofdstukken 4 en 5 maakten gebruik van volgend simulatiekader. Eerst werd een referentie hoofdmodel met een realistische schedel geconstrueerd. Vervolgens werden potentialen op het hoofd gesimuleerd door het FDM algoritme op te lossen voor het referentie hoofdmodel. Daarna werd het inverse probleem opgelost voor een vereenvoudigde schedel, met de gesimuleerde potentialen als invoer. De fout gemaakt door het vereenvoudigde testmodel werd geëvalueerd door de afstand tussen de oorspronkelijke en de bron gevonden met het testmodel te berekenen. Zo kon de geschiktheid van de verschillende testmodellen onderzocht worden.

De simulatiestudies in Hoofdstuk 4 bekeken de invloed van verschillende conductiviteitsverhoudingen, anisotropiemodellen en inhomogeni-

teiten in de schedel. In de eerste simulatiestudie werd de verhouding van de conductiviteit van het spongieuze been tot die van het compacte been bestudeerd door de invloed van verstoringen in deze conductiviteitswaarden op ESI met een drie-lagige realistische schedel (gebaseerd op een CT scan) te analyseren. We vonden dat de conductiviteit van het compacte been meer relevant is dan die van het spongieuze been voor ESI. In de tweede simulatiestudie werd de anisotropieverhouding (radiale conductiviteit tot tangentiële conductiviteit) bepaald met behulp van een sferisch hoofdmodel met een vereenvoudigde drie-lagige schedel als referentie. Verschillende testmodellen met verscheidene anisotropieverhoudingen werden gebruikt in deze simulatie en de optimale anisotropieverhouding werd gedefinieerd door het testmodel dat de kleinste fout opleverde. Realistische hoofdmodellen met deze optimale anisotropieverhouding werden ook vergeleken door verschillende methoden om de radiale en tangentiële conductiviteitswaarden van de schedel af te leiden, te bestuderen. Uit deze studie bleek het overwicht van de radiale conductiviteit over de tangentiële. In de derde studie werd de invloed van het niet modelleren van verscheidene inhomogeniteiten in de schedel, zoals luchtcaviteiten, onderzocht in realistische hoofdmodellen. Het referentiemodel en de testmodellen bevatten schedelmodellen gebaseerd op CT. Hieruit konden we besluiten dat luchtcaviteiten in de schedel weinig invloed hebben op ESI. Algeheel toonden deze drie studies aan dat de conductiviteit van het compacte been de meest belangrijke waarde is in het schedelmodel wanneer de schedel inhomogeen (drie-lagig) gemodelleerd wordt. Wanneer de schedel homogeen gemodelleerd wordt, maar met een anisotrope conductiviteit, is de radiale conductiviteit het meest belangrijk. Tenslotte mogen luchtcaviteiten in de schedel verwaarloosd worden bij het construeren van realistische schedelmodellen voor ESI.

In Hoofdstuk 5 vergeleken we de invloed van hoofdmodellen met een schedel gesegmenteerd van CT beeldvorming met MR-gebaseerde modellen op ESI. De inhomogene CT-gebaseerde schedel werd als elementaire waarheid beschouwd en verschillende vereenvoudigingen in schedelmodellering werden onderzocht. Ten eerste werd in invloed van geometrie vereenvoudiging geanalyseerd met schedelmodellen gesegmenteerd op basis van MR tegenover deze gesegmenteerd op basis van CT. Ook vereenvoudigingen in de conductiviteitsmodellering werden onderzocht: homogene compartimenten met enerzijds isotrope en anderzijds anisotrope conductiviteit, en een isotroop inhomogeen (drie-lagig) compartiment. We onderzochten wat de invloed is als we het spongieuze been compartiment modelleren als een geërodeerde versie van het compacte been compar-

timent. Deze analyse werd uitgevoerd met gesimuleerde EEG signalen met 32 en 128 kanalen voor verschillende ruisniveaus. De resultaten van deze studie toonden aan dat isotrope homogene conductiviteitsmodellering de kleinste fout oplevert van alle geteste methodes. Daarnaast toonden we aan dat het spongieuze been compartiment gemodelleerd kan worden door het compacte been compartiment te eroderen, wanneer dit spongieuze compartiment niet gemakkelijk te bepalen is. Als de schedel echter beter gemodelleerd wordt als isotroop en homogeen, kan men de conductiviteitswaarde gelijkstellen aan de radiale component van het anisotrope model ($\sim$ 0.01 S/m), waardoor anisotropie vermeden kan worden. Verder hielp deze studie mee om te bepalen hoeveel detail er nodig is om realistische schedelmodellen te construeren voor ESI en in het bijzonder het belang van het nauwkeurig modelleren van de schedelbasis. Tenslotte toonde deze studie aan dat het mogelijk is om in de klinische omgeving realistische hoofdmodellen te gebruiken die louter gebaseerd zijn op MR-beelden.

Een typische klinische toepassing van ESI is bij patiënten met refractaire epilepsie, bij wie de zone in de hersenen die verantwoordelijk is voor de epileptische aanvallen chirurgisch verwijderd moet worden. De precieze lokalisatie van deze zone is van onmiskenbaar belang voor een succesvolle operatie. Onze finale studie, Hoofdstuk 6, doelde er dan ook op om het belang van schedelmodellering in ESI bij patiënten met refractaire epilepsie te bestuderen. Hiervoor werd data van zes patiënten, die later succesvol epilepsiechirurgie ondergingen, gebruikt. Voor elke patiënt werden vier modellen geconstrueerd en vergeleken met de schedel respectievelijk gebaseerd op de CT-scan van de patiënt, het MR-beeld en een CT sjabloonmodel. Epileptische gebeurtenissen die pieken (of spikes in het Engels) worden genoemd werden gebruikt als invoer voor de ESI procedure, meer bepaald op twee tijdstippen: halve stijgtijd en op de top van de piek. De analyse werd voor zowel uitgemiddelde als afzonderlijke pieken uitgevoerd. De ESI resultaten, nl. de lokalisatie van de pieken, werd gevalideerd door ze te vergelijken met de gereseceerde zone in de hersenen, afgelijnd in het post-operatieve MR-beeld van de patiënt. De irritatieve zone werd correct geschat in alle patiënten met elk van de drie gebruikte modaliteiten: CT, MRI of een CT sjabloon. Dit toont aan dat MR-gebaseerde hoofdmodellen voldoende zijn om ESI uit te voeren in de klinische praktijk op EEG dat opgenomen is met een standaard setup. Er is geen extra CT-acquisitie nodig om de schedel te modelleren bij deze patiënten. Hoewel nauwkeurige schedelmodellering belangrijk is, is de invloed op ESI eerder beperkt wanneer een klein aantal elektroden

gebruikt wordt en de SNR van de pieken laag is. Als gevolg kunnen alle testmodellen gebruikt worden voor diagnosistische doeleinden in de preheelkundige evaluatie in epilepsie.

Samengevat werd het belang van schedelmodellering in ESI onderzocht door verschillende studies. De analyses werden uitgevoerd op gesimuleerde (1 patiënt) en echte (6 patiënten) data. De verkregen resultaten lieten ons toe verscheidene richtlijnen op te stellen voor schedelmodellering bij ESI. Daarnaast boden deze studies inzicht in hoe fouten in schedelmodellering de bronreconstructieprocedure beïnvloeden. Dit is belangrijk om de resultaten van de ESI procedure te gaan interpreteren in de klinische praktrijk, bijvoorbeeld de preheelkundige evaluatie in epilepsie. Op deze manier kunnen deze richtlijnen ervoor zorgen dat de constructie van realistische hoofdmodellen voor ESI verbeterd wordt voor de inclusie ervan in de preheelkundige evaluatie.

Chapter 1

Introduction

Somewhere, something incredible is waiting to be known
—Carl Sagan

This chapter presents the research field in which this dissertation is framed together with the addressed research questions (Section 1.1). Next, in Section 1.2, the general outline of the dissertation is presented on a chapter-by-chapter basis.

1.1 Context

Electroencephalography (EEG) is a noninvasive medical technique that records the electric field of the brain by placing electrodes on the scalp. EEG has existed for over 85 years, since Hans Berger first measured the electrical activity of the human brain using metal strips attached to the scalp. Traditionally, EEG has not been considered as a neuroimaging tool because active brain regions cannot be directly inferred from the recorded brain waves. However, owing to its high temporal resolution, portability, cost efficiency and accessibility, EEG has been widely used to study the function of the healthy and diseased brain. Furthermore, EEG is the primary tool to diagnose epilepsy, a neurological disorder characterized by seizures that affects around 1% of the world population.

EEG source imaging (ESI) is a technique that combines temporal and spatial information of the EEG to estimate brain activity from the potentials measured at the scalp. It aims at identifying the active brain regions corresponding to the events measured in the EEG, e.g., an epileptic seizure. The recent increase in computational power and imaging ca-

pabilities has allowed ESI to become a neuroimaging tool, that may be included as part of the presurgical evaluation of epilepsy. To achieve this, ESI must rely not only on good quality EEG signals but also on precise mathematical models describing the human head and the propagation of the sources throughout it—the forward problem—. Furthermore, the localization of a source given the superficial measurements is a mathematical inverse problem with non-unique solution.

The forward problem in ESI relies on an accurate representation of the human head. Realistic head models are derived from Magnetic Resonance (MR) images of the patient, using segmentation techniques that separate the image into different tissues: scalp, skull, gray matter, white matter, cerebrospinal fluid and air. In addition to the detailed geometry, each tissue has specific conductivity values.

One of the most demanding aspects in the construction of realistic head models is the segmentation of the skull. The skull not only has a very low conductivity compared to the other tissues inside the head but also it is a three-layered structure with different thicknesses throughout. Moreover, because of the low visibility of bone in MR images, it cannot be easily segmented from them. Although Computed Tomography (CT) is the modality that accurately pictures the skull, it exposes the patient to ionizing radiation. Therefore, it is important to determine the most convenient and close to reality way to model the skull in a clinical setting, without affecting the accuracy of the dipole estimation.

In this dissertation, we investigate how skull modeling influences ESI. Realistic simulations are performed in order to answer the following questions about the skull: (i) "can the geometry be accurately represented solely from MR images or from a template?"; (ii) "how should the conductivity be modeled?"; (iii) "which conductivity values have the largest influence on ESI?". Furthermore, we investigate the importance of skull modeling, using data from epilepsy patients, to define the epileptic focus. This leads to a very relevant research question in clinical ESI: (iv) "what results are obtained when ESI is performed with clinical EEG, i.e., with low spatial sampling density and low signal-to-noise ratio (SNR)?".

1.2   Outline

This thesis is organized as follows:

Chapter 2 introduces the theoretical aspects of EEG, epilepsy and ESI. The EEG is explained from its generation to its recording together

with its rhythms, artifacts and applications. A comparison of EEG with other neuroimaging techniques is also presented. Among the EEG applications, epilepsy is further explained because of its relevance in this work. The epileptiform activity, treatment and the presurgical evaluation of patients with refractory epilepsy are explained. The last section of this chapter introduces ESI that, in addition to the EEG measurements, is composed of the source and volume conductor models. The forward and inverse subproblems of ESI are also introduced, with emphasis on the forward solution based on the Finite Difference Method.

Chapter 3 explains aspects related to the volume conductor model, i.e., the human head. Initially, the anatomy of the human head is explained with special emphasis on the skull and the brain tissues. Subsequently, the imaging modalities used to visualize the head, namely MRI and CT are described with its basic principles, imaging of the brain and most common artifacts. Finally, the problem of segmentation is introduced, divided according to the type of tissue to be segmented: soft tissues or skull. For the segmentation of the soft tissues, the most popular software packages in the medical imaging community are presented, while for segmenting the skull the methods are divided according to the imaging modality used: MRI, CT or combined CT/MRI. At the end, the choice of a particular software package for the generation of realistic head models is justified.

Chapter 4 shows three simulation studies investigating different aspects of skull modeling in ESI. The first study analyzes the effects of perturbations in the conductivities of the three-layered skull compartment, i.e., with compact and spongy bone layers, on ESI. Furthermore, the brain regions most affected by these perturbations are analyzed. The second study determines the optimal anisotropy ratio of the skull by using spherical and realistic head models. This optimal ratio is further utilized to model anisotropy in subsequent studies. The third study investigates the influence of certain inhomogeneities of the skull such as air cavities (sinuses) on a realistically segmented skull model. The results obtained in this chapter allow us to determine the most relevant skull conductivity values for ESI, according to the imaging modality available.

Chapter 5 presents a simulation study comparing the influence of CT- versus MR-based skull models in ESI. The comparisons are made not only based on the geometry but also on the conductivity model of the skull. Furthermore, the analysis is performed for various SNR and spatial sampling density configurations. A method for defining the spongy bone

compartment is devised, which is based on an erosion of the compact bone. At the end, guidelines to model the skull in a clinical setting of epilepsy are provided.

Chapter 6 demonstrates the role of skull modeling in ESI for patients with refractory temporal lobe epilepsy. For this, data from six patients who later underwent surgery is included. The study is performed using realistic head models with the skull modeled either from CT, MRI or a CT-template. Single versus averaged spike analysis is carried out for the test models at two different time phases of the epileptic spike: half-rise and peak. The results are validated against the resected zone delineated from the postoperative MRI. This chapter performs a validation of the methods used in this dissertation and finds

Chapter 7 states the general conclusions of this dissertation, followed by the future work and final conclusions.

Chapter 2

Electrical activity of the brain

Ideas, like large rivers, never have just one source
—Willy Ley

The measurement of the electrical activity originated in the human brain is one of the methods to study its function. This chapter encompasses a description of the origin and measurement of brain activity together with the application of the recorded brain waves to the diagnosis of neurological diseases. For that purpose, Section 2.1 explains the physiology of the neuron, followed by the description of a technique that records the electrical activity from the brain, electroencephalography (EEG), in Section 2.2. Given that the methodology presented in this dissertation is designed for epilepsy, this neurological disease is introduced in Section 2.3. Finally, a mathematical technique that uses the measured EEG signals to localize the origin of brain activity, namely EEG source imaging (ESI), is explained in Section 2.4.

2.1   Neuronal physiology

The central nervous system (CNS) is composed of the brain and the spinal cord. The task of the CNS is to combine and handle the information received from all body parts while regulating their activity. The

human brain (explained in Section 3.1.2) consists of approximately 86 billion nerve cells of differing shape, size and functionality, interconnected in an intricate network [Azevedo et al., 2009]. Located between the nerve cells, glial cells have a supporting role in the CNS by maintaining the connection capabilities of nerve cells.

A nerve cell or *neuron* consists of three basic parts: the cell body (or soma), the dendrites and the axon (Figure 2.1a). The cell body contains the cell nucleus, where vital proteins are synthetized. The dendrites originate in the cell body and receive inputs from other neurons. The axon, covered with myelin sheath, provides contact with other neurons or with other target organs. The signal is initiated in the soma (axon hillock) and propagates through the axon encoded as a short, pulse-shaped waveform, the so-called *action potential* [Sörnmo and Laguna, 2005]. The connection between neurons occurs at a *synapse*, which consists of a gap (the *synaptic cleft*) between a presynaptic and a postsynaptic neuron. At the axon terminals, the presynaptic neuron contains small protuberances which hold the neurotransmitter substance.

The interior of the neuron has a resting potential of about -60 to -70 mV with respect to the extracellular space. This potential difference is the result of an unequal distribution of Na^+, K^+ and Cl^- ions across the cell membrane. The Na^+ and K^+ ion pumps inside the cell membrane keep this unequal distribution stable.

The interneuronal communication is carried out by an alternating chain of electrical and chemical reactions. When the presynaptic neuron is activated by an action potential, it secretes a *neurotransmitter* in the synaptic cleft (Figure 2.1b). This neurotransmitter binds to the receptors of the postsynaptic neuron, opening different ion channels. The flow of charged ions changes the permeability of the cell membrane. In case the neurotransmitter binding induces an inflow of positively charged ions (e.g. Na^+), the intracellular space depolarizes (it becomes more positive). This depolarization is called an excitatory postsynaptic potential (EPSP). In the opposite case, i.e., when the neurotransmitter binding causes an outflow of positive ions (e.g. K^+) or an inflow of negative ions (e.g. Cl^-), the intracellular volume hyperpolarizes (it becomes more negative). This potential change is also known as an inhibitory postynaptic potential (IPSP). A postsynaptic neuron thus receives signals which are both excitatory and inhibitory and the postsynaptic potential depends on how the input signals are summed together. If the number of EPSPs is larger than the number of IPSPs, the postsynaptic potential will in-

(a) The neuron
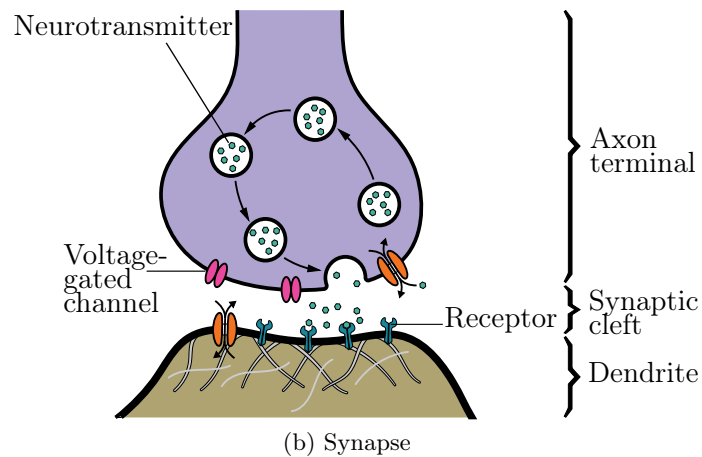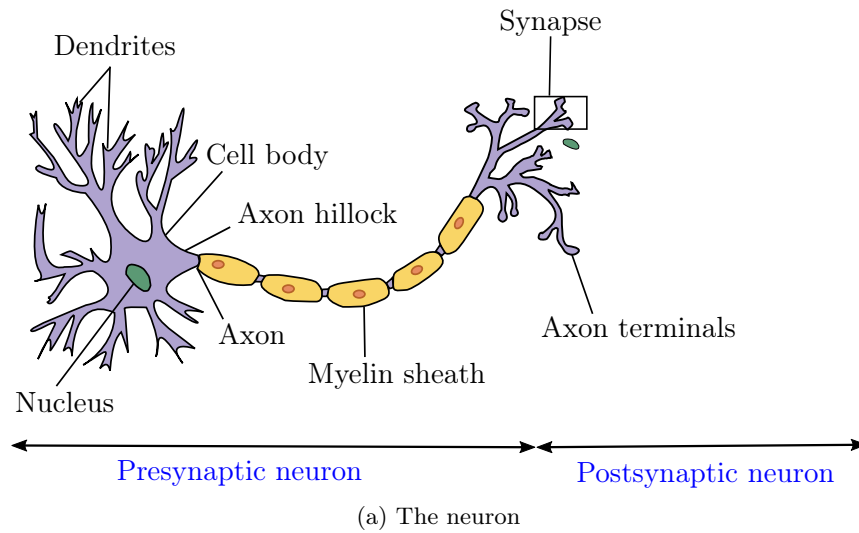
(b) Synapse

Figure 2.1: Schematic diagram of a neuron and its synapse. Adapted from: (a) `https://commons.wikimedia.org/wiki/File:Neuron.svg#file` and (b) `https://commons.wikimedia.org/wiki/File:SynapseSchematic_en.svg`.

crease. An increase in the postsynaptic potential will trigger the neuron to fire a new action potential along its axon in order to communicate with other neurons. For more information on neurophysiology, we refer the reader to [Lopes da Silva and van Rotterdam, 2005, Malmivuo and Plonsey, 1995].

2.2   Electroencephalography

The electric field generated by the interneuronal communication can be studied using electroencephalography (EEG). In the 1920s, Hans Berger was the first to measure the electrical activity of the brain on the scalp surface using metal strips [Berger, 1929]. He coined the term electroencephalogram to denote the recorded signals. Berger also noticed that certain properties of these brain waves were dependent on the general status of the subject, and described them as alpha and beta waves. Since then, EEG has become a predominant technique to study the brain function. This section describes different aspects of the EEG such as generation, recording and characteristic frequencies. The most representative artifacts and applications are also reported.

2.2.1   The generators of the EEG

The small electrical field generated by one neuron cannot be detected by an electrode placed on the scalp, which is at least 2 cm away from brain tissue. A large number ($\sim 10^8$–10^9) of synchronously active neurons is thus required to generate activity perceivable by one scalp electrode [Nunez and Srinivasan, 2005]. In neuronal populations, the action potentials, because of their short duration (1–2 ms), tend to overlap much less than the postsynaptic potentials (EPSP and IPSP), which typically last longer ($\approx$ 10–250 ms) [Lopes da Silva and van Rotterdam, 2005]. Therefore, EEG on the scalp is mainly caused by the summation of synchronously occurring extracellular postsynaptic potentials, the so-called extracellular potential field.

To produce a measurable scalp EEG signal, a population of neurons requires not only to be activated in a more or less synchronous way, but also to have their dendrites regularly arranged so that they amplify each other's extracellular potential field. The pyramidal cells are a special type of neuron with a triangular shaped cell body, a large dendritic branch (*apical dendrite*) and multiple *basal dendrites*. Neighboring pyramidal neurons are arranged so that the axes of their apical dendritic trees are parallel to each other and orthogonal to the cerebral cortex, as shown in Figure 2.2a. For this reason, they are considered as the generators of the EEG.

Figure 2.2b shows a schematic representation of the generators of the EEG. An afferent influx of action potentials at the level of the synapse causes the excitation of a pyramidal neuron, generating EPSPs at its
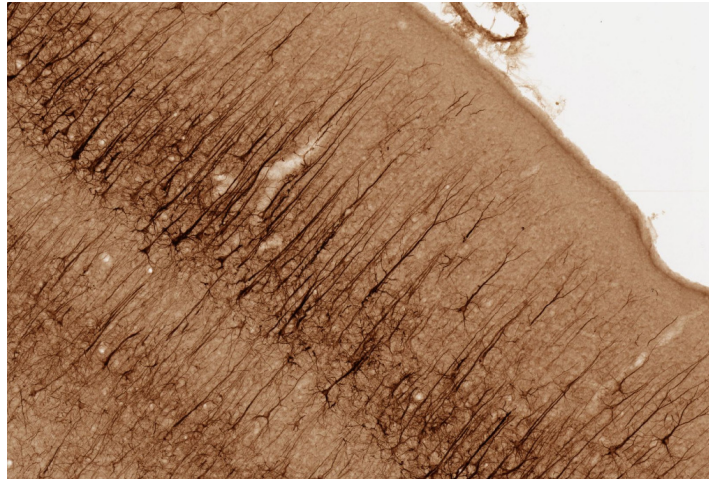
(a) Slice of cerebral cortex showing the orthogonal pyramidal neurons in black. From [Hallez, 2008].
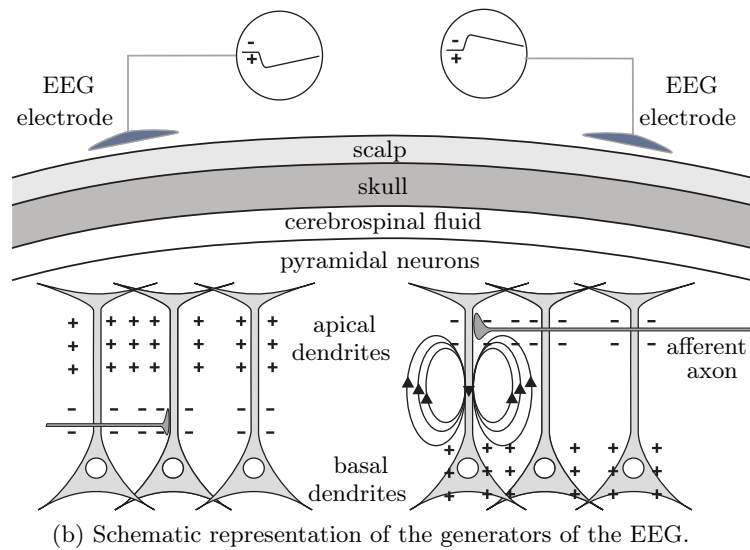
(b) Schematic representation of the generators of the EEG.

Figure 2.2: Pyramidal neurons and schematic of the generators of the EEG.

apical dendritic tree. As a consequence, the apical dendritic membrane depolarizes, becoming extracellularly electronegative with respect to the cell body and basal dendrites, which become electropositive. This potential difference causes intracellular and extracellular currents to flow from the *source*, represented by the non-excited membrane of the cell body and basal dendrites, to the *sink* located at the level of the apical dendritic membrane sustaining the EPSPs [Baillet et al., 2001, Gloor, 1985]. The electric fields originated by the massively synchronized activity of sinks and sources, produce measurable potential fields on the scalp surface of around 10–100 μV.

2.2.2   Recording

The EEG records electric potential differences between scalp electrodes, as a function of time. In a typical EEG setup, the electrodes are fixed at established positions on the scalp, attaching them with conductivity gel to reduce the scalp/electrode impedance. The international 10–20 system [Jasper, 1958] is a commonly used standard for electrode positioning in the recording of EEG. This standard consists of 21 electrodes which are placed based on the measurement of certain anatomical landmarks on the skull: the *nasion* (the depressed part at the top of the nose, between the eyes), the *inion* (the protuberant part at the lower back of the head) and the left and right *preauricular points* (felt as depressions at the root of the bony arch of the cheek). To determine the electrode positions, the lines between nasion and inion and between the two preauricular points (both passing through the *vertex*) are divided into intervals of 10% and 20%, as shown in Figure 2.3. Each electrode is given a label, according to the region where it is located: Frontal pole ('Fp'), Frontal ('F'), Central ('C'), Parietal ('P'), Occipital ('O'), Temporal ('T') and Auricle ('A'). In order to differentiate between correspondent electrodes in the left and right halves of the head, even numbers are used for the right hemisphere and odd numbers for the left hemisphere. Electrodes at the midline are designated with the letter 'z' (stands for 'zero').

Modern EEG systems allow the use of more electrodes, leading to a higher spatial sampling of the scalp. The EEG system together with the application define the total number of electrodes to be used. Although clinical EEG is normally performed with 27 to 32 electrodes, there is a trend to increase this number to 128 or 256 in order to obtain a higher spatial sampling density. This is the so-called high-density EEG [Gwin et al., 2010, Lantz et al., 2003a, Oostenveld and Praamstra, 2001]. A
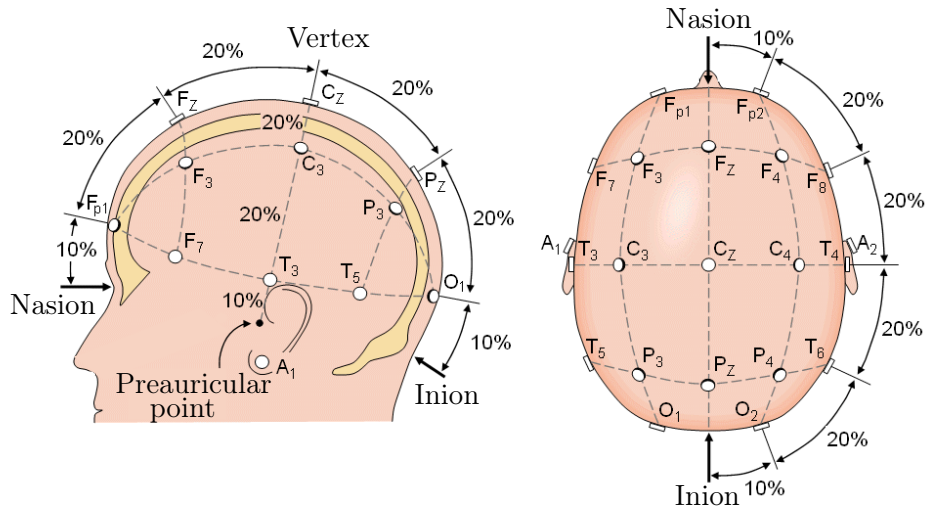
Figure 2.3: The international 10–20 electrode system, left and top view of the head. Adapted from [Malmivuo and Plonsey, 1995].

fragment of high-density EEG is shown in Figure 2.4.

2.2.3 Rhythms

The recorded EEG signals have typical frequencies between 0.5 to 30–40 Hz. The rhythms of the EEG are generally categorized into five different frequency bands: delta, theta, alpha, beta and gamma [Sörnmo and Laguna, 2005]. Every band has a brain wave pattern associated with a varying state of consciousness. Table 2.1 summarizes the EEG rhytms with corresponding waveform and characteristic state of consciousness. The identification of the EEG rhythms as normal or abnormal is based on the age and state of the subject.

2.2.4 Artifacts

EEG signals are in general contaminated by activity from sources unrelated to brain function. The EEG artifacts can be either physiological (patient-related) or extraphysiological (environmental or instrumental). The most frequently occurring *physiological* artifacts are:

Ocular: Mainly originated from eye blinks and saccades, ocular artifacts are caused by the potential difference between the cornea and the
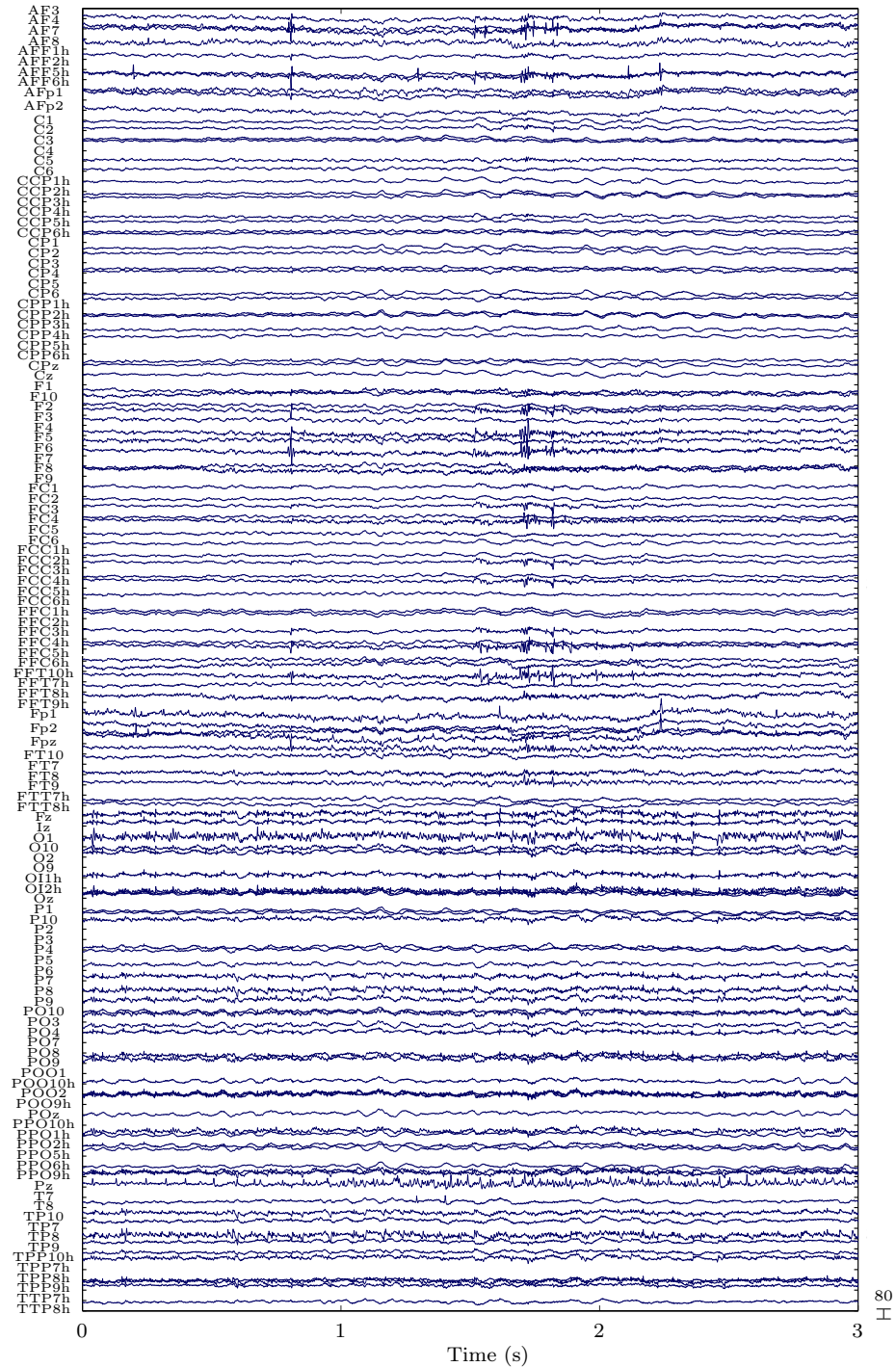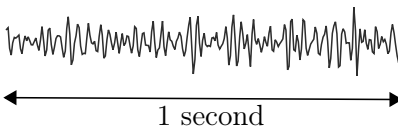
Figure 2.4: Fragment of 3 s of high-density EEG with 128 channels. The amplitude scale is given in μV.

Table 2.1: EEG rhythms, waveform and characteristic state of consciousness. f expresses the frequency band in Hz.

Rhythm f (Hz)	Waveform	State of consciousness
Delta (δ) $f < 4$		Slow-wave sleep
Theta (θ) $4 \leq f < 8$		Drowsiness or arousal
Alpha (α) $8 \leq f < 14$		Relaxation, eyes closed
Beta (β) $14 \leq f < 30$		Wakefulness, active concentration
Gamma (γ) $f > 30$	1 second	Active information processing

retina. This can be represented by an equivalent dipole in approximately the direction of gaze. While eye blink artifacts are generated by the contact of the eyelid with the cornea, eye saccade artifacts arise from the rotation of the retino-corneal dipole. Blinks generate larger potentials at the frontal pole electrodes ('Fp1' and 'Fp2') than saccades, decreasing more rapidly from the front to the back of the head [Lins et al., 1993]. Electrooculography (EOG) channels placed near the eyes record the ocular activity, generating a signal that can be used to filter the eye-induced artifacts from the EEG.

Muscle: The artifacts induced by muscle activation are produced by, among others, chewing, biting, swallowing and frowning. This type of artifact is seen in the EEG as bursts of fast activity, occurring predom-

inantly in the frontal and temporal channels. The recording of activity originated in the muscles is called electromyography (EMG).

Cardiac: Caused by the contraction of the heart muscle, cardiac artifacts are high in amplitude compared to the EEG. It is perceived by its rhythmicity/regularity and coincidence with the electrocardiogram (ECG) tracing. ECG recordings are thus routinely applied to identify and filter artifacts produced by heart activity.

In the case of *extraphysiological* artifacts, the most common are:

Power line: Characterized by 50 or 60 Hz signals (subject to the frequency of the local power system), power line artifacts can be caused by poor grounding of the EEG electrodes.

Electrode-related: These artifacts are generated when the EEG electrodes are not correctly attached to the scalp or when there are sudden changes in the impedance of an electrode, the latter being visible in the EEG as high voltage signals.

Instrumentation noise: It typically occurs in the quantization process originated from the analogue-to-digital conversion.

2.2.5   Applications

EEG is broadly used in multiple clinical and research applications, as a result of its relative simplicity, low-cost and high temporal resolution. In addition, EEG is a primary technique for the study of normal and pathologic neurological phenomena. The following are the most relevant applications of EEG:

Brain functioning: In this area, EEG is generally used to measure the response of the brain to a external stimulus, the so-called evoked (EP) or event-related (ERP) potentials. ERPs are time-locked to the stimulus and their amplitudes are considerably smaller than the spontaneous brain activity (background EEG). Therefore, numerous similar trials must be conducted and averaged in order to increase the signal-to-noise ratio of the recorded phenomena. The study of ERPs has been extensively

applied in cognitive [Luck, 2014] as well as in clinical [Chiappa, 1997] research.

Brain-computer interfaces: A brain-computer interface (BCI) refers to the use of EEG recordings to communicate with an external device. The design of a BCI encompasses two main steps: (i) Monitoring of the mental state of the subject which encodes commands in the EEG; and (ii) Translation of the EEG signal characteristics into commands that control the device, using advanced signal processing techniques. A BCI can benefit completely paralyzed subjects (the locked-in syndrome) or those with serious neuromuscular diseases [Wolpaw et al., 2002].

Sleep medicine: The most important clinical tool in the diagnosis of sleep disorders is polysomnography (PSG), in which EEG is one of the modalities involved together with EOG, ECG, EMG, nasal and oral airflow, and pulse oxymetry. In PSG, the EEG is used to determine the sleep stage (e.g. rapid eye movement (REM) or non-REM) of the patient [Szelenberger et al., 1995].

Epilepsy: EEG is the most important technique to diagnose epilepsy. Because the methods presented in this work are developed for this application area, epilepsy is discussed in Section 2.3. Three major topics in this area are: (i) Localization of the brain regions involved in the epilepsy, known as EEG source imaging and presented in Section 2.4; (ii) automatic detection of activity characteristic of epilepsy in the EEG; and (iii) prediction of epileptic seizures using the EEG. The last two topics are outside the scope of this work.

2.2.6   Comparison with other neuroimaging techniques

Multiple structural and functional imaging methods have been developed to study the brain in a noninvasive way. The structural methods visualize the anatomy of the brain and include Magnetic Resonance Imaging (MRI) and Computed Tomography (CT). The functional methods retrieve information about the activity of the brain at a specific time instant and include Positron Emission Tomography (PET), Single-Photon Emission Computed Tomography (SPECT), functional MRI (fMRI), ElectroEncephaloGraphy (EEG), MagnetoEncephaloGraphy (MEG) and functional Near InfraRed Spectroscopy (fNIRS). A brief

overview of each method is given below.

Positron Emission Tomography (PET) is a nuclear imaging technique that determines the distribution of an injected radio tracer in the brain, typically ^{18}F-fluorodeoxyglucose (^{18}F-FDG). This is a glucose analogue molecule, labeled with a positron-emitting radionuclide, that reveals the glucose uptake in different brain regions. In neurology, this technique can be used to localize the seizure focus in patients with epilepsy, which is sometimes reflected by local hypometabolism [Tai and Piccini, 2004].

Single-Photon Emission Computed Tomography (SPECT) is also a nuclear imaging technique that determines the distribution of a radio tracer labeled with a single-photon-emitting isotope. The most common tracer in neurology is the ^{99m}Tc-HMPAO (Technetium-HexaMethylPropylene Amine Oxime) which is used to assess brain perfusion, i.e., a map of the regional cerebral blood flow. In epilepsy, patients can be injected with the tracer at the time of a seizure and be imaged when the seizure has stopped. This is possible because the tracer is trapped in the tissue compartment during the first few seconds after injection and maintains that distribution for hours [Kim and Mountz, 2011]. Hyperperfused brain areas may indicate the seizure focus.

Functional Magnetic Resonance Imaging (fMRI) is a technique that uses MRI acquisition technology to measure brain activity. The technique relies on the fact that active areas in the brain require more oxygen and glucose to be delivered. The increased consumption of oxygen is compensated by excess cerebral blood flow [Logothetis and Wandell, 2004]. Therefore, fMRI uses the Blood-Oxygen-Level-Dependent (BOLD) signal to indirectly investigate neuronal activation. In active brain regions, the relative concentration of oxygenated hemoglobin increases, resulting in a positive BOLD response. Given that oxygenated hemoglobin is almost resistant to magnetism (*diamagnetic*), it interferes less with the magnetic MR signal than deoxygenated hemoglobin, which is more magnetic (*paramagnetic*).

MagnetoEncephaloGraphy (MEG) registers the magnetic field produced by the electrical currents in the brain. The magnetic field of the brain is very small (10–10^3 femtoTesla (fT)) compared to the magnetic background noise ($\sim 10^8$ fT). MEG thus requires that the magnetic field be acquired in a magnetically shielded room with highly sensitive magnetometers. As a consequence, the technique is costlier and less accessible than EEG. Unlike MEG, which is more sensitive to tangential

sources, **EEG** (explained in Section 2.2) can measure both tangential and radial sources [Baillet et al., 1999, Liu et al., 2002]. **MEG source imaging (MSI)** is a technique that, similar to **EEG source imaging (ESI)** (see Section 2.4), allows to characterize the generators of the MEG measurements. In contrast to ESI, MSI is less affected by the head model used.

Functional Near InfraRed Spectroscopy (fNIRS) is a recent technique that uses near-infrared light to measure brain activity. The technique uses the principle that hemoglobin absorbs more light than head tissues. Hence, the absorption patterns of the light irradiated on the cerebral cortex are analyzed to find variations in oxygenated or deoxygenated hemoglobin levels. In this way, the neuronal activity can be detected. Compared to fMRI, fNIRS is portable and has a higher temporal resolution. However, it is not suited to measure deep neuronal activity and its spatial resolution is more limited.
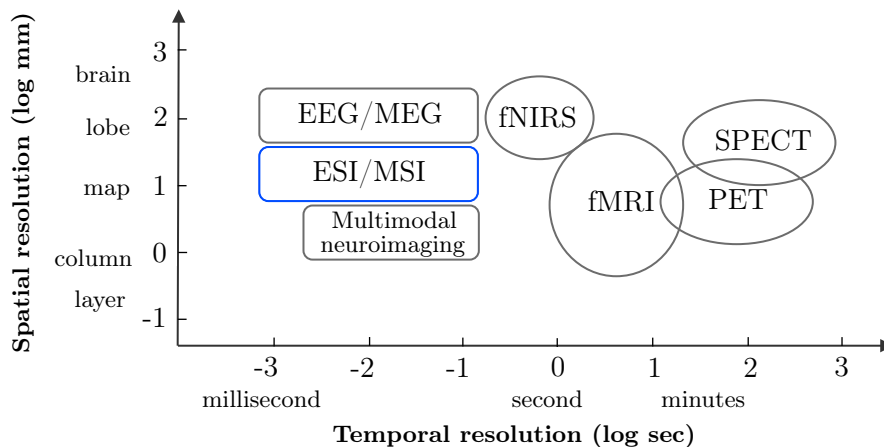
Figure 2.5: Schematic illustration of the ranges of spatial and temporal resolution of various noninvasive functional neuroimaging methods. Adapted from [He and Liu, 2008].

The spatial and temporal resolution of the mentioned functional neuroimaging methods is presented in Figure 2.5. EEG and MEG have superior temporal resolution compared to fMRI, PET, SPECT and fNIRS, but with a spatial resolution in the order of centimeters. ESI/MSI has led to the improvement of the EEG/MEG spatial resolution to a centimeter scale or even smaller. fNIRS has a similar spatial resolution to EEG/MEG, while that of fMRI is higher (in the order of millimeters).

PET and SPECT have both limited spatial and temporal resolutions but high sensitivity and specificity in the detection of tumors, metabolism changes and perfusion.

Multimodal neuroimaging refers to the combination of two or more modalities in order to increase the sensitivity and specificity of each method in the estimation of cerebral activity. Nowadays, much effort has been devoted to the design of hybrid imaging systems such as PET/MRI [Heiss, 2009], SPECT/MRI [Wagenaar et al., 2006] and MEG/MRI [Vesanen et al., 2013]. Nonetheless, these systems are not commonly used in clinical applications because of the technical difficulties that impact directly combined modalities. Other combinations such as EEG/fMRI and EEG/MEG have less technical problems and are currently used in neuroscience research, especially in epilepsy [Ebersole, 1999, Gotman et al., 2006, Pataraia et al., 2005, Salek-Haddadi et al., 2006]. EEG/fMRI benefits from the high spatial resolution of fMRI and the high temporal resolution of EEG. EEG and MEG are complementary techniques and their combination allows to obtain the maximum amount of information from the electromagnetic sources in the brain [Dassios et al., 2007].

In this thesis, we used the information from structural modalities to generate a realistic model of the human head for ESI. Therefore, MRI and CT imaging will be introduced in Section 3.2.

2.3   Epilepsy

In the world, there are at least 65 million people ($\sim 1\%$ of the population) affected by epilepsy [Ngugi et al., 2010]. Epilepsy is a neurological disease characterized by abnormal synchronous electrical activity in a group of neurons of the brain cortex. The clinical manifestation of epilepsy is an epileptic *seizure*. However, because nearly 10% of the population have at least one seizure during their lifetime, epilepsy requires at the minimum two unprovoked seizures to be diagnosed [World Health Organization, 2015].

Epileptic seizures can vary from a minor lapse of attention or muscle twitches to severe and lengthy convulsions with loss of consciousness. The frequency of the seizure ranges from less than one per year to several per day. Depending on the location in the brain where the seizure originates and how far it spreads, they can be subdivided into two types: partial and generalized. The epileptic activity in *partial* seizures origi-

nates from a limited part of the brain, whereas in *generalized* seizures it involves the entire brain.

Partial seizures, also known as focal, can be further classified according to the brain lobe involved during the seizures. The most prevailing form of partial seizures is the temporal lobe epilepsy (TLE) [Wiebe, 2000]. Forms of partial epilepsy originating outside the temporal lobe, i.e., in the frontal, occipital and parietal lobes (see Section 3.1.2), are called extra-temporal lobe epilepsies. TLE can in turn be subdivided into two main categories [Engel, 2001b]: *mesial* TLE (MTLE), the most frequent type, originating in the medial aspect of the temporal lobe, and *lateral* TLE (LTLE), which originates in the neocortex at the lateral surface of the temporal lobe.

According to its etiology (cause), epilepsy can be divided into idiopathic, symptomatic or cryptogenic [Shorvon, 2011]. *Idiopathic* refers to an epilepsy of presumed genetic origin in which there is no neuroanatomic or neuropathologic abnormality. *Symptomatic* is defined as an epilepsy of acquired or genetic cause, associated with anatomic or pathologic abnormalities. The causes of symptomatic epilepsy can be: brain damage from prenatal or perinatal injuries (e.g. lack of oxygen at birth), congenital abnormalities, genetic conditions, head trauma, stroke, brain tumors and CNS infections, among others [World Health Organization, 2015]. *Cryptogenic* indicates an epilepsy of presumed symptomatic nature in which the cause has not been established. Nonetheless, in most epilepsy cases the etiology is unknown.

2.3.1   Epileptiform activity in the EEG

The activity recorded during a seizure is called *ictal* EEG. Thus, the signal recorded in-between the seizures is called *interictal* EEG. Figure 2.6 shows ten seconds of ictal and interictal EEG.

The epileptiform activity during a seizure is usually displayed as periodic waveforms of higher amplitude compared to the interictal periods (Figure 2.6a). The ictal EEG discharges have a relatively abrupt onset/end and last for several seconds. Their wave components are generally rhythmic and differ in shape, frequency and topography. When the onset is focal, the activity tends to spread to other brain areas. Muscle artifacts may occur posteriorly during the seizure.

During the interictal period, epileptic manifestations called interictal epileptiform discharges (IEDs) can be noticed in the EEG. They are

categorized into spikes, sharp waves and spike-wave-complexes, according to their morphology. *Spikes* have a briefer time duration (20–70 ms) than *sharp waves* (70–200 ms). A *spike-wave-complex* consists of a spike followed by a wave and has a duration of 150–350 ms. Figure 2.6b shows three spikes, marked by a red line at the peak.
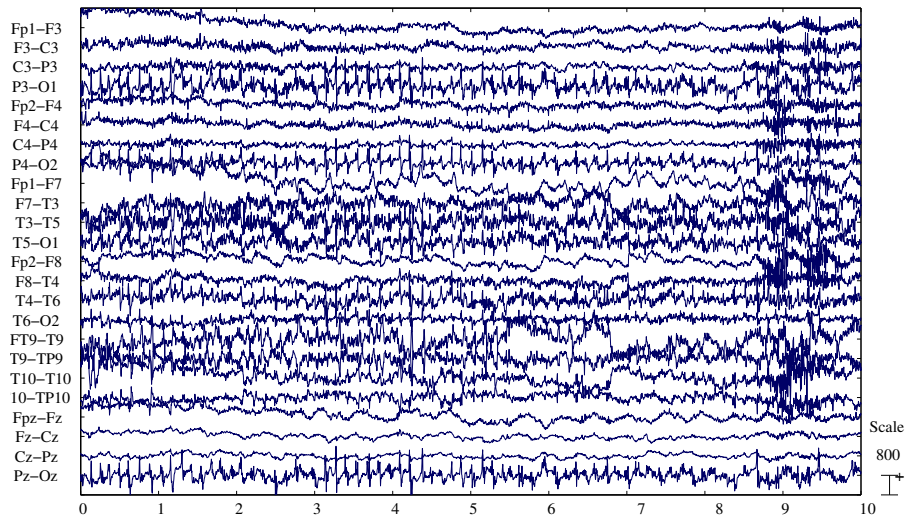
(a) Seizure showing high amplitude rhythmic activity.
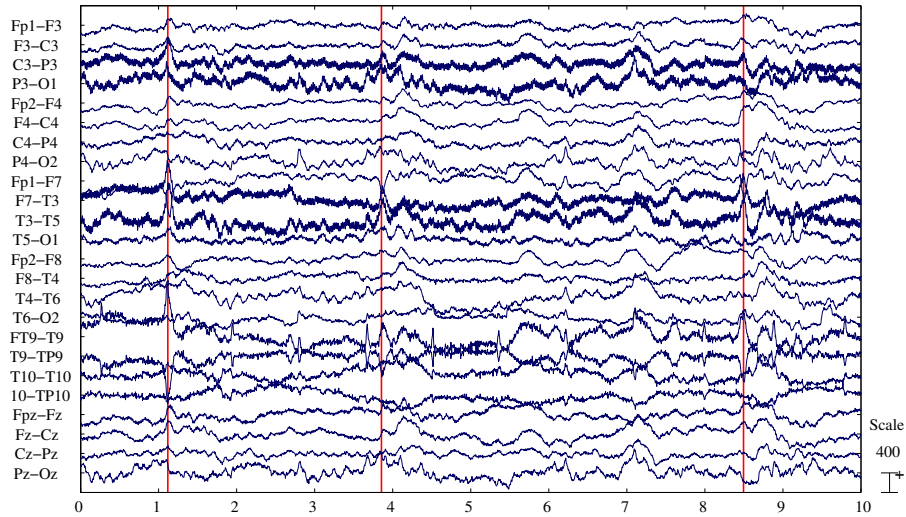
(b) Spikes, marked by a red line at the peak.

Figure 2.6: Fragment of 10 s of (a) ictal and (b) interictal activity in the EEG. The amplitude scale is given in μV.

2.3.2 Treatment

The administration of *anti-epileptic drugs* (AEDs) is the first choice for the treatment of epilepsy. About 70% of the patients respond successfully to this line of treatment [World Health Organization, 2015], but $\sim 30\%$ remains with uncontrolled seizures. This last group of patients suffers from *pharmacologically refractory epilepsy*. For this type of epilepsy, other treatment options are available such as the implantation of a device that generates electrical impulses to stimulate the vagus nerve—*Vagus Nerve Stimulation* (VNS)—or deep structures in the brain—*Deep Brain Stimulation* (DBS). *Resective Surgery* (RS) is another type of treatment that consists of the removal of the brain area responsible for the epilepsy. RS is the treatment with highest efficacy in rendering patients seizure-free, and therefore the preferred treatment option. However, RS is not reversible, while VNS and DBS are. In order to assess whether a patient is suitable for surgery, several medical examinations need to be performed. This is called presurgical examination and is explained in Section 2.3.3. Figure 2.7 summarizes the treatment options for epilepsy.
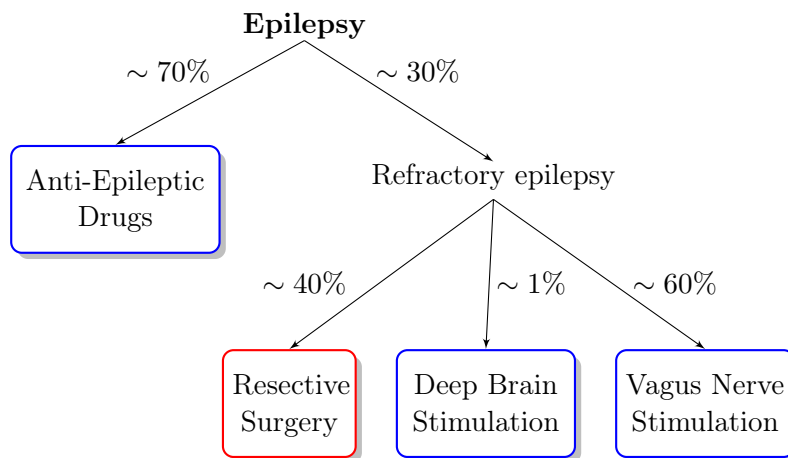
Figure 2.7: Schematic overview of the treatment options for patients with epilepsy. For refractory epilepsy, the numbers correspond to treated patients.

2.3.3 Presurgical evaluation of patients with refractory epilepsy

Resective surgery is a very successful therapy for patients with partial epilepsy, i.e., of focal origin. The objective of RS is the resection of the

epileptogenic zone (EZ), defined as the the minimum amount of cortex that must be resected to produce seizure freedom [Rosenow and Lüders, 2001]. This goal can be achieved if no additional functional deficit is caused to the patient. Therefore, the presurgical evaluation aims to accurately localize the EZ and identify overlap with eloquent cortex. Based on this assessment, the treatment option in the best interest of the patient's well-being is decided.

Figure 2.8 shows a flowchart of the presurgical evaluation protocol of epilepsy. The first part of the protocol consists of a set of noninvasive techniques, of which *Scalp Video-EEG Monitoring* (SVEM) is the centerpiece. SVEM is the simultaneous recording of EEG and video of the patient, during several consecutive days. Based on the IEDs and seizures seen in the EEG together with the corresponding behavior of the patient, i.e. the semiology, the EZ can be localized. *Magnetic Resonance Imaging* (MRI) may detect structural abnormalities in the brain, e.g., lesions, at the epileptogenic site [Lefkopoulos et al., 2005]. *Positron Emission Tomography* (PET) provides information about the cortical glucose metabolism; the indication of an interictal hypometabolic zone is a reliable indicator for lateralization of the EZ [Van Paesschen et al., 2007]. *Neuropsychological tests* investigate the higher cognitive functions of the brain (speech and memory) and can also reveal a dysfunction in certain brain areas. For more than half of the patients the information gathered during this initial phase is not sufficient to delineate a hypothesized EZ [Carrette et al., 2011]. Thus, additional tests such as ictal *Single Photon Emission Computed Tomography* (SPECT), *Magnetoencephalography* (MEG) and *EEG/functional MRI* (EEG/fMRI) can be performed.

EEG source imaging (ESI) is a mathematical technique to determine the electrical source in the brain using the superficial electrical measurements (EEG) and a model of the human head. As a consequence, ESI can be considered as an additional noninvasive examination in the presurgical evaluation of epilepsy [Boon et al., 2002]. This method is introduced in Section 2.4.

When these investigations successfully delineate the EZ, and when no major neurological deficit is expected from its removal, a multidisciplinary team decides to perform RS. On the contrary, if the results of these examinations are not congruent, a long-term invasive video-EEG monitoring (IVEM) may be considered [Carrette et al., 2010]. IVEM is associated with medical risks [Hamer et al., 2002] and for this reason it

can be performed only on patients with a hypothesized EZ. Subdural grids or depth electrodes are surgically implanted in the vicinity of the brain areas with high probability of being the EZ. If the results of the IVEM reveal an EZ, RS may be performed.
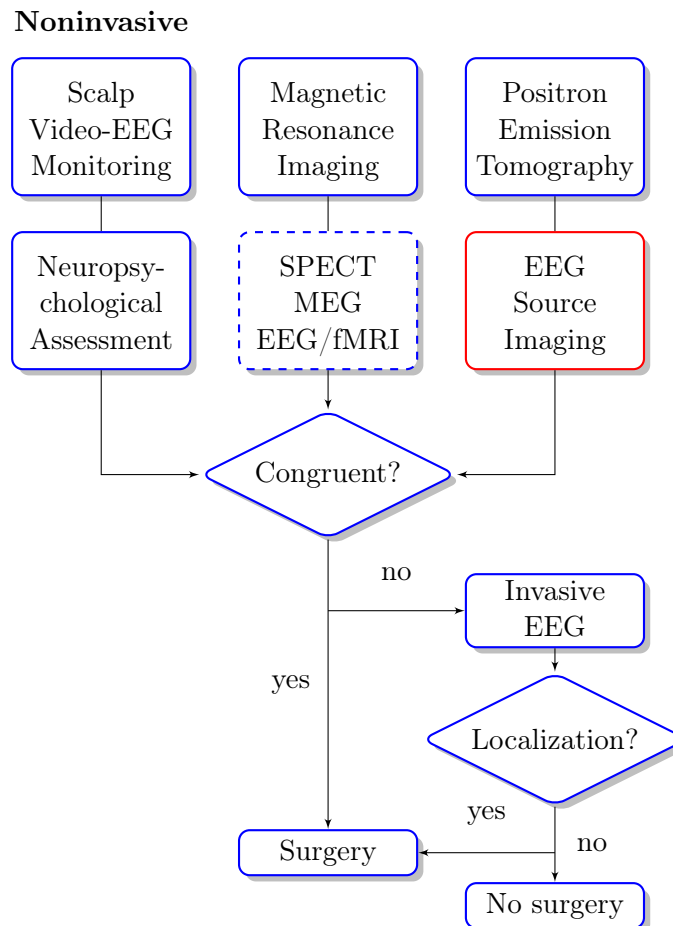
Figure 2.8: Flowchart of the presurgical evaluation protocol of epilepsy.

2.3.3.1 Cortical zones

In the presurgical evaluation of epilepsy, it is important to understand the different cortical zones involved in the generation of epilepsy. These zones are explained below [Rosenow and Lüders, 2001].

Epileptogenic Zone (EZ):   Defined as the area of cortex indispensable for the generation of epileptic seizures, there is no diagnostic modality currently available that can be used to measure it directly. Therefore, it is a theoretical concept. If the patient is seizure-free after surgery then the EZ must have been included in the resected cortex. Its location must be inferred indirectly by defining the other cortical zones.

Seizure Onset Zone (SOZ):   The SOZ is the area of the cortex from which clinical seizures are in fact generated. It is most commonly localized by either scalp or invasive EEG methods. It can also be determined by ictal SPECT. The extent of the SOZ does not necessarily correspond to that of the EZ.

Irritative Zone (IZ):   Defined as the area of cortical tissue that generates interictal spikes, it is measured by EEG (scalp or invasive), MEG or fMRI.

Epileptogenic lesion: Defined as a radiographic lesion causing the epileptic seizures, it is detected using MRI. Not all lesions seen on an epileptic patient are epileptogenic. Thus, other techniques like SVEM may be needed to verify that the lesion is responsible of the seizures. The extent of the lesion does not necessarily correspond with the EZ, as in the case of the SOZ.

2.4   EEG source imaging

EEG source imaging (ESI) is a neuroimaging tool that aims at reconstructing the electrical sources inside the brain from the potentials measured on the scalp surface. ESI is commonly used in the presurgical evaluation of patients affected by epilepsy [Boon et al., 1997, Brodbeck et al., 2011] and in the characterization of multiple psychiatric and neurological diseases [Foxe et al., 2005, Lascano et al., 2010, Saletu et al., 2005]. It consists of two subproblems: (i) the *forward* problem, that determines the electrode potentials at the scalp given a source distribution in the brain, and (ii) the *inverse* problem, in which the source parameters are estimated given a measured set of electrode potentials. Figure 2.9 illustrates the relation between the forward and inverse problems. The main elements in ESI are thus: the source model, the volume conductor model and the EEG measurements.
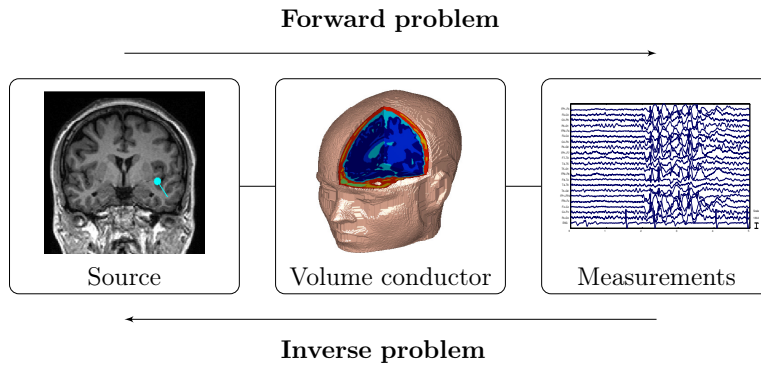
Figure 2.9: Relation between the forward and inverse problems.

2.4.1 The source model

The pyramidal neurons in layer IV of the cerebral cortex are considered to be the generators of the EEG, as described in Section 2.2.1. At the microscopic level, an active pyramidal neuron is represented by a current source and a current sink injecting and removing the same amount of current I, respectively. This is illustrated in Figure 2.10a. This configuration can be modeled by a current dipole characterized by (i) a position vector $\mathbf{r}_{\text{dip}}$ chosen in the middle of the two monopoles, and (ii) a dipole moment or orientation $\mathbf{d} = d\mathbf{e}_d$, where $\mathbf{e}_d$ is a unit vector directed from the current sink to the current source, and $d = \|\mathbf{d}\| = Is$ is the dipole intensity, with s the distance between the two monopoles.

As shown in Figure 2.10b, the dipole orientation can be decomposed into three dipoles oriented along the Cartesian axes as: $\mathbf{d} = d_x\mathbf{e}_x + d_y\mathbf{e}_y + d_z\mathbf{e}_z$, with d_x, d_y and d_z the dipole components. These components can also be expressed in spherical coordinates, with the orientation of the unit vector $\mathbf{e}_d$ determined by the azimuth (ϕ) and elevation (θ) angles.

A large group of electrically active pyramidal neurons in a small patch of cortex can be represented as an *equivalent current dipole* (ECD), at a macroscopic scale [De Munck et al., 1988, Nunez and Srinivasan, 2005]. However, if the physiological source is not limited to a specific brain area, the single dipole model is not valid. As an alternative to the ECD, the *distributed source model* describes the extent of the source region using multiple dipoles, each representing a small patch of cortex. The dipole orientations are constrained to be perpendicular to the cortical surface [Dale and Sereno, 1993], resembling the orientation of the api-
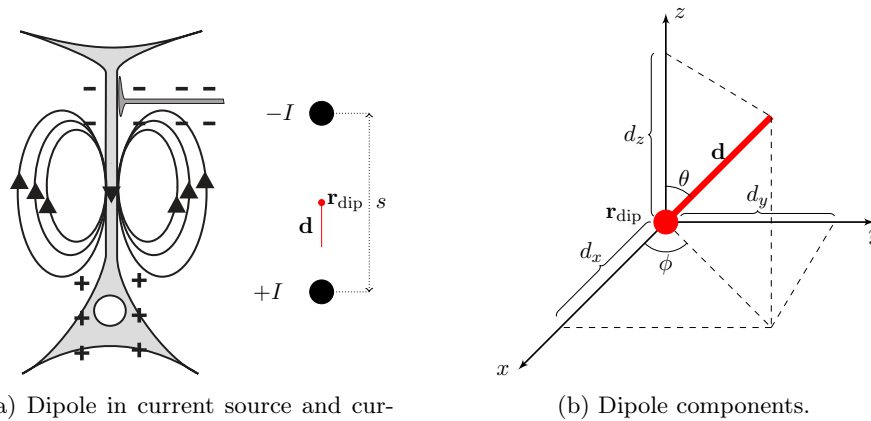
(a) Dipole in current source and current sink configuration, as a model for the postsynaptic current flow.

(b) Dipole components.

Figure 2.10: The current dipole, characterized by its location $\mathbf{r}_{\mathrm{dip}}$ and moment or orientation $\mathbf{d}$.

cal dendrites of the pyramidal neurons. The source model results in a geometrical description of the whole cortical surface with each element (brain voxel) being represented by an orthogonal dipole.

2.4.2   The volume conductor model

In bioelectromagnetism, volume conduction modeling is defined as the transmission of electric fields from a primary current source through biological tissue towards measurement sensors [Malmivuo and Plonsey, 1995]. In order to unravel the relationship between EEG and the underlying source configuration, the electrical conduction properties of the volume conductor (the human head) have to be modeled.

The first volume conductor model of the human head consisted of a single homogeneous sphere enclosing the whole head [Brody et al., 1973, Frank, 1952]. Because this model was geometrically not correct and did not take into account the skull, it had limited accuracy. The skull is located between the sources in the brain and the recording electrodes, thus it has a large influence on the potential distribution over the scalp. The three-shell *spherical head model* (Figure 2.11a) is a refinement of the single sphere model, providing a closer approximation to reality. This model consists of three concentric spheres, with each layer representing a head tissue: brain (innermost), skull (intermediate) and scalp (out-

ermost) [Ary et al., 1981, Salu et al., 1990, Sarvas, 1987]. Additional spheres can be included in this model to represent other tissues such as the cerebrospinal fluid compartment. The conductivity is assumed isotropic and homogeneous in each of these layers, with values assigned from the literature. A multi-layered spherical volume conductor model with unrestrained number of concentric spheres that can incorporate anisotropies, is presented in De Munck [1988] and De Munck and Peters [1993].

(a) Spherical.   (b) Realistic.
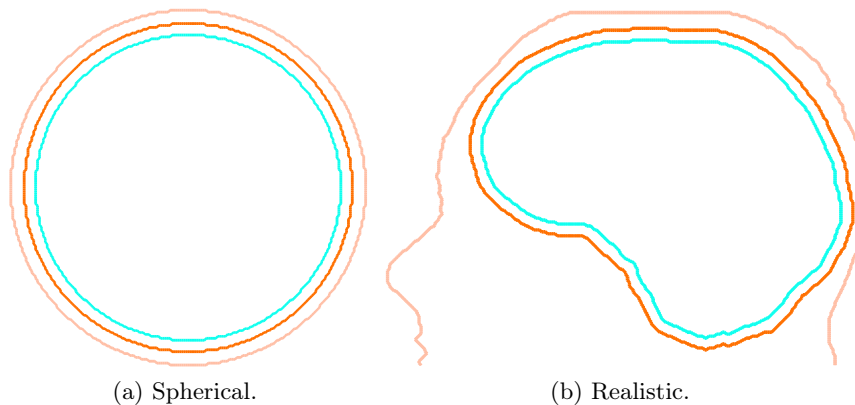
Figure 2.11: Three-layered spherical and realistic volume conductor models: ☐ Scalp, ☐ Skull and ☐ Brain.

Nowadays, it has become increasingly clear that the actual geometry of the head considerably affects the solution of the forward problem [Akalin-Acar and Makeig, 2013, Vorwerk et al., 2014]. The so-called *realistic head models* are commonly used in ESI [Song et al., 2013, Ziegler et al., 2014] and other applications [Huang et al., 2013, Windhoff et al., 2011], although their computational requirements are higher than those of a multi-layered sphere. Realistic models are based on an accurate description of the anatomy of the subject's head. High-resolution MRI of the brain can be divided into different regions in order to generate this type of model. For each region, representing a head tissue, either an isotropic or an anisotropic conductivity value is allocated. The conductivity values for all tissue classes are different and vary over subjects. Because they cannot be easily measured in vivo [Gao et al., 2006, Gonçalves et al., 2003a, Lai et al., 2005], standard values reported in literature are most commonly used.

The number of tissues included in the realistic model as well as their

geometry are still open issues in ESI [Wendel et al., 2009]. The modeling of the *skull* is one of the most challenging aspects in the construction of realistic head models. The most simplified model for the skull consists of a single isotropic homogeneous compartment, often with an approximate geometry [Stenroos and Sarvas, 2012, Vanrumste et al., 2000]. However, the actual structure of the skull is three-layered, consisting of a spongiform layer surrounded by two compact bone layers. Therefore, the skull has different conductivities and thicknesses throughout its whole structure and so it is inhomogeneous [Law, 1993, Lynnerup et al., 2005]. Chapter 5 presents a simulation study about the influence of different skull modeling approaches on ESI.

Another important tissue in realistic head modeling is the white matter [Güllmar et al., 2010, Wolters et al., 2006]. Its structure consists of many parallel nerve bundles (groups of axons) and therefore the electrical conduction is anisotropic, higher in the direction of the white matter tracts than orthogonal to them. The anisotropy information is derived from diffusion tensor data acquired with MRI. This technique provides directional information on the diffusion of the water. The conductivity is assumed higher in the direction in which the water diffuses most easily [Tuch et al., 2001].

Besides the number of head tissues and their geometry, the conductivity values used have important effects on ESI [Wang and Ren, 2013, Wendel et al., 2008]. Especially, the conductivity of the skull is very low compared to the other head tissues, highly attenuating the electric field. For that reason, techniques to determine a single and effective conductivity value, incorporating inhomogeneity and thickness of the skull should be further investigated. These techniques include electrical impedance tomography (EIT) [Gonçalves et al., 2003a, Oostendorp et al., 2000], MR-EIT [Gao et al., 2006], simultaneous intra- and extra-cranial electrical stimulation [Lai et al., 2005, Zhang et al., 2006] and methods using somatosensory evoked field and somatosensory evoked potential data to calibrate the conductivities [Baysal and Haueisen, 2004, Gonçalves et al., 2003b, Lew et al., 2009a].

The accurate determination of *electrode positions* is also crucial for the correct solution of the forward problem. The main strategies to derive the electrode positions are: (i) based on the international 10–20 electrode system, the positions are warped onto the subject's head; (ii) using a 3D digitizer system, e.g., Polhemus; (iii) attaching spherical markers on top of the electrodes on an MRI; (iv) segmenting the positions from

computed tomography (CT) images.

2.4.3 The forward problem

The basis of the forward problem are the Maxwell's equations:

$$\nabla \times \mathbf{E} = -\frac{\partial \mathbf{B}}{\partial t} \tag{2.1}$$

$$\nabla \times \mathbf{B} = \mu_0 \left(\mathbf{J} + \varepsilon_0 \frac{\partial \mathbf{E}}{\partial t} \right) \tag{2.2}$$

$$\nabla \cdot \mathbf{E} = \frac{\rho}{\varepsilon_0} \tag{2.3}$$

$$\nabla \cdot \mathbf{B} = 0 \tag{2.4}$$

where $\mathbf{E}$, $\mathbf{B}$ and $\mathbf{J}$ stand for electric field strength, magnetic flux density and electric current density, respectively. The variables ε_0 and μ_0 represent the vacuum permittivity and permeability, respectively, and ρ is the charge density.

Owing to the frequency range of the signals involved (below 1 kHz), no charge can be piled up in the conducting volume (no capacitances) [Plonsey and Heppner, 1967]. As a consequence, the effects of time variation can be neglected, leading to stationary magnetic and electric fields at each instant in time. Ignoring the time-dependencies in equations (2.1) and (2.2), results in the quasi-static approximation of the Maxwell's equations:

$$\nabla \times \mathbf{E} = 0 \tag{2.5}$$

$$\nabla \times \mathbf{B} = \mu_0 \mathbf{J} \tag{2.6}$$

together with equations (2.3) and (2.4). Because of the linearity of the quasi-static Maxwell's equations, the current density inside the volume conductor (the human head) consists of the current density imposed by the dipole source or *primary current density* $\mathbf{J}_p$ and the current density flowing in the volume conductor or *return current density* $\mathbf{J}_r$, expressed as: $\mathbf{J} = \mathbf{J}_p + \mathbf{J}_r$. The return current density $\mathbf{J}_r$ generates an electric field $\mathbf{E}$, both of which are related by Ohm's law as:

$$\mathbf{J}_r = \mathbf{\Sigma}\mathbf{E} \tag{2.7}$$

with $\mathbf{\Sigma}$ the conductivity tensor or matrix representing the direction-

dependent conductivity given by:

$$\mathbf{\Sigma} = \begin{bmatrix} \sigma_{xx} \, \sigma_{xy} \, \sigma_{xz} \\ \sigma_{xy} \, \sigma_{yy} \, \sigma_{yz} \\ \sigma_{xy} \, \sigma_{yz} \, \sigma_{zz} \end{bmatrix}. \tag{2.8}$$

The conductivity is conditioned by the material of which the conductor is composed, the state of aggregation of its parts and its temperature [Maxwell, 1954]. For isotropic conductivity, $\mathbf{\Sigma}$ is a diagonal matrix, while for the anisotropic case $\mathbf{\Sigma}$ varies according to the position in the anisotropic compartment [Hallez, 2008].

From Equation (2.5), the electric field can be represented by a scalar potential V:

$$\mathbf{E} = -\nabla V \tag{2.9}$$

The vector ∇V gives the direction in which V most rapidly increases. The negative sign in Equation (2.9) indicates that the electric field is oriented from a high to a low potential area.

The total current density $\mathbf{J}$ flowing through the volume conductor can be rewritten as:

$$\mathbf{J} = \mathbf{J}_p - \mathbf{\Sigma}\nabla V \tag{2.10}$$

Neglecting the capacitance of the head tissues translates mathematically into zero divergence of the current density, expressed as: $\nabla\cdot\mathbf{J} = 0$. Then, by applying the divergence operator to Equation (2.10) the Poisson's differential equation is obtained:

$$\nabla \cdot (\mathbf{\Sigma}\nabla V) = \nabla \cdot \mathbf{J}_p. \tag{2.11}$$

Applying the divergence operator to the primary current density $\mathbf{J}_p$ (right hand side of Equation (2.11)), and taking into account the dipole model in source $(+I)$ and sink $(-I)$ configuration (Figure 2.10a), Poisson's equation can be rewritten as:

$$\nabla \cdot (\mathbf{\Sigma}\nabla V) = I\delta(\mathbf{r} - \mathbf{r}_+) - I\delta(\mathbf{r} - \mathbf{r}_-), \tag{2.12}$$

where $\delta(\mathbf{r})$ is the Dirac delta function, and $\mathbf{r}_+ = (x_1, y_1, z_1)^T$ and $\mathbf{r}_- = (x_2, y_2, z_2)^T$ are the location of the current source and sink, respectively.

Finally, the general formulation of Poisson's equation can be expressed in the Cartesian coordinate system as:

$$\sigma_{xx}\frac{\partial^2 V}{\partial x^2} + \sigma_{yy}\frac{\partial^2 V}{\partial y^2} + \sigma_{zz}\frac{\partial^2 V}{\partial z^2} +$$
$$2\left(\sigma_{xy}\frac{\partial^2 V}{\partial x \partial y} + \sigma_{xz}\frac{\partial^2 V}{\partial x \partial z} + \sigma_{yz}\frac{\partial^2 V}{\partial y \partial z}\right) = \quad I\delta(x-x_1)\delta(y-y_1)\delta(z-z_1)$$
$$-I\delta(x-x_2)\delta(y-y_2)\delta(z-z_2).$$
$$(2.13)$$

for anisotropic conductivities with constant anisotropic tensor. In the case of isotropic conductivities, the off-diagonal elements of the conductivity tensor in (2.8) will be zero and $\sigma = \sigma_{xx} = \sigma_{yy} = \sigma_{zz}$, thereby reducing the Poisson's formulation to:

$$\sigma\frac{\partial^2 V}{\partial x^2} + \sigma\frac{\partial^2 V}{\partial y^2} + \sigma\frac{\partial^2 V}{\partial z^2} = \quad I\delta(x-x_1)\delta(y-y_1)\delta(z-z_1)$$
$$-I\delta(x-x_2)\delta(y-y_2)\delta(z-z_2) \quad (2.14)$$

2.4.3.1 Boundary conditions

At the interface between two different head tissues (Figure 2.12), boundary conditions take place. Particularly, the *Neumann boundary condition* states that all the current leaving one compartment with conductivity $\mathbf{\Sigma}_1$ through the interface enters the neighboring compartment with conductivity $\mathbf{\Sigma}_2$:

$$\mathbf{J_1} \cdot \mathbf{e}_n = \mathbf{J_2} \cdot \mathbf{e}_n$$
$$(\mathbf{\Sigma}_1 \nabla V_1) \cdot \mathbf{e}_n = (\mathbf{\Sigma}_1 \nabla V_2) \cdot \mathbf{e}_n \quad (2.15)$$

where $\mathbf{e}_n$ is the normal component on the interface. Because no current can be injected into the air outside of the human head, the current density on the surface of the head is given by

$$(\mathbf{\Sigma}_1 \nabla V_1) \cdot \mathbf{e}_n = 0, \quad (2.16)$$

the so-called homogeneous Neumann boundary condition. Likewise, the *Dirichlet boundary condition* states that the potential cannot have discontinuities when crossing the interface, i.e., $V_1 = V_2$. This condition only holds for interfaces between non-air compartments.
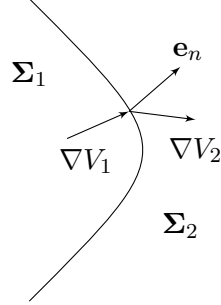
Figure 2.12: Boundary between two different head tissues with conductivities Σ_1 and Σ_2.

2.4.3.2   Algebraic formulation

The *forward problem* consists in finding the electrode potentials $V(\mathbf{r}, \mathbf{r}_{\mathrm{dip}}, \mathbf{d})$ at an electrode located at $\mathbf{r}$ caused by a dipole with position $\mathbf{r}_{\mathrm{dip}} = (x, y, z)^T \in \mathbb{R}^{3 \times 1}$ and moment $\mathbf{d} = (d_x, d_y, d_z)^T \in \mathbb{R}^{3 \times 1}$. Because of the linearity of the Poisson's equation, the potential caused by multiple dipole sources can be written as a superposition of the potential originated by each dipole source. Hence, the potential caused by an arbitrary dipole can be expressed as the sum of the potential of the three orthogonal components of the dipole as:

$$V(\mathbf{r}, \mathbf{r}_{\mathrm{dip}}, \mathbf{d}) = d_x V(\mathbf{r}, \mathbf{r}_{\mathrm{dip}}, \mathbf{e}_x) + d_y V(\mathbf{r}, \mathbf{r}_{\mathrm{dip}}, \mathbf{e}_y) + d_z V(\mathbf{r}, \mathbf{r}_{\mathrm{dip}}, \mathbf{e}_z).$$
$$(2.17)$$

For m electrodes carefully placed on the scalp at positions $\mathbf{r}_i$ with $i = 1, \ldots, m$, the electrode potentials $\mathbf{V} \in \mathbb{R}^{m \times 1}$ can be written as:

$$
\begin{aligned}
\mathbf{V} &= \begin{bmatrix} V(\mathbf{r}_1) \\ \vdots \\ V(\mathbf{r}_m) \end{bmatrix} \\
&= \begin{bmatrix} V(\mathbf{r}_1, \mathbf{r}_{\mathrm{dip}}, \mathbf{e}_x) & V(\mathbf{r}_1, \mathbf{r}_{\mathrm{dip}}, \mathbf{e}_y) & V(\mathbf{r}_1, \mathbf{r}_{\mathrm{dip}}, \mathbf{e}_z) \\ \vdots & \vdots & \vdots \\ V(\mathbf{r}_m, \mathbf{r}_{\mathrm{dip}}, \mathbf{e}_x) & V(\mathbf{r}_m, \mathbf{r}_{\mathrm{dip}}, \mathbf{e}_y) & V(\mathbf{r}_m, \mathbf{r}_{\mathrm{dip}}, \mathbf{e}_z) \end{bmatrix} \begin{bmatrix} d_x \\ d_y \\ d_z \end{bmatrix} \\
&= \mathbf{L}(\mathbf{r}) \cdot \mathbf{d} \qquad\qquad\qquad (2.18)
\end{aligned}
$$

where $\mathbf{L}(\mathbf{r}) \in \mathbb{R}^{m \times 3}$ is the *lead-field matrix*, which is dependent on the dipole position, the electrode positions and the properties of the head model. Solving the forward problem requires the computation of the

lead-field matrix. Simple head models with spherical shape can use an analytical formula, while realistic head models need numerical techniques because of its higher complexity.

2.4.3.3 Numerical solvers

The lead-fields of spherical forward models can be calculated analytically, while in the case of realistic forward models, numerical solvers are required. The most popular solvers are the Boundary Element Method (BEM) [Akalin-Acar and Gençer, 2004, Oostendorp and van Oosterom, 1989, Stenroos et al., 2007, Zanow and Peters, 1995], the Finite Element Method (FEM) [Awada et al., 1997, Buchner et al., 1997, Johnson, 1995, Van den Broek et al., 1996, Yan et al., 1991] and the Finite Difference Method (FDM) [Laarne et al., 1995, Marino et al., 1993, Mohr and Vanrumste, 2003, Turovets et al., 2014, Vanrumste et al., 2001].

The BEM approach is based on the integral formulation of the forward problem for the electric potential, first described in Barnard et al. [1967a,b] and Geselowitz [1967]. The volume conductor in the BEM is characterized by distinct closed homogeneous compartments with isotropic conductivity. The potentials are computed at the interfaces between the compartments, which are discretized into triangular meshes (Figure 2.13). The numerical accuracy of the BEM can be improved by: the isolated problem approach [Hämäläinen and Sarvas, 1989, Meijs et al., 1989], the use of linear basis functions with analytically integrated elements [De Munck, 1992], the Galerkin approach [Lynn and Timlake, 1968, Mosher et al., 1999] and the symmetric approach [Kybic et al., 2005]. The BEM has the advantage of higher computational effectiveness compared to the other numerical solvers. However, because the BEM's computational demand increases non-linearly with the number of tissues, the volume conductor model is usually limited to three compartments. Additionally, given its requirement of closed homogeneous surfaces, tissues with complex geometries such as the cerebrospinal fluid cannot be easily included in the model. Finally, the BEM cannot handle anisotropic conductivities.

In the FEM, the entire 3D volume conductor is tessellated into small elements such as tetrahedra (Figure 2.14) or hexahedra and the potential is computed at the vertices of each element [Camacho et al., 1997, Si, 2010]. The potential at an arbitrary point can be determined with FEM by interpolation of computational points in its vicinity. Different approaches are used to represent the mathematical dipole in the model:
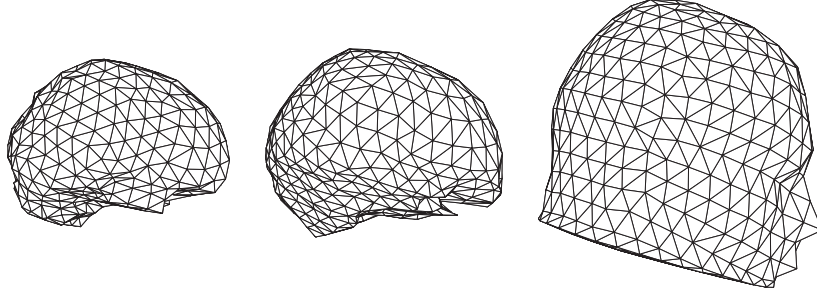
Figure 2.13: In BEM, the interfaces between the compartments (brain/skull, skull/scalp and scalp/air) are discretized into triangulated surfaces.

the subtraction approach [Schimpf et al., 2002], the partial integration approach [Weinstein et al., 2000] and the Venant approach [Wolters et al., 2007]. Because the whole volume is discretized, the system matrix is large but sparse. Efficient solver techniques [Lew et al., 2009b, Wolters et al., 2002] and transfer matrix approaches [Drechsler et al., 2009, Gençer and Acar, 2004] are necessary to find the inverse of the system matrix, reducing the computational cost of the FEM algorithm.

(a) Central tetrahedron.   (b) Corner tetrahedron.
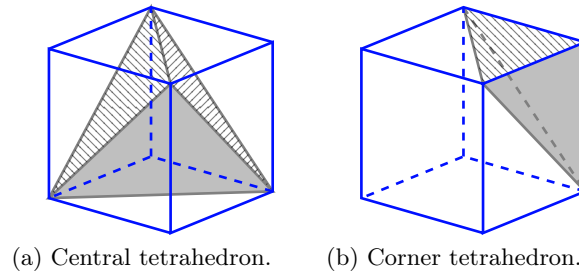
Figure 2.14: In FEM, a cubic voxel (in blue) is decomposed into five tetrahedra: one central and four at the corners.

The FDM is the method used in this work and the implementation details are explained in the next subsection. Both the FEM and the FDM can model anisotropic conductivities and perform a calculation of potentials over the entire 3D volume. The FEM is often considered to be more flexible with respect to the representation of complicated geometries. However, the main advantage of FDM over FEM is the use of the cubic voxels, particular of the MR and CT images, for the generation of the structured grid where the sources are placed. In both the BEM and the FEM, additional tessellation algorithms [Thompson

et al., 1998] are required for the construction of the surface triangles and
the tetrahedral elements, respectively.

2.4.3.4 Forward solution based on the Finite Difference Method

The calculation of the forward problem in this dissertation was carried
out with the FDM because of its possibility to model the entire volume
with both isotropic and anisotropic conductivities, while utilizing the
cubic voxels already provided by MR and CT imaging modalities. The
head is tessellated into a regular cubic grid resulting in a large number of
nodes, and for each node a linear equation is obtained. To solve the large
sparse linear system of equations, the *successive overrelaxation* (SOR)
method is used. The FDM has been adopted from Saleheen and Ng
[1997] to the solution of the forward problem in ESI on isotropic and
anisotropic media [Hallez et al., 2005].

Implementation

The differential equation (2.13) with Neumann and Dirichlet boundary
conditions (subsection 2.4.3.1) is transformed into a set of linear equa-
tions. This approach uses the voxels of the segmented head model to
form a cubic grid in which each voxel with conductivity tensor Σ has a
node (represented by a dot) at its centroid, as illustrated in Figure 2.15.
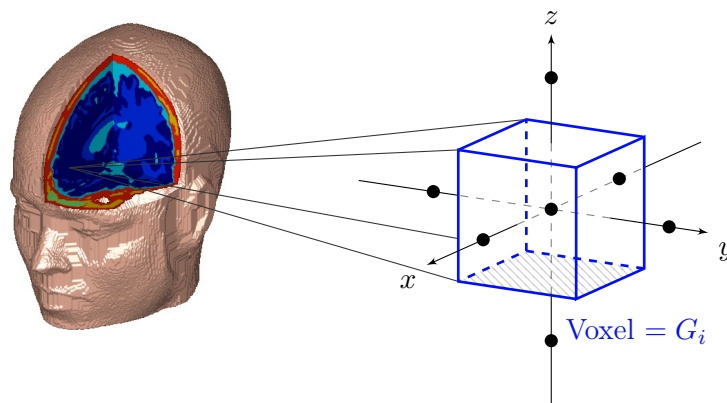
Figure 2.15: The nodes (dots) of the FDM are located in the centroid of the
voxels of the 3D head model.

A typical node **0** in the grid represents the intersection of eight neigh-
boring cubic elements with internode distance h_x, h_y and h_z, depending
on the direction, as shown in Figure 2.16. In order to obtain the finite

difference formulation of Equation (2.13), a Taylor series expansion of the potentials in the 18 nearest neighbors to the central node is used. However, because the conductivity tensor can have different values for each element of the grid, a transition layer technique is applied to avoid singularities in the Taylor series expansion [Panizo et al., 1977].
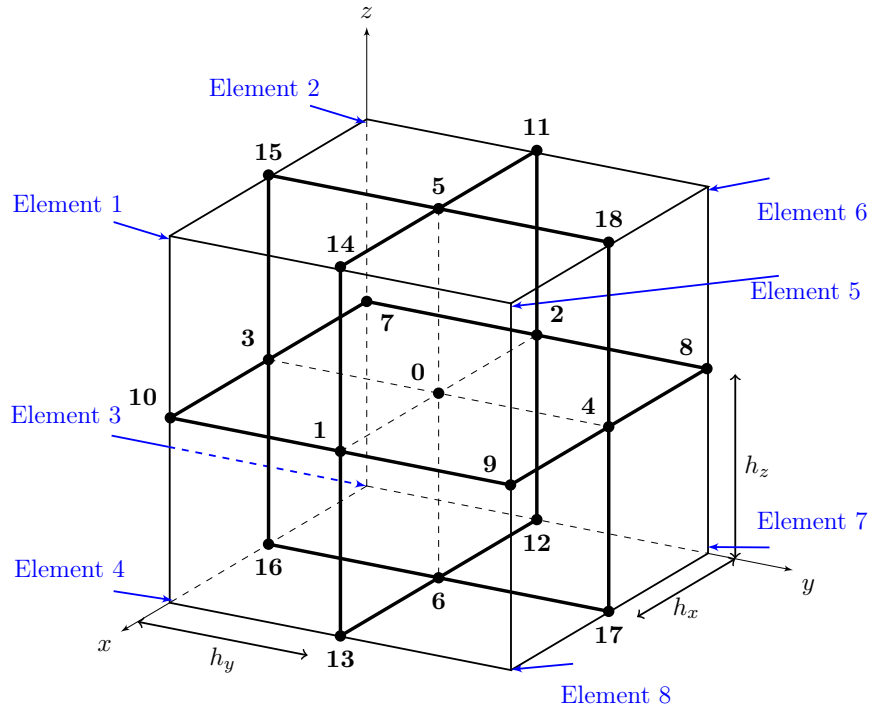
Figure 2.16: The cubic grid of the FDM. The potentials at the neighboring points $i = 1, \ldots, 18$ are used to express the partial derivatives from Equation (2.13).

The resulting finite difference approximation is expressed as:

$$\sum_{i=1}^{18} a_i \phi_i - \left(\sum_{i=1}^{18} a_i\right)\phi_0 = I\delta(\mathbf{r} - \mathbf{r}_+) - I\delta(\mathbf{r} - \mathbf{r}_-), \qquad (2.19)$$

where $\phi_0 \in \mathbb{R}$ is the discrete potential at the central node, $\phi_i \in \mathbb{R}$ is the discrete potential value at node i, $a_i \in \mathbb{R}$ are the coefficients depending on the conductivity tensor of the elements and the internode distance,

and the current I is given by

$$I = \begin{cases} +1, \text{for } \mathbf{r}_+ \in G_i \text{ and } \mathbf{r}_- \notin G_i \\ -1, \text{for } \mathbf{r}_- \in G_i \text{ and } \mathbf{r}_+ \notin G_i \\ \quad 0, \text{otherwise} \end{cases}$$

Note that a source and a sink cannot be located in the same voxel G_i. Equation (2.19) allows a discrete change or discontinuity in conductivity between neighboring elements. That is, the Neumann boundary conditions expressed in (2.15) and (2.16) are implicitly formulated in (2.19), under the condition that a natural boundary (the air with zero conductivity) is in the calculation grid. The coefficients a_i are given by [Hallez, 2008, Saleheen and Ng, 1997]:

$$a_1 = \frac{1}{4h_x^2}\left[\sigma_{xx(1)} + \sigma_{xx(4)} + \sigma_{xx(5)} + \sigma_{xx(8)}\right]$$

$$a_2 = \frac{1}{4h_x^2}\left[\sigma_{xx(2)} + \sigma_{xx(3)} + \sigma_{xx(6)} + \sigma_{xx(7)}\right]$$

$$a_3 = \frac{1}{4h_y^2}\left[\sigma_{yy(1)} + \sigma_{yy(2)} + \sigma_{yy(3)} + \sigma_{yy(4)}\right]$$

$$a_4 = \frac{1}{4h_y^2}\left[\sigma_{yy(5)} + \sigma_{yy(6)} + \sigma_{yy(7)} + \sigma_{yy(8)}\right]$$

$$a_5 = \frac{1}{4h_z^2}\left[\sigma_{zz(1)} + \sigma_{zz(2)} + \sigma_{zz(5)} + \sigma_{zz(6)}\right]$$

$$a_6 = \frac{1}{4h_z^2}\left[\sigma_{zz(3)} + \sigma_{zz(4)} + \sigma_{zz(7)} + \sigma_{zz(8)}\right]$$

$$a_7 = \frac{1}{4h_xh_y}\left[\sigma_{xy(3)} + \sigma_{xy(2)}\right]$$

$$a_8 = -\frac{1}{4h_xh_y}\left[\sigma_{xy(6)} + \sigma_{xy(7)}\right]$$

$$a_9 = \frac{1}{4h_xh_y}\left[\sigma_{xy(5)} + \sigma_{xy(8)}\right]$$

$$a_{10} = -\frac{1}{4h_xh_y}\left[\sigma_{xy(1)} + \sigma_{xy(4)}\right]$$

$$a_{11} = -\frac{1}{4h_xh_z}\left[\sigma_{xz(2)} + \sigma_{xz(6)}\right]$$

$$a_{12} = \frac{1}{4h_xh_z}\left[\sigma_{xz(3)} + \sigma_{xz(7)}\right]$$

$$a_{13} = -\frac{1}{4h_x h_z}\big[\sigma_{xz(4)} + \sigma_{xz(8)}\big]$$

$$a_{14} = \frac{1}{4h_x h_z}\big[\sigma_{xz(1)} + \sigma_{xz(5)}\big]$$

$$a_{15} = -\frac{1}{4h_y h_z}\big[\sigma_{yz(1)} + \sigma_{yz(2)}\big]$$

$$a_{16} = \frac{1}{4h_y h_z}\big[\sigma_{yz(3)} + \sigma_{yz(4)}\big]$$

$$a_{17} = -\frac{1}{4h_y h_z}\big[\sigma_{yz(7)} + \sigma_{yz(8)}\big]$$

$$a_{18} = \frac{1}{4h_y h_z}\big[\sigma_{yz(5)} + \sigma_{yz(6)}\big]$$

where $\sigma_{pq(l)}$ is the pq-th component of the conductivity tensor $\boldsymbol{\Sigma}$ defined at element l. For isotropic conductivities, the off-diagonal elements of the conductivity tensor are zero. Therefore, the finite difference formulation in the isotropic case reduces to the summation of the coefficients a_i for $i = 1, \ldots, 6$.

For each node of the cubic grid a linear equation can be written as in Equation (2.19), and for n computational points a set of linear equations is obtained:

$$\mathbf{A} \cdot \boldsymbol{\Phi} = \mathbf{I} \qquad (2.20)$$

where $\boldsymbol{\Phi} = (\phi_1, \ldots, \phi_n)^T \in \mathbb{R}^{n \times 1}$ is a vector with the potential values at each computational point; $\mathbf{I} \in \mathbb{R}^{n \times 1}$ is a vector indicating the current sources or sinks in the model; $\mathbf{A} \in \mathbb{R}^{n \times n}$ is a stiffness matrix, with a_{ij} the i-th coefficient for a cubic grid with central node j. The system matrix $\mathbf{A}$ is sparse and symmetric, with each row consisting of 19 non-zero elements in the case of anisotropic conductivities and seven in the isotropic case.

To solve the large sparse linear system given by (2.20), iterative methods have to be used. In this dissertation, the *successive over-relaxation* (SOR) method [Saad, 2003] was used because of its simplicity. The SOR is an iterative solver which convergence can be improved with an optimal over-relaxation parameter ω (see Appendix A). We used $\omega = 1.97$ for head models with a grid size within 1 mm [Hallez, 2008]. The SOR method has to be reapplied for each source configuration, making the solution of the forward problem too computationally expensive. Therefore, the *reciprocity theorem* [Rush and Driscoll, 1969] is utilized to reduce the

number of forward calculations to the number of electrode pairs, using the iterative solver. When m scalp electrodes are used to measure the EEG, $m-1$ numerical forward calculations are performed. The $m-1$ potential differences at the $m-1$ electrode pairs are then transformed into m average referenced potentials at the m electrodes. This speeds up the time necessary to do the forward calculations since the number of electrodes ($\lesssim 256$) is much smaller than the number of dipoles ($\sim$ 10,000–100,000). The reciprocity theorem is presented in detail in Appendix B.

2.4.4 The inverse problem

The inverse problem is defined as the reconstruction of the electrical source distribution given a set of EEG measurements, as depicted in Figure 2.9. The inverse problem is solved by using the lead-fields calculated in the forward problem to compute the electrode potentials produced by the source estimates. Then, the source parameters are adapted until the residual between the measured electrode potentials and those caused by the source estimates is minimal. This solution, however, is not unique because an infinite number of source configurations can originate an identical scalp potential distribution [von Helmholtz, 1853]. Furthermore, the solution is extremely sensitive to small perturbations in the data, i.e., the problem is *ill-posed*.

As it was mentioned in Section 2.4.1, the source model can be represented by a single dipole or by multiple dipoles distributed throughout the whole brain. Therefore, there are two main approaches to the inverse solution [Baillet et al., 2001, Grech et al., 2008]: (i) Equivalent current dipole models and (ii) Distributed source models.

2.4.4.1 Equivalent current dipole models

The equivalent current dipole models, also known as *parametric approaches* or *spatio-temporal dipole fit models*, assume that the electrical activity is restricted to a limited number of areas. As a consequence, this focal activity can be modeled by a few equivalent current dipoles with unknown location and moment. Unlike the dipole moment $\mathbf{d}$, the dipole location $\mathbf{r}$ is non-linearly related to the scalp potential $\mathbf{V}$ through the volume conductor model (Equation (2.18)). Therefore, the estimation of the source parameters must be carried out with a non-linear numerical method. Because the number of sources is much smaller than the

number of electrodes, the problem is *over-determined* [Fuchs et al., 1999].

Single dipole at a single time instance

Given a set of scalp potential measurements $\mathbf{V}_{\text{in}} \in \mathbb{R}^{m \times 1}$, the inverse problem is solved by the minimization of the relative residual energy (RRE), which expresses the fraction of energy that cannot be explained by the dipole model [Hallez et al., 2005]:

$$\text{RRE} = \frac{\|\mathbf{V}_{\text{in}} - \mathbf{L}(\mathbf{r}) \cdot \mathbf{d}\|_2^2}{\|\mathbf{V}_{\text{in}}\|_2^2} \qquad (2.21)$$

where $\|\cdot\|_2$ is the L_2-norm. The dipole parameters $\mathbf{r}$ and $\mathbf{d}$ are optimized so that the RRE is minimized. The six parameters (three for the location and three for the moment) that have to be optimized in (2.21) can be reduced to three by deriving the optimal dipole moment $\mathbf{d}_{\text{opt}}$:

$$\mathbf{d}_{\text{opt}} = \mathbf{L}^+(\mathbf{r}) \cdot \mathbf{V}_{\text{in}} \qquad (2.22)$$

with $\mathbf{L}^+$ denoting the Moore-Penrose pseudo inverse of $\mathbf{L}$. Substituting (2.22) in (2.21), the RRE becomes

$$\text{RRE} = \frac{\|(\mathbf{I} - \mathbf{L}(\mathbf{r})\mathbf{L}^+(\mathbf{r}))\mathbf{V}_{\text{in}}\|_2^2}{\|\mathbf{V}_{\text{in}}\|_2^2}. \qquad (2.23)$$

This way, the RRE is only a function of the dipole location $\mathbf{r}$. The minimization of the RRE cost function can be performed using non-linear optimization techniques or through a scanning of the whole brain volume (goal function scan) [Knösche, 1997]. In the former case, the Nelder-Mead simplex method [Nelder and Mead, 1965] is often used because of its relative simplicity and apparent robustness to local minima of the cost function. In this thesis, the above mentioned approaches for the minimization of the RRE were used in Chapters 5 and 6, respectively.

Subspace source localization methods

The multiple signal classification (MUSIC) [Mosher et al., 1992] is a method used to locate multiple asynchronous dipolar sources through a 3D search. First, the signal and noise-only subspaces are estimated. A projection is applied onto the estimated noise-only subspace. To locate the sources, the head volume must be searched for multiple local peaks in the projection matrix. Several extensions to the MUSIC algorithm are found in the literature [Mosher and Leahy, 1998, 1999]. The first

principle vectors (FINES) [Xu et al., 2004] is another subspace method that applies projections onto a particular set of vectors of the noise-only subspace.

Beamformers

Beamforming approaches [Van Veen and Buckley, 1988, Van Veen et al., 1997] perform spatial filtering to differentiate between signals coming from a region of interest and signals from other sources. To achieve this, the algorithm assumes that the sources are uncorrelated.

2.4.4.2 Distributed source models

The distributed source models, also referred to as *imaging methods*, consist in placing a large number of dipoles throughout the volume of the brain or on the cortical surface. Therefore, the dipoles are assumed to have fixed position but variable amplitude and orientation. Unlike equivalent current dipole models, the number of unknowns ($\sim$ 10,000–100,000) in this approach is larger than the number of electrodes ($\lesssim$ 256) and therefore the system is *under-determined* [Fuchs et al., 1999]. Additional constraints in the form of regularization schemes are required in order to solve this system [Tikhonov and Arsenin, 1977]. Some of the most popular approaches are briefly described below.

Minimum norm estimates

The minimum norm (MN) solution [Hämäläinen and Ilmoniemi, 1994] is a well-known 3D estimation in which the source with the minimum current density is selected as the estimated dipole. This algorithm, however, presents a depth-bias that favors the superficial sources. To compensate such bias, the weighted minimum norm (WMN) [Jeffs et al., 1987] and the low resolution electromagnetic tomography (LORETA) [Pascual-Marqui et al., 1994] solutions were introduced. The latter inserts a laplacian weighting to the sources, benefiting spatially smooth results.

Standardized LORETA estimates

Standardized low resolution brain electromagnetic tomography (sLORETA) [Pascual-Marqui, 2002] is based on the MN solution and not on LORETA, as it may be perceived from its name. sLORETA performs a normalization of the MN estimates by its posterior covariance to obtain a statistical map of the brain activity. To compute the current distribution instead of statistical maps, two sLORETA-based algorithms

have been introduced: Exact low resolution brain electromagnetic tomography (eLORETA) [Pascual-Marqui, 2007] and sLORETA-weighted accurate minimum norm (SWARM) [Wagner et al., 2007].

2.5 Summary

This chapter presented the generation, measurement and some applications of the electrical activity generated in the brain. First, the concepts of neuronal physiology and electroencephalography were introduced. Subsequently, an explanation about epilepsy was presented given that the methods presented in this dissertation are devoted to this application area. Finally, the EEG source imaging (ESI) technique was explained together with its forward and inverse problems, which consist of three main elements: the source model, the volume conductor model and the EEG measurements. The technique used to solve the forward problem in this dissertation, namely the finite difference method, was mathematically formulated. The source model and the EEG measurements were explained in detail, while the generation of realistic volume conductor models for ESI is the topic of the next chapter.

Chapter 3

Realistic volume conductor models

> *...when the brain is released from the constraints of reality, it can generate any sound, image, or smell in its repertoire, sometimes in complex and "impossible" combinations*
>
> —OLIVER SACKS

The volume conductor model in ESI (the human head) was roughly introduced in Section 2.4.2. This chapter begins with an explanation of the anatomy of the human head, specifically the skull and the brain, in Section 3.1. Next, Section 3.2 presents neuroimaging modalities to study the structure of the head, namely Magnetic Resonance Imaging (MRI) and Computed Tomography (CT). The basic principles, images of the head and main artifacts related to these modalities are described. Finally, the segmentation of the head tissues is explained in Section 3.3, including some of the most common neuroimaging toolboxes and methods to segment the soft and skull tissues.

3.1 Anatomy of the human head

The anatomy of the human head is visualized following certain conventions, as shown in Figure 3.1. The anatomical planes are hypothetical planes used to cut across the head, in order to characterize the location of structures. Three basic planes are used: (i) *sagittal* is a vertical plane dividing the head into right (R) and left (L); (ii) *coronal* is a vertical plane dividing the head into posterior (P) and anterior (A) portions;

and (iii) *axial* is a horizontal plane that divides the head into superior (S) and inferior (I) parts.

The human head is composed of the scalp, the soft external part encompassing the skull, which in turn protects and contains the brain. Because this dissertation focuses on the skull and the brain, these two tissues will be discussed in more detail in the next subsections.
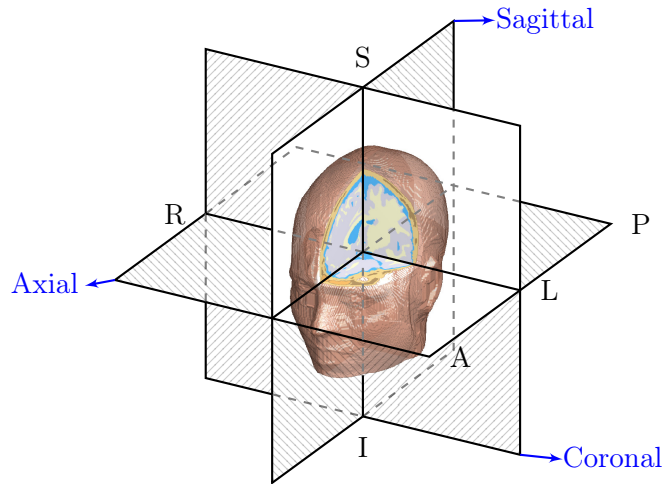
Figure 3.1: Anatomical planes and directions of the human head. Tissues: ☐ Scalp, ☐ Skull and ☐ Brain.

3.1.1   The skull

The skull is composed of a series of flattened or irregular bones that, except for the mandible, come together at immovable joints called sutures, allowing little or no movement. The skull consists of two main parts: (i) the *neurocranium* or braincase and (ii) the *viscerocranium* or facial skeleton, as shown in Figure 3.2 [Warwick et al., 1973].

The walls of the neurocranium are formed by the frontal, parietal, sphenoid, temporal and occipital bones and, to a small extent by the ethmoid bone. The upper part of the neurocranium constitutes the *cranial vault*, also known as *skull cap* or *calvaria*, while the lower part forms the base of the skull.

The base of the skull has a highly irregular geometry because of the numerous holes that allow connecting the brain with the rest of the body outside the skull. The largest opening in its floor is termed the *foramen*
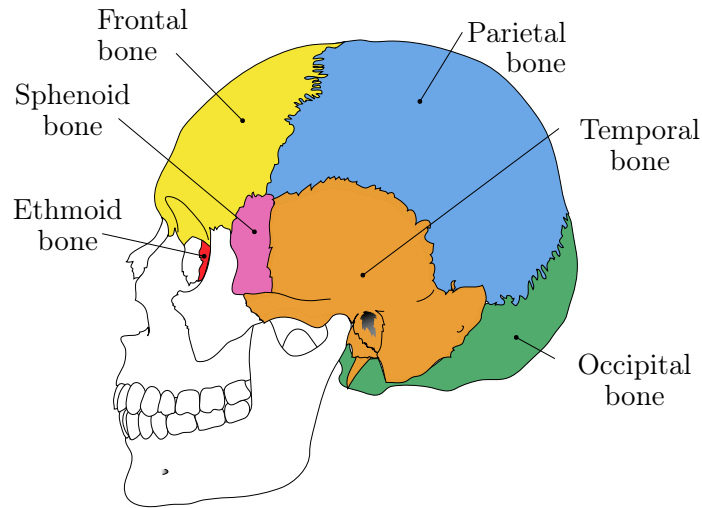
Figure 3.2: Human skull in lateral view. The neurocranium consists of eight cranial bones: Frontal, R and L parietal, R and L temporal, occipital, sphenoid and ethmoid. The viscerocranium or facial skeleton is displayed in light gray. Adapted from `http://commons.wikimedia.org/wiki/File:Cranial_bones_en_v2.svg`.

magnum, situated in the posterior part, through it the brain connects with the spinal cord. Moreover, the *paranasal sinuses* or air-filled spaces surrounding the nasal cavity, are located within the base of the skull, as can be seen in Figure 3.3. The base of the skull is thicker around the sinuses and thinner in the area surrounding the eyes.

The cranial vault consists of a large part of the frontal bone, most of the two parietal bones, the uppermost part of the temporal bone and a small portion of the occipital bone. The thickness of the cranial vault varies throughout its whole structure because it consists of two layers of compact bone separated from each other by a spongy bone layer. The spongy bone, also called *cancellous* bone or *diploë*, contains red bone marrow in its interstices [Warwick et al., 1973]. The cranial vault is thickest where there is a greater proportion of spongy bone, e.g. occipital area, and thinnest where the compact bone layers are continuous, e.g. temporal area and suture lines [Law, 1993].

Attached to the inner wall of the skull, a thick and dense inelastic membrane called the *dura mater* is found. The dura mater is one of
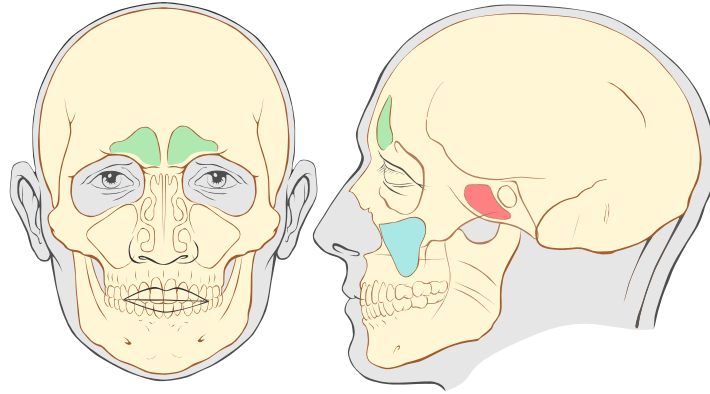
Figure 3.3: Paranasal sinuses: ☐ Frontal, ☐ Ethmoid, ☐ Sphenoid and ☐ Maxillary. From `https://commons.wikimedia.org/wiki/File:Paranasal_sinuses_numbers.svg`.

the three meninges protecting the brain against trauma. The other two meninges are the *arachnoid* and the *pia mater*. The latter is a vascular membrane that firmly adheres to the surface of the brain. The *cerebrospinal fluid* (CSF) circulates within the arachnoid and the pia mater, nourishing the brain tissue and working as a shock absorber to reduce the impact of knocks [Carter, 2014]. The CSF is produced in the ventricles, a group of interconnected cavities inside the brain (seen in Figure 3.5b). A diagrammatic section of the head showing the layers of the skull bone and the meninges is presented in Figure 3.4.
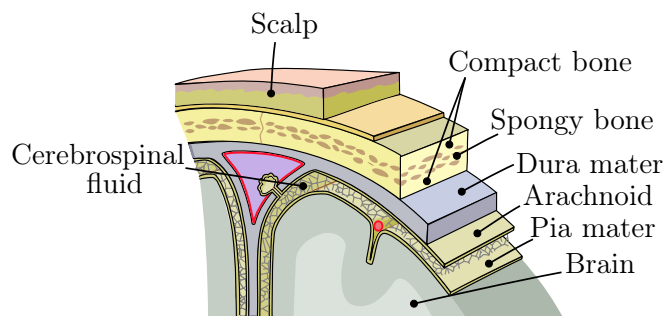
Figure 3.4: Diagrammatic section of the head showing the layers of the skull bone and the meninges. Adapted from `https://commons.wikimedia.org/wiki/File:Meninges-en.svg`.

3.1.2 The brain

The brain is contained within the skull and constitutes the upper, largely extended part of the CNS [Warwick et al., 1973]. It consists of three main parts: Cerebrum, cerebellum and brain stem, as seen in Figure 3.5a. The *brain stem* connects the brain with the spinal cord, and consists of the midbrain, pons and medulla. The function of the brain stem is to maintain the basic activities of the human body such as breathing, heart rate, temperature, sleep, attention and digestion. The *cerebellum* (latin for "little brain") processes sensory input and coordinates the output of movements and the balance. The *cerebrum* is the largest part

(a) Lateral view of the human brain.

(b) Coronal slice of the cerebrum.
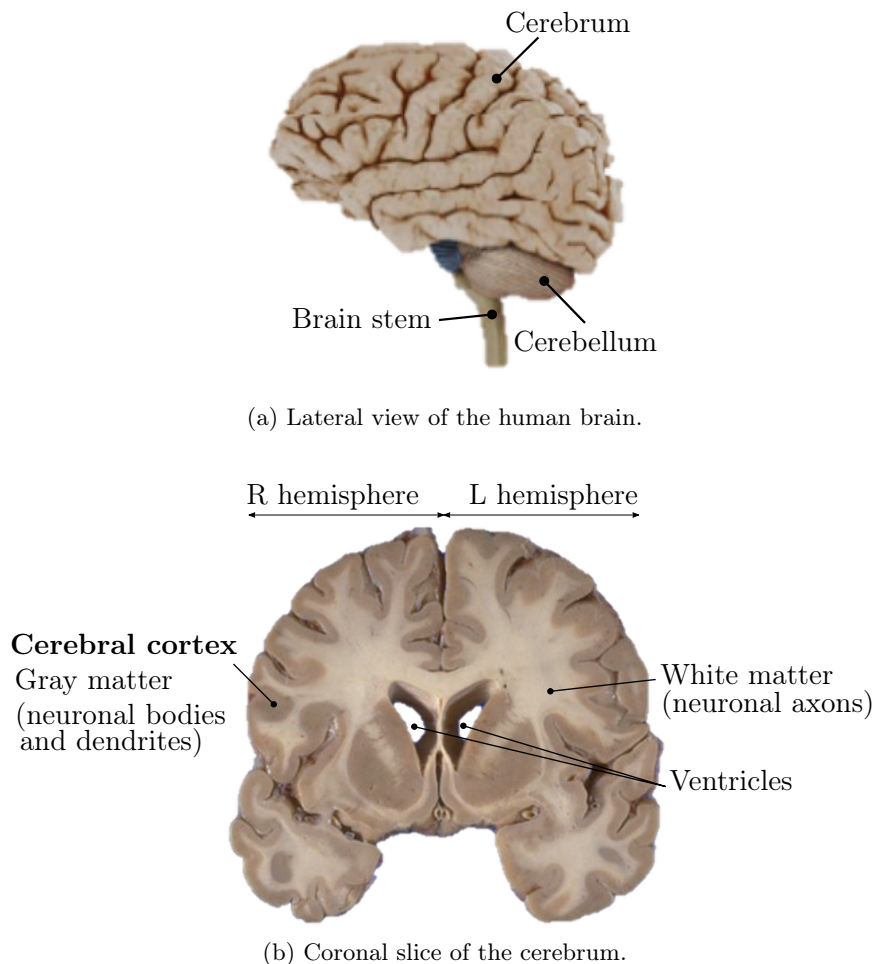
Figure 3.5: The human brain. Adapted from [Carter, 2014].

of the brain (approximately two-thirds of the total weight), responsible for higher order human functioning. It is divided into the left and right hemispheres, both controlling the muscles in the contralateral side of the body. For most of the people, the left hemisphere is dominant for language, speech and logical abilities, while the right hemisphere manages visual imagery, spatial and artistic abilities. The outermost layer of the cerebrum is the *cerebral cortex*, a two to four millimeters sheet of *gray matter* (GM) which consists of neuronal cell bodies and dendrites. The group of neuronal axons connecting several gray matter areas between each other is named the *white matter* (WM). The name WM comes from its lighter appearance compared to the GM, resulting from the lipid content of the myelin sheaths of axons. Figure 3.5b shows a coronal slice of the cerebrum.

The cerebral cortex has evolved into a folded surface in order to maximize the space within the confined volume of the skull. As a result, the cortex has foldings named *gyri* or convolutions separated by grooves termed *sulci* or fissures. With the help of these gyri and sulci as well as certain arbitrary lines, the cerebrum is divided into the following lobes (Figure 3.6) [Warwick et al., 1973]:

Frontal lobe: Bounded behind by the *central sulcus* (also called Rolandic fissure), the frontal lobe is involved in executive functions such as thinking, planning, organizing, problem solving, emotional and behavioral control, and personality. It also controls movement (*motor cortex*) and speech (*Broca's area*) [Dronkers et al., 2007].

Parietal lobe: It is associated with the perception of touch (*somatosensory cortex*), spatial orientation, arithmetic and spelling.

Temporal lobe: Inferior to the *lateral sulcus* (also called Sylvian fissure), the temporal lobe processes hearing and comprehension of written and spoken language (*Wernicke's area*) [Bogen and Bogen, 1976].

Occipital lobe: Starting behind the *parieto-occipital sulcus*, the occipital lobe receives and processes visual information (*visual cortex*).

Limbic system: The limbic system is responsible for the phyisology of emotions, memory and learning. It is a complex set of structures

(Figure 3.6b) encompassing the hippocampus and amygdala, both very important in epilepsy. Particularly, the epileptogenic origin in mesial temporal lobe epilepsy, the most common type of epilepsy in humans [Engel, 2001a], lies within the limbic system.

(a) Lateral view of the brain showing four brain lobes.

(b) Medial view of the brain depicting the limbic system, considered the fifth brain lobe.
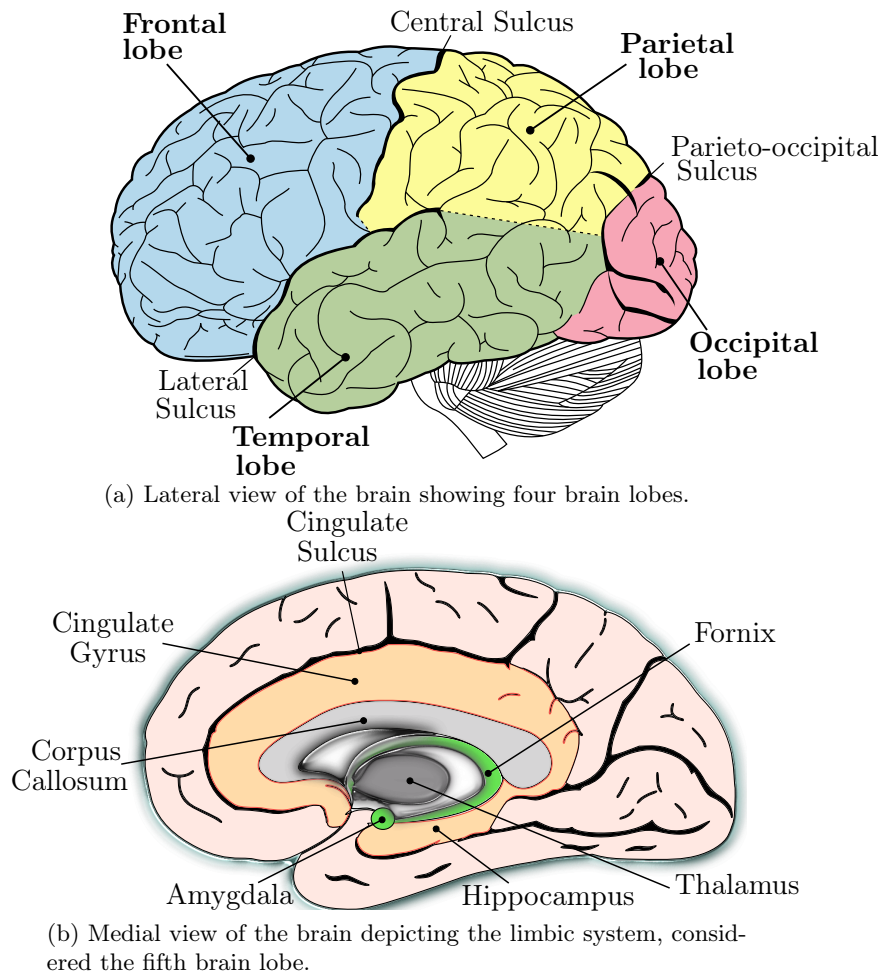
Figure 3.6: The four lobes of the brain and the limbic system. Adapted from: (a) https://commons.wikimedia.org/wiki/File:Lobes_of_the_brain_NL.svg.

The *insular cortex*, a piece of cerebral cortex deeply folded inside the lateral sulcus, can be considered as part of the temporal lobe [Kolb and Whishaw, 2009] although some authors consider it as the sixth brain lobe [Miller, 2011, Ribas, 2010]. Furthermore, based on the neuron's cytoarchitecture (structure and organization of cells), the cerebral cortex

can be divided into 52 *Brodmann areas* [Brodmann, 1909].

3.2   Structural imaging of the head

3.2.1   Magnetic Resonance Imaging

3.2.1.1   Basic principles of MRI

MRI originates from the manipulation and quantification of the magnetization of atomic nuclei inside the human body. The atomic nuclei used in clinical MRI are mostly hydrogen nuclei (consisting of a single proton), which occur abundantly as part of water molecules present in biological cells. Protons are positively charged particles constantly spinning. This spinning motion gives rise to a net magnetic moment along the axis of the spins. In the presence of an external magnetic field $\mathbf{B}_0$, the proton spins tend to align with the field generating a *net magnetization vector M*. Besides this net magnetization, the nuclei will precess around the direction of $\mathbf{B}_0$ with the *Larmor frequency ω_0*, at a random phase between each other. Once the volume has become magnetized, thermal equilibrium is reached. The net magnetization at equilibrium M_0 becomes longitudinal to the direction of the $\mathbf{B}_0$ field. To generate an MR signal, the state of equilibrium is disturbed by transmitting electromagnetic waves. A radio-frequency (RF) pulse at the Larmor frequency, i.e., in resonance with the frequency at which the nuclei precess, changes the orientation of the nuclei and aligns their phase. This originates a decrease in the longitudinal magnetization M_z and establishes a new transverse component M_{xy} in the net magnetization vector.

After the RF pulse is removed, the system attempts to return to equilibrium. During this process, a RF wave at the Larmor frequency is emitted by the nuclei. This wave, that can be measured by a receiver coil, is known as the *Free Induction Decay* (FID) signal. The FID is dominated by two mechanisms: Longitudinal and Transverse *relaxation*. Longitudinal or *spin-lattice* relaxation is the restoration of net magnetization along the longitudinal direction as spins return to their parallel state. It follows an exponential growth described by the time constant T1. Transverse or *spin-spin* relaxation is the loss of net magnetization in the transverse plane caused by loss of phase coherence (dephasing of the spins). It follows an exponential decay characterized by the time constant T2. Figure 3.7 shows both mechanisms of relaxation. The time constants T1 and T2 depend on the tissue characteristics. Moreover, T1

depends on the strength of the $\mathbf{B}_0$ field, while T2 on the temperature. Typically, T1 is longer than T2 for all tissue types [Bushberg and Boone, 2011, Wansapura et al., 1999].

(a) Longitudinal or spin-lattice relaxation.

(b) Transverse or spin-spin relaxation.
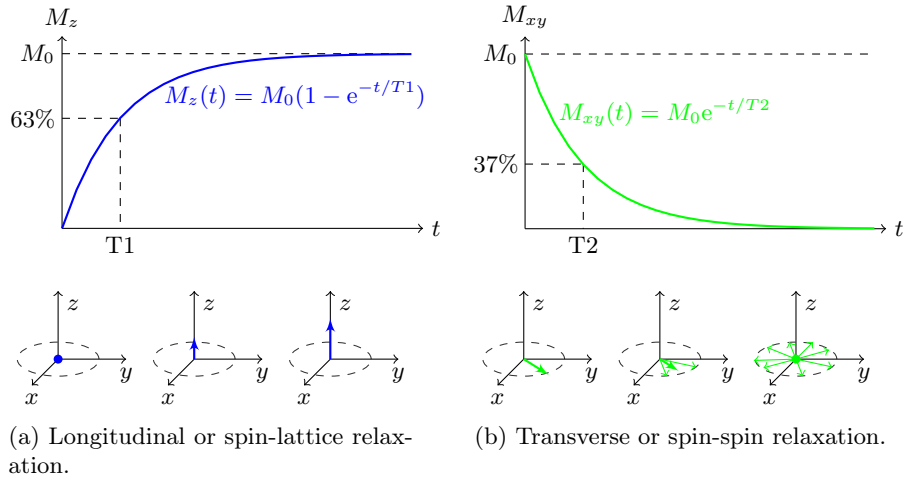
Figure 3.7: Mechanisms of relaxation of the FID signal.

The goal of MRI is to construct an image or a matrix of numbers corresponding to spatial locations. The signal described above is obtained from the whole volume but does not contain spatial information about the volume elements (voxels). To encode the location of a voxel, a *magnetic field gradient* $\mathbf{G} = (G_x, G_y, G_z)$ with components in the $x-$, $y-$ and $z-$direction is applied. Specifically, G_x is used for *frequency encoding*, G_y for *phase encoding* and G_z for *slice selection*. This way, the frequency of precession of the spins becomes a function of $\mathbf{B}_0$ and $\mathbf{G}$ at each location $(x,\ y,\ z)$ [Bernstein et al., 2004]. In the case of G_z applied in combination with an RF pulse, the resonance conditions of the spins will be fulfilled solely in a specific slice such that the signal will be produced exclusively from that slice. When G_y is applied after the RF excitation but before signal reception, the spins at different positions along the $y-$axis will precess at differing Larmor frequencies, thereby introducing phase shifts in the precession of the spins along this direction. The implementation of G_x during signal acquisition leads to the spins along the $x-$axis to process at varying Larmor frequencies. Hence, the measurements are retrieved from a particular slice with phase encoded rows and frequency encoded columns. The MR signals thus acquired are in the frequency domain, often referred to as $\mathbf{k}$-space [Ljunggren, 1983].

Subsequent to the recording of several spatially encoded MR signals, the inverse Fourier Transform can be used to reconstruct each individual voxel of the MR image. The resulting image is characterized by complex numbers that can be reconstructed as real and imaginary images.

3.2.1.2 MR images of the brain

The contrast in MRI can be controlled by altering the rate at which the nuclei are excited (*repetition time*—TR) and the time after excitation when data collection is started (*echo time*—TE). By modifying TR (in the order of seconds) and TE (in the order of milliseconds), MRI sequences can be designed to emphasize different tissues in the brain.

A T1-weighted MR image can be measured by selecting short TR and TE values. A tissue like fat has short T1, i.e., it rapidly realigns its longitudinal magnetization with $\mathbf{B}_0$ after an RF pulse (Figure 3.7a). Therefore, fat appears bright on a T1-weighted image. Contrarily, water (CSF) takes longer time to realign parallel to $\mathbf{B}_0$, having smaller transverse magnetization after an excitation pulse. As a consequence, water appears dark. The contrast between the different tissues is thus generated by selecting a TR shorter than the tissues' recovery time. The T1-weighted images used in Chapters 5 and 6 of this dissertation were acquired with the Magnetization Prepared RApid Gradient Echo (MP-RAGE) protocol [Brant-Zawadzki et al., 1992]. This protocol makes use of optimal acquisition parameters to maximize the contrast between GM and WM, which allows to inspect structures such as the hippocampus [Deblaere and Achten, 2008].

As opposed to T1-weighting, tissues with short T2s such as fat take less time to decay than tissues with longer T2 values such as water (Figure 3.7b). Thus, fat generates weaker signals and appears darker in the MR image than water (CSF). T2-weighted MRI require long TR and TE magnitudes to reveal the intrinsic differences in the T2 value of the tissues. In this dissertation, postoperative T2-weighted MR images were used in Chapter 6 to visualize the borders of resected tissue after epilepsy surgery.

When the scanning parameters are set (long TR, short TE) to minimize the effects of T1 and T2, a proton-density (PD)-weighted MR image is generated. The PD-weighted MR image is thus proportional to the density of protons in the imaging volume. The higher (lower) the number of protons, the greater (lesser) the transverse component of magnetization,

and the brighter (darker) the signal on the PD-weighted MRI. Figure 3.8 shows axial slices of T1-, T2- and PD-weighted MR images.

| (a) T1-weighted | (b) T2-weighted | (c) PD-weighted |
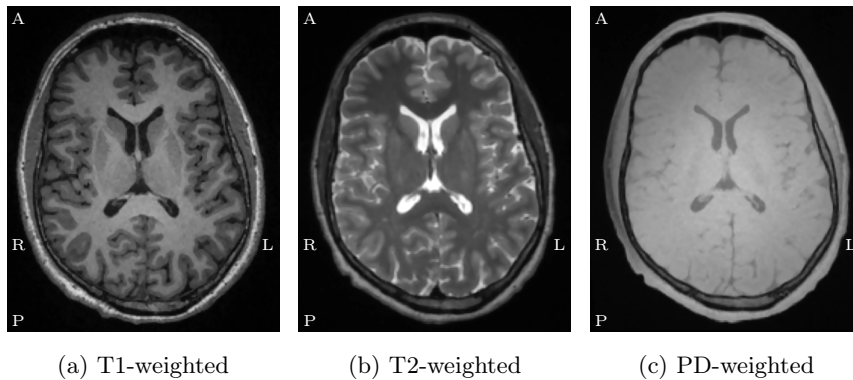
Figure 3.8: Axial slice of T1-, T2- and PD-weighted MR images of the brain. From [Güllmar, 2008]

Another important sequence in MRI is the Fluid-Attenuated Inversion Recovery (FLAIR), which is used to detect lesions. In FLAIR images, the effect of CSF is suppressed so that lesions can be easily characterized. Figure 3.9 displays a 3D FLAIR MR image.
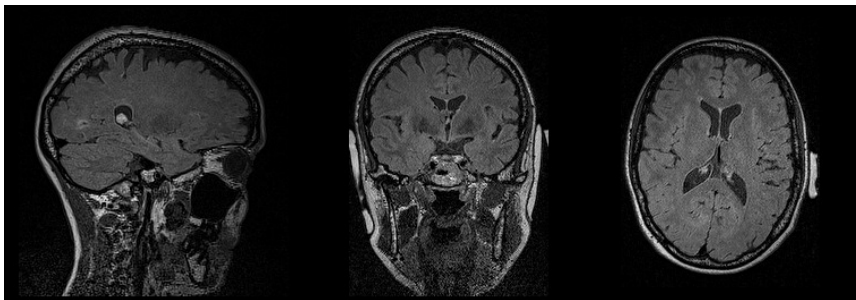
Figure 3.9: 3D FLAIR MR image.

Tissues such as bone that do not contain a lot of water generate a weak signal in MRI. Therefore, the reconstruction of bone tissue from MR images becomes challenging. In contrast, X-ray CT images allow a correct visualization of the bone as it will be presented in Section 3.2.2.

3.2.1.3   Artifacts in MR imaging

The acquired data in MRI is known to be corrupted by Gaussian white noise. After inverse Fourier transformation, the real and imaginary parts of the image are still corrupted with Gaussian noise because of the linearity of the Fourier transform. Commonly, the magnitude and phase images are used instead of the real and imaginary as they have more physical meaning. Computation of a magnitude image is a non-linear operation that changes the data from Gauss to Rice distributed [Gudbjartsson and Patz, 1995].

The noise in the MR image can be random or structured. Sources of *random noise* include thermal variations and loss of sensitivity in the scanned sample. *Structured noise* refers to non-random signal contributions that only affect a certain area of the image [Bellon et al., 1986]. The most common causes of structured noise are equipment malfunction and external interference. Examples of structured noise include ghosting, ringing and DC artifacts. Nonetheless, most sources of structured noise can be eliminated or minimized with careful engineering design and setup. Those that remain present difficulties in subsequent processing. Because of their importance in the analysis performed in this dissertation, some of the most relevant artifacts in MR imaging are introduced below and displayed in Figure 3.10.

Partial volume effects: Whenever the interface between two different tissues occurs within a voxel, the resulting voxel will be proportional to the weighted average of the signals coming from different tissues. This artifact can be reduced by using smaller, more sharply-defined voxels which results in thinner sections and higher imaging matrix sizes. Figure 3.10a displays the last slice of a PD-weighted MR image in which the boundary of the brain is blurred because the voxels in that area represent both brain and CSF, as indicated by the white arrow.

Bias field: Also known as *intensity inhomogeneity*, this artifact is caused by factors such as inhomogeneous RF excitation [McVeigh et al., 1986], non-uniform reception coil sensitivity, eddy currents driven by field gradients [Simmons et al., 1994], as well as electrodynamic interactions with the object [Bottomley and Andrew, 1978]. In modern MRI scanners using coils that produce nominally uniform fields, these variations are often difficult to detect by visual inspection [Sled and Pike, 1998]. Figure 3.10b presents intensity inhomogeneity of the WM clearly

visible in the occipital region.

Chemical shift: This artifact is originated by the difference in resonance frequency between the protons in fat and water molecules. The MR signal at a particular position produced by fat protons will be composed of lower frequencies than if it were originated by water protons. As a result, fat protons appear in the image as water protons but at an incorrect location [Weinreb et al., 1985]. Thus, the water-fat-shift artifact causes that parts of fat occlude the outer boundary of the skull [Lanfer, 2014], as shown in Figure 3.10c. The white arrows indicate the shifted fat and spongy bone layers.

(a) Partial volume effect

(b) Bias field

(c) Water-fat-shift
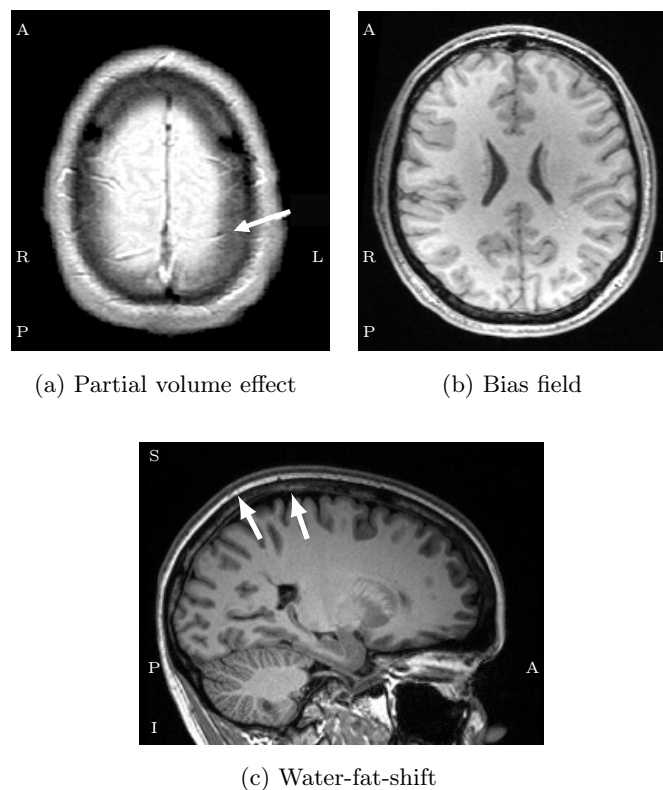
Figure 3.10: Slices of MR images displaying some of the most relevant artifacts.

3.2.2   Computed Tomography

3.2.2.1   Basic principles of CT

CT imaging originates from the measurement of the attenuation of X-ray beams through an imaged sample. In practice, the various interaction processes between X-rays and matter cannot be directly identified. This interaction can be measured, however, through the intensity of the X-rays passing through the sample. In the case of a monoenergetic beam traversing a non-homogeneous medium, the intensity I is described according to the *Lambert–Beer's* law [Swinehart, 1962].

The imaging principle in CT is based on the recording of projection views from different angles around an object with the objective of reconstructing the 3D attenuation distribution inside it. This process, allowing the visualization of slices of a 3D object, is called *tomography*. Figure 3.11a illustrates the configuration of a typical CT scanner. A rotating gantry, with attached X-ray tube and detectors, revolves around the object while emitting a fan-shaped beam of X-rays. The curved detectors capture the photons that are not attenuated along their path through the object, converting them into electrical signals. For each rotation angle, a projection view of the measured attenuation is obtained. Subsequent to the acquisition of projection views at multiple angles, the complete set of measured data can be reconstructed into a set of 2D slices with each slice corresponding to an axial cross-section of the object. *Reconstruction* is thus the process of generating a map of density values of and object from its measured projections at different angles.

The mathematical basis used to reconstruct projection data into cross-sections was first introduced in 1917 by Johann Radon [Radon, 1917]. The *Radon transform* is used to mathematically describe the measurements, taking integrals along straight lines $L_{r,\theta}$ through the object, as

$$p(r, \theta) = \mathcal{R}\{f(\mathbf{x})\} = \int_{L_{r,\theta}} f(\mathbf{x})|d\mathbf{x}|$$

where $f(\mathbf{x}) = \mu(x, y)$ represents the attenuation of the object at spatial location $\mathbf{x}$, and each line L is parameterized over the detection location r and the angle from the origin θ, as shown in Figure 3.11b. It has to be noted that the Radon transform presented here is for the case of parallel-beam projections, i.e., when the X-ray tube and the detector are shifted synchronously and parallel to each other. In order to compute the

(a) Configuration of a typical CT scanner   (b) The Radon transform
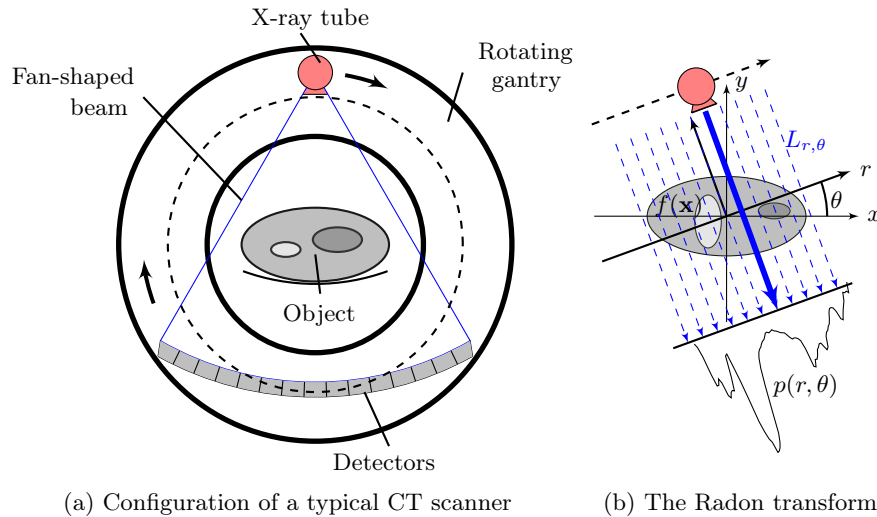
Figure 3.11: Schematic illustration of the configuration of a typical CT scanner and the Radon transform.

spatial properties of the attenuation inside the object $\mu(x, y)$, the Radon transform has to be inverted. By applying the central slice theorem in the Fourier domain, the direct inversion of the Radon transform can be computed. Nonetheless, because of the *regridding* problem, i.e., the sampling of the coordinates r and θ in the polar space, the direct inversion of $p(r, \theta)$ or simple backprojection is not used in practice. Instead, most of the current CT systems available utilize the *filtered backprojection* (FBP) for image reconstruction because of its accuracy, speed of computation and simplicity of implementation.

3.2.2.2 CT images of the brain

The slices in the CT images are pixel-by-pixel maps of X-ray beam attenuation. High values of the attenuation coefficient μ are caused by high density or high atomic number of the medium. Therefore, the gray values in CT images directly represent the physical properties of the material. Because the attenuation coefficient also depends on the energy of the X-ray beam, its reconstruction through FBP will be approximate and the so-called *beam hardening* artifact (see Section 3.2.2.3) will appear. However, the dependency of $\mu(x, y)$ on the energy can be eliminated by scaling the CT images in Hounsfield units (HU). The HU expresses the ratio of the reconstructed attenuation coefficient of a voxel $\mu(x, y)$ to

that of water μ_{water} as

$$CT(x,y) = 1000\frac{\mu(x,y) - \mu_{\text{water}}}{\mu_{\text{water}}}.$$

For a calibrated CT scan, approximate intensities of different head tissues in HU are: air -1000, water 0, CSF $+15$, WM $+25$, GM $+35$, compact bone $+1300$, spongy bone $+500$. Therefore, CT images display a high contrast between soft tissue and bone. Compact bone has a high density, and thus a high attenuation, resulting in a bright value in the CT image. Spongy bone, being less dense than compact bone, presents lower intensity in the displayed image. Soft tissues like the scalp and those found inside the cranial cavity attenuate less the X-rays, and therefore appear darker than bone in the CT image. Furthermore, the air-filled cavities inside the skull can be easily visualized in CT images. As a consequence, CT is the modality that correctly exhibits the skull and its tissues. Figure 3.12a displays an axial slice of a normal CT scan of the brain in which the contrast between the skull and the soft tissues is clearly visualized.

(a) Normal   (b) Infarction in R hemisphere
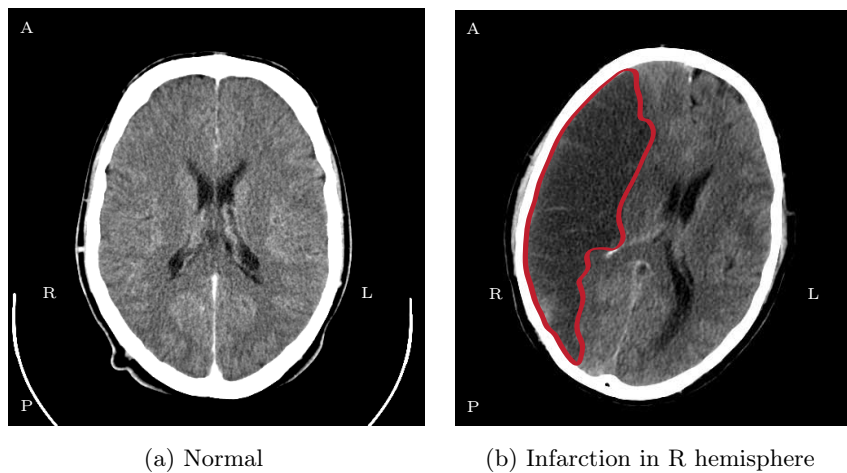
Figure 3.12: Axial slice of CT scans of the brain in normal and stroke condition. From (a) `https://commons.wikimedia.org/wiki/File:Computed_tomography_of_human_brain_(18).png` and (b) `https://commons.wikimedia.org/wiki/File:Infarction.svg`.

In clinical practice, CT imaging is routinely used for the diagnosis of head trauma because of its wide availability. CT scans of the head

accurately detect intracranial hematomas, brain contusions, edema and foreign bodies. Figure 3.12b shows a CT scan of a cerebral infarction (a type of ischemic stroke) in the right hemisphere, delineated in red.

3.2.2.3 Artifacts in CT images

In CT, an artifact refers to any systemic discrepancy between the reconstructed CT values and the actual attenuation coefficients of the object [Barrett and Keat, 2004]. Some of the most common artifacts and relevant to the work presented in this dissertation are presented below.

Beam hardening: An X-ray beam is composed of individual photons with a range of energies, i.e., it is not monoenergetic but polyenergetic. As the beam passes through an object, it becomes "harder" (its mean energy increases). This happens because the lower energy photons are absorbed more rapidly than the higher-energy photons. In order to absorb the low energy photons before hitting the object, an aluminium filter can be placed between the X-ray tube and the object. Another component called *collimator* limits the area of irradiation over the object.

Metallic materials: A metal object present in the scan field can lead to severe streaking artifacts. These streaks occur because the density of the metal is beyond the normal range that can be handled by the computer, generating partial attenuation profiles. Figure 3.13 shows axial slices of CT images with metallic teeth filling and metal electrodes that generate streaking artifacts.

3.3 Segmentation of the head tissues

Segmentation is defined as the process of dividing an image into non-overlapping regions that are homogeneous with respect to one or more features (e.g., intensity level or texture) [Gonzalez and Woods, 2002, Suetens et al., 1993]. If $\mathbf{\Omega} \in \mathbb{R}^3$ is the 3D image domain, the segmentation problem consists in finding partitions $\mathbf{\Omega}_k \subset \mathbf{\Omega}$ such that

$$\bigcup_k \mathbf{\Omega}_k = \mathbf{\Omega} \qquad \text{No vacuum}$$

$$\mathbf{\Omega}_i \cap \mathbf{\Omega}_j = \varnothing, \text{ if } i \neq j \qquad \text{Disjunct regions}$$

(a) Metallic teeth filling   (b) Metal electrodes
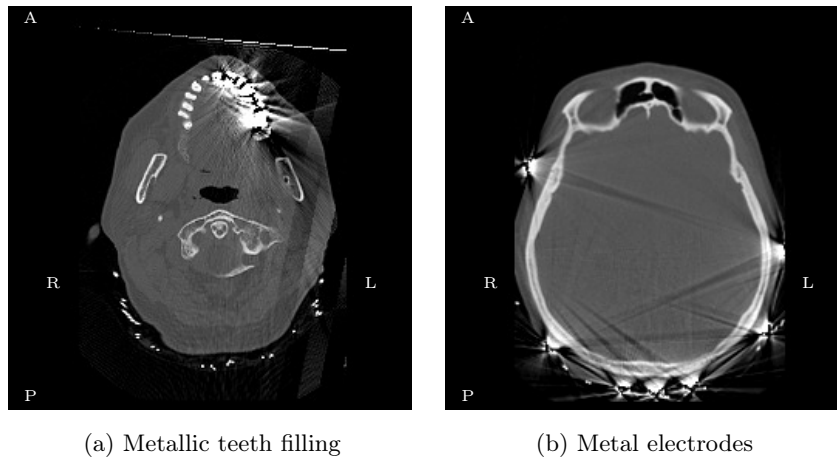
Figure 3.13: Axial slices of CT images with streaking artifacts generated by metallic materials.

Each voxel of the image is then assigned a label according to the region it belongs to. In this way, a 3D labeled image is obtained. The number of labels depends on the amount of tissues that need to be distinguished for a specific application. In this work, the realistic head model was segmented out of T1-weighted MR and CT images (see Figure 3.14) of epilepsy patients and it consists of soft tissues (scalp, cerebrospinal fluid, white matter and gray matter) and the skull (compact bone, spongy bone and air-filled cavities). An overview of the methods available in literature for the segmentation of the head tissues is presented in the next subsections.

3.3.1 Segmentation of the soft tissues of the head

The soft tissues of the head comprise the scalp and the brain (WM, GM and CSF). The segmentation of the brain tissues is key in ESI and therefore it has been addressed by multiple research groups worldwide. As a consequence, many software packages for automatic brain tissue segmentation have been developed such as: the FMRIB Software Libray (FSL) [Smith et al., 2004], FreeSurfer [Fischl et al., 2002], Statistical Parametric Mapping (SPM) [Friston, 2006], the Expectation-Maximization tool [Van Leemput et al., 1999], the EMSegmenter [Pohl et al., 2007], BrainSuite [Shattuck and Leahy, 2002], BrainVISA Morphologist [Geffroy et al., 2011], the CIVET segmentation [Tohka et al., 2004], the Sub-
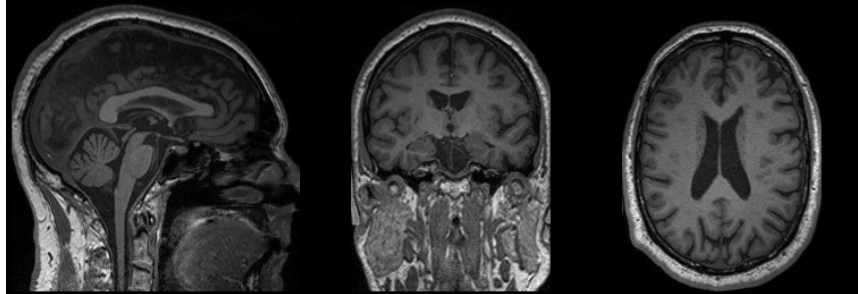
(a) T1-weighted MR image
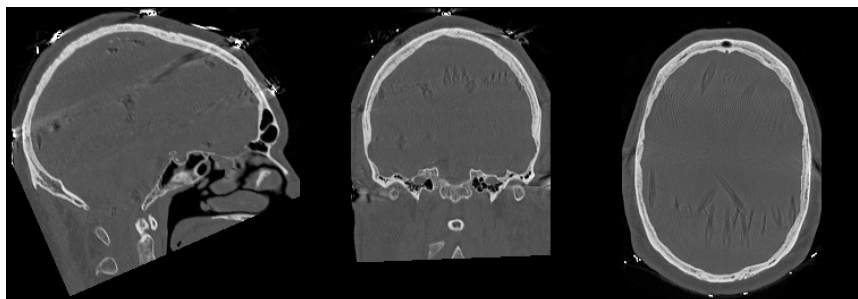
(b) CT image

Figure 3.14: MR and CT images of the head. The soft tissues of the head can be differentiated from the MR image, while the skull tissues are easily recognized in the CT image.

Volume Probabilistic Atlases Segmentation tool [Tohka et al., 2010], the segmentation module in BrainVoyager [Goebel, 2012] and Atropos based on ANTs [Avants et al., 2011]. Softwares like ITK-SNAP [Yushkevich et al., 2006] and Neuroelectromagnetic Forward Head Modeling Toolbox (NFT) [Akalin-Acar and Makeig, 2010] require user-specified seed points and therefore their segmentation is not fully automatic. Because of their broad usage in the medical imaging community, the most popular open-source software tools for brain tissue segmentation are [Despotović et al., 2015]: FSL, FreeSurfer and SPM. Therefore, our focus will be on these three packages.

3.3.1.1   FSL

FSL uses the *Brain Extraction Tool* (BET) software [Smith, 2002] to automatically extract the brain from the MR image. In BET, a triangular tessellation of a spherical surface is initialized inside the brain.

The surface will slowly deform following forces that keep it well spaced and smooth, while trying to move towards the edge of the brain. If a suitable solution is not found, the whole process is rerun with a higher smoothness constraint.

Following the application of BET to the MR image, classification of each voxel into GM, WM or CSF can be performed. This is achieved with the *FMRIB Automated Segmentation Tool* (FAST) [Zhang et al., 2001] in which the histogram is modeled as a mixture of Gaussians, each corresponding to a class with mean and variance intensity. The labeling of a voxel is performed by a Markov Random Field (MRF), taking into account not only the voxel's intensity but also the labeling of its neighbors. This generates smoothness in the segmentation and reduces considerably the effect of noise. This segmentation allows the reconstruction of an ideal image which, when subtracted from the real image, yields an estimate of the bias field. This process is iterated until the estimations of the segmentation and the bias field converge. FAST can be applied to more than one input modality, e.g., T1- with T2- or PD-weighted MR images.

3.3.1.2 FreeSurfer

The FreeSurfer image analysis suite contains two main pipelines for *surface-based* and *volume-based* (subcortical) segmentation. Because our interest lies in the differentiation between GM, WM and CSF, we will give a brief description of the surface-based stream [Dale et al., 1999, Fischl et al., 1999] in the next paragraph.

The surface-based pipeline consists of several steps. First, an affine registration with the MNI305 atlas [Collins et al., 1994] is performed on the MR image. This way, FreeSurfer can compute seed points in later processing stages. After that, the bias field is estimated by measuring the intensity variations of the WM across the entire volume. For this, points with a high probability of belonging to WM are selected based on their locations in MNI305 space as well as on their intensity and that of their local neighbors. In order to remove the effect of the bias field, the intensity at each voxel is divided by the estimated bias field at that location. Then, the skull is stripped using a hybrid watershed/surface deformation procedure [Ségonne et al., 2004]. Voxels of the skull-stripped volume are classified as WM or non-WM based on intensity and neighbor constraints. Cutting planes are chosen to separate the hemispheres from each other as well as to remove the cerebellum and brain stem. The lo-

cation of the cutting planes is based on the expected MNI305 location of
the corpus callosum and pons, along with various rule-based algorithms
that encode the habitual shape of these structures. An initial surface
is then generated for each hemisphere. Posteriorly, surface deformation
following intensity gradients allow to optimally place the GM/WM and
GM/CSF borders at the location where the greatest shift in intensity
defines the transition to the other tissue class [Dale and Sereno, 1993,
Fischl and Dale, 2000].

3.3.1.3 SPM

The segmentation routine implemented in the SPM suite is based on the
Unified Segmentation algorithm [Ashburner and Friston, 2005]. The rou-
tine combines tissue classification, registration and bias field corrections
into a single model. The model is based on the following assumptions: (i)
each voxel of the image has been produced from a known number of dis-
tinct tissue classes (clusters); (ii) the distribution of the voxel intensities
within each cluster is initially unknown and Gaussian distributed (de-
scribed by its mean, variance and mixing proportion); (iii) because the
image has been normalized to the MNI stereotaxic space [Evans et al.,
1993], prior probabilities of the voxels belonging to the GM, WM and
CSF classes are known; and (iv) the bias field in the image is spatially
smooth.

Tissue classification depends upon the registration of the images with
tissue probability maps [Ashburner and Friston, 1997]. The posterior
probability of the clusters is then provided by the Bayes rule, which
combines these priors with tissue type probabilities derived from voxel in-
tensities. Because the registration requires an initial tissue classification,
and the tissue classification requires an initial registration, the problem is
circular and must be resolved via an iterative algorithm. Thus, the mix-
ture parameters are updated using an Expectation Maximization (EM)
approach. Each iteration of the algorithm involves alternating among
classification, bias correction, and registration steps to estimate the pa-
rameters of the model that maximize the posterior probability. This
continues until a convergence criterion is satisfied.

3.3.2   Segmentation of the skull

The segmentation of the skull from MR images is the most challenging
task in the generation of realistic volume conductor models. Although

CT is the modality that accurately images the skull geometry, it exposes the patient to ionizing radiation. As a consequence, CT images should not be acquired with the sole purpose of improving skull modeling for ESI. Next, a brief overview of CT-, MRI- and CT/MRI-based methods to segment the skull is presented.

3.3.2.1   CT-based

The segmentation of the adult skull from CT images can be performed using a simple intensity thresholding procedure in combination with morphological operations. As a consequence, approaches using solely CT images to segment the adult skull are not found in literature. In neonates, the skull is composed of compact bone, sutures and fontanels. Therefore, the segmentation of the structures of the neonate skull requires additional procedures besides thresholding. Jafarian et al. [2014] utilized CT images of newborns to create a manually segmented skull model, consisting of cranial bones and fontanels, that was set as constraint for a variational level set approach. A CT-based approach for automatic segmentation of the newborn's skull was presented by Ghadimi et al. [2016]. This approach relied on propagation of a pair of interacting smooth surfaces, based on geodesic active regions, evolving in opposite directions. The surfaces served as initialization of a level set algorithm.

3.3.2.2   MRI-based

One of the first implemented methods for skull segmentation from MRI was introduced by Heinonen et al. [1997]. They developed a semi-automatic procedure using thresholding and region growing. However, this method was not appropriate for certain bone regions, such as ocular globes, because of partial volume effects. Held et al. [1997] used an MRF approach to segment the MRI volume by defining classes, including a bone class, but the method did not ensure continuous bounding contours. Rifai et al. [2000] implemented a deformable model in which the initial surface was constructed with a region growing method. The speed at which the surface propagated was a function of the estimated partial volume. Thresholding and morphological operations were applied by Dogdas et al. [2005] to generate masks for the inner and outer surfaces of the skull, as implemented in the BrainSuite toolbox (Figure 3.15a). Jenkinson et al. [2005] proposed the segmentation algorithm implemented in BET2 (part of the FSL toolbox), in which for each ver-

tex on the brain surface, the perpendicular direction is searched towards the outside. By using several rules, the estimation of the inner and outer skull surfaces is achieved (Figure 3.15b). Ghadimi et al. [2008] constructed a probabilistic skull atlas and used a level set method to reconstruct the surfaces of neonatal skulls. Lüthi et al. [2009] performed segmentation by fitting a morphable skull model into a pre-segmented version of the image. Bertelsen et al. [2010] co-registered the information of multiple skull atlases with the MRI volume. Using a label fusion approach, the most probable segmentation was obtained by the rule of majority voting [Rohlfing et al., 2004]. Lanfer and colleagues [He et al., 2013] incorporated a priori information in a MRF model and obtained the optimal segmentation with an EM type algorithm. Huang et al. [2013] developed an SPM-based automated segmentation technique, including an improved tissue probability map covering the whole head and an automated correction routine for segmentation errors. The method was further improved by encoding morphological constraints using MRF [Huang and Parra, 2015].
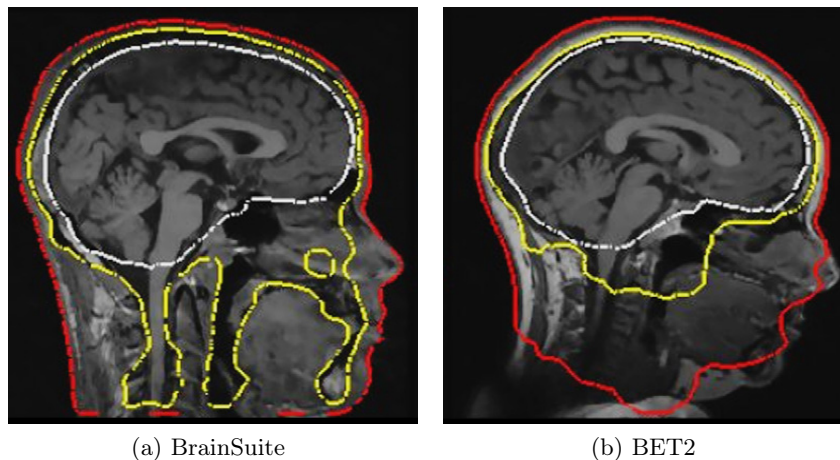
(a) BrainSuite   (b) BET2

Figure 3.15: Inner (white) and outer (yellow) surfaces of the skull, as segmented from the BrainSuite and BET2 toolboxes. From [Valdés-Hernández et al., 2009].

3.3.2.3 CT/MRI-based

Because CT exhibits a high contrast of bone compared to soft tissues, the registration of CT and MRI modalities facilitates the accurate modeling

of the skull [Studholme et al., 1996]. Nonetheless, methods that make use of both CT and MRI information are scarcely found in literature. An early work was presented by Soltanian-Zadeh and Windham [1997] in which a CT/MRI multi-resolution approach was applied to delineate the outer and inner contours of the skull. More recent works have adopted atlas-based approaches to exploit the anatomical information from the CT data. Wang et al. [2009] used statistical knowledge from CT images of a group of subjects to construct an active shape model of the skull surfaces. The model was then matched to the individual MRI so that the skull boundaries could be located. Torrado-Carvajal et al. [2015] registered the individual MRI with every volume of a multi-atlas CT database and combined the individual segmentations by label fusion.

While a CT/MRI-based method may be interesting in contributing to the precise delineation of the skull, it is not practical because the acquisition of both modalities is not commonly performed on patients. An approach based solely on MRI is preferred because it reduces the scanning time for the patient and avoids the exposure to ionizing radiation.

3.3.3 Final remarks

Despite the numerous approaches for head tissue segmentation available in literature, not a single method can be considered as the best. In the particular case of the skull segmentation, the BET2 software [Jenkinson et al., 2005] is commonly utilized in many applications [Aydin et al., 2014, Dannhauer et al., 2011, Güllmar et al., 2010, Lucka et al., 2012, Rampersad et al., 2014, Rullmann et al., 2009, Valdés-Hernández et al., 2009, von Ellenrieder et al., 2012, Windhoff et al., 2011]. However, BET2 does not provide a high level of detail at the base of the skull. Furthermore, BET2 requires T1- and T2-weighted MR images for an optimal performance, though it estimates the skull surface with less accuracy when based solely on a T1.

In this dissertation, we used the SPM toolbox [Friston, 2006], namely SPM8 and SPM12, for the segmentation of the head tissues because it provides tissue probability maps not only for the soft tissues of the head but also for the skull and the air (Figure 3.16), thereby allowing to segment more accurately the base of the skull and the air-filled cavities. Moreover, the SPM toolbox has been shown to have similar volumetric accuracy with FSL in the segmentation of WM and GM and higher than FreeSurfer [Klauschen et al., 2009]. Because the tissue masks generated with SPM tend to be noisy, a post-processing stage was performed to

ensure that the generated head models were in the required accuracy level for ESI. The procedure is explained in more detail in Chapter 6.
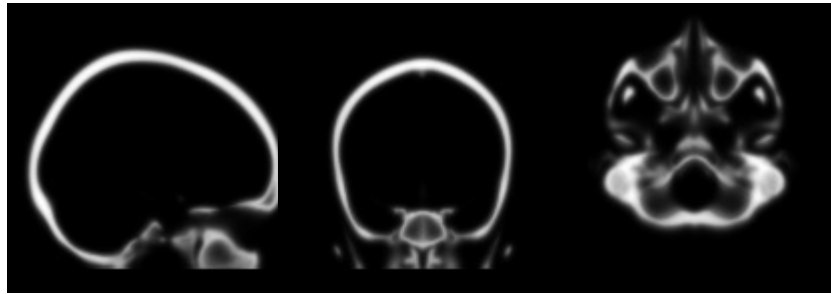
(a) Skull probability map.

(b) Air probability map.

Figure 3.16: Tissue probability maps in the MNI space for the skull and the air in the SPM toolbox.

Chapter 4

Different aspects of skull modeling in ESI

It is not my intention to be fulsome, but I confess that I covet your skull
—ARTHUR CONAN DOYLE

This chapter presents three studies to enlighten different aspects of skull modeling in ESI. The recent advances in imaging and the increase in computational power allow to incorporate high-resolution anatomical details into realistic head models [Dannhauer et al., 2011, Lanfer et al., 2012, Ramon et al., 2006]. By combining high-resolution MRI and CT, the skull tissues of the head can be accurately imaged, allowing the generation of three-layered models of the skull with isotropic conductivity for each tissue. The conductivities of the compact and spongy bone layers are however uncertain. In Study I, Section 4.1, we analyze the effects of conductivity perturbations in the three-layered model of the skull. When the spongy bone cannot be accurately segmented, e.g. if no high-resolution images are available, the skull can be modeled as a single layer with anisotropic conductivity. Study II, Section 4.2, investigates different anisotropy ratios of the skull to determine the one that introduces the lowest errors (the optimal), when compared to a three-layered skull model. In the last part of this chapter, Study III (Section 4.3) investigates the influence of skull inhomogeneities such as the air cavities (sinuses) on ESI.

4.1 Study I: Effects of conductivity perturbations of the three-layered skull

4.1.1 Motivation

ESI relies on an accurate model representing the human head. In this head model, the skull plays an important role due to its complex structure and low conductivity compared to the other tissues inside the head. The skull has often been modeled as a single compartment with isotropic conductivity. However, the actual structure of the skull is three-layered, consisting of a spongiform layer surrounded by two compact layers. Not only spongy and compact bones are part of this structure but also air-filled cavities. Therefore, the skull has different conductivities and thicknesses throughout its whole structure and so it is inhomogeneous [Law, 1993]. In this study, we analyse the effect of conductivity perturbations of the inhomogeneous skull compartment on ESI. The research questions are: (i) if the skull is modeled as a three-layered compartment, which conductivity has the largest influence on ESI: compact or spongy bone?; (ii) what errors are made when the most relevant conductivity of the three-layered skull is under- or over-estimated?; and (iii) in which brain regions do these changes in conductivity have the largest influence?.

4.1.2 Methods

4.1.2.1 Head model construction

A data set with co-registered MR and CT images of one patient was used to generate the reference head model. The MR images were acquired on a 3T scanner (Siemens Trio, Erlangen, Germany) with the MP-RAGE protocol and consisted of a matrix of $256 \times 256 \times 176$ with voxel size of 0.9 mm $\times$ 0.86 mm $\times$ 0.86 mm. CT images (Toshiba Aquilion, Tokyo, Japan) with equal dimensions as the MR image were available for the same patient. The segmentation of the head tissues was carried out with the SPM8 toolbox followed by morphological operations. For the segmentation of the soft tissues of the head, the MR images were used while the skull tissues were segmented solely from the CT image. The reference head model contained an accurately segmented skull, including spongy and compact bone as well as some air-filled cavities, as displayed in Figure 4.1. The conductivity values for the compact ($\sigma_{\text{comp}} = 0.0068$ S/m) and spongy ($\sigma_{\text{spong}} = 0.0298$ S/m) bone compartments of the skull were

selected as the average measurements of Akhtari et al. [2002], yielding a spongy to compact bone conductivity ratio ($\sigma_{\text{spong}}:\sigma_{\text{comp}}$) of 4.38:1 for the reference model. We perturbed these values by: (i) multiplying both conductivities by the same factor, thereby keeping the ratio constant, and (ii) doubling and halving the ratio. These perturbed conductivity values resulted in a total of six test head models, as shown in Table 4.1.
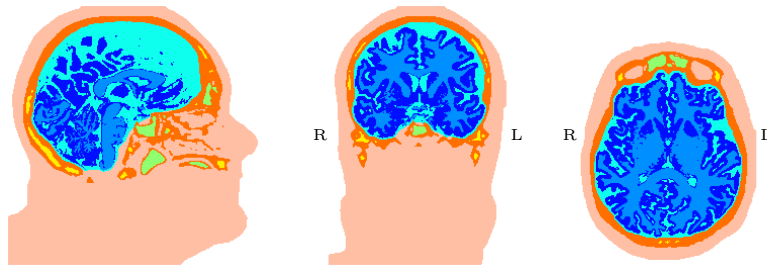
	Tissue	Conductivity (S/m)	
🟫	Scalp	0.3279	[Gonçalves et al., 2003a]
🟧	Compact bone	0.0068	[Akhtari et al., 2002]
🟨	Spongy bone	0.0298	[Akhtari et al., 2002]
🟩	Air cavities	0.0000	[Haueisen et al., 1995]
🟦	CSF	1.7857	[Baumann et al., 1997]
🟦	WM	0.1428	[Haueisen et al., 1995]
🟦	GM	0.3333	[Haueisen et al., 1995]

Figure 4.1: Reference head model used to study the effects of conductivity perturbations of the three-layered skull on ESI. The soft tissues are segmented from MRI while the skull tissues (compact and spongy bone as well as air cavities) are segmented from CT.

Table 4.1: Conductivity perturbations in the test head models.

Model	σ_{spong} (S/m)	σ_{comp} (S/m)	$\sigma_{\text{spong}}:\sigma_{\text{comp}}$
Ref.	0.0298	0.0068	4.38:1
1	0.0596	0.0136	4.38:1
2	0.0298	0.0136	2.19:1
3	0.0149	0.0034	4.38:1
4	0.0298	0.0034	8.77:1
5	0.0596	0.0068	8.77:1
6	0.0149	0.0068	2.19:1

4.1.2.2 EEG source imaging

The forward problem was solved for the reference and the test head models 1 to 6 using the Finite Difference Method (see Section 2.4.3.4). The calculation grid of the FDM consisted of 6,700,339 nodes. An electrode configuration with 27 electrodes was used, described according to the clinical setup of the Department of Neurology at Ghent University Hospital.

The inverse problem was solved using the minimization of the relative residual energy (RRE) [Hallez et al., 2005]:

$$\text{RRE} = \frac{\|\mathbf{V}_{\text{ref}} - \mathbf{V}_{\text{test}}(\mathbf{r}, \mathbf{d})\|_2^2}{\|\mathbf{V}_{\text{ref}}\|_2^2} + \mathbf{C}(\mathbf{r}) \tag{4.1}$$

where $\mathbf{V}_{\text{ref}}$ and $\mathbf{V}_{\text{test}}(\mathbf{r}, \mathbf{d})$ are the set of electrode potentials computed in the reference model and in the test models, respectively. The term $\mathbf{C}(\mathbf{r})$ is a penalization parameter which is zero when the dipole location is inside the GM and large otherwise. The minimization is performed with the Nelder-Mead simplex method [Nelder and Mead, 1965].

4.1.2.3 Simulation setup

Figure 4.2 shows the simulation setup used to study the effects of conductivity perturbations of the three-layered skull on ESI. Test dipoles were placed on a 3D grid with a distance of 5 mm between voxels. Only the voxels situated in the GM and not lower than the most inferior electrode position were considered, for a total of 6,123 test dipoles. At each dipole location, three orthogonal orientations (x, y and z) were taken into account according to the Cartesian coordinate system.

Simulated EEG data $\mathbf{V}_{\text{ref}}$ at the 27 electrodes was computed for each dipole, based on the reference model. Moreover, the electrode potentials in the test models $\mathbf{V}_{\text{test}}$ were computed and compared with the reference model.

The forward error, i.e., the error between $\mathbf{V}_{\text{ref}}$ and $\mathbf{V}_{\text{test}}$ was estimated using the *Relative Distance Measure* (RDM) [Meijs et al., 1989] and the *Logarithmized Magnitude Error* (lnMAG) [Güllmar et al., 2010]:

$$\text{RDM} = \left\| \frac{\mathbf{V}_{\text{ref}}}{\|\mathbf{V}_{\text{ref}}\|_2} - \frac{\mathbf{V}_{\text{test}}}{\|\mathbf{V}_{\text{test}}\|_2} \right\|_2 \tag{4.2}$$

$$\text{lnMAG} = \ln\left(\frac{\|\mathbf{V}_{\text{test}}\|_2}{\|\mathbf{V}_{\text{ref}}\|_2} \right) \tag{4.3}$$

The RDM is a measure of the topographical error and ranges between 0 and 2. In the lnMAG measure, positive values represent increased magnitudes while negative values reflect decreased magnitudes.
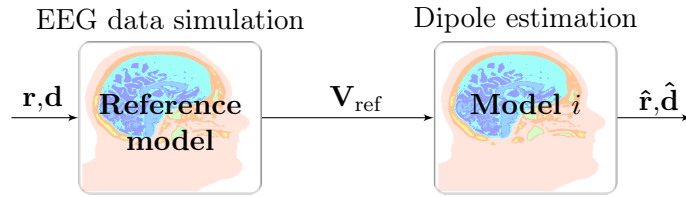
Figure 4.2: Simulation setup used to study the effects of conductivity perturbations of the three-layered skull on ESI. The reference model is compared against the test model i $\forall i = 1, \ldots, 6$, each with different spongy to compact bone conductivity ratio (σ_{spong}:σ_{comp}).

From the simulated potentials $\mathbf{V}_{\text{ref}}$, the dipoles were estimated by solving the inverse problem using models 1 to 6. As a consequence, the error caused by the use of a different σ_{spong}:σ_{comp} ratio in the solution of the inverse problem was investigated. The estimated dipole parameters, $\hat{\mathbf{r}}$ and $\hat{\mathbf{d}}$, which minimized (4.1), were the dipole position and orientation that best explained the potential $\mathbf{V}_{\text{ref}}$.

The inverse error, dipole localization error (DLE), was evaluated through the Euclidean distance between the original dipole location $\mathbf{r}$ in the reference model and the estimated dipole location $\hat{\mathbf{r}}$ in the test model:

$$\text{DLE} = \|\hat{\mathbf{r}} - \mathbf{r}\|_2 \tag{4.4}$$

In order to analyze the effect of conductivity perturbations of the three-layered skull in a specific brain region, forward and inverse errors were computed for dipoles located at clinically significant brain areas: cingulate cortex, frontal, temporal, parietal and occipital lobes (see Figure 3.6) and in the whole brain (overall).

4.1.3 Results

Figure 4.3 presents the mean RDM and lnMAG errors for dipoles located at the cingulate, frontal, temporal, parietal, occipital and overall brain

regions, using models 1 to 6. The lowest forward errors are obtained for
models 5 and 6, which have the same conductivity value for compact
bone as the reference model. Additionally, the dipoles located at the
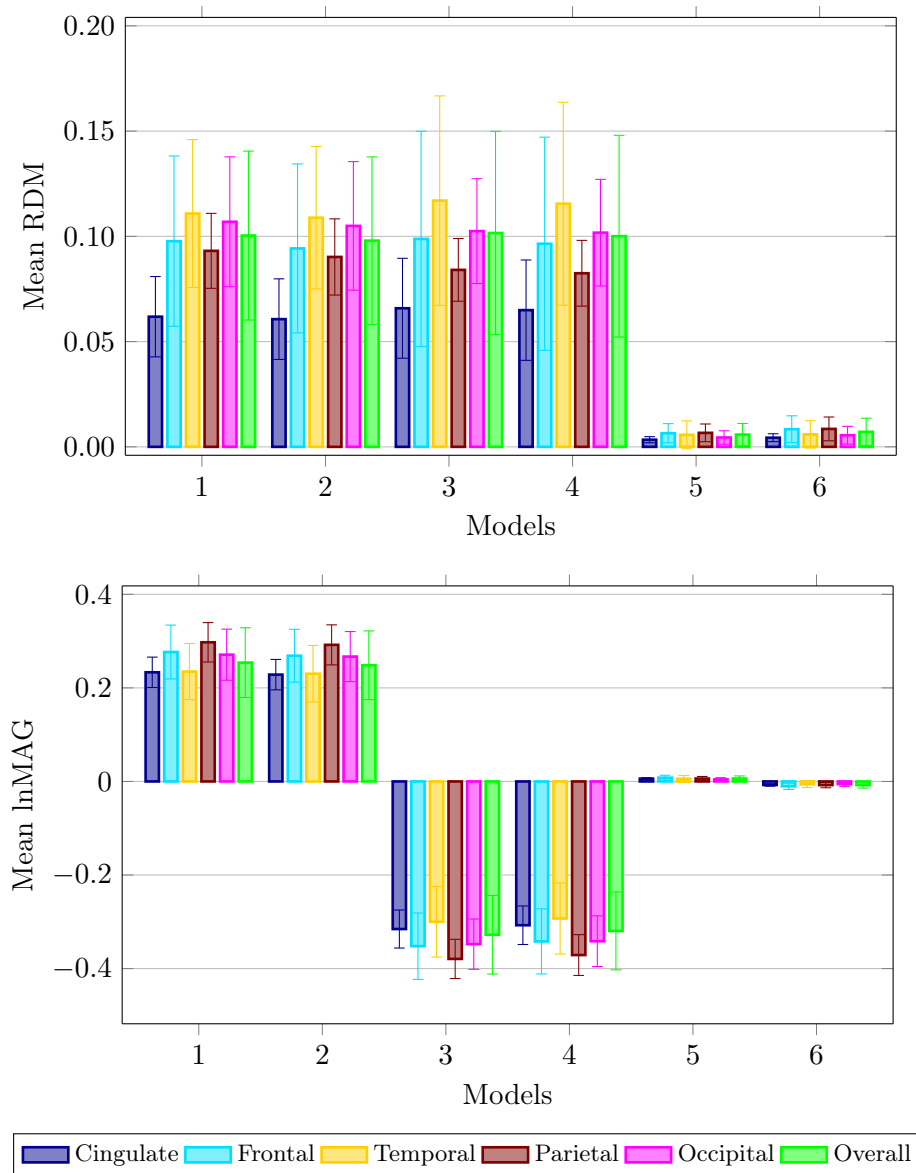
Figure 4.3: Mean RDM and lnMAG of dipoles located at the cingulate,
frontal, temporal, parietal, occipital and overall brain regions for models 1
to 6.

cingulate cortex present smaller forward errors than those located at the other analyzed regions.

The mean DLE is shown in Figure 4.4. As it can be seen, a similar trend is displayed for the inverse and forward errors. Per region, the frontal lobe presents the largest mean DLE, while the cingulate cortex the smallest. Models 5 and 6 also present the lowest mean DLE.
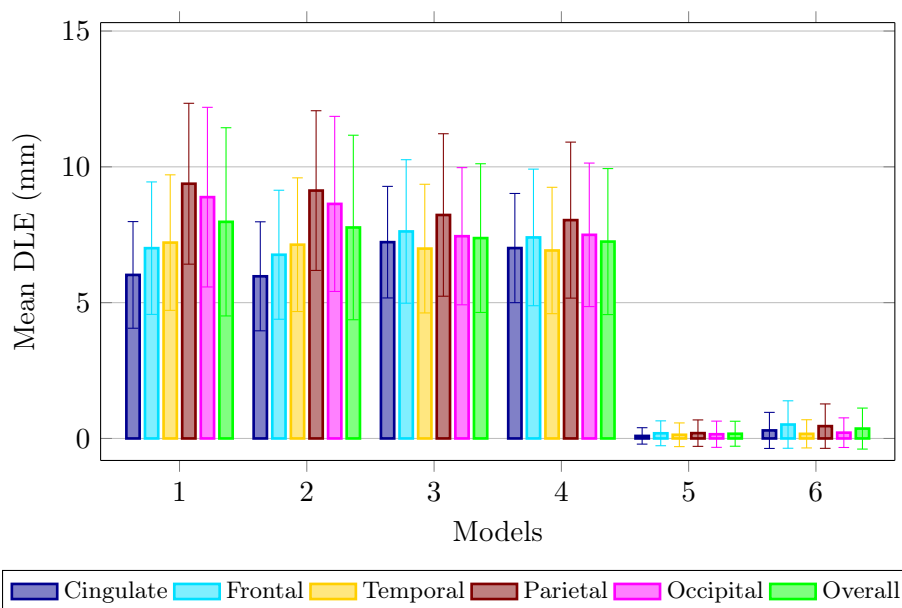
Figure 4.4: Mean DLE of dipoles located at the cingulate, frontal, temporal, parietal, occipital and overall brain regions for models 1 to 6.

To analyze the effects of over- or under-estimation of the conductivity of the compact bone compartment, the localization of a single dipole oriented along the $y-$axis in three clinically relevant brain regions is performed. For this, Models 1 and 2 (with over-estimated σ_{comp}) and Models 3 and 4 (with under-estimated σ_{comp}) are compared against the Reference Model. Figure 4.5 displays the dipole localization on the subject's MRI at the three analyzed brain areas. Conductivity over-estimation of σ_{comp} (in red) leads to a dipole located deeper than the original solution, while under-estimation of σ_{comp} (in blue) yields a more superficial dipole than the reference (in green).

Sagittal **Coronal** **Axial**

(a) Fronto-basal

(b) Cingulate cortex

(c) Mesio-temporal
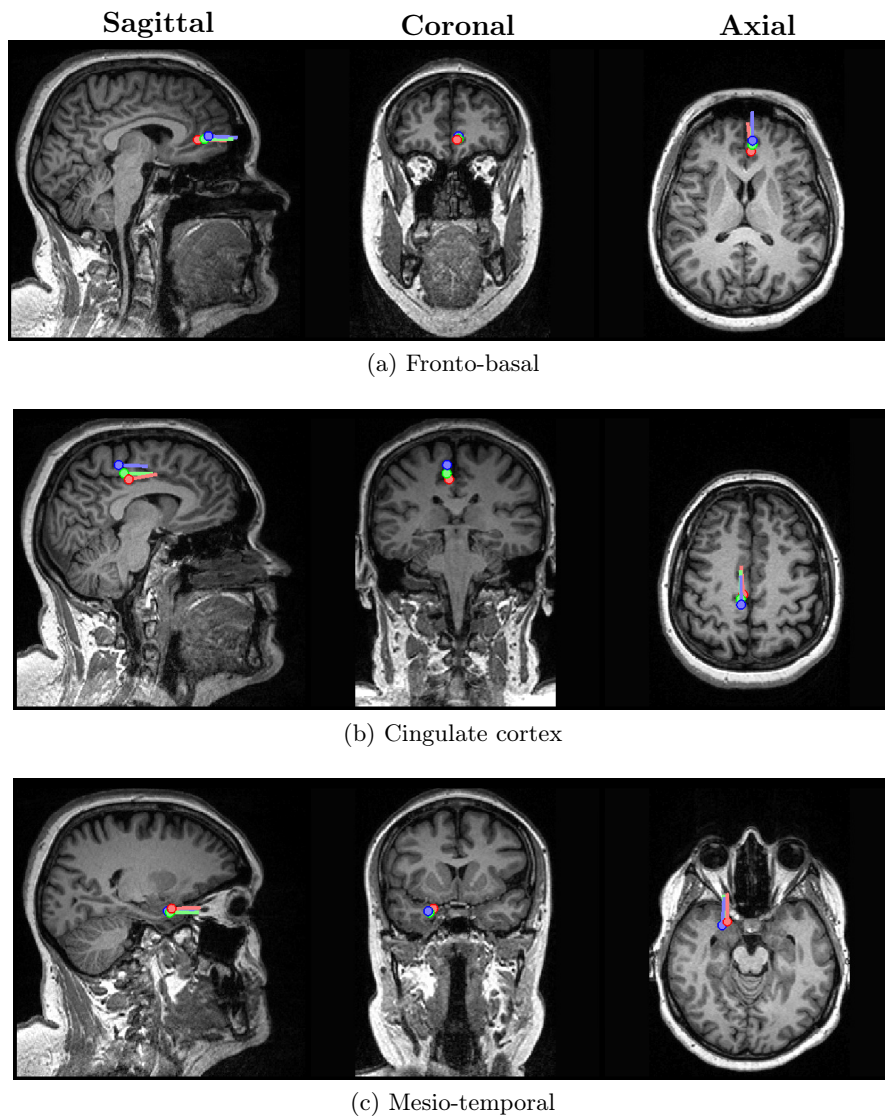
Figure 4.5: Dipole estimations at three clinically significant brain areas for the Reference Model ⬤, Models 1 and 2 ⬤ (over-estimation) and Models 3 and 4 ⬤ (under-estimation) of the compact bone conductivity σ_{comp}.

4.1.4 Conclusions

The results suggested that conductivity perturbations of the compact bone have the strongest influence on ESI. Conversely, the perturbations of the spongy bone conductivity did not show a noticeable influence on

the dipole estimation. This means that more than the spongy to compact bone conductivity ratio, the correct determination of the compact bone conductivity can improve the accuracy of the forward solution. For sources located at the cingulate cortex, the effects of conductivity perturbations were smaller than for sources located at frontal or temporal regions. The over- or under-estimation of the compact bone conductivity led to estimated dipoles located deeper or more superficial than the reference dipole, respectively.

4.2 Study II: Determination of the anisotropy ratio of the skull

4.2.1 Motivation

When spongy and compact bone cannot be discriminated from the acquired medical images, the skull can be modeled as a single layer with anisotropic conductivity. The concept of anisotropy was first introduced as a way to model the three-layered structure of the skull. Rush and Driscoll [1968] reported the first measurements for the radial and tangential conductivities of the skull in 1968. Since then, in many applications, the anisotropy ratio of the skull has been assumed to be 1:10 (σ_{rad}:σ_{tang}) [Marin et al., 1998, Wolters et al., 2006]. However, recent studies have suggested that the skull anisotropy must be lower than this ratio [Akhtari et al., 2002, Fuchs et al., 2007, Sadleir and Argibay, 2007]. Therefore, in this study we want to determine the optimal anisotropy ratio of the skull to accurately model its conductivity. This is important in patients where no detailed medical images are available to model the layered skull.

4.2.2 Anisotropy of the skull

The conductivity tensor or matrix representing the direction-dependent conductivity $\boldsymbol{\Sigma}$, Equation (2.8), was first introduced in Section 2.4.3. Given a head model, the conductivity tensor of an anisotropic tissue, e.g. the skull, at a voxel j is described by:

$$\boldsymbol{\Sigma}_{(j)} = \mathbf{T}_{(j)}^{T} \operatorname{diag}(\sigma_{\text{rad}}, \sigma_{\text{tang}}, \sigma_{\text{tang}}) \mathbf{T}_{(j)},$$

where $\mathbf{T} \in \mathbb{R}^{3 \times 3}$ is the orthogonal matrix of unit length eigenvectors, and $\sigma_{\text{rad}} \in \mathbb{R}^+$ and $\sigma_{\text{tang}} \in \mathbb{R}^+$ are the corresponding radial and tangential eigenvalues, respectively.

For a given head model, $\mathbf{T}$ is a rotation transfer matrix transforming the local coordinate system to the Cartesian coordinate system [Hinchey, 1976]. In the case of a realistic head model, $\mathbf{T}$ is based on the geometry of the skull, being composed of the norm $\mathbf{n}_{(j)}$ onto the skull surface and two orthogonal directions for each voxel j. The norm is computed by applying the Matlab (The MathWorks, Inc., Natick, Massachusetts, United States) functions *Isosurface* and *Isonormals* on the segmented skull volume, selecting the one with minimal distance to the voxel. The two orthogonal directions are chosen in the plane normal to $\mathbf{n}_{(j)}$ using the vector product [Wolters, 2003].

The values for the eigenvalues σ_{rad} and σ_{tang} can be derived following different schemes [Wolters, 2003]: (i) the volume constraint [Hallez, 2008]: $\sigma_{\text{rad}}(\sigma_{\text{tang}})^2 = \sigma_{\text{iso}}^3$, with σ_{iso} the isotropic conductivity of the skull compartment; (ii) the Wang's constraint [Wang et al., 2001]: $\sigma_{\text{rad}} \cdot \sigma_{\text{tang}} = \sigma_{\text{iso}}^2$; and (iii) using a simplified three-layered skull model, which is the approach used in this dissertation and explained in the next subsection.

4.2.3   Methods

4.2.3.1   Spherical head model with simplified three-layered skull

To determine the anisotropy ratio of the skull, a reference as well as test spherical head models were generated. The reference model, Figure 4.6a, contained a three-layered skull (a spongiform layer between two compact bone layers). The conductivities of the spongy and compact bone layers were chosen according to Fuchs et al. [2007]. The test models included anisotropic conductivity for the skull, as seen in Figure 4.6b. The conductivity values as well as the radius of each tissue are shown in Figure 4.6.

The radial σ_{rad} and tangential σ_{tang} conductivity values were based on a simplified three-layered skull model, as shown in Figure 4.7. The resistance in the radial direction is expressed as a series connection of three resistors and the tangential resistance is equivalent to its parallel connection [Fuchs et al., 2007, Wolters, 2003].

The relationship between conductivity σ_i and resistance R_i of an ith

(a) Isotropic three-layered skull

(b) Anistropic skull
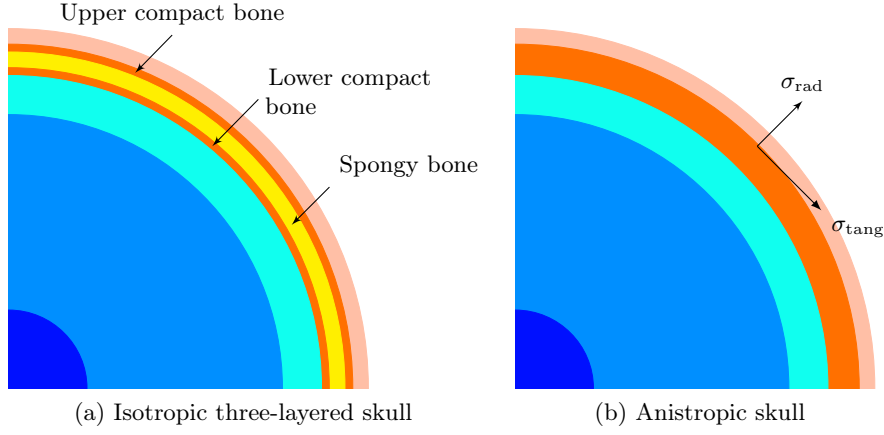
Tissue	Radius	Conductivity (S/m)	
	(m)	Ref.	Test
☐ Scalp	0.092	0.3333	0.3333
◼ Upper compact bone	0.088	0.0064	
◼ Spongy bone	0.086	0.02865	$\sigma_{\text{aniso}} \begin{cases} \sigma_{\text{rad}} \\ \sigma_{\text{tang}} \end{cases}$
◼ Lower compact bone	0.082	0.0064	
◼ Cortical sphere	0.080	0.3333	0.3333
◼ White Matter	0.070	0.3333	0.3333
◼ Thalamic sphere	0.020	0.3333	0.3333

Figure 4.6: The (a) reference and (b) test spherical head models used to determine the anisotropy ratio of the skull.

layer with thickness ℓ_i and surface A_i is defined as:

$$R_i = \frac{\ell_i}{\sigma_i A_i}.$$

The radial resistance is the sum of the three serial resistors: $R_{\text{rad}} = R_{\text{comp}} + R_{\text{spong}} + R_{\text{comp}} = 2R_{\text{comp}} + R_{\text{spong}}$, where R_{comp} and R_{spong} are the resistances of the compact and spongy bone layers, respectively. Thus,

$$R_{\text{rad}} = 2\frac{\ell_{\text{comp}}}{\sigma_{\text{comp}}A_{\text{comp}}} + \frac{\ell_{\text{spong}}}{\sigma_{\text{spong}}A_{\text{spong}}}$$
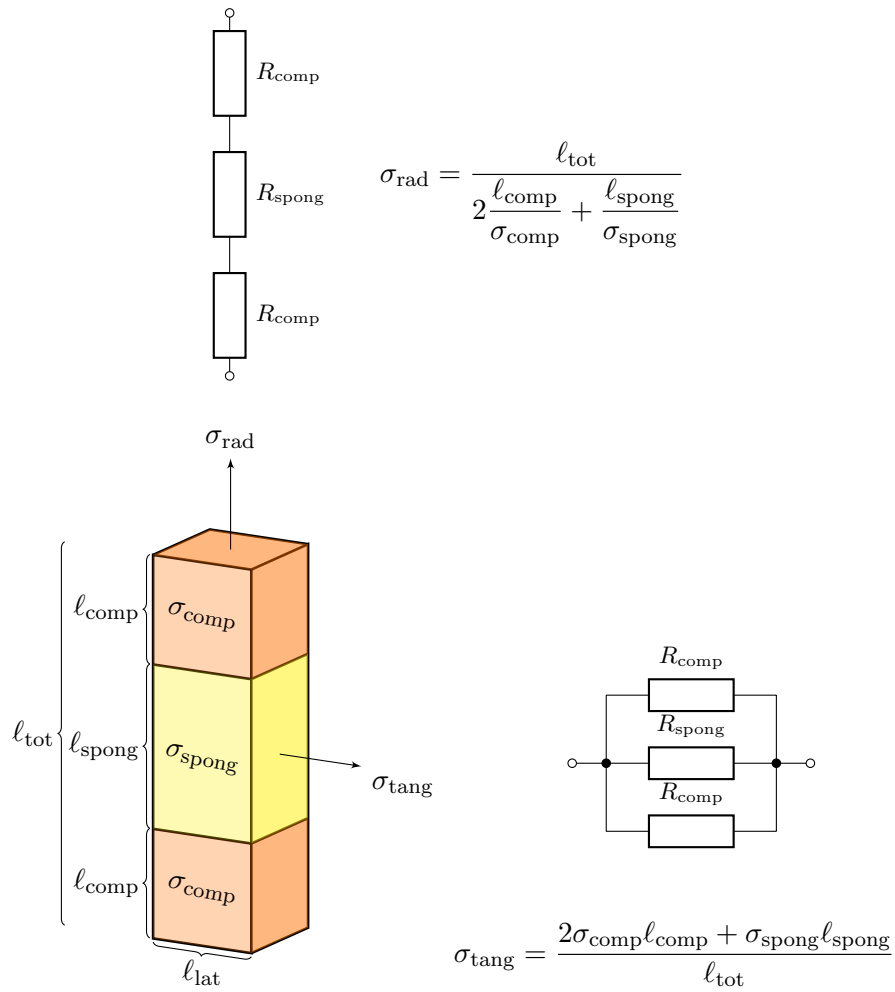
Figure 4.7: Three-layered model of the conductivities of the skull: compact σ_{comp} and spongy σ_{spong} bone. The radial σ_{rad} and tangential σ_{tang} conductivities are based on a model of serial and parallel resistors, respectively.

The radial conductivity σ_{rad} is:

$$\sigma_{\mathrm{rad}} = \frac{\ell_{\mathrm{tot}}}{R_{\mathrm{rad}}A_{\mathrm{rad}}} = \frac{\ell_{\mathrm{tot}}}{\left(2\dfrac{\ell_{\mathrm{comp}}}{\sigma_{\mathrm{comp}}A_{\mathrm{comp}}} + \dfrac{\ell_{\mathrm{spong}}}{\sigma_{\mathrm{spong}}A_{\mathrm{spong}}}\right)A_{\mathrm{rad}}}$$

$$= \frac{\ell_{\mathrm{tot}}}{2\dfrac{\ell_{\mathrm{comp}}}{\sigma_{\mathrm{comp}}} + \dfrac{\ell_{\mathrm{spong}}}{\sigma_{\mathrm{spong}}}},$$

given that in the radial direction the transversal area of the resistors is equivalent: $A_{\mathrm{rad}} = A_{\mathrm{spong}} = A_{\mathrm{comp}}$.

The tangential conductivity σ_{tang} is derived from the equivalent parallel resistor $\frac{1}{R_{\mathrm{tang}}} = \frac{2}{R_{\mathrm{comp}}} + \frac{1}{R_{\mathrm{spong}}}$ as:

$$\sigma_{\mathrm{tang}} = \frac{\ell_{\mathrm{lat}}}{R_{\mathrm{tang}}A_{\mathrm{tang}}} = \left(\frac{2\sigma_{\mathrm{comp}}A_{\mathrm{comp}}}{\ell_{\mathrm{lat}}} + \frac{\sigma_{\mathrm{spong}}A_{\mathrm{spong}}}{\ell_{\mathrm{lat}}}\right)\frac{\ell_{\mathrm{lat}}}{A_{\mathrm{tang}}},$$

where the transversal area of the individual parallel resistors and of the equivalent tangential resistor is $A_{\mathrm{comp}} = \ell_{\mathrm{lat}}\ell_{\mathrm{comp}}$, $A_{\mathrm{spong}} = \ell_{\mathrm{lat}}\ell_{\mathrm{spong}}$ and $A_{\mathrm{tang}} = \ell_{\mathrm{lat}}\ell_{\mathrm{tot}}$, respectively. The tangential conductivity is thus,

$$\sigma_{\mathrm{tang}} = \frac{2\sigma_{\mathrm{comp}}\ell_{\mathrm{comp}} + \sigma_{\mathrm{spong}}\ell_{\mathrm{spong}}}{\ell_{\mathrm{tot}}}.$$

The radial and tangential conductivities can also be expressed in terms of the proportion of spongy bone f in the skull. First, the lengths ℓ_{spong} and ℓ_{comp} are expressed in terms of f as:

$$\ell_{\mathrm{spong}} = f\ell_{\mathrm{tot}} \qquad \ell_{\mathrm{comp}} = (1-f)\frac{\ell_{\mathrm{tot}}}{2}$$

leading to the following expressions [Dannhauer et al., 2011]:

$$\sigma_{\mathrm{rad}} = \frac{1}{\dfrac{1-f}{\sigma_{\mathrm{comp}}} + \dfrac{f}{\sigma_{\mathrm{spong}}}} \tag{4.5}$$

$$\sigma_{\mathrm{tang}} = (1-f)\sigma_{\mathrm{comp}} + f\sigma_{\mathrm{spong}} \tag{4.6}$$

$$k = \frac{\sigma_{\mathrm{tang}}}{\sigma_{\mathrm{rad}}} \tag{4.7}$$

where k denotes the anisotropy ratio.

In this study, the initial values of radial and tangential conductivities were: $\sigma_{\mathrm{rad}_0} = 0.0105$ and $\sigma_{\mathrm{tang}_0} = 0.0175$ in S/m, calculated with Equations (4.5) and (4.6) for $f = 0.5$ and the values of σ_{comp} and σ_{spong} from the Reference Model of Figure 4.6. As a result, the initial anisotropy ratio was 1:1.675 (radial:tangential conductivity).

4.2.3.2   Realistic head models

In order to test the optimal anisotropy ratio of the skull found with the spherical head model, a realistic reference head model with a three-layered skull was used. This reference model was constructed as explained in Section 5.2.2 (Figure 5.1b and Table 5.1). Additionally, three test models with anisotropic skull, each using a different scheme to derive σ_{rad} and σ_{tang}, were compared against the reference model. Model 1 was based on the volume constraint, Model 2 on the Wang's constraint and Model 3 on the simplified three-layered skull (see Section 4.2.2). To determine the values of σ_{rad} and σ_{tang} for models 1 and 2, the isotropic conductivity of the skull compartment was defined as $\sigma_{\mathrm{iso}} = 0.0133$ S/m, corresponding to a skull-to-soft conductivity ratio of 25 [Lai et al., 2005, Tang et al., 2008]. The resulting radial and tangential conductivity values of the three test models are displayed in Table 4.2.

4.2.3.3   Simulation setup

To determine the optimal anisotropy ratio of the skull, we used the simulation setup shown in Figure 4.8. Test dipoles ($\mathbf{r}$, $\mathbf{d}$) were placed on a 5 mm 3D grid inside the cortical sphere and not lower than the most inferior electrode position, resulting in a total of 13,450 dipoles. For each test dipole, three orthogonal orientations were considered: $x-$, $y-$ and $z-$direction.

Subsequently, the initial radial $\sigma_{\mathrm{rad}_0} = 0.0105$ S/m and tangential $\sigma_{\mathrm{tang}_0} = 0.0175$ S/m conductivity values were perturbed as follows:

$$\sigma_{\mathrm{rad}_p} = [0.8 : 0.1 : 1.5] * \sigma_{\mathrm{rad}_0} = [0.0084 : 0.0157],$$
$$\sigma_{\mathrm{tang}_q} = [0.1 : 0.1 : 2.4] * \sigma_{\mathrm{tang}_0} = [0.0018 : 0.0421].$$

The anisotropy ratios σ_{rad_p}:σ_{tang_q} for $p = 1, \ldots, 8$ and $q = 1, \ldots, 24$ resulted in a 24×8 matrix. Thus, a total of 192 test models, each with a different anisotropy ratio, were used in the simulation.
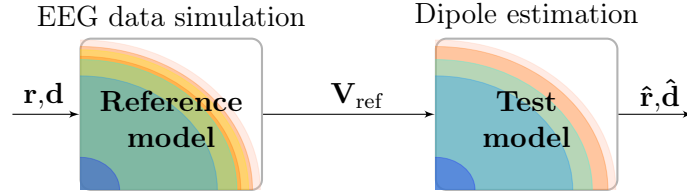
Figure 4.8: Simulation setup used to determine the anisotropy ratio of the skull. The reference model (isotropic three-layered skull) is compared against the test models (anisotropic skull). For each test dipole ($\mathbf{r}$, $\mathbf{d}$), the electrode potentials $\mathbf{V}_{ref}$ were calculated by solving the forward problem in the reference model. From these potentials, the estimated dipoles ($\hat{\mathbf{r}}$, $\hat{\mathbf{d}}$) were obtained by solving the inverse problem in the test models.

The forward problem was solved analytically in the layered anisotropic spheroidal volume, according to the formulation of De Munck [1988]. A 27-channel setup, normalized to the outermost sphere, was used in the forward solution. The inverse problem was solved using the minimization of the RRE given by (4.1).

In the case of the realistic head models, the FDM was used to calculate the forward problem in the reference and models 1 to 3. The calculation grid of the FDM consisted of 5,745,427 nodes. Moreover, a 128-channel setup was used.

We investigated forward and inverse errors caused by assuming an anisotropic head model in the inverse solution. The forward error RDM (4.2) was calculated to evaluate the accuracy of the forward solution in the test models. In addition to the forward error, the inverse error DLE (4.4) was evaluated to determine: (i) the optimal anisotropy ratio of the skull (with the spherical head model); and (ii) the method to derive the tangential and radial conductivities that generates the smallest errors (with the realistic head model).

4.2.4   Results

4.2.4.1   Spherical head models

The mean RDM error over all the dipoles for each test model showed a very similar distribution to the mean DLE. Therefore, the mean RDM surface is not displayed here. Figure 4.9 shows the surface of the mean DLE over all the dipoles for each test model.

The global minimum of this surface was found at $\sigma_{\mathrm{rad}} = 0.0105$ S/m
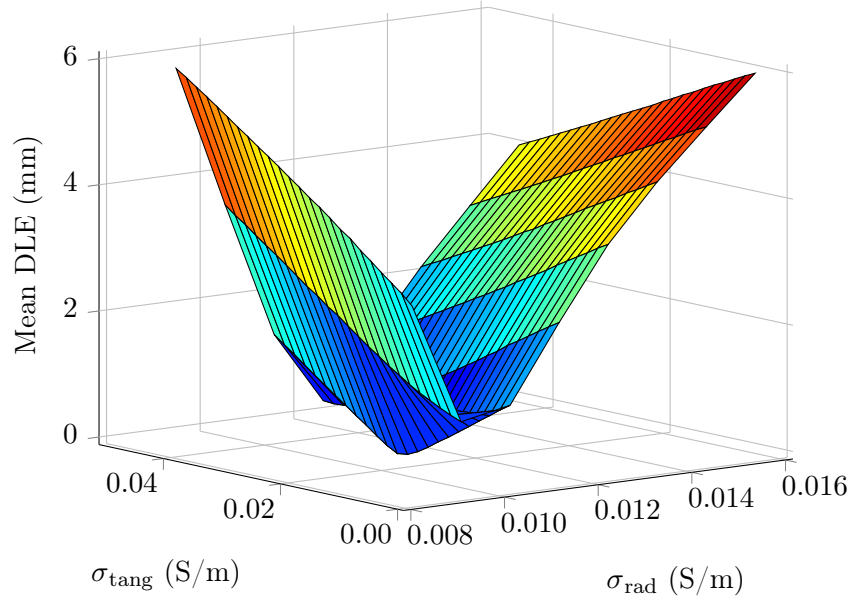
Figure 4.9: Surface showing the mean dipole localization error over all dipoles for each of the tested anisotropy ratios.

and $\sigma_{\text{tang}} = 0.0191$ S/m. This resulted in an optimal anisotropy ratio of 1:1.819 (σ_{rad}:σ_{tang}). According to the shape of the mean DLE surface, the radial conductivity is dominant in the determination of the anisotropy ratio of the skull.

The forward error RDM and the inverse error DLE for the test model with the optimal anisotropy ratio are displayed in Figure 4.10. The RDM (Figure 4.10a) presents slightly larger errors for dipoles located close to the skull. In the case of the DLE, Figure 4.10b, the largest errors are seen for posterior and anterior superficial dipoles located at the level of the nose.

4.2.4.2 Realistic head models

According to the results obtained with the spherical head models, the three realistic test models (see Section 4.2.3.2) have the anisotropic conductivity values displayed in Table 4.2. The cumulative histograms of the forward (RDM) and inverse (DLE) errors for these models are shown in Figure 4.11, presenting overall similar distributions. Model 1, with σ_{rad} and σ_{tang} computed according to the volume constraint, yields the small-

(a) RDM

(b) DLE (mm)
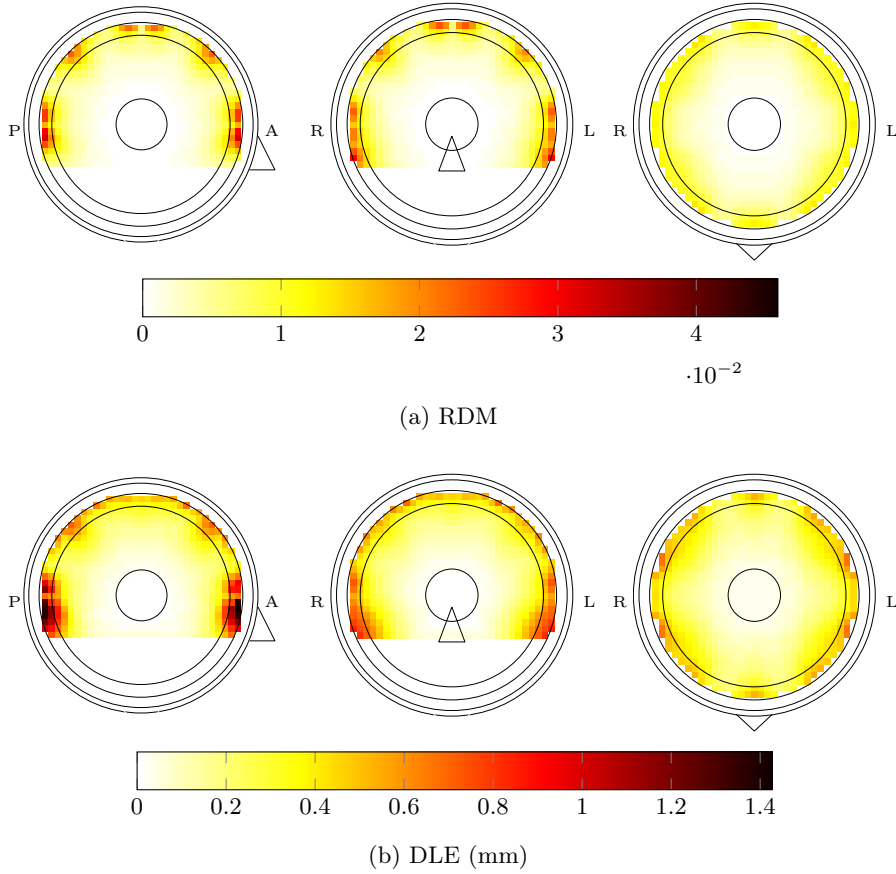
Figure 4.10: Forward and inverse error maps in sagittal, coronal and axial views for the test model with the optimal anisotropy ratio.

est forward and inverse errors while Model 3 —simplified three-layered— the largest. Approximately 90% of the DLEs are below 15 mm for the three test models. The mean DLE in millimeters are: 9.1, 10.6 and 11.5 for models 1, 2 and 3, respectively.

Table 4.2: Anisotropic conductivities of the realistic test head models.

Model	$\sigma_{\mathbf{rad}}$ **(S/m)**	$\sigma_{\mathbf{tang}}$ **(S/m)**	$\sigma_{\mathbf{rad}}$:$\sigma_{\mathbf{tang}}$
1 – Volume constraint	0.0089	0.0162	1:1.819
2 – Wang's constraint	0.0099	0.0180	1:1.819
3 – Simplified three-layered	0.0105	0.0191	1:1.819
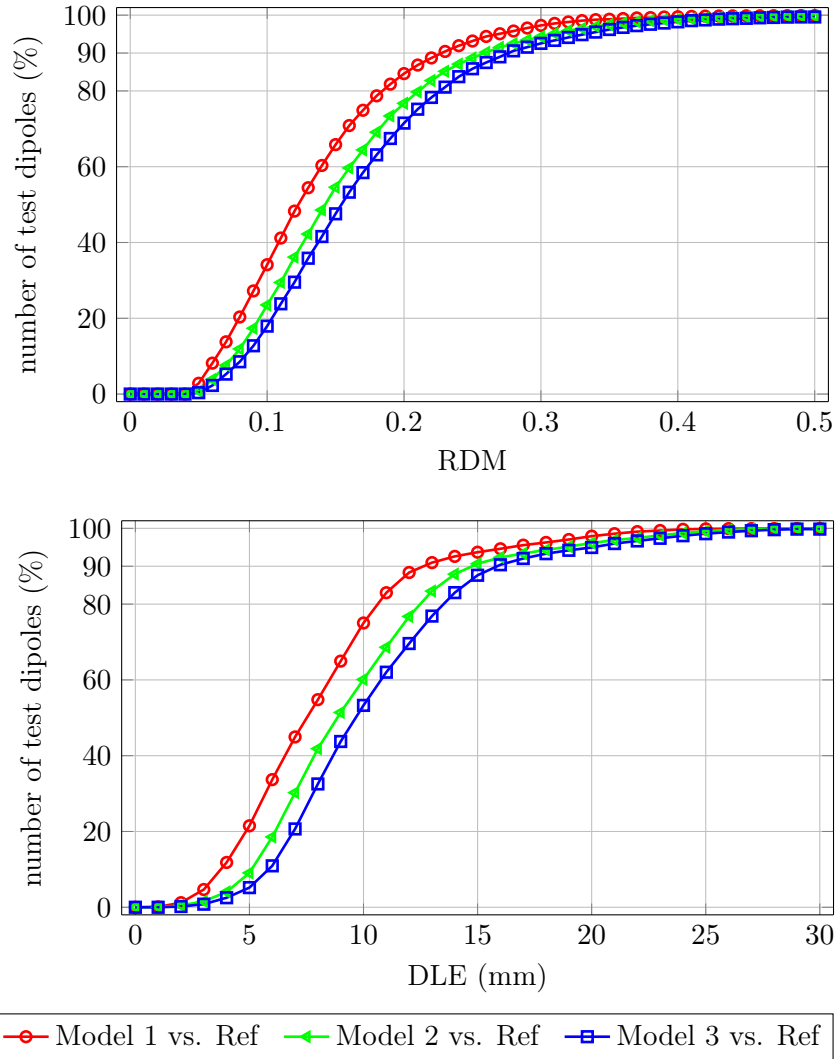
Figure 4.11: Cumulative histograms of the relative distance measure and dipole localization error for the realistic head models 1 to 3.

4.2.5 Conclusions

The radial skull conductivity has the highest influence on dipole estimation. The RDM and DLE in the spherical head models indicated that dipoles located close to the skull were more affected by the use of an anisotropic instead of a three-layered skull. The optimal anisotropy

ratio found in this study was 1:1.82 (σ_{rad}:σ_{tang}), suggesting that the commonly used value of 1:10 is over-estimated.

The simulations performed on realistic head models compared three methods to derive the radial and tangential conductivities of the skull, by using the optimal anisotropy ratio found with the spherical head model. The results showed that the volume constraint method presents slightly lower forward and inverse errors than the other two studied methods: Wang's constraint and simplified three-layered skull. However, the three methods are suitable to model the anisotropy of the skull in realistic head models.

4.3   Study III: Skull inhomogeneities

4.3.1   Motivation

The skull has often been modeled as a homogeneous isotropic compartment. However, the actual structure of the skull has different conductivities and thicknesses and so it is inhomogeneous. Not only compact and spongy bones are part of this structure but also air-filled cavities such as the paranasal sinuses and mastoid cells. Advanced CT and MR imaging allow segmenting these tissue types as well as constructing a more accurate model of the skull.

The importance of modeling the skull as a layered isotropic structure, accounting for compact and spongy bones, has been pointed out by different authors [Dannhauer et al., 2011, Pohlmeier et al., 1997, Sadleir and Argibay, 2007]. Nevertheless, their studies have modeled the skull based only on MR images, in which the bone and its different tissue types cannot be easily identified. Furthermore, it is difficult to segment the air cavities from the MR images, while they are very clear on the CT images.

The objective of this study is to analyze the influence of skull inhomogeneities on ESI. A head model with an accurately segmented skull from CT images, including spongy and compact bones as well as some air-filled cavities, is incorporated in the analysis as reference. Isotropic and anisotropic conductivity modeling are used as simplified models of the actual layered structure of the skull. The effect of omitting the air-filled cavities of the skull is also investigated through two more simplified models in which the air cavities are modeled either as compact or spongy bone.

4.3.2 Methods

4.3.2.1 Head model construction

Different realistic head models were generated from MR and CT images. The MR images were acquired using a 3T scanner (Siemens Trio, Erlangen, Germany) and consisted of a $256 \times 256 \times 176$ matrix with voxels of 0.9 mm $\times$ 0.9 mm $\times$ 0.9 mm. These images were used to segment the scalp and brain tissues. The scalp was segmented through thresholding followed by a closing with hole filling operation. The segmentation of CSF, WM and GM was carried out with the SPM8 software [Ashburner and Friston, 2005].

The CT images were acquired with a scanner (Toshiba Aquilion, Tokyo, Japan) and used to accurately segment the skull through a CT/MR gray-value based thresholding approach. Morphological operations such as dilation and erosion were also performed in order to obtain a smooth skull compartment. To distinguish between compact and spongy bones, a thresholding method based on Gaussian mixture models was applied to the CT image [Huang and Chau, 2008]. The frontal and sphenoidal sinuses were also segmented through thresholding.

The electrode positions were chosen according to the International 10–20 system, with 6 extra electrodes located at the temporal region, resulting in a total of 27 electrodes. This setup is used for clinical practice at the Department of Neurology of the Ghent University Hospital. To analyze the influence of the skull inhomogeneities on ESI, five head models with varying skulls were constructed (see Figure 4.12):

Reference model: This model consists of separate layers for the compact and spongy bones of the skull, and includes air-filled cavities such as the frontal and sphenoidal sinuses, as shown in Figure 4.12a. These cavities are assumed to have the conductivity of air. The conductivities for the compact and spongy bones are chosen according to the measurements of Akhtari et al. [2002] as: $\sigma_{\mathrm{comp}} = 0.0064$ S/m and $\sigma_{\mathrm{spong}} = 0.02865$ S/m. Table 4.3 shows the conductivity values for the other tissues in the head model.

Model 1: The skull is modeled as a single compartment, with an isotropic conductivity of 0.020 S/m for the whole compartment [Hallez et al., 2009].

(a) Reference model.

(b) Model i for i = 1: isotropic homogeneous skull and i = 2: anisotropic homogeneous skull.

(c) Model 3 – Isotropic heterogeneous skull with air cavities modeled as compact bone.

(d) Model 4 – Isotropic heterogeneous skull with air cavities modeled as spongy bone.
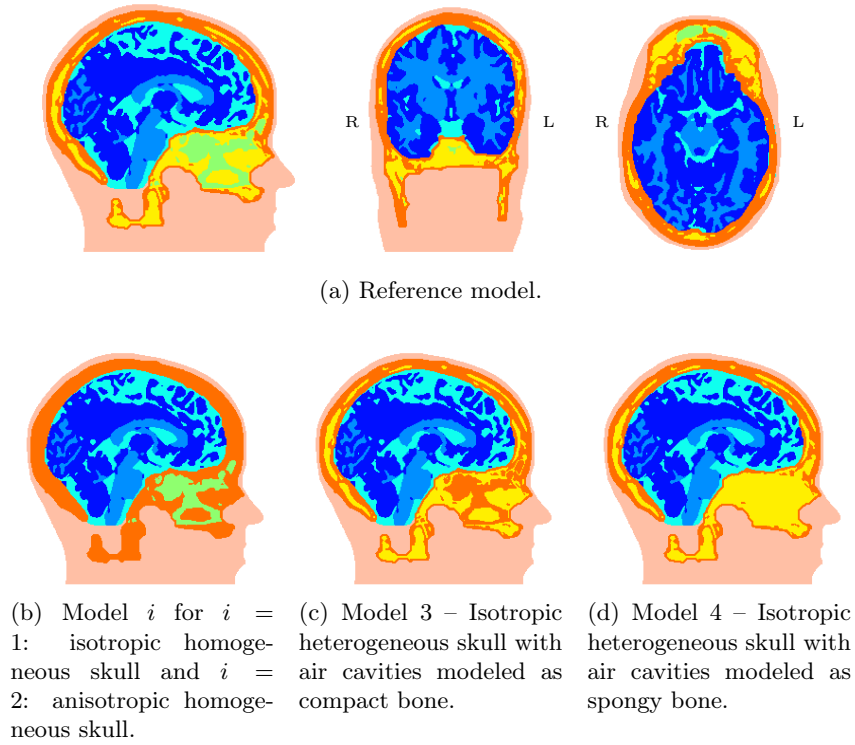
Figure 4.12: The realistic (a) reference and (b) test head models used to establish the influence of inhomogeneities on ESI. The tissues in the models are: ▢ Scalp, ▢ CSF, ▢ WM and ▢ GM, segmented from MR; ▢ Compact bone, ▢ Spongy bone and ▢ Air cavities, segmented from CT.

Table 4.3: Conductivities of the soft tissues in the analyzed head models.

	Tissue	Conductivity (S/m)	
▢	Scalp	0.3333	[Gonçalves et al., 2003a]
▢	Air cavities	0.0000	[Haueisen et al., 1995]
▢	CSF	1.7857	[Baumann et al., 1997]
▢	WM	0.1428	[Haueisen et al., 1995]
▢	GM	0.3333	[Haueisen et al., 1995]

Model 2: This model incorporates a single anisotropic compartment for the skull surface, and uses its geometry to estimate the radial and tangential conductivities. For each voxel the normal and two orthogonal directions were derived as explained in Section 4.2.2, which in conjunc-

tion with the radial and tangential conductivities form the conductivity tensor. The anisotropy ratio of the skull used for this model is based on our own study on a spherical head model [Montes-Restrepo et al., 2010]. The radial conductivity is assumed to be 0.0105 S/m and the tangential 0.0191 S/m, i.e., an anisotropy ratio of 1:1.82 (σ_{rad}:σ_{tang}) is used.

Model 3: In this model, the skull is isotropic heterogeneous but with the air cavities modeled as compact bone.

Model 4: As in Model 3, the skull compartment is isotropic heterogeneous but the air cavities are modeled as spongy bone.

4.3.2.2   EEG source imaging

The FDM was used to calculate the forward problem in the reference and models 1 to 4. The calculation grid of the FDM consisted of 5,719,372 nodes. The time required to compute the forward matrix was approximately one hour per lead pair of electrodes.

The inverse problem solution was carried out by the minimization of the RRE (4.1). In this case, the penalization parameter $\mathbf{C}(\mathbf{r})$ is zero when the dipole location is inside the GM and large otherwise.

4.3.2.3   Simulation setup

Dipole location and orientation errors were investigated when a simplified head model (model i, $\forall i \in 1, \ldots, 4$) was assumed instead of a more realistic one (reference model). The simulation setup is depicted in Figure 4.13. Test dipoles were placed on a 3D grid with a distance of 5 mm between each voxel. Only the voxels situated in the GM and not lower than the most inferior electrode position were considered. For each dipole location, three orthogonal orientations were taken into account according to the Cartesian coordinate system: $x-$, $y-$ and $z-$orientation. The total number of test dipoles was 7,568.

First, the electrode potentials $\mathbf{V}_{\text{ref}}$ were calculated by solving the forward problem in the reference model. Thus, the simulated EEG data at the 27 electrodes was obtained. The electrode potentials $\mathbf{V}_{\text{test}}$ were also computed on models 1 to 4. Then, the forward calculations were evaluated through the RDM, expressed in (4.2), and the lnMAG given by (4.3).

EEG data simulation   Dipole estimation

$\mathbf{r},\mathbf{d}$ Reference model $\mathbf{V}_{\text{ref}}$ Model i $\hat{\mathbf{r}},\hat{\mathbf{d}}$
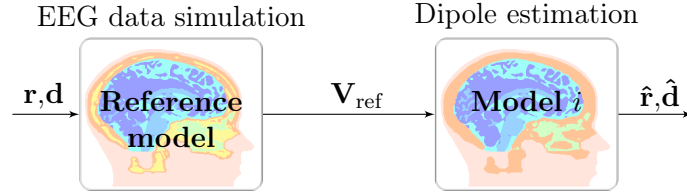
Figure 4.13: Simulation setup used to establish the influence of skull inhomogeneities on ESI. The realistic reference model (isotropic three-layered skull) is compared against Model i for $i = 1$: isotropic homogeneous skull, $i = 2$: anisotropic homogeneous skull, $i = 3$: isotropic heterogeneous skull with air cavities modeled as compact bone, and $i = 4$: isotropic heterogeneous skull with air cavities modeled as spongy bone.

Subsequently, from the simulated potentials $\mathbf{V}_{\text{ref}}$, the dipoles were estimated by solving the inverse problem using models 1 to 4. Hence, the error caused by the use of a simplified model for the skull in the solution of the inverse problem was investigated. The estimated dipole parameters, $\hat{\mathbf{r}}$ and $\hat{\mathbf{d}}$, which minimized the RRE cost function (4.1), were the dipole parameters that best explained the potential $\mathbf{V}_{\text{ref}}$ in the test models.

The inverse error was calculated with the DLE (4.4), which measures the distance between original and estimated dipole positions. The dipole orientation error (DOE), defined as the angle between the vector components of the original dipole $\mathbf{d}$ and the estimated dipole $\hat{\mathbf{d}}$, was calculated through the cosine rule:

$$\text{DOE} = \arccos\left(\frac{\hat{\mathbf{d}}^T \mathbf{d}}{\|\hat{\mathbf{d}}\|\|\mathbf{d}\|}\right) \tag{4.8}$$

4.3.3   Results

The cumulative distribution of the lnMAG errors is displayed in Figure 4.14. As can be seen, the simplification of air cavities (models 3 and 4) leads to negative lnMAG errors, i.e., decreased magnitudes, while Model 1 — isotropic homogeneous — yields the largest lnMAG errors among the tested models with $\sim 95\%$ of the errors below 0.5. For Model 2 (anisotropic skull), $\sim 95\%$ of the lnMAG errors are below 0.3, yielding lower errors compared to Model 1.

The RDM and lnMAG error maps present a similar distribution between each other. Therefore, only the RDM error maps are shown in
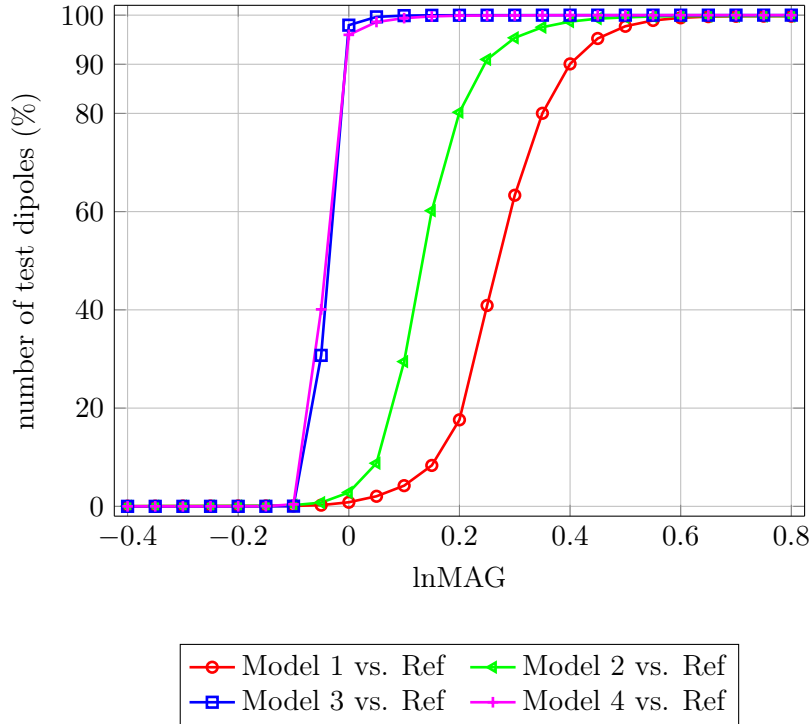
Figure 4.14: Cumulative histograms of the logarithmized magnitude error for models 1 to 4.

Figure 4.15. Large RDM errors are displayed for dipoles close to the skull in models 1 and 2, with the isotropic homogeneous skull simplification yielding the highest relative distance measure. For models 3 and 4, the RDM errors are more prominent for dipoles lying close to the air cavities, i.e. at the fronto-basal region.

Figure 4.16 shows the results for DLE on models 1 and 2. Large errors for both models can be seen in the temporal region. For Model 1, Figure 4.16a, the errors are also high in the parieto-occipital region. Although Model 2, Figure 4.16b, presents overall smaller DLEs, the error pattern in temporal and cerebellar regions is similar to that of Model 1. If the right and left hemispheres are compared, asymmetric errors can be seen for both analyzed models. This is caused by a higher amount of spongy bone in the left than in the right hemisphere of the reference head model (Figure 4.12a).

Dipole localization errors for the models simplifying the air cavities
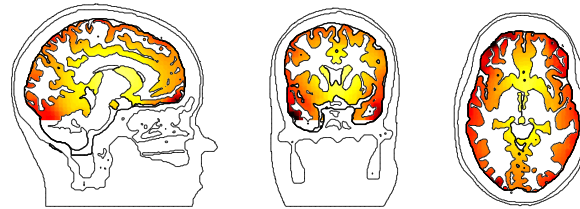
(a) Model 1 – Isotropic homogeneous skull
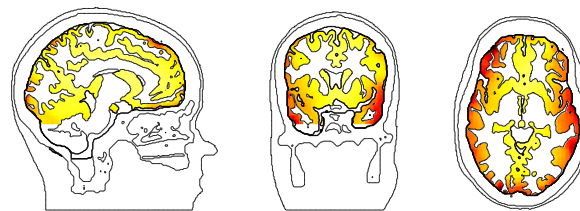
(b) Model 2 – Anisotropic homogeneous skull
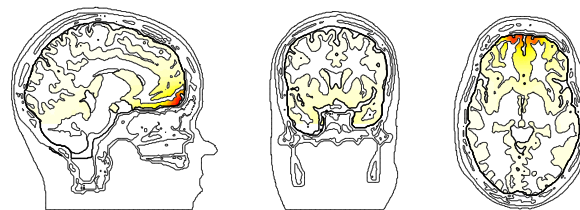
(c) Model 3 – Isotropic heterogeneous skull, air cavities as compact bone

(d) Model 4 – Isotropic heterogeneous skull, air cavities as spongy bone

RDM
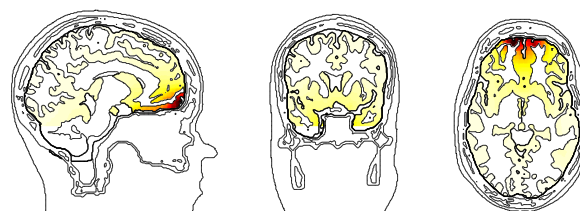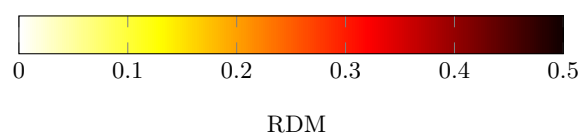
Figure 4.15: Relative distance measure for models 1 to 4.

(a) Model 1 – Isotropic homogeneous skull

(b) Model 2 – Anisotropic homogeneous skull

DLE (mm)
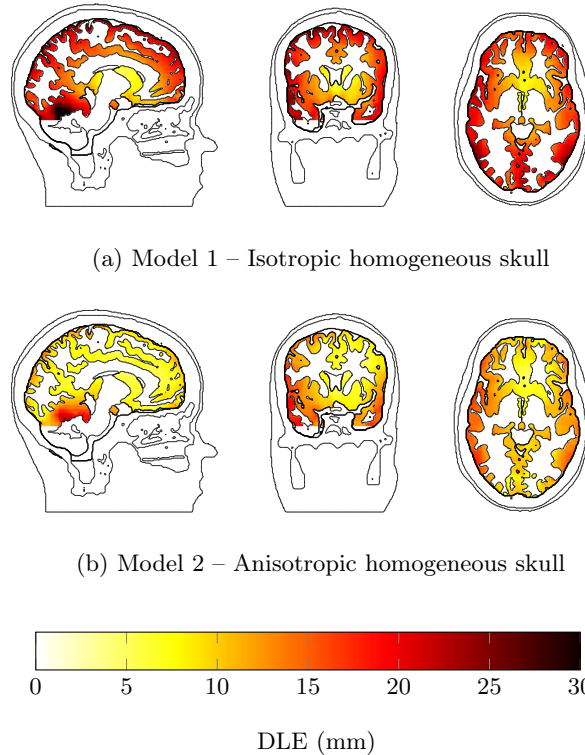
Figure 4.16: Dipole localization errors for models 1 and 2.

(models 3 and 4) are presented in Figure 4.17. The errors are overall similar between each other, with highest values at the fronto-basal region of the brain. Notice that the scale used for models 3 and 4 (Figure 4.17) is smaller than for models 1 and 2 (Figure 4.16) because of the difference in magnitude of the DLE.

The cumulative histograms of the dipole localization and orientation errors are shown in Figure 4.18. For the air cavities simplification (models 3 and 4), most of the DLE are below 3 mm. The mean DLEs are 9.8 mm for Model 1, 6.1 mm for Model 2, 0.8 mm for Model 3 and 1.1 mm for Model 4. According to the cumulative histogram of the DOE, Figure 4.18 bottom, most dipoles have DOEs below 20° for models 1 and 2. For models 3 and 4, most of the errors are below 10°. The mean orientation errors are 11.1° for Model 1, 9.5° for Model 2, 2.6° for Model 3 and 3.0° for Model 4.
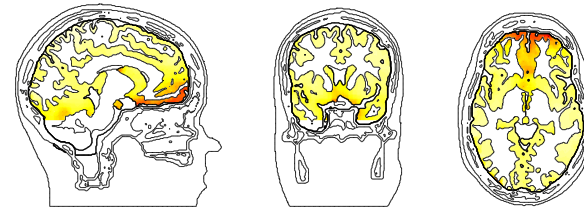
(a) Model 3 – Isotropic heterogeneous skull, air cavities as compact bone
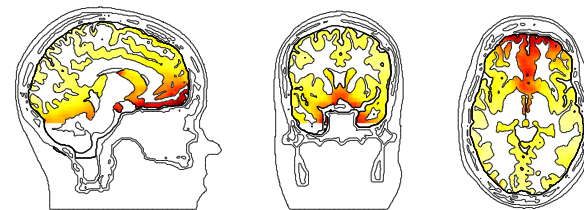
(b) Model 4 – Isotropic heterogeneous skull, air cavities as spongy bone

DLE (mm)

Figure 4.17: Dipole localization errors for models 3 and 4.

4.3.4   Conclusions

We investigated forward and inverse errors caused by assuming a simplified skull model instead of a more realistic one in the EEG dipole estimation. When the conductivity was assumed as isotropic homogeneous, the mean DLE was ~ 1 cm. The model with anisotropic skull presented overall smaller errors than the isotropic one, especially in frontal and central regions of the brain.

The air cavities of the skull showed to have little influence on the dipole estimation (DLE < 5 mm) and to be better modeled as compact bone. The forward and inverse errors were larger in the fronto-basal region of the brain, that is, in the near vicinity of these air cavities. For the other brain regions, the DLEs were lower than 2 mm.
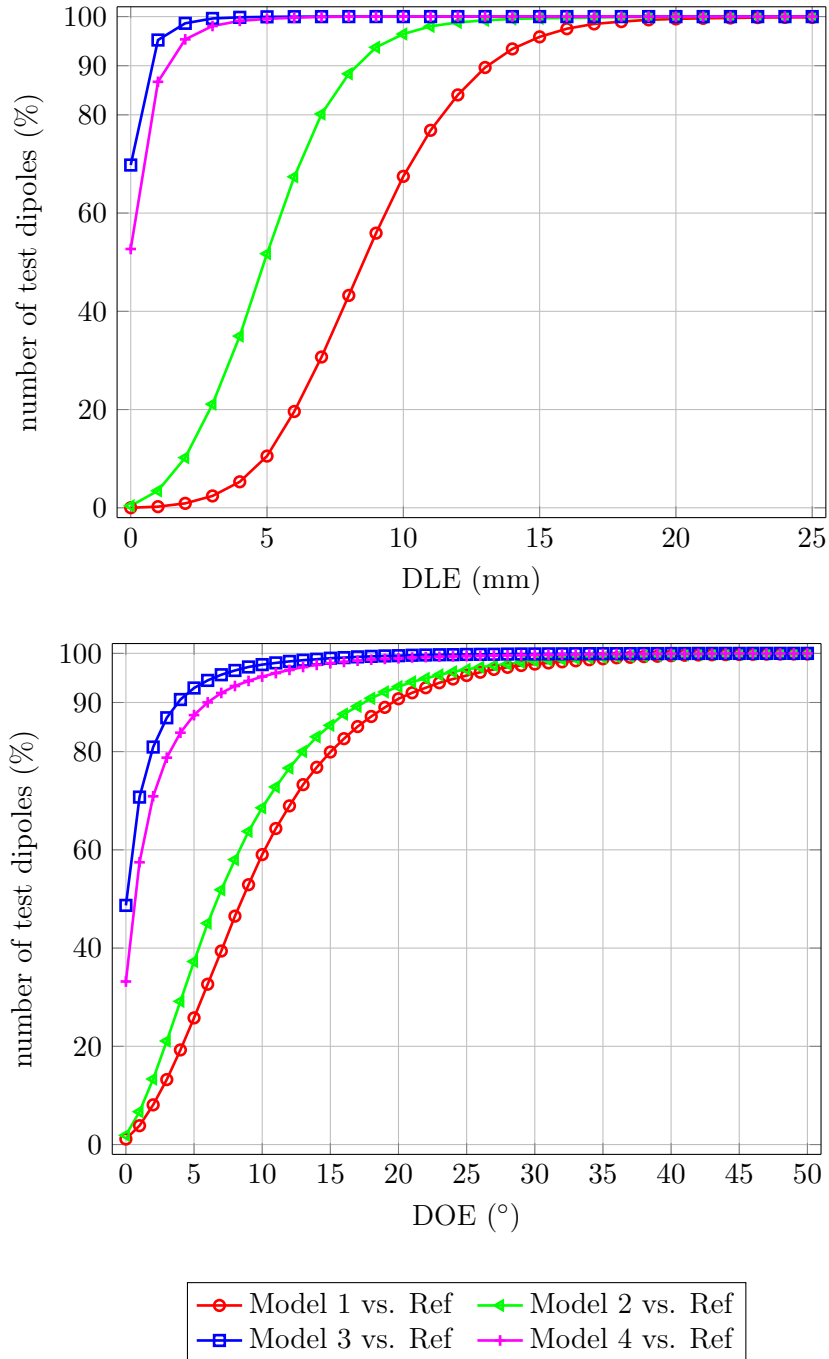
Figure 4.18: Cumulative histograms of the dipole localization and orientation errors for models 1 to 4.

4.4 Discussion and conclusions

In this chapter, three studies over the influence of different aspects of skull modeling were presented. For these studies, the relative distance measure and logarithmized magnitude forward errors as well as the inverse dipole localization and orientation errors were computed. The mentioned studies used realistic head models with the skull segmented from CT images.

Study I considered the effects of conductivity perturbations of the three-layered skull on ESI. Changes in the compact and spongy bone conductivities of the skull were analyzed by measuring forward and inverse errors in the most clinically relevant brain areas. We found that the conductivity of the compact bone had the largest influence on ESI. Additionally, the effect of conductivity perturbations of the three-layered skull was smaller for sources at the cingulate cortex than for sources located at temporal and frontal regions. The over-estimation of the conductivity of the compact bone compartment led to deeper estimated dipoles while its under-estimation yielded more superficial sources.

Study II allowed the determination of the optimal anisotropy ratio of the skull on a spherical head model. A spherical reference model with a three-layered skull was compared against 192 test models with anisotropic skulls, each with a different anisotropy ratio. The radial and tangential conductivities were modeled using an approach based on a simplified three-layered skull. This study showed that the radial skull conductivity had the highest influence on the determination of the anisotropy ratio of the skull. Furthermore, dipoles located close to the skull were more affected by the use of an anisotropic instead of a three-layered skull. The optimal anisotropy ratio of 1:1.82 (σ_{rad}:σ_{tang}) found in this study, suggests that the commonly used value of 1:10 is over-estimated, as has been previously pointed out by other studies [Dannhauer et al., 2011, Sadleir and Argibay, 2007].

Finally, in Study III, the influence of not modeling the skull as a three-layered but as a homogeneous compartment with either isotropic or anisotropic conductivity was investigated. Additionally, the effect of omitting the air-filled cavities of the skull was analyzed. The results showed that the approximation of the skull as an isotropic homogeneous compartment led to estimation errors of up to 2.5 cm, which is unacceptable for clinical diagnosis. However, the anisotropic model presented overall smaller errors. For the generation of realistic head models in ESI,

the air cavities of the skull can be neglected and be modeled as compact bone.

Three different conductivity ratios were investigated in each study: (i) spongy to compact bone conductivity, for isotropic heterogeneous skull; (ii) radial to tangential conductivity, for anisotropic homogeneous skull and (iii) skull-to-soft tissue conductivity, for isotropic homogeneous skull.

For the first ratio, as investigated in Study I, the σ_{spong} and σ_{comp} conductivities were assumed as the average values of the measurements performed by Akhtari et al. [2002], which correspond to a spongy to compact ratio of 4.38:1. A similar ratio of 4.5:1 has been used in other studies [Dannhauer et al., 2011, Fuchs et al., 2007, Lucka et al., 2012, Pursiainen et al., 2012]. Previous works [Haueisen et al., 1995, Ramon et al., 2006] have used a much higher ratio of 7.3:1. Tang et al. [2008] found an inverse relationship between skull resistivity and percentage of spongy bone in their investigated skull samples. According to their plot, the predicted value for compact bone would be 0.00465 S/m, however, they did not give an estimate for the conductivity of the spongy bone. In any case, their measurements suggest a higher spongy to compact bone ratio (> 7) than the one used here. Therefore, the lack of precise conductivity values for the compact and spongy bones of the skull remain as a difficulty in the generation of a more accurate head model [Pohlmeier et al., 1997].

The anisotropy ratio of the single skull compartment was considered in Study II. As pointed out by Sadleir and Argibay [2007], the anisotropy ratio of 1:10 (radial:tangential) is overestimated. Some authors [Rullmann et al., 2009, Steinsträter et al., 2010] have used lower anisotropy ratios than the commonly used 1:10 (radial:tangential), such as 1:3, following Fuchs et al. [2007]. The ratio found in Study II was 1:1.8, with conductivity values of $\sigma_{\mathrm{rad}} = 0.0105$ and $\sigma_{\mathrm{tang}} = 0.0191$ S/m, which is concordant with other studies. In the work of Dannhauer et al. [2011], a ratio of 1:1.6 with $\sigma_{\mathrm{rad}} = 0.0093$ and $\sigma_{\mathrm{tang}} = 0.015$ S/m was found as optimal. In addition, Fuchs et al. [2007] found an average ratio of 1:1.6 with $\sigma_{\mathrm{rad}} = 0.00863$ and $\sigma_{\mathrm{tang}} = 0.01382$ S/m, using the conductivity values for σ_{comp} and σ_{spong} from Akhtari et al. [2002]. According to these studies, a ratio of 1:1.6 can be used to model the anisotropy of the skull. However, more than this ratio, the radial conductivity seems to be the most relevant variable in the characterization of anisotropic conductivity [Vallaghé and Clerc, 2009]. Consequently, more studies that determine the optimal anisotropy ratios and radial conductivity for the

skull conductivity modeling, need to be performed.

Many studies have measured the skull-to-soft tissue conductivity ratio, reporting a large variability of results, which in chronological order are: 80 [Rush and Driscoll, 1968], 15 [Oostendorp et al., 2000], 20 to 50 [Gonçalves et al., 2003a], 8 [Hoekema et al., 2003], 72 [Gonçalves et al., 2003b], 23 [Baysal and Haueisen, 2004], 25 ± 7 [Lai et al., 2005], 18.7 ± 2.1 [Zhang et al., 2006], and 120 [Lew et al., 2009a]. Most of these approaches have used a three-compartment model, however, Lew et al. [2009a] used a four-layered model (including CSF). In our work, the brain was modeled as a heterogeneous tissue consisting of CSF, WM and GM, with different conductivities. Estimation of brain/skull conductivity ratio with highly heterogenous models has not been performed so far [Ramon et al., 2006]. Due to the higher sensitivity of scalp and skull conductivities [Vallaghé and Clerc, 2009] and to the high inhomogeneity of the brain tissue, the scalp-to-skull ratio would be a more reasonable measure. In Study III, we used a scalp-to-skull conductivity ratio of 16.5 for Model 1. A skull conductivity closer to the radial conductivity, i.e. a scalp-to-skull conductivity ratio of ~ 30, might lead to smaller localization errors in this model. Hence, techniques to determine a single and effective conductivity value such as electrical impedance tomography (EIT) [Gonçalves et al., 2003a, Oostendorp et al., 2000] should be further investigated.

4.5 Contributions

The results of the three studies were presented at national and international conferences: Study I at the *2013 International Conference on Basic and Clinical Multimodal Imaging (BaCI)* [Montes-Restrepo et al., 2013a], Study II at the *2010 PhD symposium of the Faculty of Engineering and Architecture* at Ghent University [Montes-Restrepo et al., 2010] and Study III at the *2011 8th International Symposium on Noninvasive Functional Source Imaging of the Brain and Heart & 2011 8th International Conference on Bioelectromagnetism (NFSI & ICBEM)* [Montes-Restrepo et al., 2011b] and at the *10th Annual Symposium of the IEEE EMBS Benelux Chapter* [Montes-Restrepo et al., 2011a].

Chapter 5

Comparing CT- and MR-based skull models

The true delight is in the finding out rather than in the knowing
—ISAAC ASIMOV

In this chapter, we compare skull modeling approaches based on MR and CT images by analyzing its influence on ESI. A head model with an accurately segmented skull from CT images, including spongy and compact bone compartments as well as some air-filled cavities, is used as the reference model. We investigate skull conductivity and geometry modeling simplifications, in order to determine how the skull should be modeled if no CT images are available. EEG simulations are performed for a configuration of 32 and 128 electrodes, and for both noiseless and noisy data. This chapter is organized as follows: Section 5.2 describes the construction of the realistic head models and the simulation setup used in this study. In Section 5.3 the results for the simulations with noiseless and noisy data are shown. The discussion analyzing CT- versus MR-based skull modeling is presented in Section 5.4.

5.1 Introduction

MRI is a well-known technique for the visualization of the anatomical structure of the soft tissues in the head. However, the skull bone cannot be easily segmented from T1-weighted MR images. Although T2- or proton density (PD)-weighted MR images can be used to improve the determination of the inner surface of the skull [Lew et al., 2009a,

Rullmann et al., 2009] and even that of the spongy bone compartment [Dannhauer et al., 2011, Lucka et al., 2012], these sequences do not introduce additional information for the segmentation of the air cavities and base of the skull. In contrast, CT images get a correct representation of the skull but are not commonly performed on patients due to the ionizing radiation. As a consequence, the accurate segmentation of the geometry of the skull and its layered structure remains unresolved.

In this work we investigate the influence of using different skull modeling approaches on ESI. For this purpose, co-registered MR and CT images of one patient are used. A head model with an accurately segmented skull, including spongy and compact bone as well as some air-filled cavities, is incorporated in the analysis as the reference model. Conductivity and geometry skull modeling approaches were investigated using seven different head models. EEG simulations are performed to investigate the dipole localization error caused by skull modeling alterations. Two electrode configurations are used to assess the importance of spatial sampling density in ESI. Furthermore, the effect of measurement noise is also investigated. The influence of the conductivity values for the different tissues is beyond the scope of this work.

The research questions in this study are: (i) "when the skull geometry is segmented from CT, which conductivity modeling results in smaller dipole estimation errors: isotropic heterogeneous, anisotropic homogeneous or isotropic homogeneous?"; (ii) "when the skull geometry is segmented from MR, which of the previous conductivity modeling options introduces the smallest localization errors?"; (iii) "how sensitive are the models to noise?" and (iv) "what errors are made when less electrodes are used?". Finally, the most important goal is the determination of guidelines for skull modeling in the generation of subject-specific head models in a clinical setting.

5.2   Methods

5.2.1   MR and CT data

At the Reference Center for Refractory Epilepsy of the Ghent University Hospital (Belgium), MR imaging of patients that are candidate for epilepsy surgery is performed to reveal anomalies in the brain anatomy. T1-weighted MR images were acquired on a 3T scanner (Siemens Trio, Erlangen, Germany) with the MP-RAGE protocol. The resulting images

had a dimension of $256 \times 256 \times 176$ with a voxel size of 0.86 mm $\times$ 0.86 mm $\times$ 0.9 mm.

For the visualization of the electrode positions on the scalp and the better delineation of the skull, CT was performed in some of the patients. The CT images (Toshiba Aquilion, Tokyo, Japan) were co-registered to the MR images, resulting in a CT image of dimension $256 \times 256 \times 176$ with voxel size 0.86 mm $\times$ 0.86 mm $\times$ 0.9 mm.

5.2.2   Head model construction

Different realistic head models were generated from the MR and CT images of one patient. The MR images were used to segment the scalp and brain tissues. The scalp was segmented through thresholding followed by a closing with hole filling operation. The segmentation of cerebrospinal fluid (CSF), white matter (WM) and gray matter (GM) was carried out with the SPM8 software package [Friston, 2006]. This resulted in three values for every voxel, each indicating its probability of belonging to WM, GM or CSF. The voxels were then assigned to the compartment for which the voxel had the highest probability. Afterwards, median filtering was applied to exclude isolated voxels. This way, each voxel was classified to a compartment.

The CT images were used to accurately segment the skull. These images were first manually preprocessed in order to remove artifacts such as those caused by the presence of electrodes during the acquisition. Because the image intensities of bone and soft tissue, expressed in Hounsfield units, largely differ [Rorden et al., 2012], a simple thresholding approach can be used to separate the skull and its different tissue types. A CT/MR thresholding approach, followed by the morphological operations dilation and erosion, was performed in order to obtain the skull mask. The calculated skull mask was verified manually to ensure that there were no holes in the calvaria, and to remove any segmentation inaccuracy caused by remaining artifacts in the CT image. This skull mask corresponds to the compact bone compartment. Subsequently, the skull mask was eroded once with a $3 \times 3 \times 3$ cross-shaped structuring element and multiplied by the CT image. This masked image was thresholded to distinguish the spongy bone, according to the intensity levels displayed in the histogram. The thickness of the spongy bone was kept within the normal limits for an adult skull, with maximal thickness of 7 mm in the occipital region [Lynnerup et al., 2005]. The air cavities were segmented through thresholding of the original CT image. Then,

the compact and spongy bone as well as the air cavities were assembled to form the skull compartment. It was guaranteed that compact bone was surrounding both spongy bone and air cavities. Figure 5.1a shows the MR image of the patient used in this study with the CT overlaid in red. The electrodes present during the CT acquisition are visible on the sagittal slice.
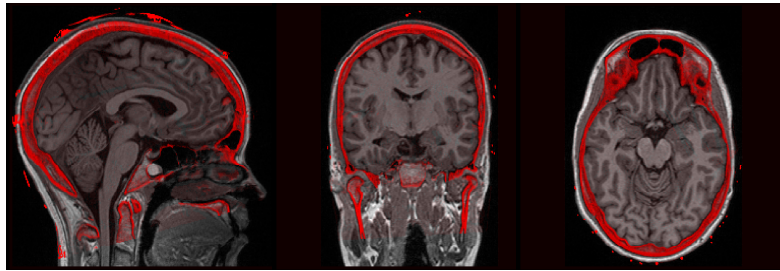
(a) MR overlaid with CT (in red)
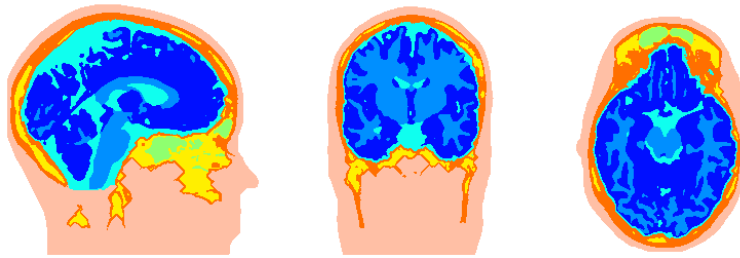
(b) Segmented reference head model

Figure 5.1: Reference head model in sagittal, coronal and axial views, showing seven different tissue types: ▢ Scalp, ▢ CSF, ▢ WM and ▢ GM segmented from MR; ▢ Compact bone, ▢ Spongy bone and ▢ Air cavities, all segmented from CT.

In order to compare different head models, a *reference* model or *ground truth* was established. This reference head model incorporates a realistic geometry for the skull, consisting of separate isotropic layers for the compact and spongy bone compartments in addition to air-filled cavities such as the frontal and sphenoidal sinuses (Figure 5.1b). These cavities (σ_{airc}) were assumed to have the conductivity of air, i.e., null conductivity. The conductivities for the compact and spongy bones were chosen according to the computations of Fuchs et al. [2007], based on the measurements of Akhtari et al. [2002], as: $\sigma_{\mathrm{comp}} = 0.0064$ S/m and $\sigma_{\mathrm{spong}} = 0.02865$ S/m. Table 5.1 shows the conductivity values for all the tissues in the reference head model. The GM, WM and CSF compartments were added to

the head model while ensuring that GM was surrounded by CSF. This assured that there was no direct contact between GM and compact bone.

Table 5.1: Conductivities for the reference head model.

	Tissue	Conductivity (S/m)	
☐	Scalp	0.3279	[Gonçalves et al., 2003a]
■	Compact bone	0.0064	[Fuchs et al., 2007]
☐	Spongy bone	0.02865	[Fuchs et al., 2007]
☐	Air cavities	0.0000	[Haueisen et al., 1995]
☐	Cerebrospinal Fluid	1.7857	[Baumann et al., 1997]
■	White Matter	0.1428	[Haueisen et al., 1995]
■	Gray Matter	0.3333	[Haueisen et al., 1995]

The influence of the skull on dipole estimation was analyzed through the generation of different head models based on the different skull modeling approaches. In the following subsections we explain the rationale and construction of these models. Table 5.2 presents a summary of the different skull models that were constructed.

5.2.2.1 Skull models based on CT images

These models use the same skull geometry as the reference model but its conductivity modeling is altered, generating models 1 to 3 as explained below (see Table 5.2). The air cavities in the three cases are modeled the same as in the reference model.

Model 1 – Isotropic heterogeneous skull (layCT): The skull is modeled as a heterogeneous compartment, but the spongy layer is not segmented directly from the CT image. It is constructed by iteratively eroding the compact layer six times with a $3 \times 3 \times 3$ cross-shaped structuring element, until its thickness in the occipital region is below 7 mm [Lynnerup et al., 2005]. Thus, it is an approximation to the actual layered structure of the skull that is useful when the skull geometry is accurate but the spongy bone cannot be easily distinguished. The conductivities for the compact and spongy bones are set as isotropic with the same values as those of the reference model.

Model 2 – Anisotropic homogeneous skull (aniCT):   This model incorporates a single anisotropic skull compartment and uses its geometry to estimate the radial and tangential conductivities. For each voxel of the skull the normal and two orthogonal directions are derived, that in conjunction with the radial and tangential conductivities form the conductivity tensor. The anisotropy ratio of the skull used for this model is based on the studies of Fuchs et al. [2007] and Dannhauer et al. [2011], and on our own simulation study with a spherical head model [Montes-Restrepo et al., 2010]. The radial conductivity is assumed to be 0.0105 S/m and the tangential 0.0191 S/m, resulting in an anisotropy ratio of 1:1.82 (radial:tangential).

Model 3 – Isotropic homogeneous skull (isoCT):   The skull is modeled as a homogeneous compartment having an isotropic conductivity of 0.0105 S/m. This value equals the radial conductivity of the anisotropic model because this conductivity has the strongest influence on the measured surface potential [Vallaghé and Clerc, 2009].

5.2.2.2   Skull models based on MR images

Models 4 to 7 use a geometry for the skull and air cavities, segmented from the MR image using the SPM toolbox. All tissues are segmented from the MR image, mimicking the situation in which no CT image is available. The conductivity values for all models are shown in Table 5.2 and correspond to those of the CT-based skull models, as explained in Section 5.2.2.1.

Model 4 – Isotropic heterogeneous skull (refMR):   This model incorporates separate layers for the spongy and compact bone, all segmented from the MR image. A skull mask is extracted from the MR using the SPM toolbox. This mask is overlaid with the original MR and the resulting image is thresholded in order to distinguish between spongy and compact bone compartments. The name given to this model is refMR because it corresponds to the most realistic skull segmented from the MR image.

Model 5 – Isotropic heterogeneous skull (layMR):   The skull is modeled as a heterogeneous compartment, but the spongy layer is not segmented from the MR image. It is constructed by iteratively eroding the

compact layer, with the same procedure as explained for Model 1. This way, the segmentation process becomes more simple because only the external geometry of the skull needs to be accurately segmented in order to construct the three-layered skull compartment.

Model 6 – Anisotropic homogeneous skull (aniMR): The skull is modeled as a homogeneous compartment with anisotropic conductivity, according to Model 2.

Model 7 – Isotropic homogeneous skull (isoMR): The skull is modeled as a homogeneous compartment with isotropic conductivity, according to Model 3.

5.2.3   EEG source imaging

In this work, the calculation of the forward problem was carried out with the FDM with reciprocity that can incorporate anisotropies [Hallez et al., 2005, Vanrumste et al., 2001]. We used 128 electrode positions that were based on the 10–5 system [Oostenveld and Praamstra, 2001], which is an extension of the International 10–20 system. The calculation grid of the FDM with reciprocity consisted of 5,745,427 nodes. The time required to compute the forward matrix using 128 electrodes was approximately 3 hours per electrode pair using one core of a CPU dual-socket quad-core Intel Xeon L5520 (Intel Nehalem microarchitecture, 2.27 GHz, 8 MB L3 cache per quad-core chip). Figure 5.2 presents a diagram explaining the steps necessary to generate the lead-field matrix $\mathbf{L}$.

The inverse problem was performed by the minimization of the RRE (2.23), with optimal dipole moment $\mathbf{d}_{\mathrm{opt}}$, using the Nelder-Mead simplex optimization.

5.2.4   Simulation setup

We investigated the dipole localization and orientation errors due to using a simplified head model (model i, $\forall i \in 1, 2, 3, 4, 5, 6, 7$) instead of the more realistic reference model, for the dipole estimation. The diagram for the experimental setup can be seen in Figure 5.3.

Test dipoles were placed in the voxels belonging to the gray matter, excluding the cerebellum. A distance of 5 mm between each voxel was

Table 5.2: Summary of the different skull models. For models 1 to 3, the skull was segmented from CT images, while for models 4 to 7 the skull was segmented from MR images. Models 1 and 5 use a spongy layer that corresponds to an erosion of the compact bone. Models 2 and 6 incorporate anisotropic conductivity (σ_aniso) while the other models use isotropic conductivities (σ_iso).

	Model		Tissue	Segm.	Conductivity (S/m)
–	Reference		Compact	CT	$\sigma_\text{iso} = \sigma_\text{comp} = 0.0064$
			Spongy	CT	$\sigma_\text{iso} = \sigma_\text{spong} = 0.02865$
			Air cavities	CT	$\sigma_\text{iso} = \sigma_\text{airc} = 0.0000$
1	layCT		Compact	CT	$\sigma_\text{iso} = \sigma_\text{comp} = 0.0064$
			Spongy	eroded compact	$\sigma_\text{iso} = \sigma_\text{spong} = 0.02865$
			Air cavities	CT	$\sigma_\text{iso} = \sigma_\text{airc} = 0.0000$
2	aniCT		Compact + Spongy	CT	$\sigma_\text{aniso} \begin{cases} \sigma_\text{rad} = 0.0105 \\ \sigma_\text{tang} = 0.0191 \end{cases}$
			Air cavities	CT	$\sigma_\text{iso} = \sigma_\text{airc} = 0.0000$
3	isoCT		Compact + Spongy	CT	$\sigma_\text{iso} = \sigma_\text{rad} = 0.0105$
			Air cavities	CT	$\sigma_\text{iso} = \sigma_\text{airc} = 0.0000$
4	refMR		Compact	MR	$\sigma_\text{iso} = \sigma_\text{comp} = 0.0064$
			Spongy	MR	$\sigma_\text{iso} = \sigma_\text{spong} = 0.02865$
			Air cavities	MR	$\sigma_\text{iso} = \sigma_\text{airc} = 0.0000$
5	layMR		Compact	MR	$\sigma_\text{iso} = \sigma_\text{comp} = 0.0064$
			Spongy	eroded compact	$\sigma_\text{iso} = \sigma_\text{spong} = 0.02865$
			Air cavities	MR	$\sigma_\text{iso} = \sigma_\text{airc} = 0.0000$
6	aniMR		Compact + Spongy	MR	$\sigma_\text{aniso} \begin{cases} \sigma_\text{rad} = 0.0105 \\ \sigma_\text{tang} = 0.0191 \end{cases}$
			Air cavities	MR	$\sigma_\text{iso} = \sigma_\text{airc} = 0.0000$
7	isoMR		Compact + Spongy	MR	$\sigma_\text{iso} = \sigma_\text{rad} = 0.0105$
			Air cavities	MR	$\sigma_\text{iso} = \sigma_\text{airc} = 0.0000$

CT-based Skulls (spanning models 1–3); *MR-based Skulls* (spanning models 4–7)
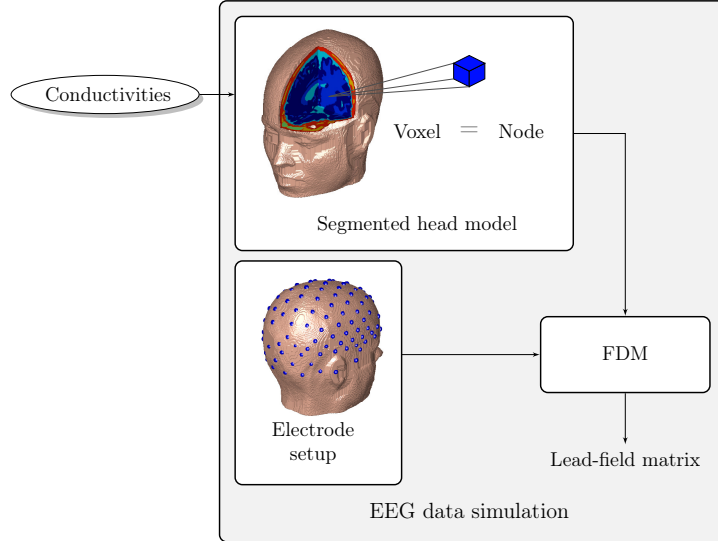
Figure 5.2: Diagram explaining the calculation of the lead-field matrix. Conductivity values are assigned to the different tissues in the segmented head model. The voxels of this model correspond to the nodes of the FDM algorithm. For a given electrode setup and head model, the lead-field matrix is calculated for each voxel.

used, resulting in a total of 6,904 dipoles. Three orthogonal orientations were considered for each dipole location according to the Cartesian coordinate system: $x-$, $y-$ and $z-$direction.

Two different electrode setups were used to analyze the influence of the spatial sampling density. From the initial setup of 128 electrodes, a subgroup of 32 electrodes was extracted following the 10–20 standard.
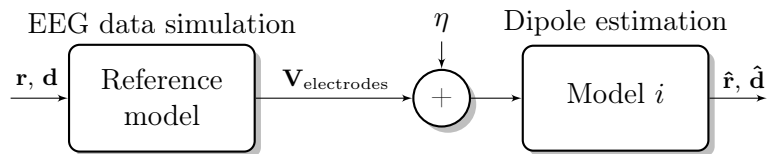
Figure 5.3: Simulation setup used to compare the reference model with the simplified head models (model i, $\forall i \in 1, 2, 3, 4, 5, 6, 7$). For each test dipole ($\mathbf{r}$, $\mathbf{d}$), the electrode potentials $\mathbf{V}_{\text{electrodes}}$ were calculated by solving the forward problem in the reference model. From these potentials, the estimated dipoles ($\hat{\mathbf{r}}$, $\hat{\mathbf{d}}$) were obtained by solving the inverse problem using models 1 to 7. The sensitivity to noise of the different models was also analyzed by adding white Gaussian noise η with three different SNRs: 0, 5 and 10 dB.

For each test dipole with parameters $\mathbf{r}$ and $\mathbf{d}$, the electrode potentials were calculated by solving the forward problem using the reference model. In this way, the simulated EEG data at the electrodes $\mathbf{V}_{\text{electrodes}}$ was obtained. Afterwards, white Gaussian measurement noise η was added to $\mathbf{V}_{\text{electrodes}}$ with SNRs of 0, 5 and 10 dB. The noiseless case in which SNR $\rightarrow \infty$ was also considered. Subsequently, ESI was performed on the simulated EEG data by solving the inverse problem based on head models 1 to 7. By minimizing the cost function in (2.23), the estimated dipole location $\hat{\mathbf{r}}$ and orientation $\hat{\mathbf{d}}$ were obtained.

Utilizing the simulation setup displayed in Figure 5.3, we investigated the dipole location and orientation errors due to skull modeling approaches based on CT (Models 1 to 3 vs. Reference) and MR (Models 4 to 7 vs. Reference) images.

The dipole localization error (DLE), Equation (4.4), was evaluated through the Euclidean distance between the original dipole location $\mathbf{r}$ and the estimated dipole location $\hat{\mathbf{r}}$. The dipole orientation error (DOE), Equation (4.8), was defined as the angle between the vector components of the original dipole $\mathbf{d}$ and the estimated dipole $\hat{\mathbf{d}}$.

A Monte-Carlo simulation for each dipole location and noise level was performed (100 trials), using both electrode setups. In order to investigate the influence of using different skull modeling approaches on each brain region, we computed the mean DLEs for the frontal, parietal, occipital and temporal lobes as well as the cingulate and insular cortices. The mean errors were computed for the noiseless and noisy cases.

5.3 Results

5.3.1 Noiseless simulations

5.3.1.1 Skull models based on CT images

Models 1, 2 and 3 were based on both the CT and the MR image. The soft tissue compartments were identical to those of the reference model. The skull was segmented from the CT image and different conductivity modeling was used, compared with the reference model.

The difference between the spongy bone compartment of the reference model and Model 1 (layCT) is displayed in Figure 5.4. The spongy bone for Model 1 is shown in red and the arrows indicate points where the largest amount of non-overlapping voxels are found. These differences

in segmentation may lead to larger dipole localization and orientation errors in the adjacent brain regions.

sagittal   coronal   axial
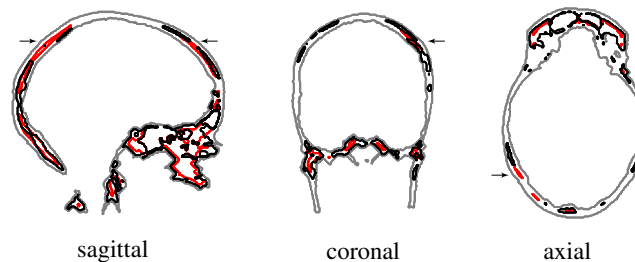
Figure 5.4: Superposition of spongy bone contours for skulls from the reference model (in black) and Model 1 (in red). The arrows indicate the maximal difference between the spongy bone for both models. The inner and outer skull surfaces are depicted in light gray.

Figure 5.5 shows the sagittal, coronal and axial views of the localization errors for models 1 to 3 with 128 electrodes. Among these three models, Model 1 (Figure 5.5a) presents the lowest errors overall.

Localization errors for Model 1, Figure 5.5a, are larger for deep sources in the brain than for superficial ones. There is asymmetry towards the right side due to the differences in spongy bone between Model 1 and the reference model, as indicated by the arrow in the coronal view of Figure 5.4. By comparing homogeneous anisotropic and isotropic conductivity simplification as given by models 2 and 3, slightly lower errors are observed for the last model (Figure 5.5c). For these models, the localization errors are larger in the temporal and superior parietal regions of the brain. In general, the error pattern for models 2 and 3 is similar but with rather larger errors for Model 2, as concluded from Figs. 5.5b and 5.5c.

The cumulative error histograms for the reference model and models 1 to 3, using 32 or 128 electrodes in the noiseless situation, are shown in Figure 5.6a. When the number of electrodes is increased, a slight decrease in the location errors is observed. The smallest localization errors are found for Model 1. Model 3 has smaller errors compared with Model 2. The mean localization errors with 32 electrodes are 4.3 mm for Model 1, 7.8 mm for Model 2 and 6.8 mm for Model 3. When 128 electrodes are used the errors decrease to 4.1 mm for Model 1, 7.3 mm for Model 2 and 6.5 mm for Model 3. These results are presented in Figure 5.10, for the noiseless case at all brain lobes (CT-based skulls).

With 32 electrodes, the mean orientation errors are 13.5° for Model

(a) Model 1 - layCT

(b) Model 2 - aniCT

(c) Model 3 - isoCT
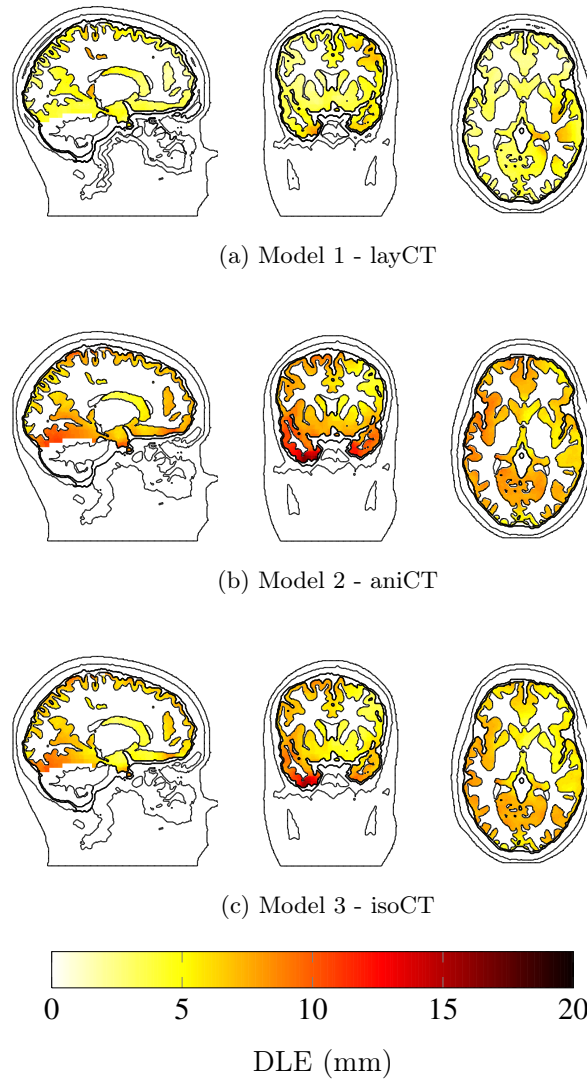
Figure 5.5: Dipole localization errors for models with CT-based skulls using the 128 electrode configuration.

1, 16.1° for Model 2 and 15.3° for Model 3. For the 128 electrodes configuration, the errors decrease to 13.0° for Model 1, 15.8° for Model 2 and 15.1° for Model 3. These results are shown in Table 5.3, for the noiseless case.
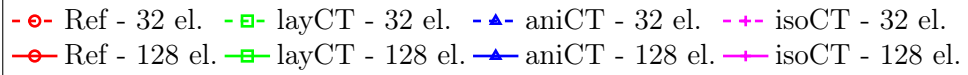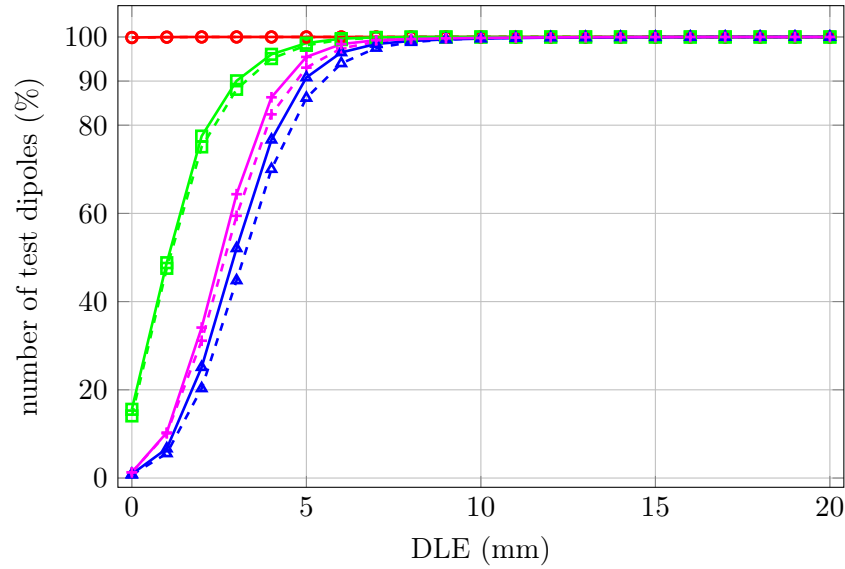
(a) Models with CT-based skulls
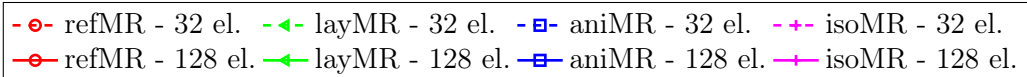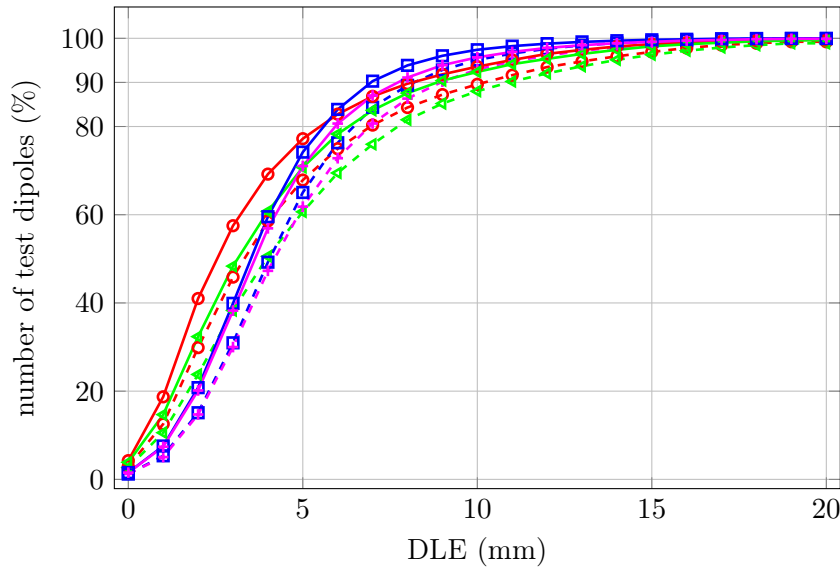
(b) Models with MR-based skulls

Figure 5.6: Cumulative histograms of the dipole localization errors for the models with (a) CT-based and (b) MR-based skulls for 32 (- -) and 128 (—) electrodes. The bin size was 1 mm.

5.3.1.2   Skull models based on MR images

The influence of using the skull geometry derived from MR images, was analyzed using models 4 to 7. In this group, models 4 (refMR) and 5 (layMR) had a layered skull but using a different spongy bone segmentation. The conductivities of all tissue classes were the same for both models. In models 6 (aniMR) and 7 (isoMR), a homogeneous skull compartment was used instead of a layered skull, in which the conductivity was assumed anisotropic and isotropic, respectively.

The difference between CT- and MR-based skull segmentations is shown in Figure 5.7. The contour of the CT-based skull is displayed in black and of the MR-based skull in red.

As can be seen in Figure 5.7a, the largest difference between the two segmentation approaches lies in the basal region of the skull, as the arrow indicates in the sagittal view. The segmentation of the air cavities has large correspondence for both modalities although for MR they are overestimated, as can be seen in Figure 5.7b.

(a) Compact bone
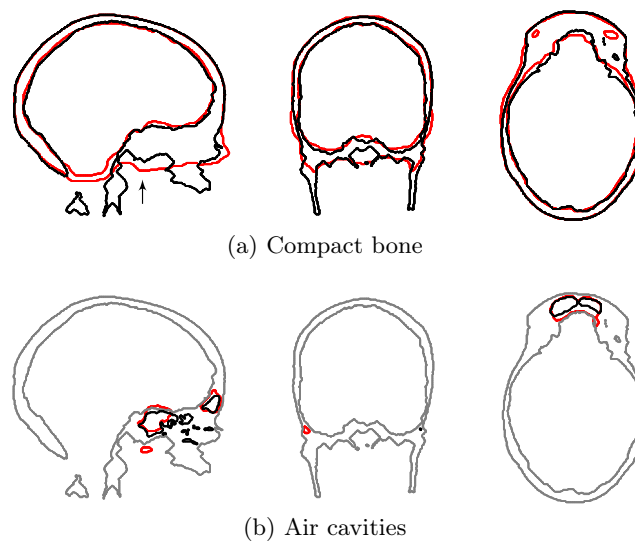
(b) Air cavities

Figure 5.7: Superposition of contours for CT-based (in black) and MR-based (in red) skulls. Comparisons for the (a) compact bone and (b) air cavities are shown. The arrow in (a) indicates the maximal difference between the two contours.

Figure 5.8 compares the spongy bone of the MR-based segmented skull versus that of the reference model. Spongy bone comparison between the reference model and Model 4, as depicted in Figure 5.8a, reveals differ-

ences in thickness mostly in the temporal and frontal regions. Spongy bone is even found outside the CT skull region, indicating that in this case scalp tissue was segmented as spongy bone (see arrows). Despite that, the spongy bone in the cranial vault is similar for the CT- and MR-based segmented skulls. The most significant differences are found in the basal region of the skull.

(a) Reference vs. Model 4 – refMR

(b) Reference vs. Model 5 – layMR
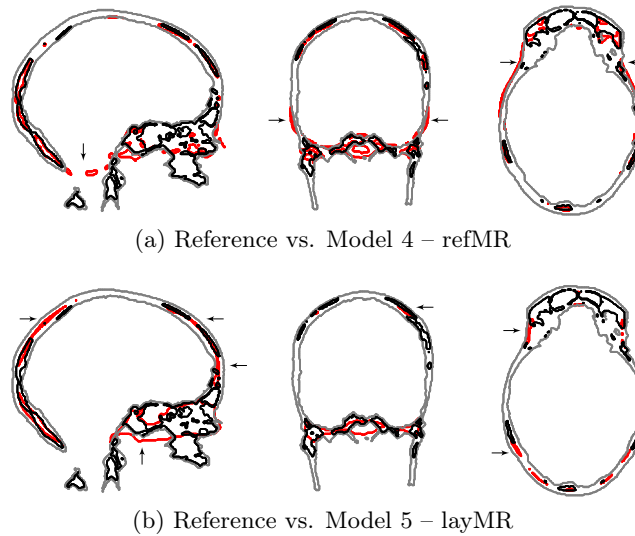
Figure 5.8: Superposition of spongy bone contours for skulls from the reference model (in black) and models (a) 4 and (b) 5 (in red). The arrows indicate the differences between the spongy bone of the MR-based skull models and the reference model. The inner and outer skull surfaces are depicted in light gray.

The differences between the skull of Model 5 and the reference model are mainly located in the vault and the base of the skull as pointed out by the arrows in Figure 5.8b.

Figure 5.9 shows the sagittal, coronal and axial views of the localization errors for models 4 to 7 using the 128 electrode setup. When the skull geometry is determined from MR images, the largest errors are made in the basal region of the brain. This is concordant with the differences in the compact bone contours shown in Figure 5.7a.

Localization errors for models 4 to 7 are large in the basal and bottom regions of the brain. For Model 4, Figure 5.9a, the errors for the superficial sources in the cranial vault are small. In the case of Model 5, Figure 5.9b, the errors made in the vault are slightly larger than for Model 4 and are biased towards the right side of the brain. These findings are

(a) Model 4 - refMR

(b) Model 5 - layMR

(c) Model 6 - aniMR

(d) Model 7 - isoMR

DLE (mm)
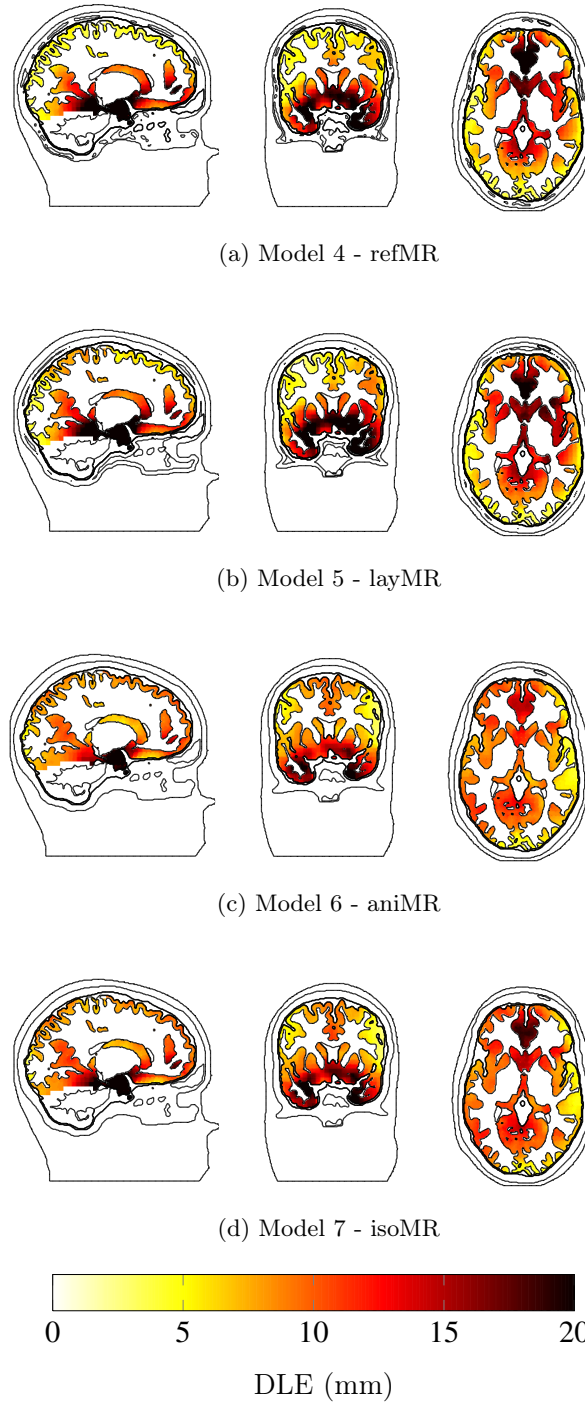
Figure 5.9: Dipole localization errors for models with MR-based skulls using the 128 electrode configuration.

explained by the different segmentation of spongy bone, visualized in Figure 5.8. Models 6 and 7 exhibit a different localization error trend, the errors at the base are still large but less extended and in the cranial vault the errors are in general larger than for models 4 and 5.

The cumulative histograms of the dipole localization errors for models 4 to 7 are shown in Figure 5.6b. Models 4 and 5 show a larger proportion ($> 60\%$) of lower localization errors (< 5 mm) than models 6 and 7. Errors larger than 6 mm are present in greater proportion in the homogeneous models (6 and 7). Models 4 (refMR) and 6 (aniMR) can be considered in this group as the ones with the lowest localization errors.

The mean localization errors for the 32 electrodes configuration are 10.2 mm for Model 4, 11.1 mm for Model 5, 10.2 mm for Model 6 and 10.8 mm for Model 7; with 128 electrodes the errors decrease to 8.4 mm for Model 4, 9.4 mm for Model 5, 9.0 mm for Model 6 and 9.5 mm for Model 7. These results are shown in Figure 5.10, for the noiseless case computed over all brain lobes (MR-based skulls).

The mean orientation errors with 32 electrodes are 23.8° for Model 4, 24.8° for Model 5, 22.7° for Model 6 and 24.0° for Model 7. For 128 electrodes, the means decrease to 22.3° for Model 4, 23.7° for Model 5, 22.0° for Model 6 and 23.1° for Model 7 as presented in Table 5.3, for the noiseless case.

5.3.2 Sensitivity to measurement noise of the simplified models

The sensitivity to measurement noise of the different models was analyzed using Monte-Carlo simulations in which 100 simulations were carried out for each dipole location. The mean dipole localization and orientation errors were obtained for the three different noise levels. Two different electrode setups were utilized in order to analyze the effect of low (32 electrodes) and high (128 electrodes) spatial sampling density on the dipole localization and orientation error, in the presence of noise. The mean DLE was computed for the main lobes of the brain, namely, frontal, parietal, occipital and temporal as well as the cingulate and insular cortices.

Figure 5.10 presents the mean DLE for all the models including the reference, for noise and noiseless cases, using the 32 and 128 electrode configuration. The mean errors are shown for three brain lobes: frontal, temporal and cingulate cortex due to its clinical relevance and similarity

in results with the other regions. Specifically, the frontal lobe presents similar results with the parietal lobe, the temporal lobe with the occipital lobe and the cingulate cortex with the insular cortex.

In the frontal lobe, no significant variation is found between the CT- and MR-based skull models. This low variation is explained by the similarity of this skull region for both modalities. Model 1 yields the best results if both CT and MR images are used. Model 4 has the best performance in the group of head models that are solely based on the MR images. This error trend is maintained when noise with SNR of 10 dB is added. For higher noise levels, there is less difference between the DLE for the models, making the model choice less important. At the cingulate cortex, head models in which the skull was segmented from CT images outperform those in which the skull was segmented from MR images. The difference between both modalities is noticeable even with noise of SNR = 5 dB using 128 electrodes ($\sim$ 4 to 5 mm). For the temporal lobe, there is a significant difference between the CT- and MR- based skull models, but it becomes less relevant when a higher number of electrodes is used. The displayed error trend is kept for a SNR of 5 dB with 128 electrodes.

In the average over all brain lobes, when the SNR = 0 dB the use of a particular model does not have any significant effect on the resultant DLE. However, a higher number of electrodes yields a lower DLE. At 5 dB, the choice of head model is not relevant when the 32-electrode setup is used. Using 128 electrodes, the lowest DLE for the CT-based skull models is given by Model 1, while for the skull models based on MR the DLE does not differ greatly. Nevertheless, the smallest localization errors are noticed for models 4 and 6. At 10 dB, the influence of the electrode setup decreases. When a CT is available, Model 1 yields the lowest DLE. Otherwise, when only MR images are available, Model 4 is recommended. In the noiseless case, the difference between 32- or 128- electrode setup is very small. However, a higher spatial sampling density (128 instead of 32 electrodes) is more important for the MR- compared with the CT-based skull models.

The averages for the DOE are shown in Table 5.3. In the case with the highest noise level, SNR = 0 dB, there is not a noteworthy difference between the models with CT- and MR-based skulls. Nonetheless, the use of a higher spatial sampling density reduces considerably the DOE. For a SNR equal to 5 dB, there is a small inter-modality variation ($\sim 3°$) when 32 electrodes are used. A higher number of electrodes slightly increases
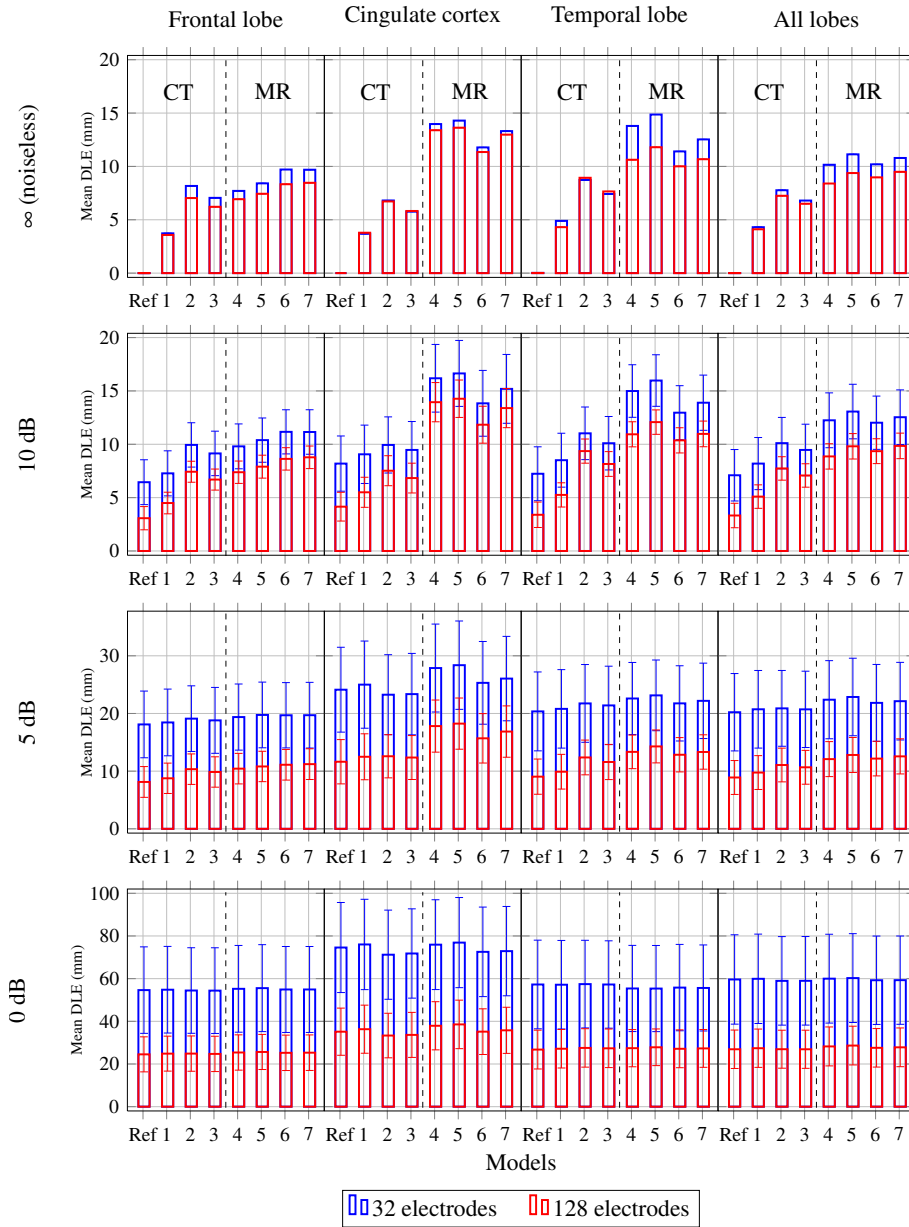
Figure 5.10: Mean dipole localization errors for the reference model and models 1 to 7 at frontal lobe, cingulate cortex, temporal lobe and all brain lobes, with 32 and 128 electrodes. The results are shown for noiseless (SNR → ∞) and noisy data (SNR = 0, 5 and 10 dB). Each bar depicts mean ± the standard deviation in mm.

this variation to $\sim 5°$. For a SNR of 10 dB, the use of a higher spatial sampling density becomes less relevant. If 128 electrodes are used, Model 1 yields the smallest DOE for the CT-based skull models, whereas models 4 and 6 give the lowest DOE for the MR-based skull models. The trends displayed for the DOE in the noiseless case (Table 5.3) are similar to those of the DLE (Figure 5.10).

Table 5.3: Dipole orientation errors for all the models with noiseless (SNR $\rightarrow \infty$) and noisy data (SNR = 0, 5 and 10 dB). Each cell displays mean $\pm$ standard deviation in degrees.

	Model	SNR (dB)			
		∞	10	5	0
32 electrodes	Ref	0.1	16.1 ± 6.6	28.0 ± 10.3	51.1 ± 17.7
	1	13.5	19.3 ± 7.1	29.9 ± 10.9	52.0 ± 17.9
	2	16.1	18.6 ± 5.6	27.3 ± 9.7	50.5 ± 17.9
	3	15.3	18.4 ± 5.8	27.7 ± 9.9	51.0 ± 18.2
	4	23.8	25.6 ± 6.8	32.3 ± 10.7	52.2 ± 17.9
	5	24.8	26.4 ± 6.7	32.4 ± 10.4	51.9 ± 17.6
	6	22.7	24.0 ± 6.0	30.2 ± 9.9	50.8 ± 17.7
	7	24.0	25.2 ± 6.2	31.2 ± 10.2	51.6 ± 18.1
128 electrodes	Ref	0.1	9.6 ± 4.4	14.5 ± 6.0	32.6 ± 12.1
	1	13.0	14.9 ± 4.7	21.1 ± 7.7	34.3 ± 12.6
	2	15.8	16.3 ± 3.6	19.8 ± 6.4	31.7 ± 11.6
	3	15.1	15.9 ± 3.7	19.8 ± 6.6	32.1 ± 11.9
	4	22.3	22.8 ± 4.6	25.6 ± 7.5	35.7 ± 12.4
	5	23.7	24.0 ± 4.6	26.4 ± 7.4	36.0 ± 12.2
	6	22.0	22.3 ± 4.0	24.5 ± 6.9	34.0 ± 11.7
	7	23.1	23.4 ± 4.2	25.5 ± 7.1	34.9 ± 12.1

5.4   Discussion

In this study the dipole localization and orientation errors due to different skull modeling approaches used in ESI were investigated. These approaches, consisting in conductivity and geometry modeling simplifications, make use of CT- and MR-based skulls to generate seven different head models. The sensitivity to noise of these models was investigated through Monte-Carlo simulations in which white Gaussian noise with

three different SNRs was added to the simulated EEG. In addition, the use of high (128 electrodes) versus low (32 electrodes) spatial sampling density was investigated. Consequently, the main goal of this study was to determine guidelines on how to model the skull for a subject-specific head model in a clinical setup.

Skulls segmented from CT images were first used, with the conductivity modeling simplified as either isotropic heterogeneous (with spongy bone as an erosion of the compact bone) for Model 1, anisotropic homogeneous for Model 2 or isotropic homogeneous for Model 3. In this group, the lowest errors were found for the isotropic heterogeneous skull (Model 1 – layCT). This is concordant with other studies [Dannhauer et al., 2011, Sadleir and Argibay, 2007] which state that modeling the skull compartment as isotropic heterogeneous yields a better approximation than the anisotropic homogeneous modeling. Furthermore, to our knowledge, the use of eroded compact bone to resemble the actual spongiform layer has not been investigated before. As a result, when the skull geometry is segmented from CT, modeling the conductivity as isotropic heterogeneous is preferred.

Modeling the conductivity in the homogeneous skull compartment as isotropic (Model 3 – isoCT) yielded lower errors than as anisotropic (Model 2 – aniCT). This can be explained on the first hand by the complex geometry of the skull base. It has been shown that the determination of well-defined skull conductivity tensors requires a smooth surface in order to obtain the radial skull anisotropy directions [Marin et al., 1998, Wolters et al., 2006]. In the case of Model 2, the complex surface of the skull base might result in tensors that do not accurately represent the geometry of this part of the skull. On the other hand, the conductivity value used for the isotropic model was the same as the radial conductivity of the anisotropic model ($\sigma_{\mathrm{iso}} = \sigma_{\mathrm{rad}} = 0.0105$ S/m), justified by the preponderance of radial over tangential conductivity [Vallaghé and Clerc, 2009].

In a second group of models, the skull was segmented solely from the MR images. Here, models 4 and 5 both had a layered skull, consisting of compact and spongy bone, that was differently segmented. For Model 4 (refMR) the spongy bone was obtained through thresholding of the MR image, while for Model 5 (layMR) it was approximated as an erosion of the compact bone. Models 6 and 7 used a single compartment for the skull but the conductivity was approximated as either anisotropic or isotropic, respectively. For all MR-based skull models, large errors at

the skull base were observed, mainly due to the large differences in the basal region between the models with MR-based skulls and the skull of the reference model (see Figure 5.7).

The MR-based skull models led to approximately the same average localization errors of around 8 to 9 mm in the noiseless case. This is a very important finding because in clinical practice the head model is usually segmented solely from MR images. Therefore, the clinicians should keep in mind that the dipole localization error made by not correctly modeling the geometry of the skull is already close to one centimeter. In addition, the error was asymmetric and depended greatly on segmentation inaccuracies, potentially (dis)favoring a particular brain region.

Contrary to the results for the CT-based skulls, in the case of MR-based skulls one of the models with isotropic heterogeneous skull (Model 5 – layMR) presented the second largest average error. Nevertheless, the average error is not the only way to determine how good a model is. By examining the noiseless cumulative histogram of Figure 5.6b it can be seen that, with 128 electrodes, Model 5 was better than the homogeneous models for more than half of the dipoles. However, the overall mean was lowered by large errors generated at the brain basal and superficial regions, due to the skull spongiform layer that was overestimated in the base and underestimated in the cranial vault.

Another disagreement between the results for CT- and MR-based skulls, is seen for the anisotropic models. Model 2 (aniCT) yielded the largest mean DLE for the CT-based skulls, while Model 6 (aniMR) was among the best MR-based models. Although this might seem contradictory, the difference can be explained by the geometry of the skull base. While Model 2 has a very complex geometry, which explains why the anisotropic tensors were not so well defined for this area, Model 6 has much more simplified geometry at the skull base and therefore the tensors can better represent the conductivity. Dannhauer et al. [2011] found that the use of anisotropy to account for the layered surface of the skull did not yield a significant improvement in the dipole estimation. In our results, although using anisotropy yielded lower localization errors for the MR-based models, the difference between anisotropic (Model 6) and isotropic (Model 7) homogeneous models was not great (~ 0.5 mm) according to Figure 5.10, for the noiseless case in all brain lobes.

Huiskamp et al. [1999] performed a simulation study in which the effect of using head geometry based on MR images could be compared with the geometry based on CT. They generated four models with the inner and

outer surfaces of the skull segmented in different ways. This study found that for a central (fronto-parietal) source the use of actual geometry, as extracted from CT, would not decrease much the localization errors. However, localization of mesial-temporal and basal frontal sources using realistic geometry based on MR was far less accurate. These findings are in agreement with the results shown in Figure 5.10, and with the fact that the complex geometry of the skull basal region is a key point in the construction of realistic head models for ESI, which is also concordant with the conclusions of Lanfer et al. [2012].

It is well known that the cranial vault can be reasonably well segmented from MR or CT imaging modalities. Nevertheless, for the skull base, advanced segmentation methods are required due to the presence of many irregularities in the bone structure as well as the air cavities. The accurate modeling of the skull is important in order to achieve reliable ESI results that are useful in a clinical environment. CT imaging is preferred to image the complex geometry of the skull. However, CT images should not be acquired with the only purpose of improving skull modeling for ESI. If CT images were measured for other purposes (e.g., for localization of depth electrodes), and their quality was high, then these data might also serve for improving skull modeling for the EEG forward problem.

While only T1-weighted MR images have been used in this examination, other authors have used T1- and T2-weighted [Dannhauer et al., 2011, Güllmar et al., 2010, Rullmann et al., 2009] or T1- and PD-weighted MRI [Akalin-Acar and Gençer, 2004, Lew et al., 2009a, Steinsträter et al., 2010, Wolters et al., 2006] for improving MR-based skull modeling. Also, as recently described by Lucka et al. [2012], T1-weighted pulse sequences with fat suppression can be well combined with T2-weighted pulse sequences with minimal water-fat shift to allow improved segmentation of head tissues for source analysis. Although the use of this approach is a good alternative to CT imaging for correctly delineating the skull, fat suppression is needed in the T1-weighted image to avoid that tissues containing fat lead to erroneous segmentation results due to the fat-shift. In addition, the use of T2-weighted MRI to improve modeling of the skull base and air cavities has, to the best of our knowledge, not yet been examined. Another possible alternative to CT imaging for the segmentation of the skull base is the use of MR images with UTE (Ultrashort Echo Time) sequences.

The study of the sensitivity to measurement noise of the different mod-

els showed that the dipole estimation errors are large for high noise levels (see Figure 5.10 and Table 5.3). The accuracy of the model becomes more important for lower noise levels. In a very noisy environment, as the one depicted by SNR = 0 dB, the choice of a particular model is not relevant as all the models have approximately the same DLE and DOE. However, the use of a higher spatial sampling density considerably reduces the DLE ($\sim$ 32 mm). For a SNR of 5 dB, typical for real EEG signals, when a higher number of electrodes is used the model choice becomes more important and the DLE improves $\sim$ 10 mm for all the models. If a SNR of 10 dB is used, characteristic of an averaged epileptic spike, the importance of accuracy in the model becomes greater and the improvement in the DLE due to the use of a higher spatial sampling density is $\sim$ 3 mm. These results are in concordance with the work of Ryynänen et al. [2006], who confirmed that there is greater advantage to be obtained with increased spatial sampling density (more electrodes) at realistic noise levels, if the skull-to-soft tissue conductivity ratio is lower than the commonly used value of 80, as was the case in our study.

5.5   Conclusions

In this study we investigated the dipole localization and orientation errors due to different skull modeling approaches in ESI. The influence of different segmentations of the compact and spongy bone compartments out of CT images as well as solely based on MR images was studied. CT-based skulls give a very precise representation of the skull geometry, especially of the base which is a key part of the skull that needs to be modeled as accurate as possible. When CT-based skull models were used, the results indicated that isotropic heterogeneous conductivity led to lower localization errors compared to anisotropic or isotropic homogeneous conductivity. In addition, we have shown that the spongy layer of the skull can be approximated as an eroded version of the compact layer (as in Model 1). In this way, the segmentation process becomes more straightforward. The alterations of the skull geometry in the MR-based models certainly increased the localization errors. In general, the geometry had a larger effect on the average localization error compared to the conductivity modeling. MR-based methods did not represent the skull base adequately, leading to average dipole estimation errors of approximately one centimeter. Therefore, advanced segmentation or advanced MR techniques are needed to better segment the base (bottom part) of

the skull.

Comparing the results obtained with 32 and 128 electrodes, we found that increasing the spatial resolution led to an improvement in the results (~ 10 mm in mean DLE), when the noise level of a realistic EEG signal was used. This is important in a clinical environment where a low spatial sampling density for the electrodes is commonly used. In order to use ESI in a clinical environment, the following guidelines should be taken into account for the generation of subject-specific head models: (i) If there are CT images available, i.e., if the geometry of the skull and its different tissue types can be accurately obtained, the conductivity should be modeled as isotropic heterogeneous in which the spongy bone can be approximated as an erosion of the compact bone compartment; (ii) when only MR images are available, the base of the skull should be segmented as accurately as possible, modeling the conductivity as isotropic heterogeneous with the spongy bone segmented directly from the MR image; (iii) the use of high spatial sampling density can diminish the dipole localization errors approximately 10 mm, for realistic noise levels.

5.6   Contributions

This study has been presented at the *18th International Conference on Biomagnetism (BIOMAG)* [Montes-Restrepo et al., 2012] and at the *35th Annual International Conference of the IEEE Engineering in Medicine and Biology Society (EMBC)* [Montes-Restrepo et al., 2013b]. The results have been published in the A1 journal *Brain Topography* [Montes-Restrepo et al., 2014].

Chapter 6

The role of skull modeling in ESI for patients with refractory temporal lobe epilepsy

*An experiment is a question which science poses to Nature, and a
measurement is the recording of Nature's answer*
—Max Planck

This chapter presents a study about the influence of skull modeling
on ESI, using data of six patients with refractory temporal lobe epilepsy
who later underwent surgery. For each patient, CT and MR images
were available. The skull was modeled based either on the individual
CT or MRI or on a CT-template warped to the individual space. The
irritative zone was estimated in each patient using interictal epileptiform
discharges scored in the EEG. The localization was compared with the
resection that rendered the patient seizure free. The chapter is organized
as follows: In Section 6.2, the clinical characteristics of the patients, the
construction of realistic FDM head models and the source localization
methodology are presented. Section 6.3 presents the source estimations
performed on each of the patient-specific head models. The analysis is
accomplished using averaged and single spikes at the half-rising phase
and peak of the spike. In Section 6.4, the advantages and disadvantages
of averaged versus single spike localization at each t_{spike} (half-rising and
peak) are explained, followed by the limitations of the study.

6.1   Introduction

The presurgical evaluation of refractory epilepsy patients is a process
that assesses whether the patients can benefit from epilepsy surgery
treatment. It consists of multiple examinations aimed at identifying
the region in the brain that generates the epileptic seizures, the so-called
epileptogenic zone (EZ) [Rosenow and Lüders, 2001]. The resection of
the EZ is sufficient and necessary to render a patient seizure-free after
surgery. In the presurgical evaluation, data from seizure semiology, neu-
ropsychological assessment, magnetic resonance imaging (MRI), long-
term scalp video/electroencephalography monitoring (SVEM), positron
emission tomography (PET), single photon emission computed tomogra-
phy (SPECT) and magnetoencephalography (MEG) help to determine
the EZ and its proximity to the eloquent cortex.

Electroencephalographic source imaging (ESI) is a highly valuable tool
in the presurgical evaluation of epilepsy to localize the irritative zone
[Brodbeck et al., 2011, Kaiboriboon et al., 2012, Plummer et al., 2008].
The irritative zone is the brain region that causes the interictal epileptic
discharges visible in the EEG [Rosenow and Lüders, 2001]. For the
accurate estimation of sources from the electroencephalogram (EEG),
the use of realistic and individual head models has become increasingly
important [Rullmann et al., 2009, Vorwerk et al., 2014, Ziegler et al.,
2014]. In realistic volume conductor models, the skull plays a crucial
role because of its complex geometry and low conductivity compared to
the other tissues inside the head [Dannhauer et al., 2011, Lanfer et al.,
2012, Montes-Restrepo et al., 2014]. The anatomical structure of the
skull is three-layered, consisting of a spongy bone layer surrounded by
two compact bone layers. Thicknesses and resistivities of these layers are
not uniform throughout the skull structure [Law, 1993]. Air-filled cavities
such as the paranasal sinuses are also part of this complex structure.

Soft tissues like the scalp and the brain can be correctly segmented
from T1-weighted MR images of the patient's head. For the bone tissue,
X-ray computed tomography (CT) is the preferred modality to image its
structure, but at the expense of exposing the patient to a dose of ionizing
radiation. As a consequence, CT imaging should not be performed with
the sole purpose of segmenting the skull [Huiskamp et al., 1999, Montes-
Restrepo et al., 2014].

Commonly used alternatives to improve the segmentation of the skull
comprise T2- and proton density (PD)-weighted MR images [Lew et al.,

2009a, Rullmann et al., 2009]. Although these sequences allow for the correct delineation of the inner skull surface, they do not add information about the geometry of the skull base and of the air-filled cavities. MRI with Ultrashort Echo Time (UTE) sequences [Robson et al., 2003] is another option to model the skull but it is currently not included in the clinical MRI protocol of epilepsy patients. The use of a CT-template [Rorden et al., 2012] inversely normalized to the subject space could be another possibility for the precise representation of the skull. To our knowledge, the application of such a skull template in ESI has not been reported in literature.

In this work we analyze the influence of different skull modeling approaches on ESI, using data of six patients with refractory temporal lobe epilepsy who underwent epilepsy surgery. For these patients, high-resolution CT images, pre- and postoperative MR images as well as 27-channel EEG with marked interictal epileptiform discharges, are available. These matched data sets allow us to analyze the influence of using the skull geometry segmented from CT compared to the geometry segmented from the MRI or from the warped CT-template, on the localization of the irritative zone. Four realistic head models with different skull compartments, based on finite difference methods [Hallez et al., 2005], are constructed for each patient: (i) Three of the models contain skulls with compact and spongy bone compartments as well as air-filled cavities that are segmented from either CT, MRI or a CT-template and (ii) one of the models includes a MRI-based skull with a single compact bone compartment. The estimated sources for each model are then validated against the resected area, as indicated by the postoperative MRI. To analyze at which time point the irritative zone localization lies closer to the resected zone, ESI is performed at two time points within the spike (t_{spike}): half-rising phase [Lantz et al., 2003b] and peak [Huppertz et al., 2001]. While averaging can improve the signal-to-noise ratio (SNR) of the epileptiform discharges, few studies have examined the clinical importance of single versus averaged spike selection in ESI [Bast et al., 2006, Chitoku et al., 2003, Plummer et al., 2010]. Therefore, we investigate the dipole estimation using single versus averaged spike analysis on the proposed models. The main goal of this study is to determine how accurate the skull should be modeled in order to localize the irritative zone of patients with refractory temporal lobe epilepsy, using standard clinical EEG (with low spatial sampling density).

6.2   Methods

6.2.1   Patient data

6.2.1.1   Inclusion criteria

For this study, the patients were selected from the database of the Reference Center for Refractory Epilepsy at Ghent University Hospital (Belgium), matching the following criteria: (1) refractory temporal lobe epilepsy; (2) presurgical evaluation with MRI, CT and scalp video-EEG monitoring (SVEM); (3) surgical resection of the presumed epileptogenic zone; and (4) seizure free after the surgery (Engel class I outcome [Engel et al., 1993], $n = 5$) or with a decrease of seizures $> 80\%$ (Engel class II outcome, $n = 1$) during a minimum follow-up of 2 years. Table 6.1 presents an overview of the clinical characteristics of the patients used in this study. The study was approved by the Ethics Committee 2014/0750 from Ghent University Hospital with registration number B670201421775.

6.2.1.2   MRI and CT data

As part of the presurgical evaluation, MRI scans were performed in all patients. The T1-weighted MR images were acquired on a 3T scanner (Siemens Trio, Erlangen, Germany) with the MP-RAGE protocol and consisted of a matrix of 256×256 with 176 sagittal slices. For patients 1, 3, 4 and 6 the images were acquired with a repetition time (TR) of 2530 ms, an echo time (TE) of 2.6 ms, and a voxel size of 0.9 mm $\times$ 0.86 mm $\times$ 0.86 mm. For patient 2, the MR images were acquired with TR = 1550 ms, TE = 2.3 ms, and voxel size of 1.0 mm $\times$ 0.98 mm $\times$ 0.98 mm. For patient 5, the parameters were TR = 2530 ms, TE = 2.5 ms, and voxel size of 0.9 mm $\times$ 0.94 mm $\times$ 0.94 mm.

Preoperative high-resolution CT images were available for the same patients. The CT images (Toshiba Aquilion, Tokyo, Japan) were co-registered and re-sliced to the MR images, resulting in a CT image of dimension $256 \times 256 \times 176$ with the same voxel size as the corresponding MR image. The scalp electrodes used during SVEM were on the patient's head at the moment of acquisition and were therefore visible in the CT images.

Table 6.1: Clinical characteristics of the patients used in this study.

Pt. #	Gndr	Age (Sx)	Epilepsy type	Ictal EEG	Interictal EEG	MRI findings	Surgery	Surgical outcome	Follow-up (years)
1	F	40	CPS without secondary generalization smacking and swallowing, subtle automatisms with both hands and postictal naming disorder	L FT rhythmicity theta activity	L FT slow sharp waves, sometimes spikes and sporadically spike and waves	L hippocampal sclerosis	L selective amygdalohippocampectomy	Engel I	3
2	F	63	CPS with possible secondary generalization chewing movements, deviation of head to the R, tonic opening of mouth with head and eyes deviated to the R, dystonic posturing of the R arm, L arm in flexion, tonic extension of the L and shortly afterwards the R arm, head to the midline, clonic phase with generalized convulsions	L FT rhythmicity slow discharge	L FT spikes and spike and waves	Lesion in the L amygdala	L selective amygdalohippocampectomy	Engel I	4
3	F	24	CPS without secondary generalization aura, sometimes the patient realizes to have had a seizure and is confused without remembering what happened, sometimes automatisms of both hands and swallowing automatisms with amnesia	Bilateral FT sometimes more pronounced on the R, sometimes on the L	R FT spikes and subclinical run of rhythmic sharp activity L T	Lesion in the R A I T gyrus	R A T lobectomy including lesionectomy and amygdalohippocampectomy	Engel I	4
4	F	41	CPS with possible secondary generalization aura (epigastric rising sensation), anxiety and dizziness, speech disorder, impaired contact with environment, motionless stare, head version to the L	R FT rhythmicity	R FT monomorphic delta activity and R FT spike and waves	R hippocampal sclerosis and an old ischemic lesion in the R O lobe	R selective amygdalohippocampectomy	Engel II	3
5	M	35	CPS without secondary generalization smacking and L hand automatisms	L FT rhythmicity	L FT spikes	Lesion in the A neocortex over the L I T gyrus	L T lesionectomy	Engel I	4
6	M	30	CPS with possible secondary generalization elevation of the L arm, followed by automatisms of the L hand, tonic trunk, tonic L leg, oral automatisms with smiling, vocalization, postictal confusion and speech disturbance	No lateralization in several seizures after 15s ED at the R hemisphere, in one seizure ED on L side	Independent L FT and parasagittal spikes and R FT spikes	Lesion in the L I T gyrus	L T lesionectomy	Engel I	2

CPS – Complex Partial Seizures, L – Left, R – Right, FT – Fronto-Temporal, T – Temporal, O – Occipital, A – Anterior, I – Inferior, ED – Epileptiform Discharges

Postoperative MR images were available for all the patients. For patients 1 and 2, axial T1-weighted postoperative MRIs were available. Patients 3 and 5 had T1-weighted postoperative MR images with the same resolution as the preoperative MRI. For patients 4 and 6, T2-weighted postoperative MRIs were available acquired in axial and coronal planes, respectively.

6.2.1.3 Electroencephalographic recordings

The EEG was recorded using a video-EEG monitoring system of Micromed (Italy) at a sampling frequency of 256 Hz. In addition to the 21 International 10-20 System electrode placements, three supplementary inferior temporal electrodes (respectively zygomatic, F9-F10; preauricular, T9-T10; and mastoid, Tp9-Tp10 positions) were placed on each side of the scalp, resulting in a total of 27 electrodes [Boon et al., 2002]. EEG data were recorded to a common reference electrode on the mastoid usually contralateral to the spike focus. During several consecutive days, interictal and ictal EEG as well as time-locked video were recorded for each patient. Video-EEG monitoring was used to document partial seizures with or without secondary generalization in all the patients (see Table 6.1).

6.2.1.4 Selection of interictal epileptiform discharges

Interictal EEG can show interictal epileptiform discharges (IEDs) that define the irritative zone [Rosenow and Lüders, 2001]. Spikes with similar morphology and surface voltage distribution were identified and marked by one of the authors (E.C.) experienced in clinical EEG reading. For the selected spikes per patient, the peak was pinpointed at the electrode showing maximum amplitude in the referential montage. Epochs of 200 ms before and 300 ms after the spike peak were selected. Afterwards, the spikes were average referenced. The procedure was performed using the BrainVision Analyzer 2.0 software (Brain Products, Germany).

6.2.2 Head model construction

The generation of the different head models involves two main steps: (i) The MRI-based segmentation of the tissues inside the head model with SPM and (ii) the incorporation of the skull compartments segmented either from MRI, CT or a CT-template into the head model. In the

following subsections the rationale behind the constructions of the head models is explained.

6.2.2.1   MRI-based segmentation using SPM

The MR images were segmented using a probabilistic segmentation routine as implemented in the Segment function of the SPM12 toolbox (an extension of Unified Segmentation [Ashburner and Friston, 2005]). In the Segment routine, each voxel is assigned the probability of belonging to a particular tissue class based on its intensity and a prior probability distribution of different tissue types, i.e., the Tissue Probability Map (TPM). The default TPM provided by SPM12 contains six tissue types: gray matter (GM), white matter (WM), cerebrospinal fluid (CSF), skull, scalp and air.

The Segment function resulted in a probability distribution for each voxel indicating the likelihood of belonging to a specific tissue type. For each voxel, this probability distribution sums to one. The subsequent modeling with the finite difference method (FDM) requires a binary mask for each tissue. Therefore, the voxels were assigned to the compartment for which they had the highest probability. In this way, initial masks for each tissue class are generated. These masks present errors as a result of image noise and low contrast in the original image. Hence, they are further refined following the procedure explained below:

Scalp mask: The scalp mask is improved by selecting the largest connected component followed by the morphological operations: hole filling, dilation with hole filling and erosion over the original scalp mask. The corrected scalp mask is required to remove spurious voxels outside the scalp.

Skull mask: Because the probability distribution of the skull does not include the spongy bone voxels, the resultant skull has internal holes. Consequently, the skull is post-processed to obtain a uniform compartment. This is achieved by selecting the largest connected component followed by the morphological operations: closing, bridging of unconnected voxels and hole filling over the original skull compartment.

Brain mask: The brain mask was extracted using the *Imcalc* function of the SPM toolbox. It consisted of the addition of GM as $i1$, WM as $i2$ and

CSF as $i3$ and its posterior thresholding: $(i1+i2+i3) > 0.8$. Afterwards, the largest connected component was selected and holes inside the mask were filled.

Spongy bone mask: The skull mask was cut along the axial plane at a distance of 40 mm below the occipital hole, using a dilated brain mask [Lanfer et al., 2012]. Posteriorly, the skull mask was eroded five times with a 3×3 cross-shaped structuring element. The spongy bone compartment was not directly segmented from the MRI because these images were not acquired with fat suppression, therefore meaning that the spongy bone is shifted upwards.

Internal air mask: The internal air mask was obtained by using the scalp mask to separate internal from external voxels of air. The internal air was median filtered to remove small internal holes and obtain a homogeneous surface.

CSF mask: A CSF layer was ensured between gray matter and skull, to avoid CSF discontinuities [Huang et al., 2013].

6.2.2.2 Head models

The head models used in this study were: Three models with seven compartments *MRI_ 7c*, *CT_ 7c* and *Tmp_ 7c*, as shown in Figure 6.1 for patient 1, and one model with five compartments *MRI_ 5c*. The isotropic conductivity values used for these head models are presented in Table 6.2. These values were compiled from the literature and measured with respect to the core body temperature of 37°C, except for the compact and spongy bone conductivities which were measured at 22°C [Akhtari et al., 2002]. As the normal temperature of the skull is higher in subjects, using the reported compact and spongy bone conductivities at 22°C is a limitation of our study. However, we assume that the variation of the skull conductivity values caused by temperature difference does not have a large effect on the result.

Model MRI_7c: This model uses the segmented skull based on MRI, as described in Section 6.2.2.1. The MRI and its resulting head model are shown in Figure 6.1a.

Table 6.2: Conductivities in S/m for the head models with seven ($\_7c$) and five ($\_5c$) compartments. // indicates that the tissue was not taken into account in the model.

Tissue		Models_7c	Model_5c
■	Scalp	0.3333 [Gonçalves et al., 2003a]	0.3333
■	Compact b.	0.0068 [Akhtari et al., 2002]	0.0105 [Dannhauer et al., 2011]
■	Spongy b.	0.0298 [Akhtari et al., 2002]	//
■	Air cav.	0.0000 [Haueisen et al., 1995]	//
■	CSF	1.7857 [Baumann et al., 1997]	1.7857
■	WM	0.1428 [Haueisen et al., 1995]	0.1428
■	GM	0.3333 [Haueisen et al., 1995]	0.3333

(a) MRI and MRI-based head model – Model *MRI_7c*

(b) MRI with overlaid CT (in *red*) and head model with CT-based skull – Model *CT_7c*

(c) MRI with overlaid template (in *red*) and head model with Template-based skull – Model *Tmp_7c*
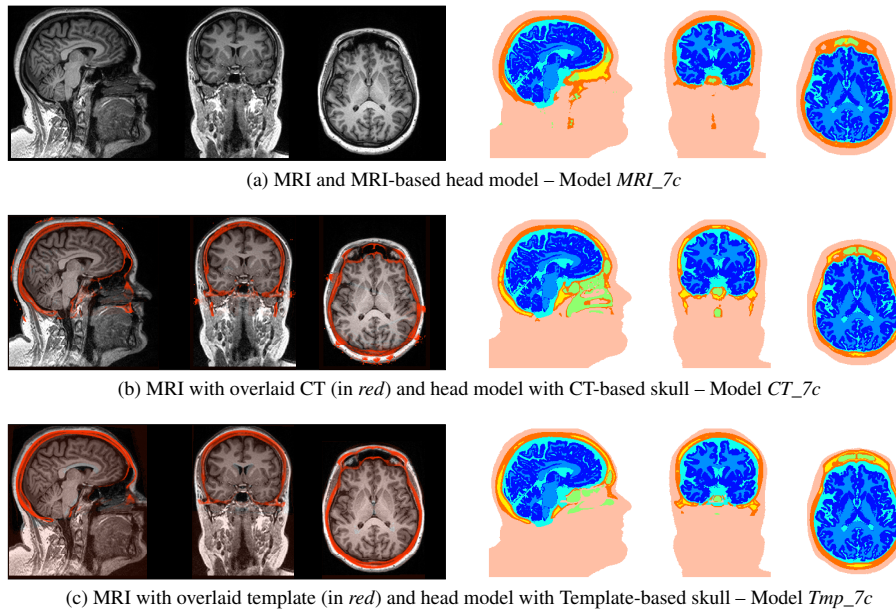
Figure 6.1: MRI of patient 1 with combined modalities for skull segmentation (left column). The head models on the right column show seven different tissue types: ■ Scalp, ■ Compact bone, ■ Spongy bone, ■ Air cavities, ■ CSF, ■ WM and ■ GM.

Model MRI_5c: This model is a simplification of model *MRI_7c* in which the spongy bone and the air cavities are modeled as compact bone by assuming a single conductivity for the whole skull compartment.

Model CT_7c: The CT images were thresholded to differentiate between compact and spongy bone as well as air cavities. The approximate intensities of air and bone tissues for a calibrated CT scan were selected as described in [Rorden et al., 2012]. Due to the existence of metal artifacts caused by electrodes during the CT image acquisition, manual correction of the segmented skull was required. The MRI with overlaid CT as well as the head model with the CT-based skull are depicted in Figure 6.1b.

Model Tmp_7c: A high-resolution CT-template constructed from high-resolution CT scans of 30 individuals was used [Rorden et al., 2012]. Because the template is in the MNI space, it has to be transformed to the individual subject space to be able to combine it with the MRI of the individual patient. To achieve this, the inverse deformation field, obtained as an output of the Segment function of SPM12, is applied to the CT-template to transform the CT-template into the subject space. Figure 6.1c shows the MRI with overlaid CT-template and the segmented head model with Template-based skull.

6.2.2.3   Electrode segmentation

For all the models, the real electrode positions were segmented from the CT image. A shrunk scalp mask was first applied to the CT image in order to remove the skull. Then, a clustering method was used to find the centroid of the electrodes. The weighted center of gravity of each voxel cluster was assigned as an electrode position. Posteriorly, these voxels were projected onto the scalp to ensure that they were in contact with the head model. Finally, they were manually labeled and ordered according to the setup used at the Ghent University Hospital, with 27 electrodes.

6.2.3   EEG source imaging

6.2.3.1   Forward problem

The relationship between the electrode potentials $\mathbf{V}_{\text{model}} \in \mathbb{R}^{m \times 1}$ (m being the number of electrodes), the dipole location, $\mathbf{r} = (x, y, z)^T \in \mathbb{R}^{3 \times 1}$, and the dipole moments, $\mathbf{d} = (d_x, d_y, d_z)^T \in \mathbb{R}^{3 \times 1}$, can be expressed as

follows:

$$\mathbf{V}_{\text{model}}(\mathbf{r}, \mathbf{d}) = \mathbf{L}(\mathbf{r}) \cdot \mathbf{d}, \tag{6.1}$$

where $\mathbf{L}(\mathbf{r}) \in \mathbb{R}^{m \times 3}$ is the lead-field matrix for a dipole at location $\mathbf{r}$.

The calculation of the forward problem in this study was carried out with the FDM with reciprocity [Hallez et al., 2005, Vanrumste et al., 2001]. The accuracy of the forward solver has been validated with respect to other inverse methods [Strobbe et al., 2014] and in combination with other methodologies such as subspace electrode selection [Crevecoeur et al., 2012] and ESI on neonates [Despotovic et al., 2013].

In this work, we used 27 electrode positions according to the setup used at the Ghent University Hospital as explained in subsection 6.2.1.3. The calculation grid of the FDM consisted of up to 7,307,914 nodes for each head model. The time required to compute the forward matrix was approximately 30 minutes per electrode pair using one core of a Dual Intel Xeon CPU E5-2670 octo-core processor (2.6 GHz, 20 MB L3 cache).

6.2.3.2   Inverse problem

The inverse problem was solved by performing a dipole scan on the gray matter surface, the so-called least-squares scanning or goal function scan (GFS) [Knösche, 1997, Mosher et al., 1992]. At each position, an optimal rotating dipole is computed for the considered location [Rullmann et al., 2009]. The cost function was the RRE,

$$\text{RRE} = \frac{\|\mathbf{V}_{\text{in}} - \mathbf{V}_{\text{model}}(\mathbf{r}, \mathbf{d})\|_2^2}{\|\mathbf{V}_{\text{in}}\|_2^2},$$

where $\mathbf{V}_{\text{in}} \in \mathbb{R}^{m \times 1}$ is the set of measured electrode potentials and $\mathbf{V}_{\text{model}}(\mathbf{r}, \mathbf{d})$ is the set of electrode potentials calculated by solving the forward problem (6.1) in the studied head models, respectively.

The GFS is not subject to the difficulties of non-linear search algorithms, such as being trapped in local minima or slow convergence. Additionally, areas of similar RRE can serve as confidence volumes [Knösche, 1997].

Once the RRE at all the locations is obtained, the dipole position with the minimum RRE value is selected as the estimated dipole. Then, the

goodness of fit (GOF) of the estimated dipole is computed as GOF = $1 - \mathrm{RRE}$ and expressed as a percentage.

6.2.3.3 Source localization using the averaged spike

Averaging optimizes the SNR of the spikes and suppresses background noise, thereby enhancing the stability and reliability of dipole analysis [Bast et al., 2006, Chitoku et al., 2003]. Using the IEDs selected as explained in section 6.2.1.4, an average of all the spikes per patient was constructed. The half-rising phase of the spike peak t_{half} was chosen as halfway from spike onset to spike peak of the averaged spike [Lantz et al., 2003b]. Figure 6.2 shows the averaged epileptic spikes in a bipolar montage and the time points t_{half} and t_{peak} used in this study. The number of spikes included in the average (N) and the electrode used to mark the spikes are shown at the bottom.
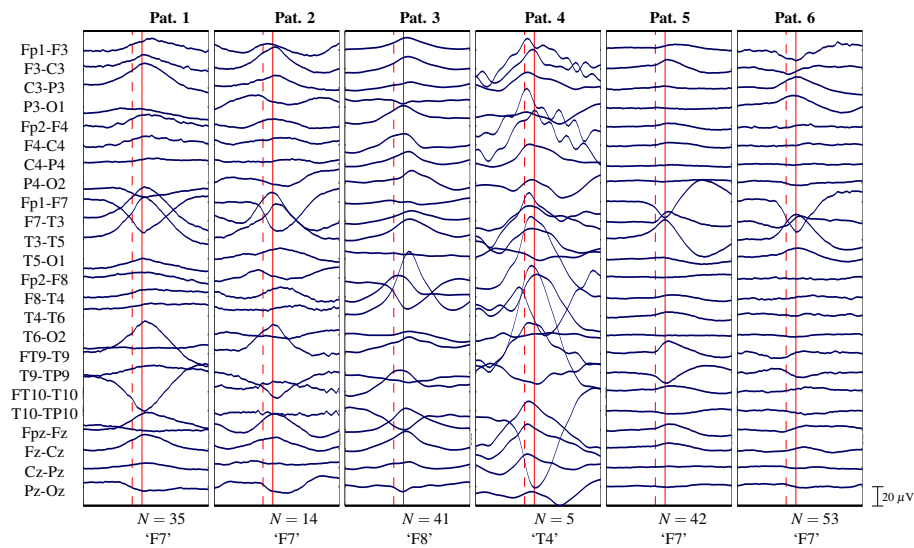
Figure 6.2: Averaged epileptic spikes for patients 1 to 6. The red vertical lines indicate the two time instants: half-rising phase ($t_{half} = -15.6$ ms, dashed line) and peak ($t_{peak} = 0$ ms, solid line) of the spike. N corresponds to the number of spikes used in the average and the last row shows the electrode used to mark the spikes.

6.2.3.4 Source localization using single spikes

Localizations from single spikes may provide more information about the focality of the irritative zone [Chitoku et al., 2003]. The inverse problem was solved for each spike per patient. Afterwards, the centroid of the dipole estimations was computed using two different procedures as explained below.

1. *Mean of selected dipoles:* Following the procedure of source reconstruction presented in [Aydin et al., 2014], the estimated dipoles with GOF $\geq 80\%$ were selected. Then, the centroid position and the distances of each selected dipole to the centroid were calculated. After determining the mean μ_0 and standard deviation σ_0 of these distances, dipoles with a distance to the centroid greater than $\mu_0+2\sigma_0$ were excluded. The final centroid was then calculated based on the remaining dipoles.

2. *Minimum of the mean RRE map:* The maximum of the mean GOF map or minimum of the mean RRE map was computed. Maps with minimum RRE $\leq 20\%$ were averaged to compute the mean RRE map $\mathbf{M}_{\mathrm{RRE}}$. Subsequently, the voxel of $\mathbf{M}_{\mathrm{RRE}}$ with minimum RRE was selected as the centroid position and the confidence volume was computed using the surfaces with RRE values within 5% from the minimum. The GOF of the centroid corresponded to GOF $= 1 - \min\{\mathbf{M}_{\mathrm{RRE}}\}$.

6.2.3.5 Distance to the resected zone

The distance to the resection area was measured to see how the complexity of the head model influences the dipole estimation. For this, the Euclidean distance between the estimated dipole and the nearest point belonging to the resected zone was computed. The resected zone was manually segmented based on the postoperative MRI of the patient.

6.2.3.6 Inter-model distance

Euclidean distance was measured between the dipole estimations obtained with the averaged spike analysis. The inter-model distance was computed between each pair of models: *MRI_7c/MRI_5c, CT_7c/MRI_7c, CT_7c/MRI_5c, CT_7c/Tmp_7c, MRI_7c/Tmp_7c* and *Tmp_7c/MRI_5c*.

6.2.3.7   Statistical analysis

We used the Student's t-test to evaluate differences between dipole estimations for each model. An unpaired $t-$test was carried out on the results of the single spike analysis. Statistical analysis was performed using Matlab (The MathWorks, Inc., Natick, Massachusetts, United States). Values of $p \leq 0.05$ were considered significant.

6.3   Results

6.3.1   Source localization using the averaged spike

In this section the results of the dipole estimations at t_{half} and t_{peak} of the averaged spike, using head models MRI_7c (green), MRI_5c (magenta), CT_7c (red) and Tmp_7c (blue), are presented. The spike is averaged according to the procedure presented in subsection 6.2.3.3.

6.3.1.1   Distance to the resected zone

Figure 6.3 displays the source localization results on the postoperative MRI of the patient at the half-rising phase and peak of the averaged spike. The number of spikes in the average (N), goodness of fit (GOF) and distance to the resection (D) are also shown. It can be seen that patients 1 and 2 presented a similar trend in their distances to the resected zone, being the largest for either model MRI_7c or MRI_5c, and the smallest for model Tmp_7c. For patient 3, the dipole estimations lay inside the resection for all the models at t_{half} and t_{peak}, with the exception of model CT_7c at the peak. No conclusive results were given by patients 5 and 6, in which all the models estimated dipoles with substantially higher distances to the resection compared to the other patients. Patient 4 presented the closest estimation to the resected zone for both MRI-based models (MRI_5c and MRI_7c); however, as a result of the low number of spikes available for this patient ($N = 5$) and because this patient had an Engel class II outcome (see Table 6.1), these results should be approached with caution.

Figure 6.4 shows a bar diagram of the distances to the resected zone of the dipole estimations for the analyzed models, using the averaged spike. The mean distances to the resection in millimeters at the half-rising phase of the spike were 10.09, 10.06, 10.09 and 7.88 for models MRI_7c, MRI_5c, CT_7c and Tmp_7c, respectively. At the peak of

Figure 6.3: Dipole estimation for patients 1 to 6 at **(a)** t_{half} and **(b)** t_{peak} of the averaged spike, with N = number of spikes. The resected zone is delineated in yellow over the postoperative MRI. The slice shown corresponds to the average of the dipole estimations for models ⬤ *MRI_ 7c*, ⬤ *MRI_ 5c*, ⬤ *CT_ 7c* and ⬤ *Tmp_ 7c*.
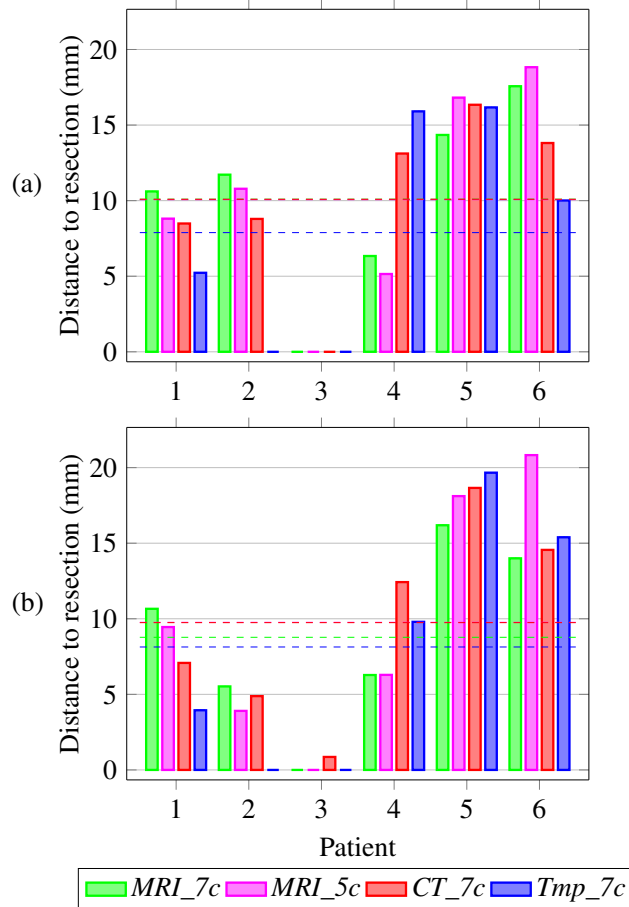
Figure 6.4: Distance to the resected zone of the dipoles estimated at **(a)** t_{half} and **(b)** t_{peak} of the averaged spike. The dashed horizontal lines indicate the mean over all patients for each model.

the spike the mean distances in millimeters were, in the same order, 8.77, 9.76, 9.74 and 8.13. This indicates that the mean distance to the resected zone was ≈ 1 cm for all the models, both at the half-rising phase and peak of the averaged spike. No significant differences between the models were observed. Over all patients, model *Tmp_7c* presented the lowest mean distance to the resected zone at both t_{half} and t_{peak}.

6.3.1.2 Inter-model distance

Table 6.3 presents the inter-model distances in millimeters at the half-rising phase and peak of the averaged spike, computed as explained in subsection 6.2.3.6. We observed a trend from lowest to largest mean intra-model distance as follows: (i) intra-modality (D_{MRI_7c/MRI_5c}), (ii) subject-specific inter-modality (D_{CT_7c/MRI_7c} and D_{CT_7c/MRI_5c}) and (iii) warped-template or not subject-specific inter-modality (D_{CT_7c/Tmp_7c}, D_{MRI_7c/Tmp_7c} and D_{Tmp_7c/MRI_5c}).

Table 6.3: Inter-model distances in mm at **(a)** t_{half} and **(b)** t_{peak} of the averaged spike. The final column shows the mean ± standard deviation across patients.

t_{spike}	Inter-model distance	Patient						$\mu \pm \sigma$
		1	**2**	**3**	**4**	**5**	**6**	
(a)	D_{MRI_7c/MRI_5c}	3.7	1.4	1.8	1.9	2.6	2.0	**2.2 ± 0.8**
	D_{CT_7c/MRI_7c}	6.9	9.8	0.9	14.5	3.2	7.0	**7.1 ± 4.8**
	D_{CT_7c/MRI_5c}	6.5	8.9	2.0	15.2	1.9	6.9	**6.9 ± 5.0**
	D_{CT_7c/Tmp_7c}	4.0	13.0	7.9	13.9	3.7	4.1	**7.8 ± 4.7**
	D_{MRI_7c/Tmp_7c}	10.4	20.9	8.8	24.2	2.2	9.7	**12.7 ± 8.3**
	D_{Tmp_7c/MRI_5c}	9.1	19.8	9.3	24.0	1.9	10.3	**12.4 ± 8.0**
(b)	D_{MRI_7c/MRI_5c}	3.0	5.8	2.8	4.0	2.0	7.1	**4.1 ± 1.9**
	D_{CT_7c/MRI_7c}	6.1	7.0	3.2	14.7	3.3	5.1	**6.6 ± 4.3**
	D_{CT_7c/MRI_5c}	5.2	5.7	3.0	18.7	1.9	8.9	**7.2 ± 6.1**
	D_{CT_7c/Tmp_7c}	5.0	13.3	8.8	12.2	5.8	1.5	**7.8 ± 4.5**
	D_{MRI_7c/Tmp_7c}	10.8	16.2	8.1	18.5	4.7	4.2	**10.4 ± 5.9**
	D_{Tmp_7c/MRI_5c}	9.3	16.0	8.1	21.6	4.1	7.6	**11.1 ± 6.5**

6.3.2 Source localization using single spikes

In this section the dipoles estimated with the single spike analysis at t_{half} and t_{peak}, using models *MRI_7c* (green), *MRI_5c* (magenta), *CT_7c* (red) and *Tmp_7c* (blue), are presented. The centroids are computed through the two procedures explained in subsection 6.2.3.4.

6.3.2.1 Distance to the resected zone

Figure 6.5 shows box plots depicting the distribution of the distances to the resected zone of the dipole estimations for models *MRI_7c*, *MRI_5c*, *CT_7c* and *Tmp_7c* using all the spikes per patient. The median of the
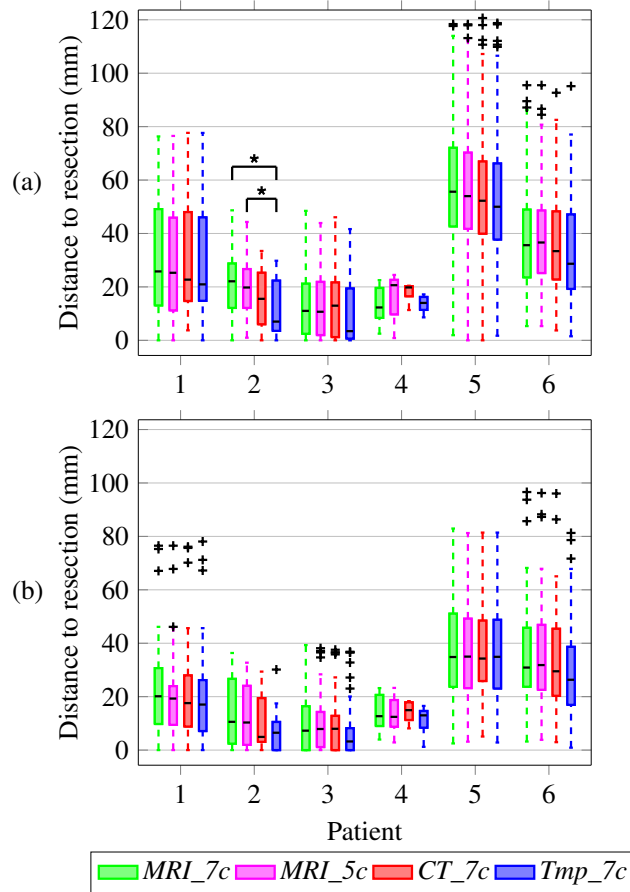
Figure 6.5: Distance to the resected zone of the dipoles estimated with the single spikes at **(a)** t_{half} and **(b)** t_{peak}. The median is displayed as a horizontal dashed line within the box. The edges of each box are the 25th and 75th percentiles, the whiskers extend to the most extreme data points the algorithm considers to be not outliers, and the outliers are plotted individually as black crosses $(+)$. Models marked with a star $(\star)$ were significantly different from each other according to the unpaired $t-$test.

distribution is depicted as a black dashed line inside the box. Overall, we did not observe statistically significant differences between the models, with the exception of models marked with a star (MRI_7c and Tmp_7c, $p = 0.0279$) and (MRI_5c and Tmp_7c, $p = 0.0294$) for patient 2 at the half-rising phase of the spike. More scattering was seen at the half-rising phase compared to the peak of the spike. In general, the peak of the single spikes led to estimations lying closer to the resected area than the

half-rising phase, for all the models, probably because of higher SNR.

Pat.	t_{spike}	Sagittal	Coronal	Axial	GOF	D (mm)
1	**(a)**				🟢 82%	0.00
					🟣 83%	0.00
					🔴 82%	1.40
					🔵 81%	2.99
	(b)				🟢 84%	0.00
					🟣 84%	0.00
					🔴 84%	0.00
					🔵 83%	0.00
2	**(a)**				🟢 84%	18.14
					🟣 85%	15.60
					🔴 85%	12.01
					🔵 84%	2.55
	(b)				🟢 84%	6.30
					🟣 83%	4.06
					🔴 84%	2.05
					🔵 84%	0.00
3	**(a)**				🟢 83%	7.81
					🟣 83%	8.10
					🔴 82%	5.69
					🔵 82%	0.00
	(b)				🟢 83%	4.62
					🟣 83%	4.24
					🔴 83%	2.01
					🔵 83%	0.00
4	**(a)**				🟢 82%	8.70
					🟣 81%	7.75
					🔴 83%	19.99
					🔵 83%	12.33
	(b)				🟢 81%	4.83
					🟣 81%	9.51
					🔴 83%	8.87
					🔵 82%	6.05
5	**(a)**				🟢 76%	41.23
					🟣 76%	41.81
					🔴 76%	42.05
					🔵 76%	42.13
	(b)				🟢 81%	28.44
					🟣 81%	30.64
					🔴 81%	30.53
					🔵 83%	32.00
6	**(a)**				🟢 83%	29.18
					🟣 83%	32.69
					🔴 83%	32.04
					🔵 82%	30.46
	(b)				🟢 83%	25.53
					🟣 83%	26.82
					🔴 83%	23.36
					🔵 83%	19.55

Figure 6.6: Mean and individual dipoles for patients 1 to 6 at **(a)** t_{half} and **(b)** t_{peak} of the single spikes for models 🟢 *MRI_ 7c*, 🟣 *MRI_ 5c*, 🔴 *CT_ 7c* and 🔵 *Tmp_ 7c*. The values of goodness of fit (GOF) and distance (D) to the resected zone are also shown.

Figure 6.6 presents the results of the mean of selected dipoles (procedure 1 in subsection 6.2.3.4), using all the head models at the (a) half-rising phase and (b) peak of the spike. The resected zone is depicted in gray. The GOF shown corresponds to the average of all the GOFs of the dipoles accounting for the final centroid.

Figure 6.7 shows the minimum and confidence volume of the mean RRE map (procedure 2 in subsection 6.2.3.4) for patients 1 to 6 for head models *MRI_7c*, *MRI_5c*, *CT_7c* and *Tmp_7c* at the (a) half-rising phase and (b) peak of the spike. The results are superimposed on the postoperative MRI of each patient, in which the resected zone is delineated in yellow and the slice displayed corresponds to the average of the centroids for all the models. The estimated centroids are similar to the method of the mean of selected dipoles. The confidence volume in patient 1 falls completely within the resection, indicating that the estimation is reliable.

Based on the results of the single spike analysis, Figure 6.6 and 6.7, we found a large amount of scatter in the final estimations evidenced by the reduced number of dipoles accounting for the final centroid. The number of dipoles accounting for the final centroid was larger at the peak than at the half-rising phase of the spike. At t_{peak}, the centroid lay inside the resection for patient 1 with all the models. Moreover, model *Tmp_7c* obtained an estimation lying inside the resected zone for patients 2 and 3 at the peak. For patients 5 and 6, all the models exhibited similar but rather large distances to the resected zone. Patient 4 in this case presented different results with respect to the rest of the patients, with model *MRI_7c* yielding the lowest distances to the resected zone. However, for patient 4 these results may be confounded because this patient had an Engel II surgical outcome and only 5 spikes were present during the analysis.

Figure 6.8 presents a bar diagram of the distances to the resection of the centroid estimations for the studied models, using single spikes. For the method of the mean of selected dipoles, the mean distances to the resection in millimeters at t_{half} were 17.51, 17.66, 18.86 and 15.08 for models *MRI_7c*, *MRI_5c*, *CT_7c* and *Tmp_7c*, respectively. At the peak, the mean distances in millimeters were, in the same order, 11.62, 12.54, 11.14 and 9.60. When the minimum of the mean RRE map was computed, the mean distances in millimeters at t_{half} were 19.35, 18.50, 20.49 and 16.19 for models *MRI_7c*, *MRI_5c*, *CT_7c* and *Tmp_7c*, respectively. At t_{peak}, the mean distances in millimeters were, for the

Pat.	t_{spike}	Sagittal	Coronal	Axial	GOF	D (mm)	n_{dip}/N
1	(a)				🟢 75%	0.00	6/35
					🟣 76%	0.00	6/35
					🔴 75%	6.95	5/35
					🔵 75%	5.16	6/35
	(b)				🟢 78%	0.00	11/35
					🟣 79%	0.00	11/35
					🔴 79%	0.00	9/35
					🔵 79%	0.00	9/35
2	(a)				🟢 81%	15.95	7/14
					🟣 81%	15.95	7/14
					🔴 81%	10.53	7/14
					🔵 80%	5.02	7/14
	(b)				🟢 80%	12.14	8/14
					🟣 81%	8.96	7/14
					🔴 82%	4.05	7/14
					🔵 81%	0.00	8/14
3	(a)				🟢 78%	5.88	3/41
					🟣 77%	6.35	3/41
					🔴 78%	6.79	3/41
					🔵 75%	0.00	3/41
	(b)				🟢 78%	4.45	12/41
					🟣 78%	5.16	13/41
					🔴 78%	4.38	13/41
					🔵 78%	0.00	11/41
4	(a)				🟢 80%	17.85	2/5
					🟣 79%	10.35	2/5
					🔴 83%	20.18	2/5
					🔵 83%	12.33	1/5
	(b)				🟢 78%	2.86	2/5
					🟣 78%	5.16	3/5
					🔴 80%	11.94	2/5
					🔵 80%	7.73	2/5
5	(a)				🟢 69%	48.41	3/42
					🟣 69%	47.73	3/42
					🔴 70%	47.90	3/42
					🔵 69%	47.67	3/42
	(b)				🟢 78%	27.98	4/42
					🟣 77%	31.09	4/42
					🔴 78%	29.96	4/42
					🔵 80%	33.49	2/42
6	(a)				🟢 73%	28.00	8/53
					🟣 72%	30.60	7/53
					🔴 73%	30.60	8/53
					🔵 72%	26.99	8/53
	(b)				🟢 76%	23.45	21/53
					🟣 75%	25.78	21/53
					🔴 76%	21.86	21/53
					🔵 76%	19.98	19/53

Figure 6.7: Minimum and confidence volume of the mean RRE map for patients 1 to 6 at **(a)** t_{half} and **(b)** t_{peak} of the single spikes for models 🟢 *MRI_7c*, 🟣 *MRI_5c*, 🔴 *CT_7c* and 🔵 *Tmp_7c*. The values of goodness of fit (GOF), distance (D) to the resected zone and number of dipoles accounting for the final centroid (n_{dip}/N) are also shown.
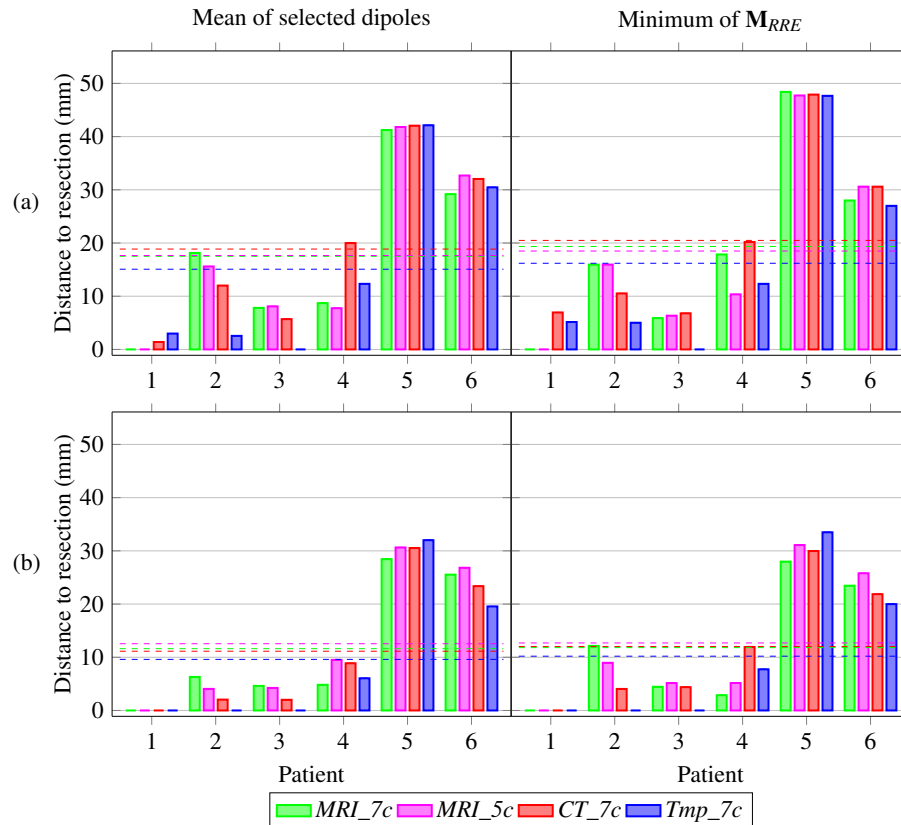
Figure 6.8: Distance to the resected zone of the centroids estimated with the single spikes at **(a)** t_{half} and **(b)** t_{peak}, using the mean of selected dipoles and the minimum of the mean RRE map. The dashed horizontal lines indicate the mean over all patients for each model.

same models, 11.81, 12.69, 12.03 and 10.20. This means that at the half-rising phase the mean distance was ≈ 2 cm, while at the peak it was ≈ 1 cm for both methods. Model Tmp_7c yielded the lowest mean distance over all patients at both t_{spike} and for both methods of centroid computation in the single spike analysis.

6.4 Discussion

In this study, we compared four different approaches to realistically model the skull based on either MRI and CT data or on a CT-template warped to the patient's head. Three out of the four approaches con-

sisted of head models with seven compartments (MRI_7c, CT_7c and Tmp_7c) and one of the models was a simplified version with five compartments (MRI_5c). The analysis was performed using data from six patients with refractory temporal lobe epilepsy for which matched CT and MRI datasets were available, as well as interictal epileptic data and postoperative MRI. Furthermore, the dipole estimations were computed for the averaged and single interictal spikes both at the half-rising phase and peak of the spike.

6.4.1 Localization of the irritative zone: Similarities and differences between the head models

Averaging of interictal spikes is a common practice in ESI [Coutin-Churchman et al., 2012, Meckes-Ferber et al., 2004, Merlet and Gotman, 1999, Michel et al., 2004, Oliva et al., 2010]. When comparing the distances to the resected zone at the half-rising phase versus the peak of the averaged spike as shown in Figure 6.4, we found similar results in all our models. The mean distance to the resected zone was approximately 1 cm for all considered models at both t_{half} and t_{peak}, meaning that clinical valuable results were obtained. No significant differences were found between the models for each patient. Although model Tmp_7c yielded the lowest mean distance, the use of a particular model did not show a remarkable influence on the dipole estimation. Both at the half-rising phase and peak of the spike, the estimated dipoles remained at similar distances to the resected area, with the exception of patient 2, where the estimations lay closer to the resection at t_{peak} (see Figure 6.3).

The inter-model distances for the averaged analysis (Table 6.3) showed that models with MR-based skulls (MRI_7c and MRI_5c) exhibited a shorter distance to model CT_7c than to model Tmp_7c. That is, the model Tmp_7c presented the largest distances to the models with subject-specific modality (MRI- or CT-based) skulls. This can be explained by the greater smoothness and thickness of the skull based on a CT-template compared to the other modalities, which could make it less sensitive to noise. Furthermore, the use of a template to segment the skull allows for certain advantages such as easier segmentation, no artifacts in the image and high resolution. Nevertheless, the template does not take into account specific features of the patient and presents different curvatures along the brain compared to the subject-specific modalities.

In [Birot et al., 2014] it was mentioned that in clinical applications,

the use of highly sophisticated and difficult to implement head models is not a crucial factor for an accurate ESI. In our study, we did not see significant differences between the tested models. Moreover, when a model with five compartments (*MRI_5c*) including a single-layered skull with an adjusted conductivity of 0.0105 S/m [Dannhauer et al., 2011, Montes-Restrepo et al., 2014] was used, the results did not seem to be different to those obtained with seven compartment models. This means that the skull can be modeled from the MR images of the patient, but with an accurate geometry at the base [Lanfer et al., 2012]. In the same direction, the negligible effect of the distinction between spongy and compact bone, has been shown in recent studies [Cho et al., 2015, Vorwerk et al., 2014]. Our advanced head models obtained similar accuracies in dipole estimation at the temporal lobe by taking into account the accurate geometry of the skull base. According to these results, all head modeling approaches presented in our study can be used in the presurgical evaluation of patients with refractory temporal lobe epilepsy (TLE) to localize the irritative zone from low-density EEG.

In addition to the use of very accurate forward modeling, the inverse solution used in our study ensured that the estimated dipoles corresponded to the global minimum of the cost function. The inverse solution used, GFS (subsection 6.2.3.2), was based on a dipole scan constrained to the gray matter surface and not on a dipole fit. The performance of GFS in ESI is comparable to that of sLORETA [Rullmann et al., 2009]. In the single spike analysis, the confidence volumes shown in Figure 6.7 represent a measure of reliability of the single dipole localization. Moreover, the confidence volumes are highly correlated with the SNR and might give an estimate of the focality of the irritative zone [Aydin et al., 2014, Bast et al., 2006]. We found that the confidence volumes had an overlap with the resected tissue for most of the patients. However, as a result of the lack of intracranial EEG recordings, we did not have a real estimation of the size of the irritative zone for the patients used in our study.

There are many factors influencing ESI such as spatial sampling density, forward modeling and inverse technique. In this study we used data acquired in a clinical monitoring setup lasting for several days. Therefore, the EEG data had limited amount of electrodes and spikes, resulting in a low SNR. This means that we should be cautious when interpreting the results, namely the distance to the resection. A closer distance to the resection does not necessarily reflect an improvement in skull modeling but could also mean that the tested model may indirectly compensate

another error source. Because we did not see a significant variation between the skull models, our results indicate that all the tested models present similar accuracies in clinical ESI. Therefore, advanced skull modeling using basic quality EEG recordings is not necessary.

6.4.2 Averaged versus single spike source localization

The single spike analysis yielded dipole estimations lying further away from the resected zone than the averaged spike analysis at the half-rising phase of the spike, with the exception of patient 1 (see Figure 6.3 compared to Figure 6.6 and 6.7). As a consequence, single spike localization was highly influenced by noise despite the use of very realistic forward models.

The distances to the resected zone displayed in Figure 6.8 showed that at the peak the mean distance to the resected zone over all patients was lower than at the half-rising phase of the spike. Although the activity at the half-rising phase of the spike is believed to most reliably localize the EEG sources [Lantz et al., 2003b, Michel et al., 2004], some studies [Bast et al., 2004, Park et al., 2015, Wennberg and Cheyne, 2014] have used the peak of the single spike to perform dipole localization due to the low SNR at the onset phase of the spike. While at the peak of the spike there is a higher SNR, there might be propagation effects [Ebersole, 2000, Lantz et al., 2003b]. However, for all the patients, the centroids were closer to the resected zone when they were estimated at the peak than at the half-rising phase of the single spikes, as displayed in Figure 6.6 and 6.7.

The advantage of single over averaged spike localization is that the former gives an estimate of the size of the irritative zone through the extent of the spread. Some studies investigated the use of averaged versus single spike source localization relying on simpler forward models [Bast et al., 2006, Chitoku et al., 2003, Plummer et al., 2010]. Bast et al. [2006] investigated the influence of SNR and multiple subaverages on the estimation of spatial extent by comparing the localization scatter of 100 single spikes in 27 spike types of 25 epilepsy patients with 1,000 different subaverages computed by random sampling and bootstrapping. They concluded that averaging increased SNR and therefore allowed for localization not only at the spike peak but also during spike onset when less cortex is active. These findings are in agreement with the results of Wennberg and Cheyne [2014] and Aydin et al. [2015], which concluded that subaveraging of around 10 spikes might provide important and ac-

curate information that neither single nor grand-averaged spike source localization can give. However, the extent of dipole scatter will still be correlated to the number of subaverages and to the SNR.

The works of Chitoku et al. [2003] and Plummer et al. [2010] compared dipole localizations of both averaged and individual spikes at selected time points within the spike. They found that the characteristics of clustered interictal spikes require careful examination before the use of dipole analysis of averaged spikes for the presurgical evaluation of epilepsy. These studies show however that there is no consensus regarding the advantages of averaged over single spike source localization. Subaveraging of the spikes according to their SNRs might yield more precise dipole estimations in ESI [Aydin et al., 2015].

6.4.3   Limitations of this study

Number of electrodes.   The number of electrodes used in the current study was 27, as used in the standard clinical setup. Studies have shown that this number of electrodes is far from optimal [Lantz et al., 2003a, Ryynänen et al., 2006]. In this work, it was shown that for patients with an inferior temporal lesion (patients 5 and 6), where the electrode coverage was very low, the distances to the resection were larger than for the rest of the patients. We believe that the use of higher spatial sampling density (more electrodes) might improve the accuracy of the estimation in these patients [Brodbeck et al., 2011, Michel et al., 2004]. In this low quality data set, the advanced skull modeling was not necessary. We achieved clinically valuable results for all head models. However, with the use of high-density EEG, skull modeling could become a more important factor in clinical ESI.

Low SNR for single spike analysis.   Interictal spike analysis is highly influenced by SNR [Kobayashi et al., 2005]. Because of the limited amount of spikes with acceptable SNR levels (> 3) [Aydin et al., 2014], single spike analysis was performed with all the available spikes per patient. Afterwards, only the spikes with GOF $\geq 80\%$ were considered to compute the final centroid. Therefore, despite our very sophisticated head models, the estimated dipoles did not lie within the resected zone for some of the studied cases.

Source location relative to skull. Four out of six patients had mesial TLE, i.e, the sources were located in the inferior central brain, which is distant from the skull under the electrodes. The influence of skull modeling could be expected to be larger for more superficial sources, e.g., somatosensory, motor or language. In contrast, patients 5 and 6 had lesional neocortical TLE. Although the neocortical lesions were close to the skull, the use of our modeling approaches did not improve the source localization for these two patients. All patients in our study had an intact skull at the time of EEG recordings. When holes are present in the skull (for instance because of previous surgery), the accurate modeling of these skull openings is of utmost importance [Lau et al., 2014].

Irritative zone versus resection. The resected zone displayed in the postoperative MRI reflects the result of a successful epilepsy surgery, i.e., the resection of the entire epileptogenic zone. Interictal epileptiform discharges (IEDs) are commonly used for ESI because of their better SNR and higher occurrence than ictal events. Nevertheless, it is known that IEDs reveal the irritative zone, an area which does not necessarily correspond to the epileptogenic or seizure onset zones and, as a consequence, to the resected tissue [Kaiboriboon et al., 2012, Rosenow and Lüders, 2001]. Therefore, the use of the resected zone for validation of our dipole estimations should be approached with caution. Although according to a recent study [Mégevand et al., 2014], ESI of IEDs provides an accurate estimate of the seizure onset and epileptogenic zones, more studies are needed to confirm the reliability of the resected zone in the validation of ESI studies using interictal spikes. In a follow-up study, high quality EEG could be used to define the irritative zone. Afterwards, the localization could be compared to intracranial EEG recordings, which give a better estimation of the irritative zone than the resected volume.

6.5 Conclusions

In this study we investigated the influence of different skull modeling approaches and spike configurations on ESI in six patients with refractory temporal lobe epilepsy who later underwent successful epilepsy surgery. The skull models were based on CT and MR images of the patient as well as on a warped CT-template. The spike configurations consisted of averaged versus single spikes, performing source localization at two different time points within the spike: half-rising phase and peak. The

results showed that the mean distance to the resection area of the dipoles estimated using the averaged spike was approximately 1 cm over all patients, which is valuable for patient diagnosis. Moreover, single spike analysis was highly influenced by SNR, yielding estimations lying closer to the resected volume at the peak of the spike. Our skull modeling approaches did not lead to significant differences in the localization of the irritative zone from low-density EEG. Furthermore, we showed that a simple skull model (MRI-based) obtained similar accuracy in dipole estimation compared to more complex head models (based on CT- or CT-template). Therefore, all our models can be used in the presurgical evaluation of refractory temporal lobe epilepsy for patient diagnosis.

6.6   Contributions

This study has been presented at the *2015 International Conference on Basic and Clinical Multimodal Imaging (BaCI)* [Montes-Restrepo et al., 2015] and published in the A1 journal *Brain Topography* [Montes-Restrepo et al., 2016].

Chapter 7

General conclusions and future research

It is not who is right, but what is right, that is of importance
—Thomas Huxley

In this chapter, the main contributions and conclusions of the work developed in this dissertation are summarized in Section 7.1. Subsequently, possible future research directions are discussed in Section 7.2. A final conclusion is stated in Section 7.3.

7.1 Summary

The main objective of this dissertation was to investigate the importance of skull modeling in ESI. Therefore, different skull modeling approaches based on CT and MR images have been studied. Simulations were performed to determine optimal parameters and relevant aspects for accurate skull representation in the generation of realistic head models. In a final stage, patient data was used to investigate the role of skull modeling on ESI in clinical practice.

Chapter 2 gave the theoretical foundations of neuronal physiology, electroencephalography and epilepsy. Furthermore, ESI was introduced together with its main elements: the source, the volume conductor model and the EEG measurements. The subproblems of ESI: forward and inverse were also explained. For the forward problem, the solution based on the Finite Difference Method (FDM), as used in this dissertation, was mathematically formulated.

Chapter 3 started with the description of the anatomy of the human head followed by techniques to perform structural imaging of the head, namely MRI and CT. Additionally, the problem of segmenting the tissues of the human head using MR and CT images was described. The most popular open-source software tools for brain tissue segmentation along with an overview of methods for skull segmentation were presented.

In Chapter 4, three studies to elucidate different aspects of skull modeling in ESI were presented: (i) Study I—conductivity perturbations of the three-layered skull, (ii) Study II—anisotropy ratio, and (iii) Study III—inhomogeneities. In the first study, using a realistic head model with the skull segmented from CT images, the effects of conductivity perturbations of the three-layered skull on ESI were analyzed. The results of this study showed a greater significance of the compact over the spongy bone conductivity. Additionally, the compact bone conductivity showed to have an impact on the depth at which the dipole was estimated, being deeper for over-estimated conductivity values and more superficial for under-estimated values.

The second study in Chapter 4 used a spherical head model to determine the optimal anisotropy ratio of the skull. To achieve that, a reference model with three-layered skull was compared against test models with anisotropic skull. Based on a simplified three-layered skull model and conductivity values for the compact and spongy bone compartment from the literature [Akhtari et al., 2002], the initial radial and tangential conductivity values were estimated. These values were perturbed generating a total of 225 different anisotropy ratios. The results of this study showed an optimal anisotropy ratio of 1:1.57 (radial:tangential), confirming that the value of 1:10 used in previous studies is over-estimated. Furthermore, the optimal anisotropy ratio was applied on a realistic head model in which three methods to determine the radial and tangential conductivities were compared: The volume constraint, the Wang's constraint and a simplified three-layered skull. The simulations on the realistic head models showed that the smallest errors were obtained when the radial and tangential conductivities were determined using the volume constraint. However, the three methods presented overall similar errors.

In the third study of Chapter 4, a realistic head model with a CT-based skull was used. The influence of not modeling some inhomogeneities of the skull on ESI was investigated. The inhomogeneities referred to the three layers and the air-filled cavities of the skull. By modeling

the inhomogeneous three-layered skull as an homogeneous compartment with anisotropic conductivity, smaller errors were obtained than for the isotropic case. Not modeling the air cavities of the skull yielded small errors on the dipole estimation (< 5 mm). The errors were smaller when the air cavities were modeled as compact than as spongy bone.

A study about the influence of head models with CT-based versus MR-based skulls on ESI was shown in Chapter 5. Different skull conductivity and geometry simplifications were compared against a reference head model with a skull segmented from CT. SNR and spatial sampling density effects were also analyzed. The results indicated that when CT images were utilized, isotropic heterogeneous conductivity led to the smallest localization errors. If the skull segmentation is based solely on MR images, the errors are larger especially at the base of the skull. Based on these results, we determined guidelines for skull modeling in ESI: Whenever available, CT images should be used to segment the skull as a three-layered compartment. If only MR images were available, the base of the skull should be adequately represented in order to reduce the localization errors. In addition, the use of high-density EEG (128 electrodes) diminished the localization errors to ~ 1 cm, for realistic noise levels.

Chapter 6 presented an ESI study using data from six patients with refractory temporal lobe epilepsy who later underwent epilepsy surgery. The analysis was carried out on four head models with different skull modeling approaches based on either MRI, CT or a CT-template, for each patient. Moreover, averaged versus single spike localization at two phases of the epileptic activity (half-rising and peak) was performed to localize the irritative zone. This localization was compared to the resection that rendered the patients seizure free. The averaged spike led to localization errors of around 1 cm, while the single spike analysis was highly influenced by the SNR. The tested skull modeling approaches did not lead to significant differences in the localization of the irritative zone using clinical (low-density) EEG. Therefore, highly sophisticated skull modeling was not necessary in this setup. Nevertheless, it could become a more important factor in ESI with high-density EEG.

7.2   Future research

Future lines of work include the improvement of the volume conductor model, the combination of EEG with MEG, the use of more complex

inverse solutions, a more exhaustive validation of the skull modeling approaches proposed here, and utilization in other applications (e.g. in other neurological diseases).

The **volume conductor model** can be improved by including accurate individual conductivity values of the head tissues. The measurement of *in-vivo* conductivity values of the human head is challenging, especially for the skull because of its anisotropic nature. Methods currently used to estimate tissue conductivities, namely Electrical Impedance Tomography (EIT) and MR-EIT, attempt to recover the head conductivity values from surface measurements caused by an injected current. Other methods use simultaneous intra- and extra-cranial stimulation and somatosensory evoked field/potential data. However, analogous to ESI, the determination of subject-specific conductivity values requires the solution of an *ill-posed* inverse problem.

Modeling the geometry of the skull solely from MR images can be achieved by using the Ultrashort Echo time (UTE) sequence. These sequences allow to visualize tissues with short T2 components such as compact bone [Robson et al., 2003]. Nonetheless, MRI with UTE sequences is not yet included in the clinical protocol of epilepsy patients.

Another way in which the volume conductor model can be improved is by adding other tissues into it, e.g., the dura mater. A study by Ramon et al. [2014] suggests that the dura layer reduces the magnitude of scalp potentials significantly and should be included in human head models for accurate simulation of scalp potentials. Nevertheless, the segmentation of the thinnest parts of the dura layer is complicated and its conductivity value is not well established, having a wide range between 0.02 and 0.1 S/m [Oozeer et al., 2005]. The advances in scanner resolution and computational power make the generation of high-resolution (7T) MRI-based volume conductor models computationally feasible. The addition of blood vessels can be as important as white matter anisotropy or dura layer in ESI [Fiederer et al., 2016].

Combined EEG/MEG has shown to reconstruct sources more reliably than either modality alone in the presurgical evaluation of epilepsy [Aydin et al., 2015]. Both modalities are complimentary, with their signal topographies almost orthogonal to each other. However, although MEG has a higher SNR and is less sensitive to the conductivity of the skull than EEG, it cannot be recorded over long periods of time. Moreover, MEG is costly and not portable. Hence, more studies investigating combined EEG/MEG source imaging are needed to determine a cost-

effective solution for the inclusion of MEG as part of the presurgical evaluation of epilepsy [Carrette, 2011].

In this dissertation, a single dipole model was used for the solution of the **inverse problem**. This inverse model is suitable for representing epileptic spikes in which the activity is assumed to originate from a single source, and is therefore commonly used in focal epilepsy. In contrast, distributed dipole models assume that the activity originates from multiple sources at the same time, thus being able to represent extended source configurations. Nonetheless, because distributed models are based on complex mathematical assumptions, its combination with sophisticated forward models for ESI has yet to be clinically validated.

The *gold standard* for ESI validation is simultaneously recorded EEG and intracranial EEG or stereo-EEG [Cossu et al., 2005]. This would allow us to compare the brain activity measured within the skull, with the one estimated from the scalp EEG. Although here we must keep in mind that the modeling of the burr-holes necessary to place the electrodes and the modeling of the electrodes itself might be difficult.

Other applications in which an accurate skull modeling is relevant are: (i) ESI on neonates, in which a precise characterization of the fontanels and sutures of the newborn's skull is of utmost importance, and (ii) Transcranial direct current stimulation (tDCS), where patient-specific head models allow for realistic electric field calculations indispensable for a more accurate determination of the affected brain areas.

7.3   Final conclusion

This dissertation presented several studies of different aspects of skull modeling in order to determine optimal guidelines for the generation of subject-specific head models in ESI. A study with patient data intended to investigate the clinical value of realistic skull modeling in ESI for the presurgical evaluation of patients with refractory epilepsy.

Our studies using simulated data (Chapters 4 and 5) showed that the skull was better modeled as an isotropic heterogeneous compartment, i.e., composed of a spongy bone layer surrounded by two compact bone layers. Additionally, the spongy bone might be segmented from the compact bone layer by applying the morphological operation of erosion. If the skull is to be modeled as three-layered, it has to be kept in mind that the chosen conductivity value for the compact bone is more important than the one of the spongy bone. Furthermore, the base of the skull

should be carefully modeled, taking into account important holes such as the foramen magnum. The air cavities of the skull did not show to have a large significance in the head model.

If the skull is modeled as an anisotropic homogeneous compartment, i.e., because of lack of high-resolution images, the anisotropy ratio must be much lower than the usual 1:10. More than this ratio, a radial conductivity of ~ 0.01 S/m might allow for a better representation of the conductivity of the skull. Likewise, when modeling the skull as an isotropic homogeneous compartment, the conductivity value can be set to 0.01 S/m.

The results of our study using data of six patients with refractory epilepsy, Chapter 6, showed no significant difference between various skull modeling approaches with the use of clinical EEG. Therefore, all our models can be used in the presurgical evaluation of epilepsy. The geometry of the skull can be accurately derived from MR images or using a CT-template warped to the patient's head. Despite this, skull modeling continues to be an important factor in the generation of realistic head models for ESI. More studies with high-density EEG in a large cohort of patients are required to demonstrate the clinical value of skull modeling in the presurgical evaluation of patients with epilepsy.

Appendix A

Successive Over-Relaxation

A.1 Properties of the system matrix

Given the linear system of equations

$$\mathbf{A}\mathbf{x} = \mathbf{b}, \qquad\qquad (A.1)$$

with $\mathbf{A} \in \mathbb{R}^{n \times n}$, $\mathbf{x} \in \mathbb{R}^{n \times 1}$ the unknowns and $\mathbf{b} \in \mathbb{R}^{n \times 1}$ the right hand side term, for n computational points. The system matrix $\mathbf{A}$ has the following properties:

  – $\mathbf{A}$ is square and sparse.

  – $\mathbf{A}$ is a symmetric matrix with weak diagonal dominance. This is because the coefficients connecting the same pair of neighbouring voxels are identical.

  – The linear system of equations (A.1) possesses infinite solutions differing only in an additive constant, if $\sum_{i=1}^{n} b_i = 0$. This holds because the summation of the elements of the vector $\mathbf{b}$ is equal to zero due to the monopoles of the current sources and sinks.

A.2 Successive Over-Relaxation (SOR)

The SOR method is a representative of classical stationary methods. It is known to be a non-optimal choice as far as convergence is concerned, but its structure is very simple.

The linear system of equations given by (A.1),

$$a_{i1}x_1 + \cdots + a_{ii}x_i + \cdots + a_{in}x_n = b_i,$$

for $i = 1, \ldots, n$, can be rewritten as

$$x_i = \frac{1}{a_{ii}} \left(b_i - \sum_{j=1, j \neq i}^{n} a_{ij}x_j \right).$$

Let $\mathbf{x}^{(k)}$ be an approximation to the solution after k iterations. The SOR method updates the unknowns in the following fashion: To compute $x_i^{(k+1)}$, first an intermediate value is determined as

$$\bar{x}_i^{(k+1)} = \frac{1}{a_{ii}} \left(b_i - \sum_{j=1}^{i-1} a_{ij}x_j^{(k+1)} - \sum_{j=i+1}^{n} a_{ij}x_j^{(k)} \right), \qquad \text{(A.2)}$$

the new values of $\mathbf{x}^{(k+1)}$ are used as soon as they are available. The new approximation then becomes

$$x_i^{(k+1)} = \omega \bar{x}_i^{(k+1)} + (1 - \omega)x_i^{(k)} = x_i^{(k)} + \omega \left(\bar{x}_i^{(k+1)} - x_i^{(k)} \right). \qquad \text{(A.3)}$$

The over-relaxation parameter ω is a weighting parameter used to place more weight onto the correction in order to improve convergence. According to the Young theorem [Young, 1954], the optimal value for ω can be computed as:

$$\omega_{opt} = \frac{2}{1 + \sqrt{1 - \rho(\mathbf{B})^2}}, \qquad \text{(A.4)}$$

where $\rho(\mathbf{B})$ is the spectral radius or the maximum of the absolute eigenvalues of the Jacobi iteration matrix. During the SOR procedure, the ω can be altered using this formula to obtain a faster convergence [Saad, 2003].

Appendix B

The reciprocity theorem

The forward problem can be solved either in the conventional way, that is, by calculating the surface potentials for every dipole via the Poisson's equation, or using reciprocity, as explained below.

B.1   The general idea of reciprocity

Consider a circuit with clamp AB representing a pair of scalp electrodes, and a clamp on a location described by index r measuring a dipolar source in the brain region illustrated in Figure B.1.

First a current I_r at clamp r is introduced. This source will generate a potential $V_{AB}(I_r)$ at AB as illustrated in Figure B.1a. Next a current I_{AB} is introduced at clamps A and B. This will give rise to a potential difference $\phi_r(I_{AB})$ at r as illustrated in Figure B.1b. The reciprocity theorem in circuit analysis states that [Rush and Driscoll, 1969]:

$$V_{AB}\ I_{AB} = \phi_r\ I_r \qquad\qquad (B.1)$$

B.2   Application of reciprocity to compute EEG lead-fields using finite differences

Considering Equation (B.1) we assume a dipole oriented in the $x-$direction at a location described by index r of the computational grid. The dipole is represented by two current monopoles, a current source and sink, providing I_r and $-I_r$, on opposite nodes along the $x-$direction separated by a distance $2h_x$, with h_x the spacing of the
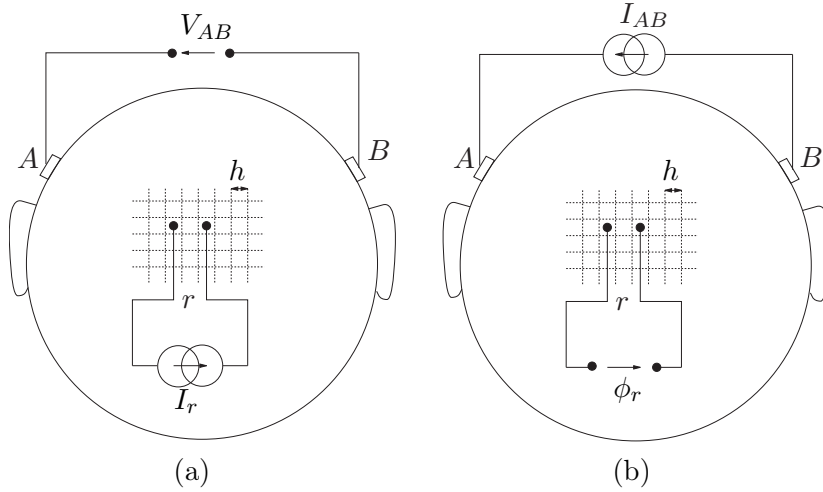
Figure B.1: A schematic representation of the reciprocity theorem. A network where a current source is introduced in the brain and a potential difference is measured at an electrode pair, and vice versa: (a) a current source I_r is introduced and the potential V_{AB} is measured, and (b) a current source I_{AB} is introduced and a potential ϕ_r is measured. Adapted from [Vanrumste, 2002].

nodes in the $x-$direction. The dipole is oriented from the negative to the positive current monopole and the central node with index r of the two monopoles is the dipole position. The magnitude of the dipole moment is then $2h_x I_r$. Because the scalp electrodes are located sufficiently far from the sources compared with the distance $2h_x$ between the sources, we can assume a dipolar field. Equation (B.1) can be rewritten as:

$$V_{AB} = \frac{\phi_r I_r}{I_{AB}}. \tag{B.2}$$

To explicitly include the orientation of the dipole in $x-$, $y-$ or $z-$direction in Equation (B.2), we describe a dipole based on its location $\mathbf{r} = [ih_x, jh_y, kh_z]$ in the 3D computational grid, with h_x, h_y and h_z the spacing of the nodes in the $x-$, $y-$ or $z-$direction and the indices i, j, k the number of nodes along the $x-$, $y-$ and $z-$direction. Rewriting Equation (B.2) with $d_x = 2h_x I_r$ and

$$\frac{\partial \phi(\mathbf{r})}{\partial x} \approx \frac{[\phi(\mathbf{r} + h_x \mathbf{e}_x) - \phi(\mathbf{r} - h_x \mathbf{e}_x)]}{2h_x},$$

being $\mathbf{e}_x$ the unit vector in the $x-$direction, gives:

$$V_{AB} = \frac{d_x(\mathbf{r})\dfrac{\partial\phi(\mathbf{r})}{\partial x}}{I_{AB}}, \tag{B.3}$$

meaning that the potential V_{AB} can be calculated for a dipole oriented along the $x-$axis on location $\mathbf{r}$ given $\frac{\partial\phi(\mathbf{r})}{\partial x}$. In a similar way, V_{AB} can be calculated for a dipole located at $\mathbf{r}$ oriented along the $y-$axis and the $z-$axis. Consider a dipole at position $\mathbf{r}$ and with dipole components $\mathbf{d} = (d_x, d_y, d_z)^T \in \mathbb{R}^{3\times1}$, the potential V_{AB} reads:

$$V_{AB}(\mathbf{r}, \mathbf{d}) = \frac{\mathbf{d}^T \cdot \nabla\phi(\mathbf{r})}{I_{AB}}, \tag{B.4}$$

with $\nabla\phi(\mathbf{r}) = (\partial\phi(\mathbf{r})/\partial x, \partial\phi(\mathbf{r})/\partial y, \partial\phi(\mathbf{r})/\partial z)^T \in \mathbb{R}^{3\times1}$.

Based on Equation (B.4), the approach based on reciprocity to calculate the EEG lead-fields goes as follows for two electrodes on the scalp surface:

- A fictive current $I_{AB} = 1$ with unit amplitude is assumed, which enters the head at electrode A and leaves the head at electrode B.

- Utilizing the FDM, the potentials $\phi(ih_x, jh_y, kh_z)$ can be calculated for every position. Figure B.2 illustrates the equipotential lines and current density vectors $\mathbf{J} = -\sigma\nabla\phi$ in the brain region, with $\nabla\phi = (\partial\phi/\partial x, \partial\phi/\partial y, \partial\phi/\partial z)^T$. The partial derivative $\partial\phi/\partial x$ is approximated by $[\phi((i+1)h_x, jh_y, kh_z) - \phi((i-1)h_x, jh_y, kh_z)]/2h_x$. The partial derivatives $\partial\phi/\partial y, \partial\phi/\partial z$ are obtained in a similar way.

- V_{AB} the potential difference between the scalp electrodes A and B generated by the dipole at position $\mathbf{r}$ and dipole moment $\mathbf{d}$ is obtained by applying Equation (B.4).

If m scalp electrodes are used to measure the EEG, $m-1$ electrode pairs can be found with linear independent potential differences. For each electrode pair, Equation (B.4) can be used to calculate the V_{AB} for each position $\mathbf{r}$ in the brain [Hallez et al., 2005].
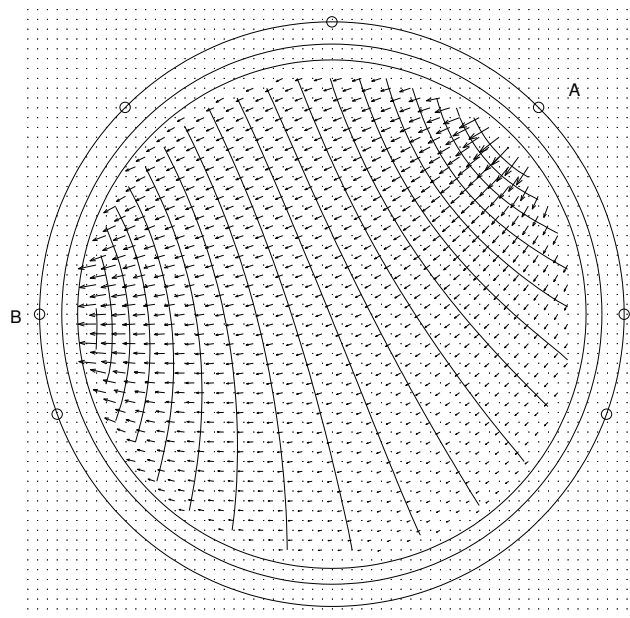
Figure B.2: Potential field calculated using the finite difference modeling approach for a current introduced between two electrodes A and B on the scalp. Adapted from [Vanrumste, 2002].

References

Z. Akalin-Acar and N. G. Gençer. An advanced boundary element method (BEM) implementation for the forward problem of electromagnetic source imaging. *Physics in Medicine and Biology*, 49(21): 5011–5028, Nov. 2004. ISSN 0031-9155.

Z. Akalin-Acar and S. Makeig. Neuroelectromagnetic Forward Head Modeling Toolbox. *Journal of Neuroscience Methods*, 190(2):258–270, 2010.

Z. Akalin-Acar and S. Makeig. Effects of forward model errors on EEG source localization. *Brain Topography*, 26(3):378–396, 2013.

M. Akhtari, H. Bryant, A. Mamelak, E. Flynn, L. Heller, J. Shih, M. Mandelkern, A. Matlachov, D. Ranken, E. Best, et al. Conductivities of three-layer live human skull. *Brain Topography*, 14(3):151–167, 2002.

J. P. Ary, S. A. Klein, and D. H. Fender. Location of sources of evoked scalp potentials: corrections for skull and scalp thicknesses. *Biomedical Engineering*, 28(6), 1981.

J. Ashburner and K. Friston. Multimodal image coregistration and partitioning – a unified framework. *NeuroImage*, 6(3):209–217, 1997.

J. Ashburner and K. Friston. Unified segmentation. *NeuroImage*, 26(3): 839–851, 2005.

B. B. Avants, N. J. Tustison, J. Wu, P. A. Cook, and J. C. Gee. An open source multivariate framework for n-tissue segmentation with evaluation on public data. *Neuroinformatics*, 9(4):381–400, 2011.

K. A. Awada, D. R. Jackson, J. T. Williams, D. R. Wilton, S. B. Baumann, and A. C. Papanicolaou. Computational aspects of finite el-

ement modeling in EEG source localization. *IEEE Transactions on Biomedical Engineering*, 44:736–752, 1997.

Ü. Aydin, J. Vorwerk, P. Küpper, M. Heers, H. Kugel, A. Galka, L. Hamid, J. Wellmer, C. Kellinghaus, S. Rampp, et al. Combining EEG and MEG for the Reconstruction of Epileptic Activity Using a Calibrated Realistic Volume Conductor Model. *PloS ONE*, 9(3): e93154, 2014.

Ü. Aydin, J. Vorwerk, M. Dümpelmann, P. Küpper, H. Kugel, J. Wellmer, C. Kellinghaus, J. Haueisen, S. Rampp, H. Stefan, and C. Wolters. Combined EEG/MEG Can Outperform Single Modality EEG or MEG Source Reconstruction in Presurgical Epilepsy Diagnosis. *PloS ONE*, 2015. doi: DOI:10.1371/journal.pone.0118753.

F. A. Azevedo, L. R. Carvalho, L. T. Grinberg, J. M. Farfel, R. E. Ferretti, R. E. Leite, R. Lent, S. Herculano-Houzel, et al. Equal numbers of neuronal and nonneuronal cells make the human brain an isometrically scaled-up primate brain. *Journal of Comparative Neurology*, 513 (5):532–541, 2009.

S. Baillet, L. Garnero, G. Marin, and J.-P. Hugonin. Combined MEG and EEG source imaging by minimization of mutual information. *IEEE Transactions on Biomedical Engineering*, 46(5):522–534, 1999.

S. Baillet, J. Mosher, and R. Leahy. Electromagnetic brain mapping. *IEEE Signal Processing Magazine*, 18(6):14–30, 2001.

A. Barnard, I. Duck, and M. Lynn. The application of electromagnetic theory to electrocardiology: I. Derivation of the integral equations. *Biophysical Journal*, 7(5):443, 1967a.

A. Barnard, I. Duck, M. Lynn, and W. Timlake. The application of electromagnetic theory to electrocardiology: II. Numerical solution of the integral equations. *Biophysical Journal*, 7(5):463, 1967b.

J. F. Barrett and N. Keat. Artifacts in CT: Recognition and Avoidance. *Radiographics*, 24(6):1679–1691, 2004.

T. Bast, O. Oezkan, S. Rona, C. Stippich, A. Seitz, A. Rupp, S. Fauser, J. Zentner, D. Rating, and M. Scherg. EEG and MEG source analysis of single and averaged interictal spikes reveals intrinsic epileptogenicity in focal cortical dysplasia. *Epilepsia*, 45(6):621–631, 2004.

T. Bast, T. Boppel, A. Rupp, I. Harting, K. Hoechstetter, S. Fauser, A. Schulze-Bonhage, D. Rating, and M. Scherg. Noninvasive source localization of interictal EEG spikes: effects of signal-to-noise ratio and averaging. *Journal of Clinical Neurophysiology*, 23(6):487–497, 2006.

S. Baumann, D. Wozny, S. Kelly, and F. Meno. The electrical conductivity of human cerebrospinal fluid at body temperature. *IEEE Transactions on Biomedical Engineering*, 44(3):220–223, 1997.

U. Baysal and J. Haueisen. Use of a priori information in estimating tissue resistivities–application to human data in vivo. *Physiological Measurement*, 44(3):1677–1689, 2004.

E. M. Bellon, E. Haacke, P. Coleman, D. Sacco, D. Steiger, and R. Gangarosa. MR artifacts: a review. *American Journal of Roentgenology*, 147(6):1271–1281, 1986.

H. Berger. Über das elektrenkephalogramm des menschen. *European Archives of Psychiatry and Clinical Neuroscience*, 87(1):527–570, 1929.

M. A. Bernstein, K. F. King, and X. J. Zhou. *Handbook of MRI pulse sequences*. Elsevier, 2004.

A. Bertelsen, A. Munoz-Barrutia, S. Tejada, C. Ortiz-de Solorzano, and D. Borro. Segmentation of the skull from MR T1 images using label fusion. In *Proceedings of the 32nd Annual International Conference of the IEEE Engineering in Medicine and Biology Society*, pages 3121–3124. IEEE, 2010.

G. Birot, L. Spinelli, S. Vulliémoz, P. Mégevand, D. Brunet, M. Seeck, and C. M. Michel. Head model and electrical source imaging: a study of 38 epileptic patients. *NeuroImage: Clinical*, 5:77–83, 2014.

J. E. Bogen and G. Bogen. Wernicke's region–Where is it? *Annals of the New York Academy of Sciences*, 280(1):834–843, 1976.

P. Boon, M. D'Havé, C. Adam, K. Vonck, M. Baulac, T. Vandekerckhove, and J. De Reuck. Dipole modeling in epilepsy surgery candidates. *Epilepsia*, 38(2):208–218, 1997.

P. Boon, M. D'Havé, B. Vanrumste, G. Van Hoey, K. Vonck, P. Van Walleghem, J. Caemaert, E. Achten, and J. De Reuck. Ictal source localization in presurgical patients with refractory epilepsy. *Journal*

of Clinical Neurophysiology, 19(5):461–8, Oct. 2002. ISSN 0736-0258. URL http://www.ncbi.nlm.nih.gov/pubmed/12477991.

P. Bottomley and E. R. Andrew. RF magnetic field penetration, phase shift and power dissipation in biological tissue: implications for NMR imaging. *Physics in Medicine and Biology*, 23(4):630, 1978.

M. Brant-Zawadzki, G. D. Gillan, and W. R. Nitz. MP RAGE: a three-dimensional, T1-weighted, gradient-echo sequence–initial experience in the brain. *Radiology*, 182(3):769–775, 1992.

V. Brodbeck, L. Spinelli, A. Lascano, M. Wissmeier, M. Vargas, S. Vulliemoz, C. Pollo, K. Schaller, C. Michel, and M. Seeck. Electroencephalographic source imaging: a prospective study of 152 operated epileptic patients. *Brain*, 134(10):2887–2897, 2011.

K. Brodmann. *Vergleichende Lokalisationslehre der Gro hirnrinde*. 1909.

D. Brody, F. Terry, and R. Ideker. Eccentric dipole in a spherical medium: generalized expression for surface potentials. *IEEE Transactions on Biomedical Engineering*, BME-20(2):141–143, March 1973.

H. Buchner, G. Knoll, M. Fuchs, A. Rienäcker, R. Beckmann, M. Wagner, J. Silny, and J. Pesch. Inverse localization of electric dipole current sources in finite element models of the human head. *Electroencephalography and Clinical Neurophysiology*, 102(4):267–278, 1997.

J. T. Bushberg and J. M. Boone. *The essential physics of medical imaging*. Lippincott Williams & Wilkins, 2011.

D. L. Camacho, R. H. Hopper, G. M. Lin, and B. S. Myers. An improved method for finite element mesh generation of geometrically complex structures with application to the skullbase. *Journal of Biomechanics*, 30(10):1067–1070, 1997.

E. Carrette. *The optimization of the presurgical evaluation of patients with refractory epilepsy*. PhD thesis, Ghent University, 2011.

E. Carrette, K. Vonck, V. De Herdt, A. Van Dycke, R. El Tahry, A. Meurs, R. Raedt, L. Goossens, M. Van Zandijcke, G. Van Maele, et al. Predictive factors for outcome of invasive video-EEG monitoring and subsequent resective surgery in patients with refractory epilepsy. *Clinical Neurology and Neurosurgery*, 112(2):118–126, 2010.

E. Carrette, K. Vonck, and P. Boon. The management of pharmacologically refractory epilepsy. *International Journal of Clinical Reviews*, 1 (02), 2011.

R. Carter. *The human brain book*. Penguin, 2014.

K. H. Chiappa. *Evoked potentials in clinical medicine*. Lippincott Williams & Wilkins, 1997.

S. Chitoku, H. Otsubo, T. Ichimura, T. Saigusa, A. Ochi, A. Shirasawa, K.-i. Kamijo, T. Yamazaki, E. Pang, J. T. Rutka, et al. Characteristics of dipoles in clustered individual spikes and averaged spikes. *Brain and Development*, 25(1):14–21, 2003.

J.-H. Cho, J. Vorwerk, C. Wolters, and T. Knösche. Influence of the head model on EEG and MEG source connectivity analysis. *NeuroImage*, 110:60–77, 2015. ISSN 10538119.

D. L. Collins, P. Neelin, T. M. Peters, and A. C. Evans. Automatic 3D intersubject registration of MR volumetric data in standardized Talairach space. *Journal of Computer Assisted Tomography*, 18(2): 192–205, 1994.

M. Cossu, F. Cardinale, L. Castana, A. Citterio, S. Francione, L. Tassi, A. L. Benabid, and G. L. Russo. Stereoelectroencephalography in the presurgical evaluation of focal epilepsy: a retrospective analysis of 215 procedures. *Neurosurgery*, 57(4):706–718, 2005.

P. E. Coutin-Churchman, J. Y. Wu, L. L. Chen, K. Shattuck, S. Dewar, and M. R. Nuwer. Quantification and localization of EEG interictal spike activity in patients with surgically removed epileptogenic foci. *Clinical Neurophysiology*, 123(3):471–485, 2012.

G. Crevecoeur, V. Montes-Restrepo, and S. Staelens. Subspace electrode selection methodology for the reduction of the effect of uncertain conductivity values in the EEG dipole localization: A simulation study using a patient-specific head model. *Physics in Medicine and Biology*, 57:1963–1986, 2012.

A. Dale and M. Sereno. Improved localization of cortical activity by combining EEG and MEG with MRI cortical surface reconstruction: a linear approach. *Journal of Cognitive Neuroscience*, 5(2):162–176, 1993.

A. Dale, B. Fischl, and M. I. Sereno. Cortical surface-based analysis: I. Segmentation and surface reconstruction. *NeuroImage*, 9(2):179–194, 1999.

M. Dannhauer, B. Lanfer, C. Wolters, and T. Knösche. Modeling of the human skull in EEG source analysis. *Human Brain Mapping*, 32(9): 1383–1399, 2011. doi: DOI:10.1002/hbm.21114.

G. Dassios, A. Fokas, and D. Hadjiloizi. On the complementarity of electroencephalography and magnetoencephalography. *Inverse Problems*, 23(6):2541, 2007.

J. De Munck. The potential distribution in a layered anisotropic spheroidal volume conductor. *Journal of Applied Physics*, 64(2):464–470, July 1988.

J. De Munck. A linear discretization of the volume conductor boundary integral equation using analytically integrated elements. *IEEE Transactions on Biomedical Engineering*, 39(9):986–990, 1992.

J. De Munck and M. Peters. A fast method to compute the potential in the multisphere model. *IEEE Transactions on Biomedical Engineering*, 40(11):1166–1174, November 1993.

J. De Munck, B. Van Dijk, and H. Spekreijse. Mathematical dipoles are adequate to describe realistic generators of human brain activity. *IEEE Transactions on Biomedical Engineering*, 35(11):960–966, November 1988.

K. Deblaere and E. Achten. Structural magnetic resonance imaging in epilepsy. *European Radiology*, 18(1):119–129, 2008.

I. Despotovic, P. J. Cherian, M. Vos, H. Hallez, W. Deburchgraeve, P. Govaert, M. Lequin, G. H. Visser, R. M. Swarte, E. Vansteenkiste, et al. Relationship of EEG sources of neonatal seizures to acute perinatal brain lesions seen on MRI: A pilot study. *Human Brain Mapping*, 34(10):2402–2417, 2013.

I. Despotović, B. Goossens, and W. Philips. MRI segmentation of the human brain: challenges, methods, and applications. *Computational and Mathematical Methods in Medicine*, 2015, 2015.

B. Dogdas, D. W. Shattuck, and R. M. Leahy. Segmentation of skull and scalp in 3-D human MRI using mathematical morphology. *Human Brain Mapping*, 26(4):273–285, 2005.

F. Drechsler, C. Wolters, T. Dierkes, H. Si, and L. Grasedyck. A full subtraction approach for finite element method based source analysis using constrained Delaunay tetrahedralisation. *NeuroImage*, 46(4): 1055–1065, 2009.

N. F. Dronkers, O. Plaisant, M. T. Iba-Zizen, and E. A. Cabanis. Paul Broca's historic cases: high resolution MR imaging of the brains of Leborgne and Lelong. *Brain*, 130(5):1432–1441, 2007.

J. S. Ebersole. Non-invasive pre-surgical evaluation with EEG/MEG source analysis. *Electroencephalography and Clinical Neurophysiology*, 50:167–174, 1999.

J. S. Ebersole. Noninvasive localization of epileptogenic foci by EEG source modeling. *Epilepsia*, 41(s3):S24–S33, 2000.

J. Engel. Mesial temporal lobe epilepsy: what have we learned? *The Neuroscientist*, 7(4):340–352, 2001a.

J. Engel. A Proposed Diagnostic Scheme for People with Epileptic Seizures and with Epilepsy: Report of the ILAE Task Force on Classification and Terminology. *Epilepsia*, 42(6):796–803, 2001b.

J. J. Engel, P. Van Ness, T. Rasmussen, and L. Ojemann. Outcome with respect to epileptic seizures. In J. J. Engel, editor, *Surgical treatment of the epilepsies*, pages 609–621. Raven Press, 1993.

A. C. Evans, D. L. Collins, S. Mills, E. Brown, R. Kelly, and T. M. Peters. 3D statistical neuroanatomical models from 305 MRI volumes. In *Proceedings of the IEEE Nuclear Science Symposium and Medical Imaging Conference*, pages 1813–1817. IEEE, 1993.

L. Fiederer, J. Vorwerk, F. Lucka, M. Dannhauer, S. Yang, M. Dümpelmann, A. Schulze-Bonhage, A. Aertsen, O. Speck, C. Wolters, et al. The role of blood vessels in high-resolution volume conductor head modeling of EEG. *NeuroImage*, 128:193–208, 2016.

B. Fischl and A. Dale. Measuring the thickness of the human cerebral cortex from magnetic resonance images. *Proceedings of the National Academy of Sciences*, 97(20):11050–11055, 2000.

B. Fischl, M. I. Sereno, and A. Dale. Cortical surface-based analysis: II. Inflation, flattening, and a surface-based coordinate system. *NeuroImage*, 9(2):195–207, 1999.

B. Fischl, D. H. Salat, E. Busa, M. Albert, M. Dieterich, C. Haselgrove, A. Van Der Kouwe, R. Killiany, D. Kennedy, S. Klaveness, et al. Whole brain segmentation: automated labeling of neuroanatomical structures in the human brain. *Neuron*, 33(3):341–355, 2002.

J. Foxe, M. Murray, and D. Javitt. Filling-in in schizophrenia: a high-density electrical mapping and source-analysis investigation of illusory contour processing. *Cerebral Cortex*, 15(12):1914–1927, 2005.

E. Frank. Electric potential produced by two point current sources in a homogeneous conduction sphere. *Journal of Applied Physics*, 23(11): 1225–1228, 1952. doi: 10.1063/1.1702037.

K. Friston, editor. *Statistical Parametric Mapping: The Analysis of Functional Brain Images*. Academic Press Inc., U. S., 2006.

M. Fuchs, M. Wagner, T. Köhler, and H. Wischmann. Linear and non-linear current density reconstructions. *Journal of Clinical Neurophysiology*, 16(3):267–295, 1999.

M. Fuchs, M. Wagner, and J. Kastner. Development of volume conductor and source models to localize epileptic foci. *Journal of Clinical Neurophysiology*, 24(2):101–119, 2007.

N. Gao, S. A. Zhu, and B. He. A new magnetic resonance electrical impedance tomography (MREIT) algorithm: the RSM-MREIT algorithm with applications to estimation of human head conductivity. *Physics in Medicine and Biology*, 51(12):3067–83, June 2006. ISSN 0031-9155. doi: 10.1088/0031-9155/51/12/005.

D. Geffroy, D. Rivière, I. Denghien, N. Souedet, S. Laguitton, and Y. Cointepas. BrainVISA: a complete software platform for neuroimaging. In *Python in neuroscience workshop*. Euroscipy Paris, 2011.

N. G. Gençer and C. E. Acar. Sensitivity of EEG and MEG measurements to tissue conductivity. *Physics in Medicine and Biology*, 49(5): 701, 2004.

D. B. Geselowitz. On bioelectric potentials in an inhomogeneous volume conductor. *Biophysical Journal*, 7(1):1, 1967.

S. Ghadimi, H. Abrishami-Moghaddam, K. Kazemi, R. Grebe, C. Goundry-Jouet, and F. Wallois. Segmentation of scalp and skull in neonatal MR images using probabilistic atlas and level set method. In

Proceedings of the 30th Annual International Conference of the IEEE Engineering in Medicine and Biology Society, pages 3060–3063. IEEE, 2008.

S. Ghadimi, H. Abrishami-Moghaddam, R. Grebe, and F. Wallois. Skull segmentation and reconstruction from newborn CT images using coupled level sets. *IEEE Journal of Biomedical and Health Informatics*, 20(2):563–573, 2016.

P. Gloor. Neuronal Generators and the Problem of Localization in Electroencephalography: Application of Volume Conductor Theory to Electroencephalography. *Journal of Clinical Neurophysiology*, 2(4): 327–354, 1985.

R. Goebel. BrainVoyager – past, present, future. *NeuroImage*, 62(2): 748–756, 2012.

S. Gonçalves, J. De Munck, J. Verbunt, F. Bijma, R. Heethaar, and F. Lopes da Silva. In vivo measurement of the brain and skull resistivities using an EIT-based method and realistic models for the head. *IEEE Transactions on Biomedical Engineering*, 50(6):754–767, 2003a.

S. Gonçalves, J. De Munck, J. Verbunt, R. Heethaar, and F. Lopes da Silva. In vivo measurement of skull and brain resistivities with EIT based method and analysis of SEF/SEP data. *IEEE Transactions on Biomedical Engineering*, 50(9):1124–1128, 2003b. URL `http://www.ncbi.nlm.nih.gov/pubmed/12943281`.

R. C. Gonzalez and R. E. Woods. *Digital image processing*. Prentice hall Upper Saddle River, 2002.

J. Gotman, E. Kobayashi, A. P. Bagshaw, C.-G. Bénar, and F. Dubeau. Combining EEG and fMRI: a multimodal tool for epilepsy research. *Journal of Magnetic Resonance Imaging*, 23(6):906–920, 2006.

R. Grech, T. Cassar, J. Muscat, K. P. Camilleri, S. G. Fabri, M. Zervakis, P. Xanthopoulos, V. Sakkalis, and B. Vanrumste. Review on solving the inverse problem in EEG source analysis. *Journal of NeuroEngineering and Rehabilitation*, 5(1):1, 2008.

H. Gudbjartsson and S. Patz. The Rician distribution of noisy MRI data. *Magnetic Resonance in Medicine*, 34(6):910–914, 1995.

D. Güllmar. *Anisotropic EEG-MEG Volume Conductor Modeling Based on Diffusion Tensor Imaging*. PhD thesis, Technische Universität Ilmenau, 2008.

D. Güllmar, J. Haueisen, and J. R. Reichenbach. Influence of anisotropic electrical conductivity in white matter tissue on the EEG/MEG forward and inverse solution. A high-resolution whole head simulation study. *NeuroImage*, 51(1):145–63, May 2010.

J. T. Gwin, K. Gramann, S. Makeig, and D. P. Ferris. Removal of movement artifact from high-density EEG recorded during walking and running. *Journal of Neurophysiology*, 103(6):3526–3534, 2010.

H. Hallez. *Incorporation of anisotropic conductivities in EEG source analysis*. PhD thesis, Ghent University, 2008.

H. Hallez, B. Vanrumste, P. Hese, Y. D'Asseler, I. Lemahieu, and R. Walle. A finite difference method with reciprocity used to incorporate anisotropy in electroencephalogram dipole source localization. *Physics in Medicine and Biology*, 50:3787–3806, 2005.

H. Hallez, S. Staelens, and I. Lemahieu. Dipole estimation errors due to not incorporating anisotropic conductivities in realistic head models for EEG source analysis. *Physics in Medicine and Biology*, 54:6079–6093, 2009.

M. S. Hämäläinen and R. J. Ilmoniemi. Interpreting magnetic fields of the brain: minimum norm estimates. *Medical & Biological Engineering & Computing*, 32(1):35–42, 1994.

M. S. Hämäläinen and J. Sarvas. Realistic conductivity geometry model of the human head for interpretation of neuromagnetic data. *IEEE Transactions on Biomedical Engineering*, 36(2):165–171, 1989.

H. Hamer, H. Morris, E. Mascha, M. Karafa, W. Bingaman, M. Bej, R. Burgess, D. Dinner, N. Foldvary, J. Hahn, et al. Complications of invasive video-EEG monitoring with subdural grid electrodes. *Neurology*, 58(1):97–103, 2002.

J. Haueisen, C. Ramon, P. Czapski, and M. Eiselt. On the influence of volume currents and extended sources on neuromagnetic fields: A simulation study. *Annals of Biomedical Engineering*, 23(6):728–739, 1995.

B. He and Z. Liu. Multimodal functional neuroimaging: integrating functional MRI and EEG/MEG. *IEEE Reviews in Biomedical Engineering*, 1:23–40, 2008.

B. He et al. Abstracts of Presentations at the International Conference on Basic and Clinical Multimodal Imaging (BaCI), a Joint Conference of the International Society for Neuroimaging in Psychiatry (ISNIP), the International Society for Functional Source Imaging (IS-FSI), the International Society for Bioelectromagnetism (ISBEM), the International Society for Brain Electromagnetic Topography (IS-BET), and the EEG and Clinical Neuroscience Society (ECNS), in Geneva, Switzerland, September 5-8, 2013. *Clinical EEG and Neuroscience*, 44(4):E1–E121, 2013. doi: 10.1177/1550059413507209. URL `http://eeg.sagepub.com/content/44/4/E1.short`.

T. Heinonen, H. Eskola, P. Dastidar, P. Laarne, and J. Malmivuo. Segmentation of T1 MR scans for reconstruction of resistive head models. *Computer Methods and Programs in Biomedicine*, 54(3):173–181, 1997.

W.-D. Heiss. The potential of PET/MR for brain imaging. *European Journal of Nuclear Medicine and Molecular Imaging*, 36(1):105–112, 2009.

K. Held, E. R. Kops, B. J. Krause, W. M. Wells III, R. Kikinis, and H.-W. Muller-Gartner. Markov random field segmentation of brain MR images. *IEEE Transactions on Medical Imaging*, 16(6):878–886, 1997.

F. A. Hinchey. *Vectors and Tensors for Engineers and Scientists*. Wiley, John & Sons, Inc., 1976. ISBN 0470151943.

R. Hoekema, G. Wieneke, F. Leijten, C. Van Veelen, P. Van Rijen, G. Huiskamp, J. Ansems, and A. Van Huffelen. Measurement of the conductivity of skull, temporarily removed during epilepsy surgery. *Brain Topography*, 16(1):29–38, 2003.

Y. Huang and L. C. Parra. Fully automated whole-head segmentation with improved smoothness and continuity, with theory reviewed. *PloS ONE*, 10(5):e0125477, 2015.

Y. Huang, J. P. Dmochowski, Y. Su, A. Datta, C. Rorden, and L. C. Parra. Automated MRI segmentation for individualized modeling of current flow in the human head. *Journal of Neural Engineering*, 10 (6):066004, 2013.

Z.-K. Huang and K.-W. Chau. A new image thresholding method based on gaussian mixture model. *Applied Mathematics and Computation*, 205(2):899 – 907, 2008. ISSN 0096-3003. doi: DOI:10.1016/j.amc. 2008.05.130. Special Issue on Advanced Intelligent Computing Theory and Methodology in Applied Mathematics and Computation.

G. Huiskamp, M. Vroeijenstijn, R. van Dijk, G. Wieneke, and A. van Huffelen. The need for correct realistic geometry in the inverse EEG problem. *IEEE Transactions on Biomedical Engineering*, 46(11):1281–1287, November 1999. ISSN 0018-9294. doi: 10.1109/10.797987.

H.-J. Huppertz, E. Hof, J. Klisch, M. Wagner, C. H. Lücking, and R. Kristeva-Feige. Localization of interictal delta and epileptiform EEG activity associated with focal epileptogenic brain lesions. *NeuroImage*, 13(1):15–28, 2001.

N. Jafarian, K. Kazemi, H. A. Moghaddam, R. Grebe, M. Fournier, M. S. Helfroush, C. Gondry-Jouet, and F. Wallois. Automatic segmentation of newborns' skull and fontanel from CT data using model-based variational level set. *Signal, Image and Video Processing*, 8(2):377–387, 2014.

H. H. Jasper. The ten-twenty electrode system of the International Federation. *Electroencephalography and Clinical Neurophysiology*, 10:371–375, 1958.

B. Jeffs, R. Leahy, and M. Singh. An evaluation of methods for neuromagnetic image reconstruction. *IEEE Transactions on Biomedical Engineering*, 34(9):713–723, 1987.

M. Jenkinson, M. Pechaud, and S. Smith. BET2: MR-based estimation of brain, skull and scalp surfaces. In *Eleventh annual meeting of the Organization for Human Brain Mapping*, volume 17, page 167, 2005.

C. R. Johnson. Numerical methods for bio-electric field problems. In J. D. Bronzino, editor, *The biomedical engineering handbook*, chapter 12. CRC press, 1995.

K. Kaiboriboon, H. O. Lüders, M. Hamaneh, J. Turnbull, and S. D. Lhatoo. EEG source imaging in epilepsy – practicalities and pitfalls. *Nature Reviews Neurology*, 8(9):498–507, 2012.

S. Kim and J. M. Mountz. SPECT imaging of epilepsy: an overview and comparison with F-18 FDG PET. *International Journal of Molecular Imaging*, 2011, 2011.

F. Klauschen, A. Goldman, V. Barra, A. Meyer-Lindenberg, and A. Lundervold. Evaluation of automated brain MR image segmentation and volumetry methods. *Human Brain Mapping*, 30(4):1310–1327, 2009.

T. Knösche. *Solutions of the Neuroelectromagnetic Inverse Problem – an Evaluation Study*. PhD thesis, University of Twente, Netherlands, 1997.

K. Kobayashi, H. Yoshinaga, Y. Ohtsuka, and J. Gotman. Dipole modeling of epileptic spikes can be accurate or misleading. *Epilepsia*, 46 (3):397–408, 2005.

B. Kolb and I. Q. Whishaw. *Fundamentals of human neuropsychology*. Macmillan, 2009.

J. Kybic, M. Clerc, T. Abboud, O. Faugeras, R. Keriven, and T. Papadopoulo. A common formalism for the integral formulations of the forward EEG problem. *IEEE Transactions on Medical Imaging*, 24(1): 12–28, 2005.

P. Laarne, H. Eskola, J. Hyttinen, V. Suihko, and J. Malmivuo. Validation of a detailed computer model for the electric fields in the brain. *Journal of Medical Engineering & Technology*, 19(2-3):84–87, 1995.

Y. Lai, W. Van Drongelen, L. Ding, K. Hecox, V. Towle, D. Frim, and B. He. Estimation of in vivo human brain-to-skull conductivity ratio from simultaneous extra- and intra-cranial electrical potential recordings. *Clinical Neurophysiology*, 116(2):456–465, 2005. URL `http://www.ncbi.nlm.nih.gov/pubmed/15661122`.

B. Lanfer. *Automatic Generation of Volume Conductor Models of the Human Head for EEG Source Analysis*. PhD thesis, Westfälische Wilhelms-Universität Münster, Münster, 2014.

B. Lanfer, M. Scherg, M. Dannhauer, T. Knösche, M. Burger, and C. Wolters. Influences of skull segmentation inaccuracies on EEG source analysis. *NeuroImage*, 62(1):418–431, 2012.

G. Lantz, R. G. de Peralta, L. Spinelli, M. Seeck, and C. Michel. Epileptic source localization with high density EEG: how many electrodes are needed? *Clinical Neurophysiology*, 114(1):63–69, 2003a.

G. Lantz, L. Spinelli, M. Seeck, R. G. de Peralta Menendez, C. C. Sottas, and C. M. Michel. Propagation of interictal epileptiform activity can lead to erroneous source localizations: a 128-channel EEG mapping study. *Journal of Clinical Neurophysiology*, 20(5):311–319, 2003b.

A. Lascano, T. Hummel, J. Lacroix, B. Landis, and C. Michel. Spatio-temporal dynamics of olfactory processing in the human brain: an event-related source imaging study. *Neuroscience*, 167(3):700–708, 2010.

S. Lau, L. Flemming, and J. Haueisen. Magnetoencephalography signals are influenced by skull defects. *Clinical Neurophysiology*, 125(8):1653–1662, 2014.

S. Law. Thickness and resistivity variations over the upper surface of the human skull. *Brain Topography*, 6(2):99–109, 1993. ISSN 0896-0267.

A. Lefkopoulos, A. Haritanti, E. Papadopoulou, D. Karanikolas, N. Fotiadis, and A. Dimitriadis. Magnetic resonance imaging in 120 patients with intractable partial seizures: a preoperative assessment. *Neuroradiology*, 47(5):352–361, 2005.

S. Lew, C. Wolters, A. Anwander, S. Makeig, and R. MacLeod. Improved EEG source analysis using low-resolution conductivity estimation in a four-compartment finite element head model. *Human Brain Mapping*, 30(9):2862–2878, 2009a.

S. Lew, C. Wolters, T. Dierkes, C. Röer, and R. MacLeod. Accuracy and run-time comparison for different potential approaches and iterative solvers in finite element method based EEG source analysis. *Applied Numerical Mathematics*, 59(8):1970–1988, 2009b.

O. G. Lins, T. W. Picton, P. Berg, and M. Scherg. Ocular artifacts in EEG and event-related potentials I: Scalp topography. *Brain Topography*, 6(1):51–63, 1993.

A. K. Liu, A. Dale, and J. W. Belliveau. Monte Carlo simulation studies of EEG and MEG localization accuracy. *Human Brain Mapping*, 16 (1):47–62, 2002.

S. Ljunggren. A simple graphical representation of Fourier-based imaging methods. *Journal of Magnetic Resonance*, 54(2):338–343, 1983.

N. K. Logothetis and B. A. Wandell. Interpreting the BOLD signal. *Annual Review of Physiology*, 66:735–769, 2004.

F. H. Lopes da Silva and A. van Rotterdam. Biophysical aspects of EEG and Magnetoencephalogram generation. In E. Niedermeyer and F. Lopes da Silva, editors, *Electroencephalography. Basic principles, clinical applications and related fields*, chapter 5, pages 107–125. Williams and Wilkins, Philadelphia, 5 edition, 2005.

S. J. Luck. *An introduction to the event-related potential technique*. MIT press, 2014.

F. Lucka, S. Pursiainen, M. Burger, and C. Wolters. Hierarchical Bayesian inference for the EEG inverse problem using realistic FE head models: Depth localization and source separation for focal primary currents. *NeuroImage*, 61(4):1364–1382, 2012. ISSN 10538119. doi: 10.1016/j.neuroimage.2012.04.017.

M. Lüthi, A. Lerch, T. Albrecht, Z. Krol, and T. Vetter. A hierarchical, multi-resolution approach for model-based skull-segmentation in MRI volumes. Technical report, Technical report, University of Basel, 2009.

M. Lynn and W. Timlake. The numerical solution of singular integral equations of potential theory. *Numerische Mathematik*, 11(1):77–98, 1968.

N. Lynnerup, J. Astrup, B. Sejrsen, et al. Thickness of the human cranial diploe in relation to age, sex and general body build. *Head & Face Medicine*, 1(13), 2005.

J. Malmivuo and R. Plonsey. *Bioelectromagnetism*. Oxford University Press, New York, 1995.

G. Marin, C. Guerin, S. Baillet, L. Garnero, and G. Meunier. Influence of skull anisotropy for the forward and inverse problem in EEG: simulation studies using FEM on realistic head models. *Human Brain Mapping*, 6(4):250–269, 1998.

F. Marino, E. Halgren, J.-M. Badier, M. Gee, and V. Nenov. A finite difference model of electric field propagation in the human head: Implementation and validation. In *Proceedings of the 1993 IEEE Nineteenth Annual Northeast Bioengineering Conference*, pages 82–85. IEEE, 1993.

J. C. Maxwell. *A treatise on electricity and magnetism (1873), Clarendon Press (1891)*. Dover, 1954.

E. McVeigh, M. Bronskill, and R. Henkelman. Phase and sensitivity of receiver coils in magnetic resonance imaging. *Medical Physics*, 13(6): 806–814, 1986.

S. Meckes-Ferber, A. Roten, C. Kilpatrick, and T. J. O'Brien. EEG dipole source localisation of interictal spikes acquired during routine clinical video-EEG monitoring. *Clinical Neurophysiology*, 115(12): 2738–2743, 2004.

P. Mégevand, L. Spinelli, M. Genetti, V. Brodbeck, S. Momjian, K. Schaller, C. M. Michel, S. Vulliemoz, and M. Seeck. Electric source imaging of interictal activity accurately localises the seizure onset zone. *Journal of Neurology, Neurosurgery & Psychiatry*, 85(1):38–43, 2014.

J. W. Meijs, O. W. Weier, M. J. Peters, and A. Van Oosterom. On the numerical accuracy of the boundary element method. *IEEE Transactions on Biomedical Engineering*, 36(10):1038–1049, 1989.

I. Merlet and J. Gotman. Reliability of dipole models of epileptic spikes. *Clinical neurophysiology*, 110(6):1013–1028, 1999.

C. M. Michel, G. Lantz, L. Spinelli, R. G. De Peralta, T. Landis, and M. Seeck. 128-channel EEG source imaging in epilepsy: clinical yield and localization precision. *Journal of Clinical Neurophysiology*, 21(2): 71–83, 2004.

K. Miller. *Biomechanics of the Brain*. Springer Science & Business Media, 2011.

M. Mohr and B. Vanrumste. Comparing iterative solvers for linear systems associated with the finite difference discretisation of the forward problem in electro-encephalographic source analysis. *Medical & Biological Engineering & Computing*, 41(1):75–84, 2003.

V. Montes-Restrepo, H. Hallez, and S. Staelens. Determination of anisotropic ratio of the skull for EEG source localization in patients with epilepsy. In *Abstracts of the 11th FirW PhD Symposium*, page 62, Ghent, Belgium, 2010. Ghent University.

V. Montes-Restrepo, H. Hallez, and S. Staelens. Influence of air cavities of the skull on EEG source localization. In *10th Annual symposium*

of the IEEE EMBS Benelux Chapter. IEEE Engineering in Medicine and Biology Society (EMBS). Benelux Chapter, 2011a.

V. Montes-Restrepo, H. Hallez, and S. Staelens. Influence of skull inhomogeneities on EEG source localization. In *Noninvasive Functional Source Imaging of the Brain and Heart & 2011 8th International Conference on Bioelectromagnetism (NFSI & ICBEM), 2011 8th International Symposium on*, pages 72 –76, may 2011b. doi: 10.1109/NFSI.2011.5936823.

V. Montes-Restrepo, P. van Mierlo, H. Hallez, and S. Staelens. Accurate skull modeling from MRI for EEG source localization. In *Book of Abstracts of the 18th International Conference on Biomagnetism (BIOMAG)*, pages 338–339, Paris, France, Aug. 2012.

V. Montes-Restrepo, G. Strobbe, P. van Mierlo, and S. Vandenberghe. Effects of conductivity perturbations of the tri-layered skull on EEG source analysis. In *Abstracts of Presentations at the International Conference on Basic and Clinical Multimodal Imaging (BaCI)*, page 66, Geneva, Switzerland, September 2013a.

V. Montes-Restrepo, P. van Mierlo, J. D. López, H. Hallez, and S. Vandenberghe. Influence of isotropic skull models on EEG source localization. In *35th Annual International Conference of the IEEE Engineering in Medicine and Biology Society (EMBC)*, pages 3295–3298, Osaka, Japan, July 2013b.

V. Montes-Restrepo, P. van Mierlo, G. Strobbe, S. Staelens, S. Vandenberghe, and H. Hallez. Influence of Skull Modeling Approaches on EEG Source Localization. *Brain Topography*, 27(1):95–111, 2014.

V. Montes-Restrepo, G. Strobbe, E. Carrette, S. Vandenberghe, P. Boon, K. Vonck, and P. van Mierlo. Skull modeling in EEG source localization: comparative analysis in six operated epileptic patients. In *Abstracts of Presentations at the International Conference on Basic and Clinical Multimodal Imaging (BaCI)*, Utrecht, The Netherlands, September 2015.

V. Montes-Restrepo, E. Carrette, G. Strobbe, S. Gadeyne, S. Vandenberghe, P. Boon, K. Vonck, and P. van Mierlo. The Role of Skull Modeling in EEG Source Imaging for Patients with Refractory Temporal Lobe Epilepsy. *Brain Topography*, 29(4):572–589, 2016.

J. C. Mosher and R. M. Leahy. Recursive MUSIC: a framework for EEG and MEG source localization. *IEEE Transactions on Biomedical Engineering*, 45(11):1342–1354, 1998.

J. C. Mosher and R. M. Leahy. Source localization using recursively applied and projected (RAP) MUSIC. *IEEE Transactions on Signal Processing*, 47(2):332–340, 1999.

J. C. Mosher, P. S. Lewis, and R. M. Leahy. Multiple dipole modeling and localization from spatio-temporal MEG data. *IEEE Transactions on Biomedical Engineering*, 39(6):541–557, 1992.

J. C. Mosher, R. M. Leahy, and P. S. Lewis. EEG and MEG: forward solutions for inverse methods. *IEEE Transactions on Biomedical Engineering*, 46(3):245–259, 1999.

J. A. Nelder and R. Mead. A simplex method for function minimization. *The Computer Journal*, 7(4):308–313, 1965.

A. K. Ngugi, C. Bottomley, I. Kleinschmidt, J. W. Sander, and C. R. Newton. Estimation of the burden of active and life-time epilepsy: A meta-analytic approach. *Epilepsia*, 51(5):883–890, 2010.

P. Nunez and R. Srinivasan. *Electric Fields of the Brain: The Neurophysics of EEG*. Oxford University Press, New York, 2005.

M. Oliva, S. Meckes-Ferber, A. Roten, P. Desmond, R. J. Hicks, and T. J. O'Brien. EEG dipole source localization of interictal spikes in non-lesional TLE with and without hippocampal sclerosis. *Epilepsy Research*, 92(2):183–190, 2010.

T. Oostendorp and A. van Oosterom. Source parameter estimation in inhomogeneous volume conductors of arbitrary shape. *IEEE Transactions on Biomedical Engineering*, 36(3):382–391, 1989.

T. Oostendorp, J. Delbeke, and D. Stegeman. The conductivity of the human skull: results of in vivo and in vitro measurements. *IEEE Transactions on Biomedical Engineering*, 47(11):1487–1492, 2000.

R. Oostenveld and P. Praamstra. The five-percent electrode system for high-resolution EEG and ERP measurements. *Clinical Neurophysiology*, 112(4):713–719, 2001.

M. Oozeer, C. Veraart, V. Legat, and J. Delbeke. Simulation of intra-orbital optic nerve electrical stimulation. *Medical and Biological Engineering and Computing*, 43(5):608–617, 2005.

M. Panizo, A. Castellanos, and J. Rivas. Finite-difference operators in inhomogeneous anisotropic media. *Journal of Applied Physics*, 48(3): 1054–1057, 1977.

C. J. Park, J. H. Seo, D. Kim, B. Abibullaev, H. Kwon, Y.-H. Lee, M.-Y. Kim, K. Kim, J. S. Kim, E. Y. Joo, et al. EEG Source Imaging in Partial Epilepsy in Comparison with Presurgical Evaluation and Magnetoencephalography. *Journal of Clinical Neurology*, 2015.

R. Pascual-Marqui. Standardized low resolution brain electromagnetic tomography (sLORETA): technical detail. *Methods and Findings in Experimental and Clinical Pharmacology*, 24(Suppl D):5–12, 2002.

R. Pascual-Marqui, C. Michel, and D. Lehmann. Low resolution electro-magnetic tomography: a new method for localizing electrical activity in the brain. *International Journal of Psychophysiology*, 18(1):49–65, 1994.

R. D. Pascual-Marqui. Discrete, 3D distributed, linear imaging methods of electric neuronal activity. Part 1: exact, zero error localization. *arXiv preprint arXiv:0710.3341*, 2007.

E. Pataraia, G. Lindinger, L. Deecke, D. Mayer, and C. Baumgartner. Combined MEG/EEG analysis of the interictal spike complex in mesial temporal lobe epilepsy. *NeuroImage*, 24(3):607–614, 2005.

R. Plonsey and D. B. Heppner. Considerations of quasi-stationarity in electrophysiological systems. *The bulletin of mathematical biophysics*, 29(4):657–664, 1967.

C. Plummer, A. S. Harvey, and M. Cook. EEG source localization in focal epilepsy: where are we now? *Epilepsia*, 49(2):201–218, 2008.

C. Plummer, M. Wagner, M. Fuchs, A. Harvey, and M. Cook. Dipole versus distributed EEG source localization for single versus averaged spikes in focal epilepsy. *Journal of Clinical Neurophysiology*, 27(3): 141–162, 2010.

K. M. Pohl, S. Bouix, M. Nakamura, T. Rohlfing, R. W. McCarley, R. Kikinis, W. E. L. Grimson, M. E. Shenton, and W. M. Wells. A

hierarchical algorithm for MR brain image parcellation. *IEEE Transactions on Medical Imaging*, 26(9):1201, 2007.

R. Pohlmeier, H. Buchner, G. Knoll, A. RienÄcker, R. Beckmann, and J. Pesch. The influence of skull-conductivity misspecification on inverse source localization in realistically shaped finite element head models. *Brain Topography*, 9:157–162, 1997. ISSN 0896-0267. 10.1007/BF01190384.

S. Pursiainen, F. Lucka, and C. Wolters. Complete electrode model in EEG: relationship and differences to the point electrode model. *Physics in Medicine and Biology*, 57(4):999, 2012.

J. Radon. On determination of functions by their integral values along certain multiplicities. *Ber. der Sachische Akademie der Wissenschaften Leipzig*, 69:262–277, 1917.

C. Ramon, P. Schimpf, and J. Haueisen. Influence of head models on EEG simulations and inverse source localizations. *Biomedical Engineering Online*, 5, 2006. doi: DOI:10.1186/1475-925X-5-10.

C. Ramon, P. Garguilo, E. A. Fridgeirsson, and J. Haueisen. Changes in scalp potentials and spatial smoothing effects of inclusion of dura layer in human head models for EEG simulations. *Frontiers in Neuroengineering*, 7, 2014.

S. M. Rampersad, A. M. Janssen, F. Lucka, Ü. Aydin, B. Lanfer, S. Lew, C. Wolters, D. F. Stegeman, and T. Oostendorp. Simulating transcranial direct current stimulation with a detailed anisotropic human head model. *IEEE Transactions on Neural Systems and Rehabilitation Engineering*, 22(3):441–452, 2014.

G. C. Ribas. The cerebral sulci and gyri. *Neurosurgical focus*, 28(2):E2, 2010.

H. Rifai, I. Bloch, S. Hutchinson, J. Wiart, and L. Garnero. Segmentation of the skull in MRI volumes using deformable model and taking the partial volume effect into account. *Medical Image Analysis*, 4(3): 219–233, 2000.

M. D. Robson, P. D. Gatehouse, M. Bydder, and G. M. Bydder. Magnetic resonance: an introduction to ultrashort TE (UTE) imaging. *Journal of Computer Assisted Tomography*, 27(6):825–846, 2003.

T. Rohlfing, R. Brandt, R. Menzel, and C. R. Maurer. Evaluation of atlas selection strategies for atlas-based image segmentation with application to confocal microscopy images of bee brains. *NeuroImage*, 21 (4):1428–1442, 2004.

C. Rorden, L. Bonilha, J. Fridriksson, B. Bender, and H.-O. Karnath. Age-specific CT and MRI templates for spatial normalization. *NeuroImage*, 61(4):957–65, July 2012. ISSN 1095-9572.

F. Rosenow and H. Lüders. Presurgical evaluation of epilepsy. *Brain*, 124(9):1683–1700, 2001.

M. Rullmann, A. Anwander, M. Dannhauer, S. Warfield, F. Duffy, and C. Wolters. EEG source analysis of epileptiform activity using a 1 mm anisotropic hexahedra finite element head model. *NeuroImage*, 44(2): 399–410, 2009.

S. Rush and D. Driscoll. Current distribution in the brain from surface electrodes. *Anesthesia and analgesia*, 47(6):717–723, 1968.

S. Rush and D. Driscoll. EEG electrode sensitivity-An application of reciprocity. *IEEE Transactions on Biomedical Engineering*, BME-16 (1):15–22, 1969.

O. Ryynänen, J. Hyttinen, and J. Malmivuo. Effect of measurement noise and electrode density on the spatial resolution of cortical potential distribution with different resistivity values for the skull. *IEEE Transactions on Biomedical Engineering*, 53(9):1851–1858, 2006.

Y. Saad. *Iterative methods for sparse linear systems*. Siam, 2003.

R. Sadleir and A. Argibay. Modeling skull electrical properties. *Annals of Biomedical Engineering*, 35(10):1699–1712, 2007.

H. Saleheen and K. T. Ng. New finite difference formulations for general inhomogeneous anisotropic bioelectric problems. *IEEE Transactions on Biomedical Engineering*, 44(9):800–809, 1997.

A. Salek-Haddadi, B. Diehl, K. Hamandi, M. Merschhemke, A. Liston, K. Friston, J. S. Duncan, D. R. Fish, and L. Lemieux. Hemodynamic correlates of epileptiform discharges: an EEG-fMRI study of 63 patients with focal epilepsy. *Brain Research*, 1088(1):148–166, 2006.

B. Saletu, P. Anderer, G. Saletu-Zyhlarz, and R. Pascual-Marqui. EEG mapping and low-resolution brain electromagnetic tomography (LORETA) in diagnosis and therapy of psychiatric disorders: evidence for a key-lock principle. *Clinical EEG and Neuroscience*, 36(2):108–115, 2005.

Y. Salu, L. Cohen, D. Rose, S. Sato, C. Kufta, and M. Hallett. An improved method for localizing electric brain dipoles. *IEEE Transactions on Biomedical Engineering*, 37(7):699–705, 1990. doi: 10.1109/10.55680.

J. Sarvas. Basic mathematical and electromagnetic concepts of the biomagnetic inverse problem. *Physics in Medicine and Biology*, 32:11–22, 1987.

P. Schimpf, C. Ramon, and J. Haueisen. Dipole models for the eeg and meg. *IEEE Transactions on Biomedical Engineering*, 49(5):409–418, 2002.

F. Ségonne, A. Dale, E. Busa, M. Glessner, D. Salat, H. Hahn, and B. Fischl. A hybrid approach to the skull stripping problem in MRI. *NeuroImage*, 22(3):1060–1075, 2004.

D. W. Shattuck and R. M. Leahy. BrainSuite: an automated cortical surface identification tool. *Medical Image Analysis*, 6(2):129–142, 2002.

S. D. Shorvon. The etiologic classification of epilepsy. *Epilepsia*, 52(6): 1052–1057, 2011.

H. Si. Constrained Delaunay tetrahedral mesh generation and refinement. *Finite elements in Analysis and Design*, 46(1):33–46, 2010.

A. Simmons, P. S. Tofts, G. J. Barker, and S. R. Arridge. Sources of intensity nonuniformity in spin echo images at 1.5 T. *Magnetic Resonance in Medicine*, 32(1):121–128, 1994.

J. G. Sled and G. B. Pike. Standing-wave and RF penetration artifacts caused by elliptic geometry: an electrodynamic analysis of MRI. *IEEE Transactions on Medical Imaging*, 17(4):653–662, 1998.

S. M. Smith. Fast robust automated brain extraction. *Human Brain Mapping*, 17(3):143–155, 2002.

S. M. Smith, M. Jenkinson, M. W. Woolrich, C. F. Beckmann, T. E. Behrens, H. Johansen-Berg, P. R. Bannister, M. De Luca, I. Drobn-jak, D. E. Flitney, et al. Advances in functional and structural MR image analysis and implementation as FSL. *NeuroImage*, 23:S208–S219, 2004.

H. Soltanian-Zadeh and J. P. Windham. A multiresolution approach for contour extraction from brain images. *Medical physics*, 24(12): 1844–1853, 1997.

J. Song, K. Morgan, S. Turovets, K. Li, C. Davey, P. Govyadinov, P. Luu, K. Smith, F. Prior, L. Larson-Prior, et al. Anatomically accurate head models and their derivatives for dense array EEG source local-ization. *Functional Neurology, Rehabilitation, and Ergonomics*, 3(2/3): 275, 2013.

L. Sörnmo and P. Laguna. *Bioelectrical Signal Processing in Cardiac and Neurological Applications*. Elsevier Academic Press, 2005.

O. Steinsträter, S. Sillekens, M. Junghoefer, M. Burger, and C. Wolters. Sensitivity of beamformer source analysis to deficiencies in forward modeling. *Human Brain Mapping*, 31(12):1907–1927, 2010. URL http://www.ncbi.nlm.nih.gov/pubmed/21086549.

M. Stenroos and J. Sarvas. Bioelectromagnetic forward problem: isolated source approach revis(it)ed. *Physics in Medicine and Biology*, 57(11): 3517, 2012.

M. Stenroos, V. Mäntynen, and J. Nenonen. A matlab library for solving quasi-static volume conduction problems using the boundary element method. *Computer methods and programs in biomedicine*, 88(3):256–263, 2007.

G. Strobbe, P. van Mierlo, M. De Vos, B. Mijović, H. Hallez, S. Van Huf-fel, J. D. López, and S. Vandenberghe. Bayesian model selection of template forward models for EEG source reconstruction. *NeuroImage*, 93:11–22, 2014.

C. Studholme, D. L. Hill, and D. J. Hawkes. Automated 3-D registration of MR and CT images of the head. *Medical Image Analysis*, 1(2):163–175, 1996.

P. Suetens, E. Bellon, D. Vandermeulen, M. Smet, G. Marchal, J. Nuyts, and L. Mortelmans. Image segmentation: methods and applications

in diagnostic radiology and nuclear medicine. *European Journal of Radiology*, 17(1):14–21, 1993.

D. Swinehart. The Beer-Lambert Law. *Journal of Chemical Education*, 39(7):333, 1962.

W. Szelenberger, J. Wackermann, M. Skalski, S. Niemcewicz, and J. Drojewski. Analysis of complexity of EEG during sleep. *Acta Neurobiologiae Experimentalis*, 56(1):165–169, 1995.

Y. Tai and P. Piccini. Applications of positron emission tomography (PET) in neurology. *Journal of Neurology, Neurosurgery & Psychiatry*, 75(5):669–676, 2004.

C. Tang, F. You, G. Cheng, D. Gao, F. Fu, G. Yang, and X. Dong. Correlation between structure and resistivity variations of the live human skull. *IEEE Transactions on Biomedical Engineering*, 55(9):2286–2292, 2008.

J. F. Thompson, B. K. Soni, and N. P. Weatherill. *Handbook of grid generation.* CRC press, 1998.

A. Tikhonov and V. Arsenin. *Solutions of Ill-Posed Problems.* Vh Winston, New York, 1977.

J. Tohka, A. Zijdenbos, and A. Evans. Fast and robust parameter estimation for statistical partial volume models in brain MRI. *NeuroImage*, 23(1):84–97, 2004.

J. Tohka, I. D. Dinov, D. W. Shattuck, and A. W. Toga. Brain MRI tissue classification based on local Markov random fields. *Magnetic Resonance Imaging*, 28(4):557–573, 2010.

A. Torrado-Carvajal, J. L. Herraiz, J. A. Hernandez-Tamames, S. Jose-Estepar, Y. Eryaman, Y. Rozenholc, E. Adalsteinsson, L. L. Wald, N. Malpica, et al. Multi-atlas and label fusion approach for patient-specific MRI based skull estimation. *Magnetic Resonance in Medicine*, 2015.

D. S. Tuch, V. J. Wedeen, A. Dale, J. S. George, and J. W. Belliveau. Conductivity tensor mapping of the human brain using diffusion tensor MRI. *Proceedings of the National Academy of Sciences*, 98(20):11697–11701, 2001.

S. Turovets, V. Volkov, A. Zherdetsky, A. Prakonina, and A. D. Malony. A 3D finite-difference BiCG iterative solver with the Fourier-Jacobi preconditioner for the anisotropic EIT/EEG forward problem. *Computational and Mathematical Methods in Medicine*, 2014, 2014.

P. A. Valdés-Hernández, N. Von Ellenrieder, A. Ojeda-Gonzalez, S. Kochen, Y. Alemán-Gómez, C. Muravchik, and P. A. Valdés-Sosa. Approximate average head models for EEG source imaging. *Journal of Neuroscience Methods*, 185(1):125–132, 2009.

S. Vallaghé and M. Clerc. A global sensitivity analysis of three and four-layer EEG conductivity models. *IEEE Transactions on Biomedical Engineering*, 56(4):988–995, 2009.

S. Van den Broek, H. Zhou, and M. Peters. Computation of neuromagnetic fields using finite-element method and Biot-Savart law. *Medical & Biological Engineering & Computing*, 34(1):21–26, 1996.

K. Van Leemput, F. Maes, D. Vandermeulen, and P. Suetens. Automated model-based tissue classification of MR images of the brain. *IEEE Transactions on Medical Imaging*, 18(10):897–908, 1999.

W. Van Paesschen, P. Dupont, S. Sunaert, K. Goffin, and K. Van Laere. The use of SPECT and PET in routine clinical practice in epilepsy. *Current Opinion in Neurology*, 20(2):194–202, 2007.

B. D. Van Veen and K. M. Buckley. Beamforming: A versatile approach to spatial filtering. *IEEE ASSP Magazine*, 5(2):4–24, 1988.

B. D. Van Veen, W. Van Drongelen, M. Yuchtman, and A. Suzuki. Localization of brain electrical activity via linearly constrained minimum variance spatial filtering. *IEEE Transactions on Biomedical Engineering*, 44(9):867–880, 1997.

B. Vanrumste. *EEG dipole source analysis in a realistic head model*. PhD thesis, Ghent University, 2002.

B. Vanrumste, G. Van Hoey, R. Van de Walle, M. D'Havé, I. Lemahieu, and P. Boon. Dipole location errors in electroencephalogram source analysis due to volume conductor model errors. *Medical & Biological Engineering & Computing*, 38(5):528–534, 2000.

B. Vanrumste, G. Van Hoey, R. Van de Walle, M. D'Havè, I. Lemahieu, and P. Boon. The validation of the finite difference method and reciprocity for solving the inverse problem in EEG dipole source analysis. *Brain Topography*, 14(2):83–92, 2001. ISSN 0896-0267.

P. T. Vesanen, J. O. Nieminen, K. C. Zevenhoven, J. Dabek, L. T. Parkkonen, A. V. Zhdanov, J. Luomahaara, J. Hassel, J. Penttilä, J. Simola, et al. Hybrid ultra-low-field MRI and magnetoencephalography system based on a commercial whole-head neuromagnetometer. *Magnetic Resonance in Medicine*, 69(6):1795–1804, 2013.

N. von Ellenrieder, L. Beltrachini, and C. H. Muravchik. Electrode and brain modeling in stereo-EEG. *Clinical Neurophysiology*, 123(9):1745–1754, 2012.

H. von Helmholtz. Ueber einige Gesetze der Vertheilung elektrischer Ströme in körperlichen Leitern mit Anwendung auf die thierisch-elektrischen Versuche. *Annalen der Physik*, 165(6):211–233, 1853.

J. Vorwerk, J.-H. Cho, S. Rampp, H. Hamer, T. Knösche, and C. Wolters. A guideline for head volume conductor modeling in EEG and MEG. *NeuroImage*, 100:590–607, 2014.

D. J. Wagenaar, M. Kapusta, J. Li, and B. E. Patt. Rationale for the combination of nuclear medicine with magnetic resonance for preclinical imaging. *Technology in cancer research & treatment*, 5(4): 343–350, 2006.

M. Wagner, M. Fuchs, and J. Kastner. SWARM: sLORETA-weighted accurate minimum norm inverse solutions. In *International Congress Series*, volume 1300, pages 185–188. Elsevier, 2007.

D. Wang, L. Shi, W. C. Chu, J. C. Cheng, and P. A. Heng. Segmentation of human skull in MRI using statistical shape information from CT data. *Journal of Magnetic Resonance Imaging*, 30(3):490–498, 2009.

G. Wang and D. Ren. Effect of brain-to-skull conductivity ratio on EEG source localization accuracy. *BioMed Research International*, 2013, 2013.

Y. Wang, D. R. Haynor, and Y. Kim. An investigation of the importance of myocardial anisotropy in finite-element modeling of the

heart: methodology and application to the estimation of defibrillation efficacy. *IEEE Transactions on Biomedical Engineering*, 48(12): 1377–1389, 2001.

J. P. Wansapura, S. K. Holland, R. S. Dunn, and W. S. Ball. NMR relaxation times in the human brain at 3.0 tesla. *Journal of Magnetic Resonance Imaging*, 9(4):531–538, 1999.

R. Warwick, P. L. Williams, et al. *Gray's Anatomy*, volume 1302. Longman Edinburgh, 1973.

J. C. Weinreb, L. Brateman, E. E. Babcock, K. R. Maravilla, J. M. Cohen, and S. Horner. Chemical shift artifact in clinical magnetic resonance images at 0.35 T. *American Journal of Roentgenology*, 145 (1):183–185, 1985.

D. Weinstein, L. Zhukov, and C. Johnson. Lead-field bases for electroencephalography source imaging. *Annals of Biomedical Engineering*, 28 (9):1059–1065, 2000.

K. Wendel, N. G. Narra, M. Hannula, P. Kauppinen, and J. Malmivuo. The influence of CSF on EEG sensitivity distributions of multilayered head models. *IEEE Transactions on Biomedical Engineering*, 55(4): 1454–1456, 2008.

K. Wendel, O. Väisänen, J. Malmivuo, N. G. Gençer, B. Vanrumste, P. Durka, R. Magjarevic, S. Supek, M. L. Pascu, H. Fontenelle, et al. EEG/MEG source imaging: methods, challenges, and open issues. *Computational Intelligence and Neuroscience*, 2009:13, 2009.

R. Wennberg and D. Cheyne. EEG source imaging of anterior temporal lobe spikes: validity and reliability. *Clinical Neurophysiology*, 125(5): 886–902, 2014.

S. Wiebe. Epidemiology of temporal lobe epilepsy. *Canadian Journal of Neurological Sciences/Journal Canadien des Sciences Neurologiques*, 27(Suppl 1):S6–S10, 2000.

M. Windhoff, A. Opitz, and A. Thielscher. Electric field calculations in brain stimulation based on finite elements: An optimized processing pipeline for the generation and usage of accurate individual head models. *Human Brain Mapping*, 2011.

J. R. Wolpaw, N. Birbaumer, D. J. McFarland, G. Pfurtscheller, and T. M. Vaughan. Brain–computer interfaces for communication and control. *Clinical Neurophysiology*, 113(6):767–791, 2002.

C. Wolters. *Influence of tissue conductivity inhomogeneity and anisotropy on EEG/MEG based source localization in the human brain*. PhD thesis, Max Planck Institute of Cognitive Neuroscience Leipzig, 2003.

C. Wolters, M. Kuhn, A. Anwander, and S. Reitzinger. A parallel algebraic multigrid solver for finite element method based source localization in the human brain. *Computing and Visualization in Science*, 5 (3):165–177, 2002.

C. Wolters, A. Anwander, X. Tricoche, D. Weinstein, M. Koch, and R. MacLeod. Influence of tissue conductivity anisotropy on EEG/MEG field and return current computation in a realistic head model: A simulation and visualization study using high-resolution finite element modeling. *NeuroImage*, 30(3):813–826, 2006. ISSN 1053-8119.

C. Wolters, A. Anwander, G. Berti, and U. Hartmann. Geometry-adapted hexahedral meshes improve accuracy of finite-element-method-based EEG source analysis. *IEEE Transactions on Biomedical Engineering*, 54(8):1446–1453, 2007.

World Health Organization. Epilepsy. Fact sheet No. 999, May 2015.

X.-L. Xu, B. Xu, and B. He. An alternative subspace approach to EEG dipole source localization. *Physics in Medicine and Biology*, 49(2):327, 2004.

Y. Yan, P. Nunez, and R. Hart. Finite-element model of the human head: scalp potentials due to dipole sources. *Medical & Biological Engineering & Computing*, 29(5):475–481, 1991.

D. Young. Iterative methods for solving partial difference equations of elliptic type. *Transactions of the American Mathematical Society*, 76 (1):92–111, 1954.

P. A. Yushkevich, J. Piven, H. C. Hazlett, R. G. Smith, S. Ho, J. C. Gee, and G. Gerig. User-guided 3D active contour segmentation of anatomical structures: significantly improved efficiency and reliability. *NeuroImage*, 31(3):1116–1128, 2006.

F. Zanow and M. Peters. Individually shaped volume conductor models of the head in EEG source localisation. *Medical & Biological Engineering & Computing*, 33(4):582–588, 1995.

Y. Zhang, M. Brady, and S. Smith. Segmentation of brain MR images through a hidden Markov random field model and the expectation-maximization algorithm. *IEEE Transactions on Medical Imaging*, 20 (1):45–57, 2001.

Y. Zhang, W. Van Drongelen, and B. He. Estimation of in vivo brain-to-skull conductivity ratio in humans. *Applied Physics Letters*, 89(22): 223903–2239033, 2006.

E. Ziegler, S. L. Chellappa, G. Gaggioni, J. Q. Ly, G. Vandewalle, E. André, C. Geuzaine, and C. Phillips. A finite-element reciprocity solution for EEG forward modeling with realistic individual head models. *NeuroImage*, 103:542–551, 2014.

List of Publications

Journal papers

[1] **Montes-Restrepo, V.**, Carrette, E., Strobbe, G., Gadeyne, S., Vandenberghe, S., Boon, P., Vonck, K., van Mierlo, P., (2016). The Role of Skull Modeling in EEG Source Imaging for Patients with Refractory Temporal Lobe Epilepsy. *Brain Topography*, 29(4), p. 572–589.

[2] Strobbe, G., Carrette, E., López, J.D., **Montes-Restrepo, V.**, Van Roost , D., Meurs, E., Vonck, K., Boon, P., Vandenberghe, S., van Mierlo, P. (2016). Electrical source imaging of interictal spikes using multiple sparse volumetric priors for presurgical epileptogenic focus localization. *NeuroImage: Clinical*, 11, p. 252–263.

[3] **Montes-Restrepo, V.**, van Mierlo, P., Strobbe, G., Staelens, S., Vandenberghe, S., Hallez, H. (2014). Influence of Skull Modeling Approaches on EEG Source Localization. *Brain Topography*, 27(1), p. 95–111.

[4] Crevecoeur, G., **Montes-Restrepo, V.**, Staelens, S. (2012). Subspace electrode selection methodology for the reduction of the effect of uncertain conductivity values in the EEG dipole localization: a simulation study using a patient-specific head model. *Physics in Medicine and Biology*, 57(7), p. 1963–1986.

Conference proceedings

[1] **Montes-Restrepo, V.**, van Mierlo, P., López, J.D., Hallez, H., Vandenberghe, S. (2013). Influence of isotropic skull models on EEG source localization. In *35th Annual International Conference*

of the IEEE Engineering in Medicine and Biology Society (EMBC), p. 3295–3298.

[2] **Montes-Restrepo, V.**, Hallez, H., Staelens, S. (2011). Influence of skull inhomogeneities on EEG source localization. In *8th International Symposium on Noninvasive Functional Source Imaging of the Brain and Heart 2011 8th International Conference on Bioelectromagnetism (NFSI & ICBEM)*, p. 72–76.

[3] van Mierlo P., **Montes-Restrepo V.**, Hallez, H., Staelens, S. (2011). Epileptic brain network from scalp EEG: identifying the epileptic driver by connectivity analysis on brain waveforms. In *8th International Symposium on Noninvasive Functional Source Imaging of the Brain and Heart 2011 8th International Conference on Bioelectromagnetism (NFSI & ICBEM)*, p. 114–118.

Conference abstracts

[1] **Montes-Restrepo, V.**, Strobbe, G., Carrette, E., Vandenberghe, S., Boon, P., Vonck, K., van Mierlo, P. (2015). Skull modeling in EEG source localization: comparative analysis in six operated epileptic patients. In *Abstracts of Presentations at the International Conference on Basic and Clinical Multimodal Imaging (BaCI)*.

[2] **Montes-Restrepo, V.**, Strobbe, G., van Mierlo, P., Vandenberghe, S. (2013). Effects of conductivity perturbations of the tri-layered skull on EEG source analysis. *Abstracts of Presentations at the International Conference on Basic and Clinical Multimodal Imaging (BaCI)*, p. 66.

[3] Strobbe, G., Cárdenas, D., **Montes-Restrepo, V.**, van Mierlo, P., Vandenberghe, S. (2013). Selecting volume conductor models for EEG source localization of epileptic spikes: preliminary results based on 4 operated epileptic patients. *Abstracts of Presentations at the International Conference on Basic and Clinical Multimodal Imaging (BaCI)*, p. 63.

[4] **Montes-Restrepo, V.** (2012). Localizing sources in the brain: How should we model the skull?. *13th FirW PhD Symposium*, Ghent University.

[5] Strobbe, G., López, J., **Montes-Restrepo, V.**, van Mierlo, P., Hallez, H., Vandenberghe, S. (2012). Comparing finite difference forward models using free energy based on multiple sparse priors. *18th Annual Meeting of the Organization for Human Brain Mapping*, p. 181.

[6] **Montes-Restrepo, V.**, van Mierlo, P., Hallez, H., Staelens, S. (2012). Accurate skull modeling from MRI for EEG source localization. In *Book of Abstracts of the 18th International Conference on Biomagnetism (BIOMAG)*, p. 338.

[7] van Mierlo, P., Strobbe, G., **Montes-Restrepo, V.**, Hallez, H., López, J.D., Staelens, S. (2012). Added value of connectivity analysis on brain waveforms in EEG source reconstruction to detect the epileptic driver during seizures. *Book of Abstracts of the 18th International Conference on Biomagnetism (BIOMAG)*, p. 98.

[8] **Montes-Restrepo, V.**, Hallez, H., Staelens, S. (2011). Influence of air cavities of the skull on EEG source localization. *IEEE EMBS Benelux Chapter, Annual symposium, Abstracts*.

[9] **Montes-Restrepo, V.** (2010). Determination of anisotropic ratio of the skull for EEG source localization in patients with epilepsy. *11th FirW PhD Symposium*, Ghent University, p. 62.